Nuclear structure at the neutron emission threshold and below explored via beta-decays of ^{2}, ^{3}Ga and As

Lama Al Ayoubi

THESE DE DOCTORAT

NNT : 2023UPASP045

Nuclear structure at the neutron emission threshold and below explored via beta-decays of ^{82,83}Ga and ^{86}As

Structure nucléaire au seuil d'émission d'un neutron et en dessous explorée par la décroissance béta de ^{82,83}Ga et ^{86}As

Thèse de doctorat de l'université Paris-Saclay et de l'université de Jyväskylä

École doctorale n° 576 : particules hadrons énergie et noyau : instrumentation, imagerie, cosmos et simulation (PHENIICS)
Spécialité de doctorat : Physique nucléaire
Graduate School : Physique. Référent : Faculté des sciences d'Orsay

Thèse préparée dans les unités de recherche **IJCLab** (Université Paris-Saclay, CNRS) et **Accelerator laboratory** (University of Jyväskylä), sous la direction de **Iolanda MATEA MACOVEI**, Maître de Conférence, la co-direction d'**Anu KANKAINEN**, Professeure, et le co-encadrement d'**Ari JOKINEN**, Professeur.

Thèse soutenue à Jyväskylä, le 25 Avril 2023, par

Lama AL AYOUBI

Composition du jury

Membres du jury avec voix délibérative

María José GARCÍA BORGE Professeure, Consejo Superior de Investigaciones Cientificas (CSIC)	Présidente
Muhsin N. HARAKEH Professeur, University of Groningen	Rapporteur & Examinateur
Robert PAGE Professeur, University of Liverpool	Rapporteur & Examinateur
David VERNEY Directeur de recherche,CNRS, IJCLab, Orsay	Examinateur

université PARIS-SACLAY

ÉCOLE DOCTORALE
Particules, hadrons, énergie et noyau : instrumentation, imagerie, cosmos et simulation (PHENIICS)

Titre : Structure nucléaire au seuil d'émission d'un neutron et en dessous explorée par la décroissance béta de ^{82,83}Ga et ^{86}As.

Mots clés : Structure nucléaire, décroissance béta, résonance dipolaire pygmée, processus r, noyaux riches en neutrons, spectroscopie de désintégration, probabilité d'émission de neutrons.

Résumé : Le travail présenté dans cette thèse est axé sur l'étude de la décroissance β des noyaux riches en neutrons autour de la fermeture de couches N=50, en s'interessant particulièrement à la population des états de haute énergie, autour du seuil d'émission des neutrons. Quelle est la structure de ces états, s'agit-il d'états dipolaires pygmées (PDR), comment la décroissance bêta est-elle liée aux états PDR sont quelques-unes des questions qui ont motivé cette étude. Les recherches ont été menées au moyen de deux expériences complémentaires. La première a été réalisée auprès d'ALTO (Accélérateur Linéaire et Tandem d'Orsay) et a été dédiée à l'étude de la spectroscopie γ-retardée de ^{82,83}Ge en utilisant les scintillateurs PARIS (Photon Array for studies with Radioactive Ion and Stable beams) et les détecteurs HPGe. La seconde expérience, visant à étudier la spectroscopie γ retardée de ^{86}Se, a été réalisée dans l'installation IGISOL (Ion Guide Isotope Separator On-Line) du JYFL Accelerator Laboratory de l'Université de Jyväskylä. Pour cette dernière expérience, le piège de Penning JYFLTRAP a été utilisé pour fournir des échantillons purs de ^{86}As et la spectroscopie gamma retardée β a été réalisée avec des détecteurs HPGe.

Une analyse détaillée des deux expériences est présentée dans ce manuscrit. Les schémas de niveaux des noyaux fils de la décroissance β, ^{82}Ge (N=50), ^{83}Ge (N=51), et ^{86}Se (N=52), ont été mis à jour, et plus de 80 nouvelles transitions γ ont été observées. Des transitions gamma d'une énergie supérieure au seuil de séparation d'un neutron ont été détectées pour la première fois dans ^{82}Ge. De plus, de nouvelles transitions gamma suivant l'émission bêta retardée des neutrons ont été observées à la fois dans le ^{81}Ge et le ^{85}Se. Les demi-vies du ^{82,83}Ga et du ^{86}As ont été mesurées ainsi que les probabilités d'émission de neutrons, P_n, du ^{83}Ga et du ^{86}As.

Les états de haute énergie peuplés dans la décroissance β de ^{82}Ga se trouvent dans une région où l'on s'attend à ce que la PDR apparaisse. Les calculs QRPA et pnQRPA ont été effectués pour les distributions B(E1) et B(GT) pour ^{82}Ge. Les distributions calculées de la force de B(E1) montrent une force dipolaire basse compatible avec le PDR. La composition des états PDR calculés est accessible en termes d'excitations quasi-particulaires (qp) et aux densités de transition des neutrons et des protons. En comparant les spectres B(E1) et B(GT) expérimentaux et calculés et en gardant à l'esprit que la décroissance β ne peut se connecter aux états finaux qu'à travers des règles de sélection particulières, on discute la structure des états situés à haute énergie autour du seuil de séparation des neutrons peuplées par la décroissance bêta et qui se connectent directement à l'état fondamental ou à l'état 2^+ dans ^{82}Ge, ainsi que de l'éventuel caractère dipolaire des transitions.

université PARIS-SACLAY

ÉCOLE DOCTORALE
Particules, hadrons, énergie et noyau : instrumentation, imagerie, cosmos et simulation (PHENIICS)

Title : Nuclear structure at the neutron emission threshold and below explored via beta-decays of ^{82,83}Ga and ^{86}As

Keywords : Nuclear structure, β-decay, pygmy dipole resonance, r-process, neutron-rich nuclei, decay spectroscopy, neutron emission probability.

Abstract : The work presented in this Ph.D. thesis focuses on the β-decay studies of neutron-rich nuclei around the N=50 shell closure, with a particular interest in the population of high energy states around the neutron emission threshold. What is the structure of these states, are they Pygmy Dipole States (PDR), and how does beta-decay connect to PDR states are some of the questions that motivated this study. The research was conducted through two complementary experiments. The first was performed at the ALTO facility (Accélérateur Linéaire et Tandem d'Orsay) and aimed at studying β-delayed gamma spectroscopy of ^{82,83}Ge using PARIS (Photon Array for studies with Radioactive Ion and Stable beams) scintillators and HPGe detectors. The second experiment, aiming at the study of β-delayed gamma spectroscopy of ^{86}Se, was carried out at the Ion Guide Isotope Separator On-Line (IGISOL) facility of the JYFL Accelerator Laboratory at the University of Jyväskylä. For the latter experiment, the JYFLTRAP Penning trap was used to provide pure samples of ^{86}As and the β-delayed gamma spectroscopy was performed with high-resolution germanium detectors.
A detailed analysis of the two experiments is presented. The level schemes of the β-decay daughters, ^{82}Ge (N=50), ^{83}Ge (N=51), and ^{86}Se (N=52), were updated, and more than 80 new γ-ray transitions were observed. γ-ray transitions with energies higher than the neutron separation energy were detected for the first time in ^{82}Ge. In addition, new gamma-ray transitions following the beta-delayed neutron emission were observed in both ^{81}Ge and ^{85}Se. The half-lives of ^{82,83}Ga and ^{86}As were measured as well as the neutron emission probabilities, P_n, of both ^{83}Ga and ^{86}As.
The high-energy states populated in the β-decay of ^{82}Ga lie in a region where PDR is expected to appear. QRPA and pnQRPA calculations have been performed for the electric dipole B(E1) and Gamow-Teller strength B(GT) distributions for ^{82}Ge. Calculated B(E1) strength distributions show a low-lying dipole strength compatible with PDR. The composition of the calculated PDR states can be accessed in terms of quasi-particle (qp) excitations and neutron and proton transition densities. Comparing the experimental and calculated B(E1) and B(GT) distributions and keeping in mind that β-decay can only connect with final states through particular selection rules, this work discusses the structure of states populated by beta-decay lying at high energy around the neutron separation energy that connect directly to the ground or the 2^+ state in ^{82}Ge and their eventual dipole character.

Author

Lama Al Ayoubi
Department of Physics
University of Jyväskylä
Jyväskylä, Finland

Department of Physics
University of Paris-Saclay
Orsay, France

Supervisors

Prof. Anu Kankainen
Department of Physics
University of Jyväskylä
Jyväskylä, Finland

Prof. Iolanda Matea Macovei
Department of Physics
University of Paris-Saclay
Orsay, France

Reviewers

Prof. Muhsin N. Harakeh
University of Groningen
Groningen, Norway

Prof. Robert Page
University of Liverpool
Liverpool, United Kingdom

Opponent

Prof. María José García Borge
Consejo Superior de Investigaciones Cientificas (CSIC)
Madrid, Spain

TIIVISTELMÄ (ABSTRACT IN FINNISH)

Ydinrakenteen tutkimusta neutronin sidosenergian lähellä ja sen alapuolella ^{82,83}Ga- ja ^{86}As -ytimien beetahajoamisten kautta

Tässä väitöskirjassa keskitytään neutronirikkaiden, lähellä neutronikuorta $N = 50$ olevien ydinten beetahajoamisten tutkimukseen. Erityisenä kiinnostuksen kohteena ovat beetahajoamisen syöttämät korkean viritysenergian tilat lähellä neutronin sidosenergiaa. Tutkimuksessa pyrittiin ymmärtämään, mikä on näiden tilojen rakenne, ovatko ne pygmidipoliresonanssi (PDR) -tiloja, ja kuinka beetahajoaminen kytkeytyy näihin PDR-tiloihin. Tutkimus koostui kahdesta toisiaan täydentävästä tieteellisestä kokeesta. Ensimmäinen koe suoritettiin ALTO (Accélérateur Linéaire et Tandem d'Orsay) -kiihdytinlaboratoriossa. Kokeessa tutkittiin beetaviivästettyä gammaspektroskopiaa käyttäen ^{82,83}Ge -ydinten rakennetta hyödyntäen PARIS (Photon Array for studies with Radioactive Ion and Stable beams) -tuikeilmaisinjärjestelmää sekä germaniumilmaisimia. Toinen koe suoritettiin Jyväskylän yliopiston kiihdytinlaboratorion IGISOL (Ion Guide Isotope Separator On-Line) -laitteistolla ja siinä tutkittiin ^{86}Se-ytimen rakennetta beetaviivästetyllä gammaspektroskopialla käyttäen korkean resoluution germaniumilmaisimia ja JYFLTRAP -Penningin loukun toimittamaa puhtaasti $^{86}As^{+}$ -ioneista koostuvaa suihkua.

Kokeissa kerätyn aineiston analyysi käydään yksityiskohtaisesti lävitse. Tutkittujen beetahajoamisten tytärydinten, ^{82}Ge ($N = 50$), ^{83}Ge ($N = 51$), ja ^{86}Se ($N = 52$), energiatasokaaviot päivitettiin lisäämällä niihin yhteensä yli 80 mittauksissa havaittua uutta gammasiirtymää. ^{82}Ge-ytimessä havaittiin ensimmäistä kertaa gammasiirtymiä energiatasoilta, jotka ovat neutronin sidosenergian yläpuolella. ^{82}Ga-ytimen beetahajoamisen syöttämät korkean viritysenergian tilat ^{82}Ge-tytärytimessä sijaitsevat alueella, jossa PDR-tilojen odotetaan olevan. Tämän tutkimiseksi QRPA- ja pnQRPA- menetelmillä laskettiin sähköisen dipolisiirtymän voimakkuuden $B(E1)$ sekä Gamow-Teller -siirtymän voimakkuuden $B(GT)$ jakautumista ^{82}Ge-ytimessä. $B(E1)$-jakauman voimakkuus erityisesti matalahkon energian alueella sopisi yhteen PDR:n kanssa. Uusia beetaviivästettyä neutroniemissiota seuraavia gammasiirtymiä havaittiin sekä ^{81}Ge- että ^{85}Se-ytimissä. ^{82,83}Ga- ja ^{86}As-ydinten puoliintumisajat määritettiin samoin kuin beetaviivästetyn neutroniemission todennäköisyydet (P_n) ^{83}Ga- ja ^{86}As-ytimille. Tulosten merkitystä pohditaan niin ydinrakenteen kuin astrofysikaalisen *r*-prosessin kannalta.

PREFACE

The work presented in this thesis was conducted between 2019 and 2023 at the Department of Physics, University of Jyväskylä, Finland, and at the IJCLab, University of Paris-Saclay, France, as part of my cotutelle Ph.D. program. I would like to express my gratitude to all those who have contributed to the successful completion of my Ph.D. thesis.

I am particularly grateful to my Ph.D. supervisors, Anu Kankainen and Iolanda Matea, for their unwavering support, encouragement, and guidance throughout my academic journey. Their expert supervision and positive attitude made my experience both comfortable and pleasant. Having one great supervisor is widely regarded as a matter of chance, and I was lucky enough to have two! I would like to thank also my co-supervisors, Ari Jokinen and David Verney, for providing me with valuable advice and suggestions.

I am also grateful to my reviewers, Prof. Muhsin N. Harakeh and Prof. Robert Page, for thoroughly examining my work and to Prof. María José García Borge for accepting to be my Opponent.

I would like to thank Isabelle Deloncle, Sophie Peru Desenfants, Kamila Sieja, and Elena Litvinova for their significant contributions to this thesis by providing their expertise in theoretical calculations. Additionally, thanks to Stylianos Nikas for providing his astrophysical calculations. Their contributions have been crucial in completing the research presented in this thesis, and I am genuinely thankful for their support.

I have a special thought for Hicham Al Falou and Beyhan Bastin. I am grateful for your introduction to the fascinating world of nuclear physics, for believing in me, for giving me my first chances, and for your recommendations that ultimately led me to pursue and complete my Ph.D.

The cotutelle program offered me the opportunity to work with different research groups. I would like to acknowledge the IGISOL and FIIRST groups for their support and encouragement. My gratitude also goes to the Ph.D. students and post-docs in both universities. Special thanks to Clément Delafosse and Marek Stryjczyk for their invaluable assistance. They were always available whenever I needed help, and working with them in the lab has shaped my current knowledge.

Among the many accomplishments I achieved during those 4 years, the friendships I formed were undoubtedly one of the most meaningful. I would like to express my gratitude to Marjut, George, Minna, and Daniel for the wonderful memories we created together. Your companionship was truly a highlight of my journey, and I am grateful for the support and joy you brought into my life.

The Soukouti Family, Hussam and Eve, thank you for all the help you provided from the day I arrived in Jyväskylä. The moments we have shared have made it easier for me to be away from home, and I sincerely thank you for your kindness and companionship.

It’s true that moving to France at the beginning of the COVID-19 pandemic made my experience more difficult than expected, but on the other side, I was fortunate to have had the company of my sister, Hanane, and the Mahfoud Family during that challenging period. Spending quality time with Hanane and my niece, Yasmine, has been a source of comfort for me, making everything feel better. I want to extend a special thanks here to Marwa, the best lockdown mate I could ask for!

I would like to equally thank my hometown friends, Rokaya, Hanadi, and Baraa, for always being supportive despite the long distances.

And now, to my husband, Khaled. No words are enough to acknowledge your support and encouragement. You believed in me when I didn’t believe in myself and always pushed me to be my best. You listened to my endless complaints, celebrated my successes, and comforted me during my failures. This Ph.D. would not have been the same without you.

Finally, to my family..

لن تكفي جُمل الشُكر، حتى لو بلغت ملء الأرض والسماء، أن تُعبِّر عن فضل عائلتي. إن كان لبحثي قيمة، فهذا بفضل الله و فضلكم. أبي الكريم، مثلي الأعلى، قدوتي، فخري و عزّي، حفظكَ الله لنا، وجعلك ذخرًا لنا، وقلبًا نابضًا أستلهم منه طاقتي الإيجابية. أُمي الحنون، التي جعلتني أتمسك بالأمل وأتجاوز الصعاب بكل ثبات، أطال الله في عمرك، وسلمك من جميع الأسقام. إخوتي وأخواتي، يا من أفضتم عليّ من جمال روحكم على الدوام، أدامكم الله لي سنداً و قوة. اهدي بحثي هذا لكم، شكراً من القلب، و الحمد لله رب العالمين.

Jyväskylä, Wednesday 14th June, 2023
Lama Al Ayoubi

ACKNOWLEDGEMENTS

This project has received funding from the European Union's Horizon 2020 research and innovation program under grant agreement No 771036 (ERC CoG MAIDEN) and under grant agreement No 654002 (ENSAR2). The use of the IFIN-HH Clover detectors in the I281 experiment at IGISOL is gratefully acknowledged, as well as the use of the PARIS detectors at ALTO for the NRI15 experiment.

CONTENTS

1 GENERAL INTRODUCTION

Nuclear physics is an intriguing and rapidly developing field that has played a crucial role in shaping our understanding of the universe. Nuclear physics is at the forefront of scientific research, from the energy that powers our homes and cities to the processes that drive the stars and the elements that make up our world. It fundamentally focuses on the behavior of protons and neutrons that make up the nucleus of atoms. The protons in the nucleus have a positive electric charge, while the neutrons have no electric charge. In the nucleus, the protons and neutrons are held together by the strong nuclear force, one of the four fundamental forces of nature. The number of protons in the nucleus, also known as the atomic number, determines the element to which an atom belongs. The number of neutrons in the nucleus, however, does not affect the element to which an atom belongs but determines the isotope of that element.

Nuclei can be classified into two main categories: stable and unstable. Stable nuclei are characterized by an infinite lifetime. Atomic nuclei are the building blocks of all matter around us. Unstable nuclei, also known as radioactive nuclei, are those that undergo radioactive decay by emitting radiation (α, β, γ, X-ray..), or in the case of heavier nuclei by emitting a nucleus heavier than an α-particle (cluster decay and nuclear fission). Most of these elements are not found in nature in large quantities and are usually produced artificially in the laboratory or in nuclear reactions that occur in the universe. Understanding the properties of unstable nuclei is essential for comprehending the processes that led to the formation of the elements and the properties of stars and galaxies. It is also crucial for applying nuclear physics in technology, including nuclear power, medical imaging, or cancer treatment.

The technical advances have made it possible to produce more exotic nuclei (i.e., further away from the valley of stability) and to collect data that constrain the nuclear models and highlight unusual behaviors that remain to be explained. Moreover, β-decay studies give access to phenomena governed by the weak interaction. Today, β-decay is still the subject of much experimental and theoretical research. β-decay studies are at the so-called « discovery frontier» meaning that even a low counting rate can provide important structure information. In the astro-

physical field, the understanding of the nucleosynthesis of elements beyond iron is still limited by the models describing nuclear systems. Some key observables, such as half-lives or masses, are not always reliably reproduced. However, many exotic nuclei playing a key role in nucleosynthesis are very difficult or even impossible to produce and study in laboratories. This highlights the importance of the β-decay studies of nuclei far from the valley of stability to validate the theoretical models and increase their predictability. Not to mention that the β^--decay process, converting a neutron into a proton, changes the element in question, making the β-decay studies important for elemental nucleosynthesis.

This thesis contributes to the current understanding of nuclear physics by presenting research on the structure of neutron-rich nuclei close to the doubly magic ^{78}Ni nucleus. This region is particularly interesting for the r-process since the first r-process abundance peak is located at A $\approx$ 80 close to ^{78}Ni , which is the first waiting point of the r-process (the point in the nuclear chart where the (n, γ) and (γ, n) reactions equilibrate allowing the nucleus to decay by β-decay). Beta decay spectroscopy of nuclei in this area is important to enhance our knowledge of the nuclear structure, which is beneficial in refining nucleosynthesis process modeling, that can impact the prediction of the r-process path [1].

Two beta-decay spectroscopy experiments were performed for this Ph.D. thesis project. The first was carried out at the ALTO facility at IJCLab, Orsay, in 2019. It was dedicated to studying the β-decay of ^{82}Ga and ^{83}Ga isotopes using high-purity germanium detectors and the PARIS array for gamma-ray detection. The second experiment of this thesis was performed in 2022 at the IGISOL facility at the University of Jyväskylä, Finland. It was dedicated to studying the decay of the neutron-rich ^{86}As, selected with the double Penning trap JYFLTRAP, and measured using high-purity germanium detectors. The physics background and motivation behind these experiments are presented in this manuscript's second and third chapters. The fourth chapter explains the experimental setup utilized for data collection in the two experiments. The fifth chapter describes the analysis of the obtained data. In the sixth chapter, we present the results obtained from studying all the nuclei, including level schemes, half-life measurements, and estimations of neutron emission probability. Furthermore, the seventh chapter compares some observed properties of the studied nuclei with HFB-QRPA and shell-model calculations. Finally, we conclude the study by providing some perspectives on the work conducted.

2 SELECTED EXPERIMENTAL AND THEORETICAL TOOLS FOR NUCLEAR STRUCTURE STUDIES

2.1 Beta and γ decay

In 1900, Henri Becquerel [2] identified β radiation to be an electron and called the process β^- decay. Then, after the positron was identified in cosmic ray interactions by Carl David Anderson [3], β^+ decay was observed from ^{30}P by Frédéric and Irène Joliot-Curie in 1934 [4]. In the same year, Wick [5] and Yukawa [6] developed the theory of electronic capture, first observed in 1937 by Luiz Alvarez [7]. The continuous character of the energy spectrum of electrons emitted during a β^--decay remained a mystery for many years. This effectively contradicts the energy conservation law in the hypothesis that only a β-particle would be emitted. Similarly, during a β-decay, the nucleus mass number is conserved, which implies an integer spin change. However, the emission of a single electron, carrying a spin of 1/2, induces a half-integer spin change. Faced with these contradictions, Wolfgang Pauli [8], in 1930, proposed that a third, very light, and uncharged particle is involved in this disintegration process. He named it neutron, assumed it is in the nucleus, and is emitted during the decay. In 1933, Enrico Fermi [9] took up this formalism and renamed the particle a "neutrino." He also assumed that both the neutrino and the β particle are created in the process. Equation 2.1 summarizes the three β-decay processes. In the case of a neutron-rich nucleus, a β^- decay occurs, corresponding to a neutron that transforms into a proton. While in the case of neutron-deficient nuclei, a β^+ decay or an electron capture (EC) occurs, transforming a proton into a neutron.

$$\begin{aligned} \beta^- &: {}^{A}_{Z}X_N \rightarrow {}^{A}_{Z+1}X'_{N-1} + e^- + \bar{\nu_e} \\ \beta^+ &: {}^{A}_{Z}X_N \rightarrow {}^{A}_{Z-1}X''_{N+1} + e^+ + \nu_e \\ EC &: {}^{A}_{Z}X_N + e^- \rightarrow {}^{A}_{Z-1}X''_{N+1} + \nu_e \end{aligned} \tag{2.1}$$

In equation 2.1, ${}^{A}_{Z}X_N$ represents a nucleus with Z protons (chemical element X), N neutrons, and a mass number A = Z+N. X′ and X″ denote the elements with Z+1 and Z-1 protons, respectively.

When considering neutron-rich nuclei far from the valley of stability, the β^- decay can be illustrated in Fig. 2.1 below. The parent and daughter nucleus mass difference determines the energy window available for the decay process. This quantity is denoted Q_β and must be positive for the process to take place. The decay can leave the daughter nucleus in an excited state. There are many excited states (or levels), and each has a different probability of being fed. This feeding is denoted I_β. The nucleus then de-excites by one or more de-excitation γ-ray transitions. It is also possible that the populated level lies above the neutron emission threshold S_n. A β-delayed neutron can then be emitted, and the produced nucleus has two neutrons fewer than the parent nucleus and one proton more.

In conclusion, the beta decay within a large Q_β window provides valuable insights into the structure of the daughter nucleus through its access to a significant part of the excitation spectrum. Several observables, including $\log ft$ and I_β, as well as the γ-decay of the excited states in the daughter nuclei, play critical roles in the work presented in this thesis. More explanations are provided in the coming sections.

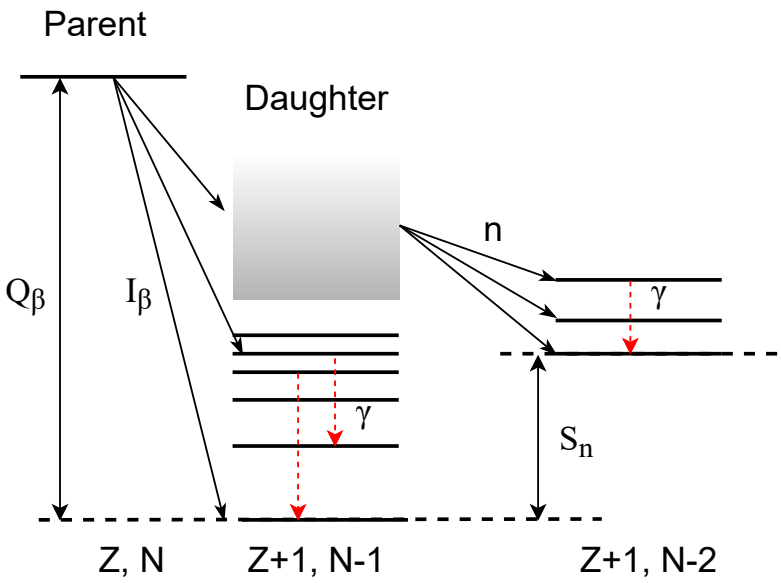

Figure 2.1: Diagram illustrating the β-decay of a neutron-rich nucleus with Z protons and N neutrons.

2.1.1 Comparative half-life

The weak interaction (beta decay) is weak compared with the strong interaction governing the initial and final states of the nuclei involved. Consequently, the transition rate λ of the decay from an initial state to a final state, commonly called Fermi's Golden Rule, can be written as [10]:

$$\lambda = \frac{2\pi}{\hbar}|V_{fi}|^2\rho(E_f) \tag{2.2}$$

where $\rho(E_f)$ represents the density of final states and V_{fi} the matrix elements associated with the β-decay between the initial state i and the final state f. The decay probability is factorized in these three main factors:

1. A statistical factor $p_e^2(Q_\beta - T_e)^2$ from the final states available for the emitted particles, where p_e and T_e are the momentum and kinetic energy of the β-particle, respectively.
2. The Fermi function $F(Z', p_e)$ that takes into account the influence of the Coulomb field of the nucleus, where Z′ is the atomic number of the daughter nucleus.
3. The matrix elements $|M_{fi}|^2$, which contain all the spectroscopy information, meaning it is a measure of how the initial and final states connect through the weak interaction and a corrective term $S(p_e, q)$ to account for forbidden transitions.

$$N(p_e) \propto p_e^2(Q_\beta - T_e)^2 F(Z', p_e)|M_{fi}|^2 S(p_e, q) \tag{2.3}$$

The total decay rate can be rewritten, starting from equation 2.2, and integrating the $N(p_e)$ expression 2.3 over all electron momenta. For the allowed β-decay, it is written as [10]:

$$\lambda = \frac{G^2|M_{fi}|^2}{2\pi^3\hbar^7c^3}\int_0^{p_e^{max}} F(Z', p)p_e^2(Q_\beta - T_e)^2 dp_e \tag{2.4}$$

The Fermi integral depends only on Z' and the maximum electron energy E_0, and it is expressed as

$$f(Z', E_0) = \frac{1}{(m_ec)^3(m_ec^2)^2}\int_0^{p_e^{max}} F(Z', p_e)p_e^2(E_0 - E_e)^2 dp_e \tag{2.5}$$

where the constants in front of the integral are introduced to obtain a dimensionless value of f. By introducing the relation between the transition rate and the partial decay half-life ($t_{1/2}$), $\lambda = ln2/t_{1/2}$, one obtains what is called the comparative half-life or the ft value :

$$ft_{1/2} = ft = \frac{2\pi^3\hbar^7 ln2}{G^2|M_{fi}|^2 m_e^5 c^4} \tag{2.6}$$

Where G = 1.166371(6) $\times$ 10^5 GeV^2 [11].The comparative half-life depends only on the weak nuclear matrix element between the initial and final states. The log ft values connected to different types of beta transitions are shown in Fig. 2.2.

2.1.2 Selection rules

Considering the initial angular momentum of the parent nucleus $\boldsymbol{I}_i$ and final angular momentum of the daughter nucleus $\boldsymbol{I}_f$, the following relation denotes the total angular momentum conservation :

$$\boldsymbol{I_i} = \boldsymbol{I_f} + \boldsymbol{L} + \boldsymbol{S} \tag{2.7}$$

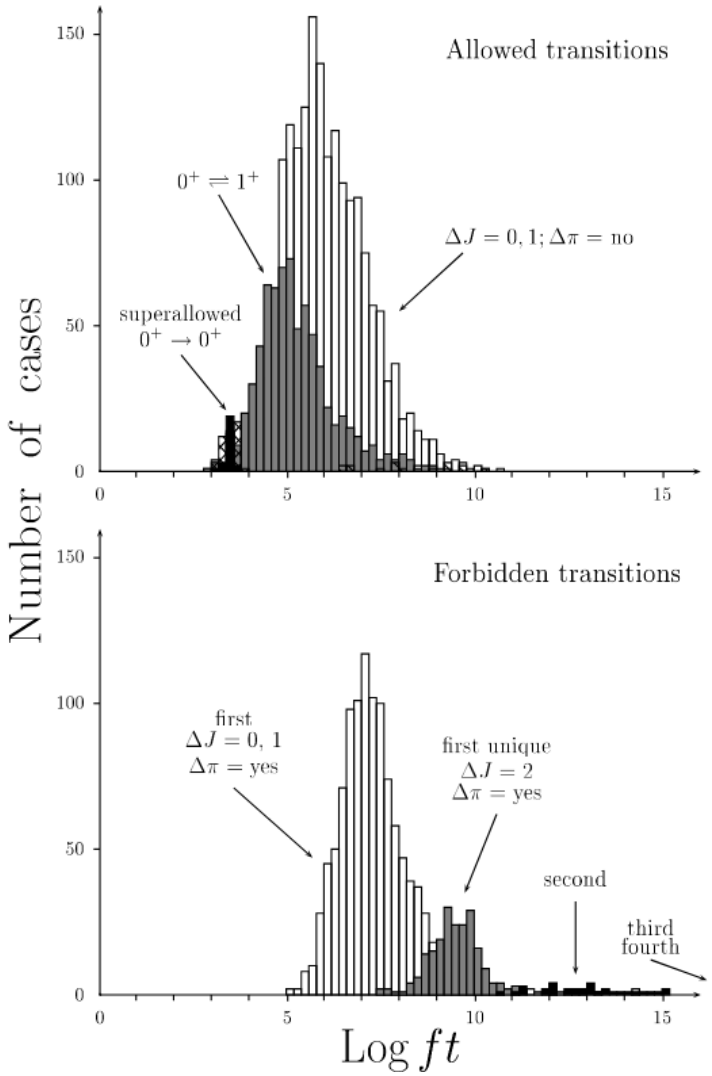

Figure 2.2: Systematics of log *ft* values. Reprinted figure from [12], with permission from Elsevier.

where ***L*** represents the orbital angular momentum carried by the leptons (electron and antineutrino) system and ***S*** their spin. The allowed approximation implies $L = 0$, and Fermi also assumes that the β-decay does not change the spin of the nucleus, i.e., $\Delta I = I_i - I_f = S = 0$. The lepton pair is thus emitted with two antiparallel spins; these transitions are called allowed Fermi transitions. Despite the success of the Fermi theory (shape of the β-spectrum, decay rate), some experiments indicated a violation of the Fermi transition selection rule ($\Delta I = 1$) [13]. Faced with these inconsistencies, Gamow and Teller [14] proposed, in 1936, to include the nuclear spin dependence in the decay process. This addition permits to allow transitions with nuclear spin change according to the relation 2.7: $\Delta I = S = 1$, and this implies that the lepton pair is emitted with parallel spins. These transitions are called allowed Gamow-Teller transitions.

The introduction of the nuclear spin change in β-decay thus allows transitions of type $\Delta I = 0, 1$. The previously called allowed Fermi transitions (anti-parallel electron and antineutrino spins) are renamed super-allowed. They are a subcate-

gory of the so-called allowed transitions characterized by $L = 0$. When $L \neq 0$, i.e., when the lepton pair carries orbital angular momentum, we speak of forbidden β-transitions. Moreover, a non-zero value of this orbital angular momentum L can cause a parity change, the two being related by the following relation:

$$\Delta\pi = \pi_i \pi_f = (-1)^L \tag{2.8}$$

Table 2.1 summarizes the selection rules for various β- transitions.

Table 2.1: The β transition selection rules.

Transition type	ΔI	L	$\Delta\pi$
Allowed	$0, \pm 1$	0	No
First forbidden non unique	$0, \pm 1$	1	Yes
First forbidden unique	± 2		
Second forbidden non unique	$\pm 1, \pm 2$	2	No
Second forbidden unique	± 3		

2.1.3 Beta-delayed gamma-ray transitions

As mentioned in section 2.1, a nucleus that undergoes beta decay can end up in an excited state in the daughter nucleus. One way for the nucleus to release this excess energy and return to a lower energy state is by emitting electromagnetic radiation in the form of γ-rays or conversion electrons. The energy of the γ-ray is equal to the energy difference between the initial and final states of the nucleus (nuclear recoil should be taken into consideration for the case of lighter nuclei and high γ-ray energies). During the transition from an initial state i to a final state f, the angular momentum is conserved, and the angular momentum selection rules are expressed as

$$|I_i - I_f| \leq L \leq |I_i + I_f| \tag{2.9}$$

The anuglar momentum L, carried away by the emitted photon, is related to the multipolarity of the electromagnetic radiation emitted by the nucleus. The term "multipolarity" refers to the type of electromagnetic radiation. Transitions with $L = 1$ are referred to as dipole transitions, transitions with $L = 2$ are referred to as quadrupole transitions, and so on. The electromagnetic radiation can be either of electric (E) or magnetic (M) type for each L value. Electric and magnetic radiations are different in their parity. For each radiation type, the parity can be defined as

$$\begin{aligned} \pi_\gamma(ML) &= (-1)^{L+1} \\ \pi_\gamma(EL) &= (-1)^L \end{aligned} \tag{2.10}$$

The type of electromagnetic radiation emitted in a particular transition can be identified by considering the parity of the initial and final states of the nucleus as

follows [10]

$$\begin{aligned} \Delta\pi = \text{No:} \quad & L = \text{even for electric, odd for magnetic,} \\ \Delta\pi = \text{Yes:} \quad & L = \text{odd for electric, even for magnetic,} \end{aligned} \tag{2.11}$$

where $\Delta\pi$ is the parity change between the initial and final state.

Probability of electromagnetic transition

Considering a transition by photon emission from an initial state i to a final state f, the γ-decay transition rate can be expressed as [15]

$$\lambda(\sigma L, I_i \rightarrow I_f) = \frac{8\pi(L+1)}{\hbar L[(2L+1)!!]^2} \left(\frac{E_\gamma}{\hbar c}\right)^{2L+1} B(\sigma L, I_i \rightarrow I_f) \tag{2.12}$$

where E_γ is the energy of the emitted γ-ray and $B(\sigma L, I_i \rightarrow I_f)$ is the reduced transition probability. $B(\sigma L, I_i \rightarrow I_f)$ is determined by the initial and final states of a transition. Single-particle transitions only involve a single nucleon, resulting in a smaller transition probability compared to collective transitions, which typically involve multiple particles. The level of collectivity in a transition can be measured by comparing the observed transition probability to the estimated single-particle transition probability provided by the Weisskopf estimates [15]:

$$\begin{aligned} B(EL, I_i \rightarrow I_f) &= \frac{1}{4\pi} \left(\frac{3}{L+3}\right)^2 (1.2A^{1/3})^{2L} \\ B(ML, I_i \rightarrow I_f) &= \frac{10}{\pi} \left(\frac{3}{L+3}\right)^2 (1.2A^{1/3})^{2L-2} \left(\frac{\hbar}{2m_p c}\right)^2 \end{aligned} \tag{2.13}$$

where m_p is the mass of the proton. The transition probability in Weisskopf units (W.u.) is calculated as the ratio of the experimental value to the Weisskopf estimate. A pure single-particle transition probability is close to 1 W.u., whereas collective transitions have a significantly higher value.

2.2 The Pygmy Dipole Resonance

In 1937, W. Bothe and W. Gentner [16] observed a significant increase in the effective cross section of the photo-dissociation of specific nuclei for the first time. A. Migdal successfully interpreted these resonances as a dipolar oscillation of protons and neutrons in the nucleus [17]. When the protons and neutrons oscillate in opposite phases, the resonances are called isovector resonances. The various studies carried out during the following years showed that these Giant Dipole Resonances (GDR) carry nearly 100% of the sum rule of the isovector electric dipole transition (E1) (Thomas-Reiche-Kuhn Sum Rule [18]). The remaining strength is then attributed to so-called Pygmy Dipole Resonances (PDR). The PDRs appear at lower energies than the GDRs, usually around the neutron emission threshold in neutron-rich nuclei, as studied in this thesis. The PDR is an oscillation mode where excess neutrons oscillate against a core consisting of protons and neutrons.

Several methods have been used to study PDR excitation and decay. For a more detailed description of the experimental techniques, see Ref. [19].

1. One method for studying dipole excitations is through real photon scattering, such as Nuclear Resonance by Fluorescence (NRF) [20]. This technique is highly selective for dipolar excitation states with $J = 1$ due to the angular momentum carried by the photon. However, NRF can only be used for stable or long-lived nuclei, which limits its applicability. An alternative approach is the Coulomb scattering method [21], which induces excitations by virtual photons from scattering on heavy targets followed by detection of de-excitation γ-rays or neutrons if the nucleus is excited above S_n.. This method allows the study of unstable nuclei with short lifetimes, but lacks the $J = 1$ selectivity of NRF and is subject to background noise from radiation of atomic origin. To overcome this, the detection of a neutron emitted by the nucleus is used to distinguish nuclear excitations from electronic excitations. The resonances beyond the neutron emission threshold can be observed with a higher signal-to-noise ratio and the excitation energy can be reconstructed using the invariant-mass method.

2. The inelastic proton scattering at small scattering angles is an experimental method that can efficiently extract the total B(E1) strength. It yields additional information compared to the photon scattering method, which can provide only a part of the B(E1) strength. This method yields additional information compared to the (γ, γ') method, including strong fragmentation of the E1 strength [22], but it suffers from the same bias: it can only be used to study stable or long-lived nuclei.

3. Finally, the third technique used is the hadronic probe. It involves scattering light nuclei on the nuclei of interest and analyzing the Y (X, X' γ) reaction results. Thus, experiments involving α-particle scattering [23] or alternatively using ^{17}O [24] have allowed, in comparison with the (γ, γ') method, to refine the understanding of the intrinsic nature of the PDR. Nevertheless, the hadronic scattering method is less efficient in the selection of states of interest for pygmy dipole resonances ($J^{\pi} = 1^{-}$), and it is restricted to stable nuclei.

The PDR's unique characteristic is the enhancement of E1 transitions rather than 1^{-} states. This means a medium-spin PDR may exist, which can be built on excited states. However, such PDR states are rarely available for the aforementioned conventional experimental methods. An opportunity for studying these states arises from β-decay experiments, which offer precursor-like specificity. Since exotic nuclei have high Q_{β} values, β-decay has emerged as a new way for PDR research [25], which will be discussed in more detail in the upcoming chapter's section labeled 3.3.

2.3 Elements on the theoretical description of the atomic nucleus

The atomic nucleus is a system of A nucleons, differentiated in neutrons and protons by their isospin projection number, t_z. The internal structure of the nucleons within the nucleus does not affect the low-energy nuclear structure, and the nucleons can be considered as basic spin 1/2 fermions. The nucleons interact through an exchange force that is the residual manifestation of the strong interaction between the quarks they are composed of. Protons, having a charge, also interact through electromagnetic force.

The nuclear Hamiltonian, which describes the behavior of this A-nucleon system, is the sum of the kinetic energies of the individual nucleons and the interaction potential between the nucleons. In order to calculate the stationary states such a system can occupy, in a non-relativistic approximation, one needs to solve the time-independent Schrödinger equation:

$$\hat{H}\,|\Psi\rangle = E\,|\Psi\rangle \tag{2.14}$$

$$\left[\sum_{i=1}^{A} -\tfrac{\hbar^2}{2m}\Delta_i + \sum_{i<j}^{A} W(i,j)\right]|\Psi\rangle = E\,|\Psi\rangle \tag{2.15}$$

where $|\Psi\rangle$ represents A-body wave function having a total energy E and W the 2-body interaction. One usually separates in the Hamiltonian a nuclear average potential, allowing then to separate a single particle and a residual part in the equation 2.14 [26].

Making the hypothesis that such a nuclear average potential exists, we then need to find the best one allowing for the minimization of the residual interaction. From this point, we can use two different formalisms to solve the A-body Schrödinger equation:

- The Hartree-Fock theory starts from a two-body interaction with some global parameterization, and then calculates the best mean-field potential by minimizing the total energy of the system based on a variational principle. The correlations are added beyond this mean-field approximation.
- The nuclear shell model starts with a known, suitable potential (harmonic oscillator, Wood-Saxon ...). The solutions of this potential are then used as a basis for a further diagonalization of the residual interaction into a limited valence space[1].

More about the nuclear shell model and a brief description of the particular mean field theory that is HFB+QRPA is presented in the next sections.

[1] The set of single-particle states corresponding to the nucleons located at the outermost shell of a nucleus.

2.3.1 Nuclear shell model

In 1933, the existence of special numbers for which the nuclei are exceptionally stable was presented in Ref. [27]. These numbers have been named magic numbers, and the nuclei having these numbers of protons or neutrons are called "magic nuclei" or "doubly magic" if both proton and neutron numbers are magic. The first of their features is that they are more bound than their neighboring nuclei. The second feature is higher energy of the first excited level compared to the neighboring nuclei.These magic numbers are 2, 8, 20, 28, 50, 82, and 126.

In the shell-model, each nucleon is considered to be moving independently within an average potential created by the interaction of all the nucleons. The Hamiltonian of equation 2.14 can then be written as:

$$\hat{H} = \left[\sum_{i=1}^{A}\left(-\frac{\hbar^2}{2m}\Delta_i + U(i)\right)\right] + \left[\sum_{i<j}^{A} W(i,j) - \sum_{i=1}^{A} U(i)\right] = \hat{H}^{(0)} + \hat{V} \qquad (2.16)$$

where $U(i)$ is the single-particle potential, $\hat{H}^{(0)}$ the independent-particle motion and $\hat{V}$ the residual interaction. The use of a suitable potential can make the residual interaction negligible in the independent-particle model.

In 1949, a potential for individual particles that included a spin-orbit component was introduced [28, 29]. The spin-orbit term split the energy levels with angular momentum quantum number $l \geq 1$ into two, where the level with total angular momentum j=l+1/2 has lower energy than the level with j=l-1/2. The relevant part of the single-particle shell model levels for this work is illustrated in Fig. 2.3.

The independent particle model is limited in its ability to describe nuclei, as it can only accurately be applied for nuclei with magic numbers of protons and neutrons ($\pm$ one or two nucleons). Additionally, this model presumes that nuclei are spherical in shape, an assumption that holds only for nuclei that are located close to closed shells. In other words, going further away from the magic numbers, it becomes mandatory to consider the residual interaction between the nucleons outside the closed shell (commonly referred to as the core) where the two-body interaction starts playing a significant role.

2.3.2 HFB+QRPA theoretical model

2.3.2.1 Hartree-Fock Bogolyubov

The Hartree-Fock method uses a set of equations called Hartree-Fock equations, which are based on the many-body Schrödinger equation and an effective force (called D1M Gogny force in this work) for the nucleon-nucleon interaction. The equations are solved iteratively until the convergence of wave functions and energies of the orbitals. This process is called self-consistent, and the result gives a set of single-particle wave functions that minimize the total energy of the system

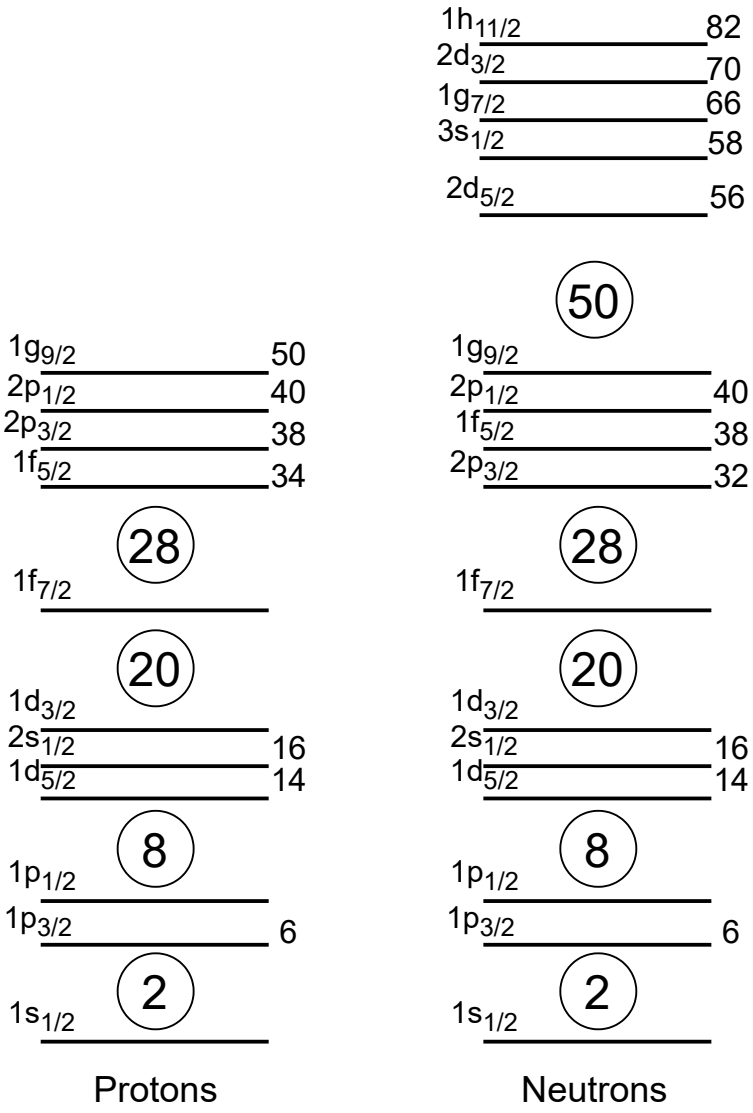

Figure 2.3: A schematic representation of the shell model energy levels pertinent to this work. The level spacings are not to scale.

and describe the properties of the ground state of the nuclei. The Hartree-Fock Bogolyubov (HFB) method is an extension of the HF method that takes into account pairing correlations between nucleons. The HFB method describes these pairing correlations by introducing a pairing potential, which is treated on the same footing as the mean-field potential used in the HF method. Together, the mean-field and pairing potentials determine the properties of nuclei. The HFB method can be utilized to acquire the single-particle level spectrum related to one or multiple quasi-particle (qp) excitations. In this work, HFB calculations were performed to obtain the single-particle level spectrum associated with the ground state.

2.3.2.2 QRPA and pnQRPA approximations

QRPA refers to the Quasi-Particle Random-Phase Approximation for electromagnetic excitations and pnQRPA to QRPA charge-exchange excitations. These solutions are constructed from the quasi-particle states determined in Hartree-Fock-Bogolyubov calculations carried out with a harmonic oscillator basis, which supports either spherical or axial symmetry. The QRPA calculations construct a collective phonon state from coherent protons or neutrons excitations in the single-particle level spectrum acquired with HFB calculations. The phonon states obtained in a QRPA calculations represent collective vibrations in the nucleus of interest and are formed from a coherent superposition of proton-proton 2qp excitations and neutron-neutron 2qp excitations. However, in pnQRPA calculations, the coherent excitations resulting from proton-neutron 2qp excitations correspond to transitions from a mother nucleus to its daughter nucleus. A numerical tool based on this model has been developed by a team of the CEA-DAM of Bruyères-le-Châtel (a more detailed description can be found in Refs. [30, 31]). The calculations performed using this tool for the decay of the ^{82}Ga to ^{82}Ge, together with the results of shell-model calculations for ^{86}Se are presented in chapter 7.

3 MOTIVATION TO STUDY NUCLEAR STRUCTURE AROUND THE N=50 SHELL CLOSURE

3.1 Nuclear astrophysics: the r-process

The r-process, or the rapid neutron capture process [32], is a process that allows the creation of nuclei in a medium that is very hot (T $\sim 10^9$ K) and very dense in neutrons ($N_n > 10^{20}$ cm^{-3}) by the capture of the latter, within a relatively short time (t $\sim$ 1s). This process is essential in elemental nucleosynthesis because it is the origin of half of the elements heavier than iron in the universe. For a long time, type II supernovae explosions have been considered the preferred astrophysical sites for the r-process [33] because of their explosive character. Nevertheless, the fusion of two highly dense bodies, like neutron stars or black holes, was also recognized as a possible site [34].

The observation of gravitational waves by the LIGO and Virgo collaborations [35, 36] marked a turning point in the r-process studies. The GW170817 gravitational wave signal originating from two neutron-star mergers was observed, and it was followed 1.74 s later by a γ-ray burst (GRB 170817A) [36]. Following the merger, the AT2017gfo kilonova was observed, and it was driven by the radioactive decay of the r-process elements. Namely, the multiple neutron captures (n, γ) make the r-process path proceed far away from the valley of stability. The produced radioactive nuclei will decay back to the valley of stability, mainly via β-decays. Moreover, heavy neutron-rich nuclei can decay via fission to lighter-mass regions. The fission products can be later used as seed nuclei (fission recycling). These decays power the observed kilonova, which showed clear evidence of the r-process occurrence in neutron-star mergers and highlighted their importance in the production of r-process products.

A large fraction of nuclei formed with the r-process is experimentally unknown. Therefore, the calculations to model the phenomenon rely on theoretical calculation of the necessary input values for experimentally unknown nuclei. However, microscopic models have difficulties reproducing specific parameters such as half-lives, the masses of nuclei, and β-delayed neutron particle emission

probabilities [37], especially far from the valley of stability.

It has also been shown [38] that pygmy dipole resonances can impact the calculations of neutron-capture reaction rates. Furthermore, the PDR above the neutron separation threshold enhances the reverse process of (γ, n) photodisintegration. Therefore, the PDR distribution relative to the neutron emission threshold of neutron-rich nuclei can significantly impact the formation of heavy elements in the universe [39, 40, 41].

3.2 Experimental knowledge of the N = 50 shell gap in the vicinity of ^{78}Ni

As seen in Fig. 2.3, the magic number N = 50 corresponds to the gap between the shell-model orbitals $\nu 1g_{9/2}$ and $\nu 2d_{5/2}$. This gap emerges naturally in the shell model when the spin-orbit interaction is included. The same is true for the gap between the proton shells $\pi 1f_{7/2}$ and $\pi 1f_{5/2}$ corresponding to the magic number Z = 28, making the ^{78}Ni nucleus to be one of the most neutron-rich doubly magic nuclei.

In the following, we present the status of experimental knowledge regarding the N=50 shell gap and the magicity of ^{78}Ni.

3.2.1 Mass measurements

Mass measurements are an important tool in studying nuclear structure because they can provide information about the binding energies of atomic nuclei. The two-neutron separation energy, which is defined as the energy required to remove two neutrons from a nucleus, is a measure of the stability of a nucleus and is related to the binding energy of the nucleus. By measuring the masses of different atomic nuclei and calculating the two-neutron separation energy, it is possible to identify shell closures since it is expected to be much higher in the case of a closed shell. The two-neutron separation energy is defined as:

$$S_{2n}(Z,N) = [M(Z,N-2) + 2M(^1n) - M(Z,N)]c^2 = B(Z,N) - B(Z,N-2) \tag{3.1}$$

where M is the atomic mass and B is the binding energy of the considered nuclei. The atomic masses of neutron-rich isotopes of Zn, Ga, Ge, As, and Se have been measured using the JYFLTRAP Penning trap mass spectrometer of IGISOL at the University of Jyväskylä [43]. The evolution of S_{2n} as a function of the neutron number in the nickel region is shown in Fig. 3.1. The steep decrease when passing N = 50 can be observed for all nuclei and is characteristic of a shell closure. The evolution of the N = 50 shell gap is even more visible when looking at the evolution of S_2n as a function of the proton number, shown in Fig. 3.1. The opening of the N = 50 gap when moving towards Ni (Z=28) is a signature of its magicity.

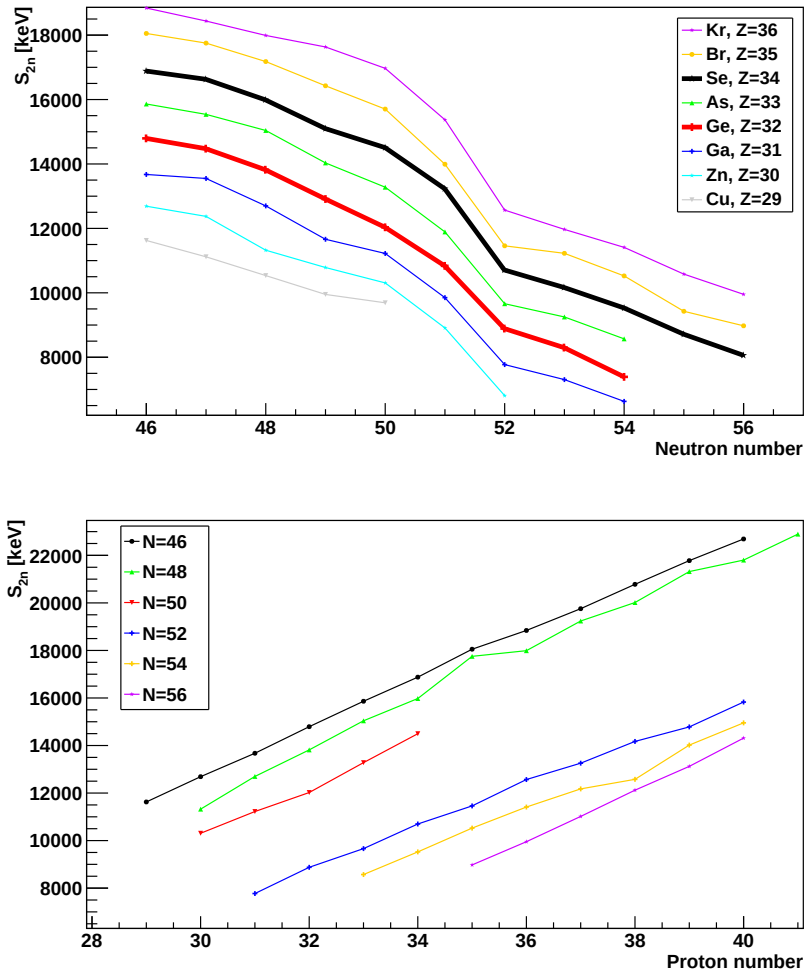

Figure 3.1: Two-neutron separation energies of (top) the Z = 29 to 36 isotopic and (bottom) the N = 46 to 56 isotonic chains. Data are taken from Ref. [42].

3.2.2 β-decay half-lives

Evidence of the magicity of ^{78}Ni can be seen by examining the half-lives of nearby isotopes in the Z=27 to 31 isotopic chains. The pattern of β-decay half-lives for these isotopes is depicted in Fig. 3.2. The half-lives of neutron-rich nuclei with Z = 27–30 were measured at RIKEN [44]. The rapid decrease in half-life for nickel isotopes with N> 50 was interpreted as evidence for the magicity of the neutron number 50, meaning that the energy required to add the 51st neutron is very high. This would result in a large increase in the Q_β value, leading to a significant decrease in the half-life.

3.2.3 Systematics of the first 2^+ states

The evolution of the first 2^+ state in the iron, nickel, zinc, germanium, and selenium isotopic chains is shown in Fig. 3.3. The magic signature of N = 50 is reflected by the sudden rise in the energy of the 2^+ state when crossing the N=50 shell closure. At the same time, the Z=28 isotopic chain is observed at higher

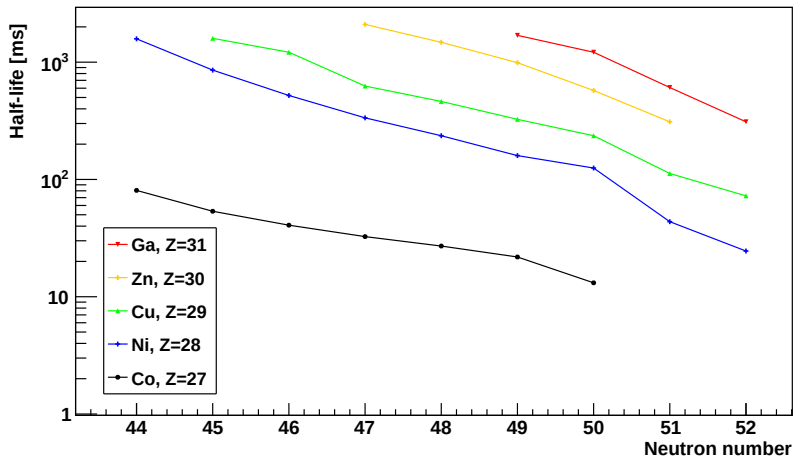

Figure 3.2: Experimental β-decay half-lives of the Z = 27 to 31 isotopic chains as a function of neutron number. Data are taken from Refs. [44, 45].

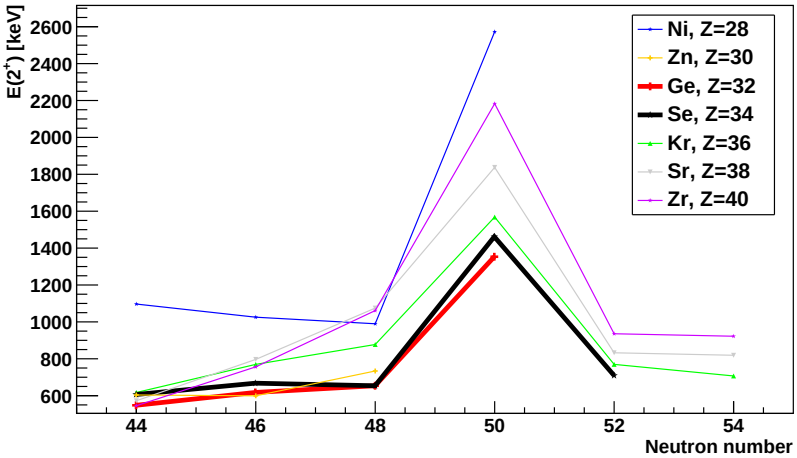

Figure 3.3: Systematics of the first excited 2^+ state in the Z = 28 to 40 isotopic chains as a function of neutron number. Data are taken from Refs. [45, 46, 47, 48, 49, 50].

energy than the others, showing the magic character of Z=28.

Finally, the question of the ^{78}Ni magicity has been settled by Seastar at RIKEN in 2017 [51]. This experimental campaign allowed the spectroscopy of many neutron-rich nuclei from the RIBF (Radioactive Isotope Beam Factory) facility by coupling the MINOS (MagIc Numbers Off Stability) experimental setup with the γ spectrometer DALI2 (Detector Array for Low Intensity radiation 2). The steep rise at N=50 of the 2^+ state energy is clearly visible (the blue plot of Fig. 3.3), providing direct experimental evidence for the N=50 magic character.

3.3 PDR at the N=50 shell closure

The experiments and theoretical investigations carried out to study the pygmy resonances made it possible to shed light on these resonances, but many questions remain open. Their nature, their degree of collectivity, and their location, for example, are still subject to discussion. Even for the nature of the isoscalar-isovector separation of the PDR detected by the hadronic probe: does the isovector part correspond to the GDR's tail? These questions require diversification of experiments and a deepening of theoretical models. The work of [52] studied the E1 strength evolution in the stable N=50 isotones through NRF using polarized γ beams. Their work showed that a measurable portion of the dipole strength has been recorded at energy levels below 10 MeV, and there is a rise in relation to the N/Z ratio. By analyzing the development of the transition densities from 6 to 11 MeV, the authors arrived at a conclusion that, for all stable isotopes with N=50, the majority of the 1^- states located at energy levels less than 9 MeV possess properties typical of PDR states and that there is no significant increase of the PDR strength with increasing N/Z ratio. Nevertheless, there is a clear lack of data on PDR for unstable nuclei along isotonic chains. The difficulty of producing exotic nuclei along an isotonic chain for PDR studies, where usually one needs accelerated beams, is one of the main reasons.

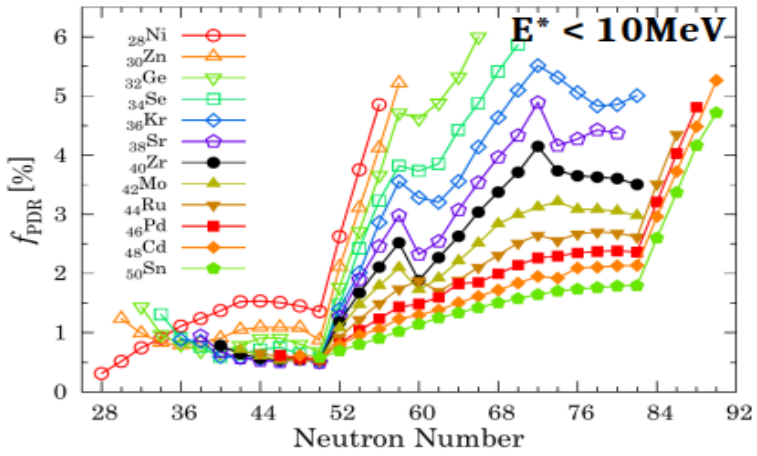

Figure 3.4: The PDR fraction as a function of the neutron number for even-even isotopes with Z = 28–50, and N $\geq$ Z. Reprinted figure with permission from [53]. Copyright (2023) by the American Physical Society.

Moreover, systematic investigation of low-lying dipole modes using the canonical-basis time-dependent Hartree-Fock-Bogoliubov theory along the Z and N axis [53] shows a strong neutron shell effect, as can be seen in Fig. 3.4. The PDR fraction (the ratio of the energy-weighted E1 strengths below 10 MeV to the total E1 sum rule) increases by a factor of two to three in the most neutron-rich isotopes when crossing the N=50 shell closure. This means that higher PDR strength is expected around the ^{78}Ni region, which, on the other hand, calls for a different study tool more adequate to this region, e.g., the β-decay.

Indeed, M. Scheck and his colleagues have recently shown that β-decay may be a new way to study the PDR [25]. They showed that γ-ray spectroscopy following high Q value β-decay could be exploited as a probe for revealing the structure of PDR in even-even nuclei. Their work showed that the β-decay populates only a fraction of the 1^- PDR states by comparing photon scattering data for ^{136}Xe(γ, γ') and ^{136}I[J$^\pi$(GS)=1$^-$]$\rightarrow$^{136}Xe* β-decay. These states seem to have complex wave functions and they are very weekly populated in inelastic scattering (see Fig. 3.5). The advantage of studying PDRs via the β-decay path lies in its ability to access

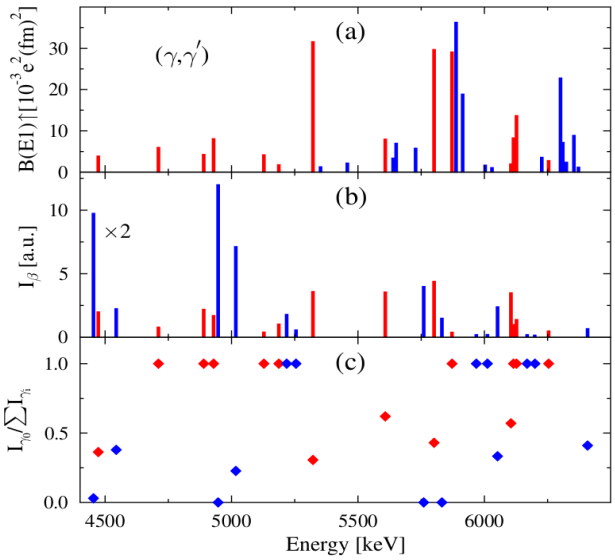

Figure 3.5: 1^- candidate states in ^{136}Xe. Part (a) shows *B(E1)* strength distribution as extracted from (γ, γ') reaction. In part (b) the 1^- population intensity in the β-decay of ^{136}I is shown, and part (c) shows the ground-state branching ratios from the β-decay. The levels populated in both reactions are marked with red. Reprinted figure with permission from [53]. Copyright (2023) by the American Physical Society.

excitations both above and below the neutron emission threshold. It also makes it possible to study unstable nuclei with short lifetimes. On the other hand, only a fraction of the resonance would be accessible because of the quantum selection rules (matching β-decay with PDR states' quantum numbers).

In this regard, experiments of [54] and [55] have recently shown the importance of this method by observing high-energy γ de-excitations corresponding to dipole excitations that could be identified with pygmy resonances. The experiment described in [54] was performed at the ALTO facility in 2017. Unexpected high-energy β-delayed gamma-rays (8-9 MeV) were observed in the β-decay of ^{83}Ga ($T_{1/2}$ =308.1 (10) ms; Q_β =11.719 (4) MeV [45]) compared to the decay of ^{80}Ga. This experiment triggered the start of a program at ALTO (of which this Ph.D. project is part) to investigate the structure of neutron-rich isotopes around the N=50 shell closure. Microscopic calculations around the neutron separation energy using the QRPA method have revealed that the GT decay of deeply bound neutrons can cause coherent dipole oscillations (PDR). These oscillations can then lead to significant emission of E1 gamma-radiation. This effect is more pronounced

in the decay of ^{83}Ga than in the decay of ^{80}Ga because of the rapid development of a neutron skin in nuclei with N> 50 [53].

3.4 The choice of the studied nuclei

Following the argumentation in the previous section, we have identified the best candidates to perform this study at the N=50 shell closure. The relevant information is summarized in Table 3.1.

Table 3.1: Properties of the nuclei studied in this work (data are taken Refs. [45, 42]).

Parent	J^π (GS)	$T_{1/2}$ [ms]	Daughter	Q_β [MeV]	S_n [MeV]	P_n [%]
^{82}Ga	(1^-,2^-,3^-)	599 (2)	^{82}Ge	12.484 (3)	7.194 (3)	19.8(10)
^{83}Ga	($5/2^-$)	308.1 (10)	^{83}Ge	11.719 (4)	3.632 (3)	62.8 (25)
^{86}As	(1^-,2^-)	945 (8)	^{86}Se	11.541(4)	6.160(4)	35.5(9)

3.4.1 The ^{82}Ge nucleus

In even-even nuclei, PDR states built on the ground state are 1^- states, and in order to populate them in β-decay, the parent nucleus has to have a low-spin ground state, high Q_β, and relatively high $Q_{\beta n}$[1] values. The N=50 nucleus, ^{82}Ge (Z=32, N=50), is a very compatible candidate (see ^{82}Ga decay chain in Fig. 3.6). A laser spectroscopy measurement of ^{82}Ga suggests that the spin is 2 [56]; however, the spins of 1 and 3 could not be ruled out. If we start from the assumption that the ground state is (2^-), then the allowed β-decays can populate 1^-, 2^-, and 3^- states in ^{82}Ge, while the first-forbidden β-decay transition can populate states from 0^+ to 4^+ in ^{82}Ge. Thus, we would expect to observe E1 γ-ray transitions from the 1^- to the 0^+ ground state of ^{82}Ge, which is the signature of the PDR in this nucleus. Furthermore, ^{82}Ga has a large Q_β value, 12.484 (3) MeV [42], with a relatively low S_n value of 7.194 (3) MeV [42], which makes the population of levels around S_n very probable. Despite this, no γ-ray transitions are reported from states above the neutron separation threshold and the highest β-delayed γ transition reported is at 5.3 MeV. ^{82}Ge has been studied many times by various methods. The first method was the β-decay of ^{82}Ga, which was used to investigate the structure of ^{82}Ge in 1981 [57] and in 2016 [58] . ^{82}Ge was also studied via the β-delayed neutron emission from ^{83}Ga in 2010 [59] and in 2017 [60, 61] . On the other hand, direct reactions are another production mechanism that can be utilized to study higher-spin states in ^{82}Ge. Several experiments have used direct reactions to generate and study this nucleus, as in Refs. [62], [63], [64] and [65].

[1] The energy difference between Q_β value and S_n value.

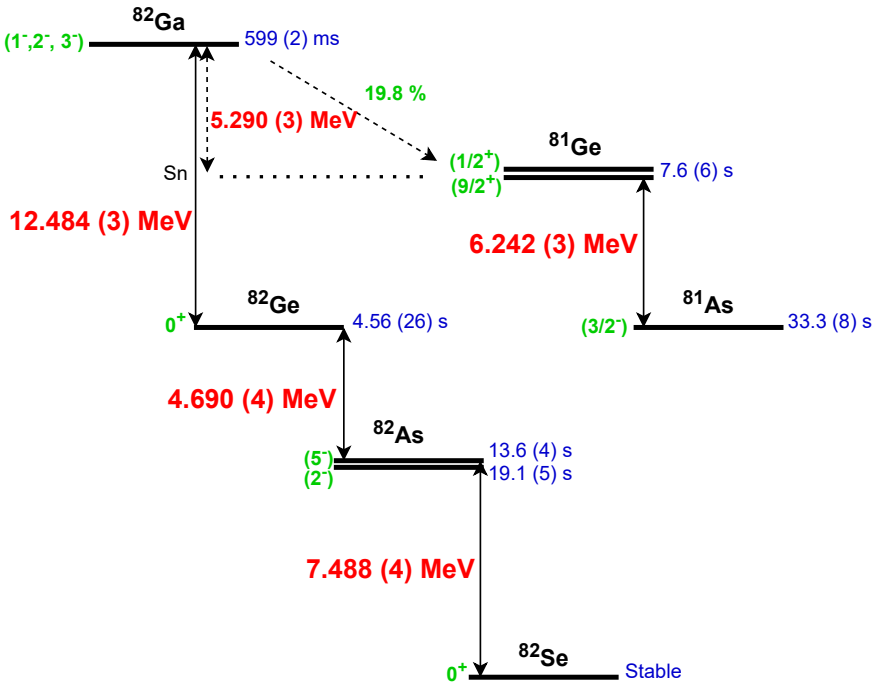

Figure 3.6: Decay chain of ^{82}Ga. The data are taken from Ref. [45].

3.4.2 The ^{83}Ge nucleus

Even though the work of [54] showed high-energy γ-transitions emitted from states 2-3 MeV above the neutron separation energy in ^{83}Ga, the resolution of the detector used was not good enough for these γ-ray transitions to be identified precisely. Hence, we decided to study the ^{83}Ge (Z=32, N=51) again, but this together with ^{82}Ge in the same experiment to identify the γ-ray transitions that belong to the β and β-n decay channels of ^{83}Ga. The ^{83}Ga β-decay chain is presented schematically in Fig. 3.7.

The ground-state spins of ^{83}Ga and ^{83}Ge were deduced from systematic trend studies [66] to be $(5/2^-)$ and $(5/2^+)$, respectively. This means a first-forbidden β-transition between the ground states is likely to happen. In addition, $3/2^-$, $5/2^-$ and $7/2^-$ states can be populated in ^{83}Ge by allowed β-decay transitions, while the first forbidden ones can populate states from $1/2^+$ to $9/2^+$ in ^{83}Ge. The Q_β value of ^{83}Ga is 11.719 (4) MeV [42], and the neutron separation energy in ^{83}Ge is at 3.632 (3) MeV [42], making the population of neutron-unbound states very probable. The structure of ^{83}Ge has been extensively researched at HRIBF through the reactions of ^{2}H(^{82}Ge,p)^{83}Ge [67, 68] and β-decay of ^{83,84}Ga produced in proton-induced fission of ^{238}U [59]. Furthermore, at ALTO, the ^{83}Ge was studied through neutron-induced fission [66], photo-induced fission of ^{238}U [69, 70], and β-decay of ^{83}Ga [71, 72].

3.4.3 The ^{86}Se nucleus

The As isotopes around the N=50 shell closure are similar to their Ga isotones

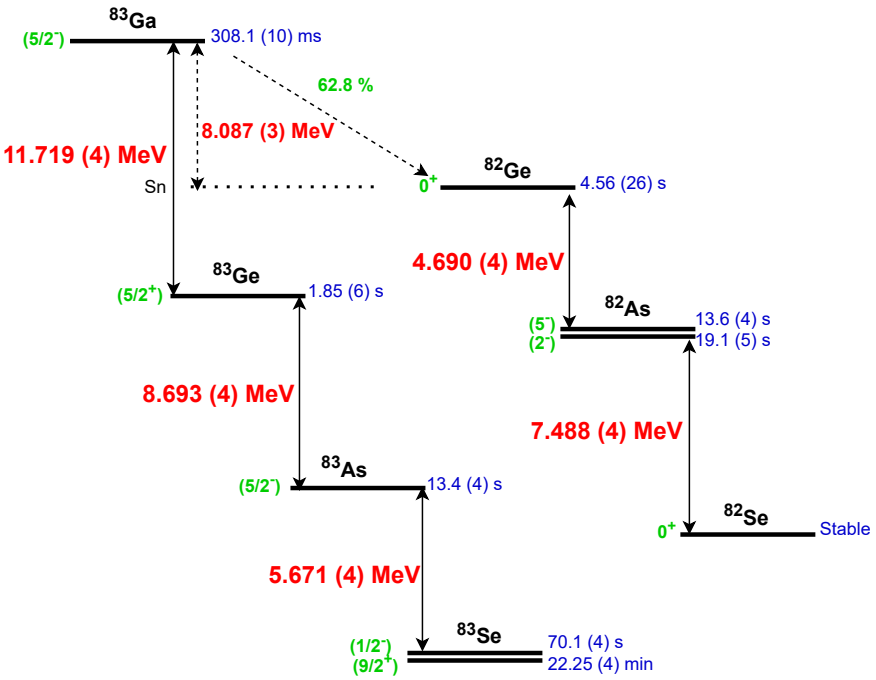

Figure 3.7: Decay chain of ^{83}Ga. The data are taken from Ref. [45].

in that they have large $Q_{\beta n}$ windows, which makes studying their β-decay a reliable way to populate energy levels near S_n. We decided to study the β-decay of ^{86}As to ^{86}Se (Z=34, N=52), going thus two protons less exotic than the gallium to germanium decay experiment. The β-delayed neutron branch has been measured using the BELEN detector setup at the IGISOL facility to be P_n = 35.5(6) % [73]. The β-decay chain of the ^{86}As ground state is shown in Fig. 3.8. No γ-transitions were measured from states above S_n even though the $Q_{\beta n}$ window is 5.38 MeV.

The structure of ^{86}Se has been studied using a variety of experimental methods. One of the main methods is the β-decay of ^{86}As. This method was used in the 1970s [74, 75], for example, and more recently in 2015 [76, 77] . In addition, Ref. [78] used the β-n decay of ^{86}As to provide new information about the structure of ^{86}As. Furthermore, ^{86}Se was also studied at Vanderbilt University, Nashville, Tennessee, via prompt γ-ray spectroscopy of ^{252}Cf spontaneous fission [79] [80]. Also, at the INFN Legnaro National Laboratory, ^{86}Se was studied by a recoil distance Doppler shift (RDDS) experiment in 2015 [81]. No β-delayed γ transitions have been reported above 4.7 MeV in ^{86}Se. This leaves a gap of about 2 MeV between the highest populated state observed in β-decay and the neutron separation energy.

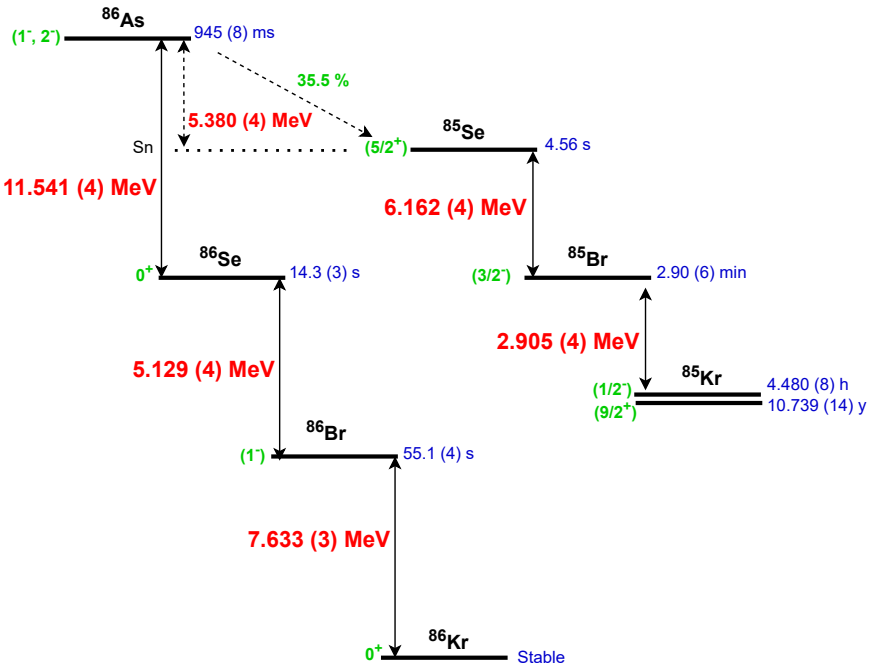

Figure 3.8: Decay chain of ^{86}As. The data are taken from Ref. [45].

4 EXPERIMENTAL METHODS

In this chapter, the methods used to perform the two experiments addressed in this Ph.D. will be described. To assist the reader, NRI15 will be used for the experiment performed at ALTO facility, and I281 will be used for the experiment performed at IGISOL facility.

4.1 The NRI15 experiment

The first experiment of this work was dedicated to studying the β-decay of ^{82}Ga and ^{83}Ga isotopes at the ALTO[1] facility.

4.1.1 Radioactive ion beams at the ALTO facility

The neutron-rich gallium isotopes of interest were produced at the ALTO, an experimental platform belonging to the IJCLab[2][82]. The historical part of this installation consists of a 15 MV electrostatic negative ion accelerator of the Van de Graaff type known as a Tandem. It was put into operation in 1972 to answer the time's major questions concerning the structure of nuclei and reaction mechanisms using stable beam induced reactions. The more recent part of ALTO has been operational since 2006 and concerns the production of radioactive ISOL[3] beams. The developments and the constant improvement of the techniques for producing radioactive nuclei have made it possible to obtain many essential results both in fundamental research (nuclear structure, nuclear reactions, nuclear astrophysics) as well as in applied research (nuclear safety). As we can see in Fig. 4.1, the experimental hall 110 of ALTO contains the following tools and instruments:

---

1 Accélérateur Linéaire et Tandem d'Orsay

2 Laboratoire de Physique des 2 Infinis Irène Joliot Curie, Paris Saclay University/CNRS, Orsay, France

3 Isotope Separation On Line

- BEDO[4] [83, 54]: a set of detectors dedicated to β-delayed decay spectroscopy using γ-spectroscopy (and Fast Timing) , electron spectroscopy or neutron spectroscopy with the MONSTER [84] neutron spectrometer;
- TETRA [85]: ^{3}He counter for β-delayed neutron emission probability measurements ;
- PolarEx [86]: Low-temperature nuclear orientation and nuclear magnetic resonance;
- LINO: Laser Spectroscopy and Laser-Assisted Nuclear Orientation;
- MLLTRAP [87]: Double Penning trap for mass measurements and trap-assisted decay studies;
- CoeCo [88]: A decay station dedicated to beta-delayed conversion electron spectroscopy. It is composed of a movable tape collector for beam collection and descendant activity control. Close to the collection point are placed a plastic detector for beta tagging and a HPGe detector for gamma-ray spectroscopy. A Si(Li) junction is placed 15 cm away for electron spectroscopy.

At ALTO, radioactive ion beams are produced by the ISOL technique. The ISOL

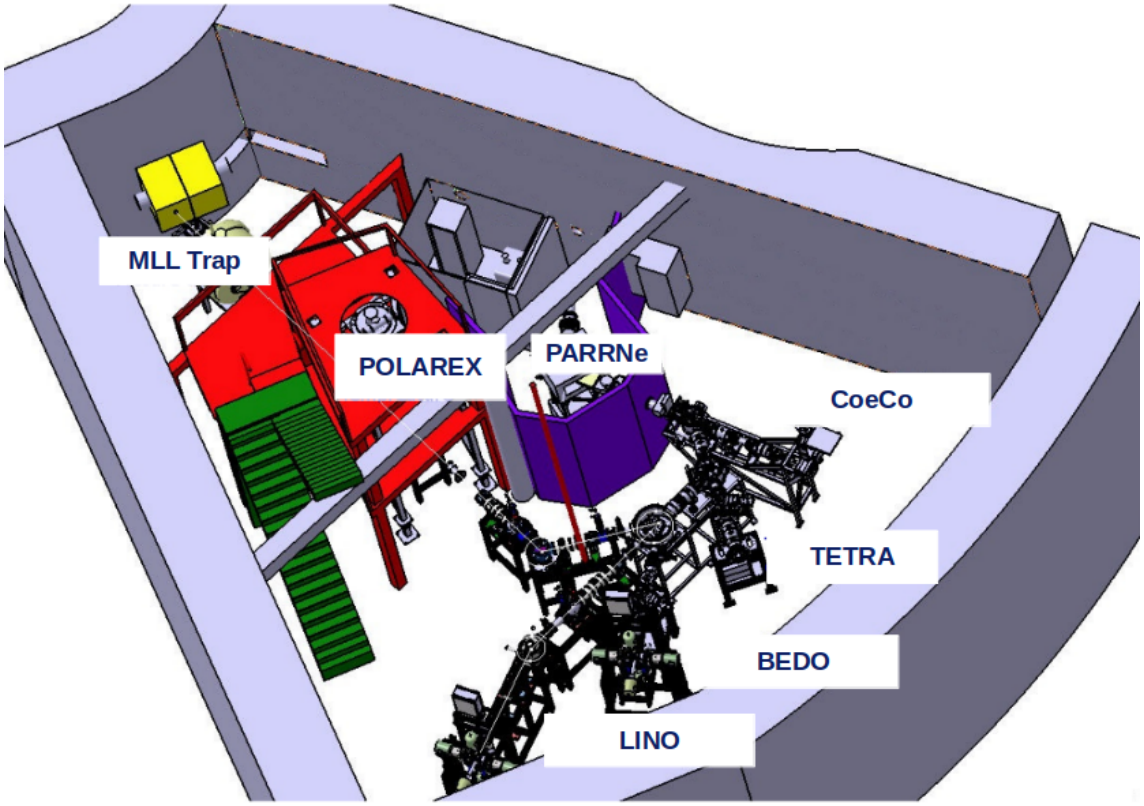

Figure 4.1: Overview of the Radioactive Beam cave of ALTO facility. In this work, the detection system used to study the ^{82,83}Ga isotopes was installed at the BEDO setup.

technique is a method used in many large accelerators around the world, such as ISOLDE (CERN), SPIRAL (GANIL), ISAC (TRIUMF), and others. It has benefited from many recent technical contributions to meet the experimental constraints of

[4] BEta Decay studies in Orsay

physicists (exoticism, intensity). This production technique can be broken down into the following steps:

- creation of radioactive nuclei,
- diffusion out of the target,
- effusion to the ionisation source,
- ionisation,
- extraction,
- separation.

The ions of interest are accelerated to a few tens of keV. An extra step of post-acceleration can be used in order to reach a kinetic energy of a few to about 10 MeV/nucleon. A history of the invention of the ISOL technique and the need for it is presented in Ref. [89].

Different methods can be used to produce the radioactive beams for ISOL techniques. ALTO's method consists of bombarding a thick UC_x target with a light and a high-intensity primary beam. The target is heated to promote the diffusion and effusion of radioactive atoms from it. It should be noted that, unlike in-flight production techniques, the kinematics of the nuclear reaction are not preserved, which means all the energy of the primary beam is deposited in the target, and the reaction products are thermalized and neutralized. These atoms are extracted from the target, ionized, and then accelerated to form a beam of 30-60 keV energy.

Regarding the experiment under consideration, the ^{82,83}Ga ions were produced by photo-induced fission. The photo-fission is briefly defined as follows: accelerated electrons interact with atoms, creating a continuous gamma-ray emission that initiates the fission process in the target. The procedure starts with accelerating an electron beam at 50 MeV by a linear accelerator (see Fig. 4.2). This beam is then incident on a uranium carbide target (UC_x) [90]. The target is placed in a Ta oven in order to facilitate the diffusion of fission products. After being ionized by LASER, these products are then selected in mass by the magnetic spectrometer PARRNe ($\frac{M}{\Delta M}$ = 1500) and finally guided through the beamline by a set of electrostatic dipoles and quadrupoles to the BEDO setup.

4.1.2 BEDO experimental setup

BEDO is an experimental setup aiming to study exotic neutron-rich nuclei by β-decay [83, 54]. It was developed as a continuation of a research project in the N =50 region towards ^{78}Ni, initiated in the early 2000s at ALTO. It is composed of a tape station for the implantation and evacuation of the radioactivity, a plastic detector for beta-decay tagging, and different instruments for the detection of the delayed radioactivity emitted after beta decay (HPGe or scintillators for gamma decay)

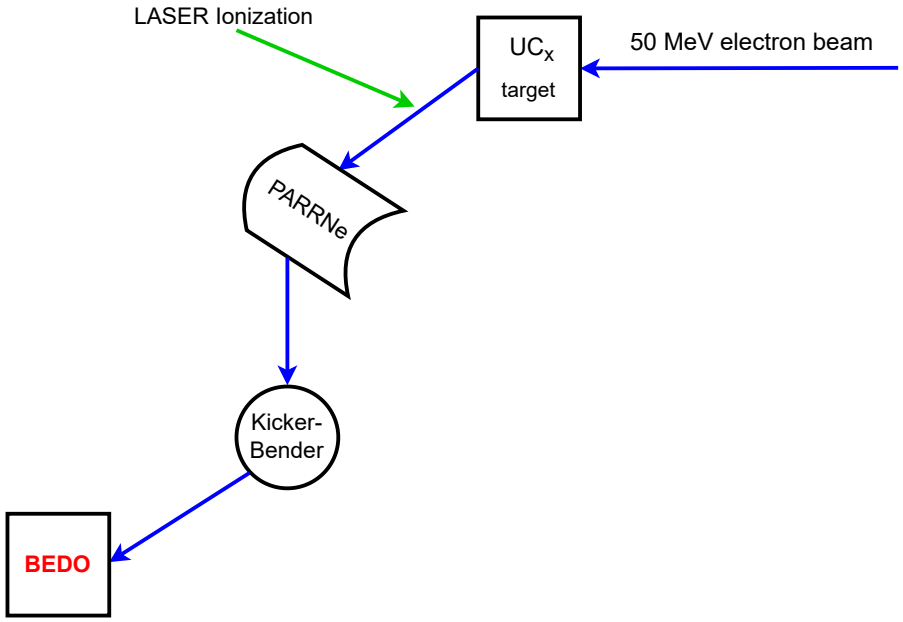

Figure 4.2: A schematic view of the beam production at ALTO.

4.1.2.1 Tape and measurement cycle

The selected radioactive beam is implanted on an Al-coated mylar tape. A dedicated engine (see Fig. 4.3) allows moving the tape to follow a defined pattern in time. The whole system is maintained under the same vacuum as the beamline.

Figure 4.3: The tape station in BEDO.

In order to avoid accumulating long-lived daughter activities of the studied ^{82,83}Ga nuclei, the tape was periodically moved with cycles adapted to the nucleus of interest's half-life. A cycle started when a "clean" tape area was positioned at the beam level, which is called a "collection point." First, the tape was left for 0.5 s with no beam for "background measurement" (t_{bck}). Then, the beam was implanted at

this point for a specified time, which is called the "collection time"(t_c). The nuclei implanted on the tape and their descendants β-decayed during a second period called "decay time"(t_d) without beam implantation. At the end of this period, the tape was moved until the accumulated activity was sufficiently far ($\approx$ 1.3 m) from the collection point. During the tape's movement, the beam was deflected. The time behavior for the activity of the collected sample for a cycle that is represented in Fig. 4.4 is described by Eq. :

$$A(t) = \begin{cases} \phi(1 - e^{-\lambda t}) & t_0 < t \leq t_1 \\ \phi(e^{-\lambda t_1} - 1)e^{-\lambda t} & t_1 < t < t_2 \end{cases} \tag{4.1}$$

where:

- A is the parent nucleus activity,
- ϕ represents the ion of interest production rate,
- λ is its decay constant,
- t_0 is the starting time of the cycle,
- t_1 is the time when the accumulation stops (t_0+t_{bck}+t_c),
- and t_2 is the cycle ending time (t_0+t_{bck}+t_c+t_d).

These equations were later applied to get the $\beta - \gamma$-gated activity during the data analysis.

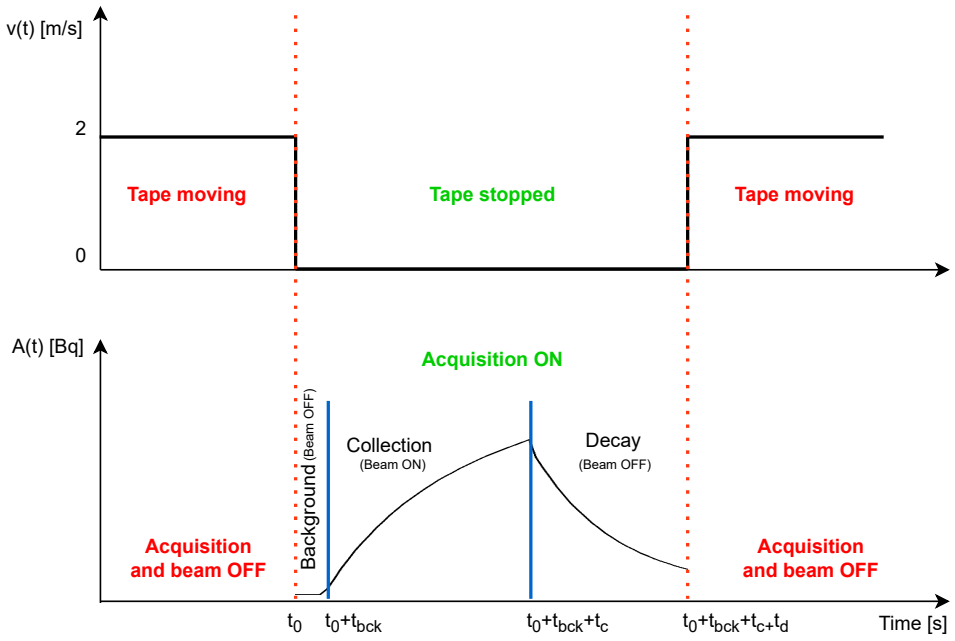

Figure 4.4: The principle of the tape controller: the upper diagram shows the velocity of the tape with respect to the cycle, and the bottom one shows the evolution of the activity on the tape as a function of time.

The details of tape settings during the experiment are listed in Table 4.1. Moreover, the collection point of the beam was surrounded by a BC408 plastic

detector (called $4\pi\beta$) covering about 74 % of the solid angle and placed under vacuum to detect the β particles. The thickness of this detector was 3 mm in order to be almost insensitive to γ-radiation.

Table 4.1: The choice of the tape cycles for the measurements of the ^{82,83}Ga decays. The half-lives are taken from [45].

Isotope	$T_{1/2}$ (ms)	t_{bck} (s)	t_c(s)	t_d(s)
^{82}Ga	599	0.5	3	2
^{83}Ga	308	0.5	2	2

4.1.2.2 The γ detection setup

Different γ-detector types were mounted around the implantation point in the configuration shown in Fig. 4.5.

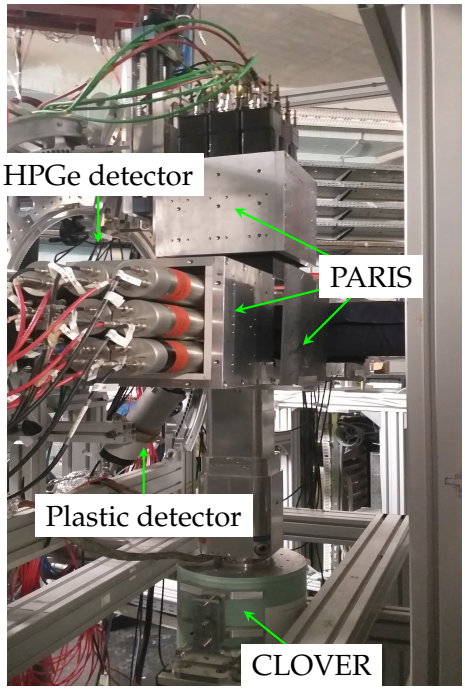

Figure 4.5: A photograph of the BEDO detectors' arrangement.

- Three PARIS [5] clusters, each composed of nine phoswich detectors [91], were utilized in the experiment. The PARIS array had a total efficiency of approximately 1.5% at 5 MeV, with each cluster positioned 12 cm away from the centeral source. More details about PARIS can be found in section 4.1.2.3.
- A segmented small EXOGAM CLOVER detector from the prototype series was also used in this experiment, with an energy range set to 10 MeV. The measured efficiency of the CLOVER detector was 0.41(4)% at 1.17 MeV, with

[5] Photon Array for studies with Radioactive Ion and Stable beams

the detector placed 7 cm away from the source. At 1.3 MeV, the energy resolution of the CLOVER detector was 2.43(1) keV.

– A coaxial HPGe[6] detector of type EUROGAM-1 was also utilized, positioned at zero degrees with respect to the beam, with an efficiency of 2.12(2)% at 1.17 MeV. The detector was located 50 mm from the calibration source and had an energy resolution of 2.60(1) keV at 1.3 MeV.

4.1.2.3 The PARIS detector

The PARIS project aims to study nuclear structures and reaction dynamics. The aim is to detect γ-rays of widely varying energy and multiplicity emitted during fusion-evaporation or fusion-fission reactions, for example. In this work, PARIS was used for the first time in a beta decay experiment. The PARIS detector setup was designed to be as efficient as possible in the energy range from 50 keV to 40 MeV and also with good energy resolution at low energies. Furthermore, as neutrons may be produced by some reactions, a time resolution of less than one nanosecond allows discrimination of neutrons from γ-rays by the time of flight. Other essential qualities of this detector are that it has good granularity, it is modular and transportable. The PARIS detector consists of clusters containing 9 phoswiches in an aluminum cup transparent to γ-rays and lined with a reflector to collect the optical photons produced inside the phoswiches (see Fig. 4.6). The

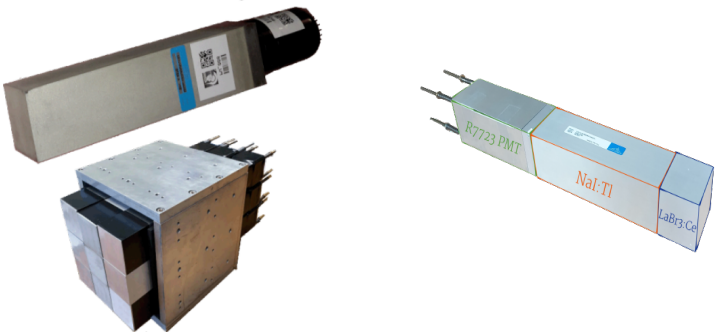

Figure 4.6: PARIS cluster and a phoswich detector.

phoswiches are composed of two crystals whose dimensions are given in inches: a 2″x2″x2″ $LaBr_3$(Ce) crystal (blue contour in Fig. 4.6) and a 2″x2″x6″ NaI(Tl) crystal (orange contour in Fig. 4.6). The $LaBr_3$(Ce) crystals show excellent energy resolution of 4 - 4.5 % at 661 keV, and high detection efficiency. These characteristics are superior to those of NaI(Tl) crystals, whose resolution can hardly go below 7% at 661 keV. Moreover, NaI(Tl) crystals are transparent to the scintillation photons produced by $LaBr_3$(Ce). Coupling them makes it possible to have a fairly good detector that takes advantage of the exceptional properties of $LaBr_3$(Ce) crystals, offering high efficiency due to its depth while remaining within acceptable price ranges.

[6] High Purity Germanium

The two crystals of $LaBr_3$(Ce) and NaI(Tl) are coupled to a common photomultiplier, so each phoswich had only one output signal. In principle, the presence of a single photomultiplier to recover the scintillation photons from two different crystals may sound challenging. However, studies already carried out show that the decay times of these two crystals are different enough to separate the signals correctly. Indeed, knowing the time of the two signals produced by the crystals, separating them by taking the fast component for $LaBr_3$(Ce) and the slow one for NaI(Tl) is totally sufficient. This can be seen in Fig. 4.7 where the photons absorbed predominantly in one or both of the crystals can be distinguished. The Q-long and

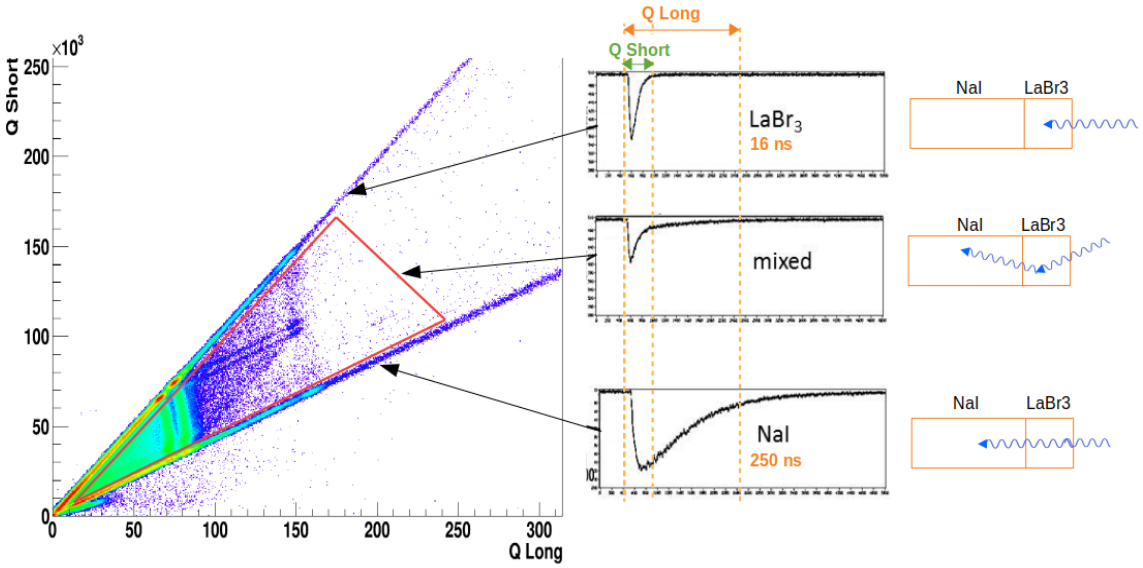

Figure 4.7: Explanatory figure to show how to distinguish signals from different crystals in one PARIS phoswich. The data are taken from the ^{60}Co source files. See text for the explanation.

Q-short in Fig. 4.7 correspond to the charge collected in a long and a short time gate, respectively. Based on the difference in the time constant of each crystal, it is possible to distinguish signals from different crystals. If there is only interaction in the $LaBr_3$(Ce) crystal, Q-short and Q-long should be equivalent. This results in corresponding events appearing along the x=y line in Fig. 4.7. However, if there is an interaction just in the NaI(Tl) crystal, Q-long will be greater than Q-short. The events shown in the red triangle in the figure are those recorded when the γ rays are interacting in both crystals simultaneously. The energy deposited in one phoswich is obtained by the off-line add-back procedure of the energies deposited in both parts of the phoswich. The procedure of the analysis will be explained in chapter 4.

4.1.3 FASTER data-acquisition system

FASTER (Fast Acquisition SysTem for nuclEar Research) is a modular digital acquisition system developed at LPC-Caen, France [92]. It is based on a synchronized tree model and can handle up to a few hundred signals. FASTER hardware is

composed of two parts :

- the daughterboards connected to detectors
- the motherboards in charge of communication, synchronization, and different functions programming on embarked FPGAs.

The system is trigger-less, with data from each detector being timestamped (10 MHz clock distribution). In our experiment, we used two types of daughter boards: CARAS and MOHSAR.

The MOHSAR (MOdule for Signal Acquisition, High Resolution) daughter-board provides 4-channel readout with a frequency sampling of 125 MHz and a 14-bit resolution depth. It can be used with a dynamic input range of $\pm$ 1V, $\pm$ 2V, $\pm$ 5V, and $\pm$ 10V. For our experiment, it was used for the HPGe preamplifier readout, providing time-stamp, TDC and amplitude measurements.

The CARAS (CARte d'Acquisition du Signal) daughter-board provides 2-channel readout with a frequency sampling of 500 MHz and a 12-bit resolution depth. It has a dynamic input range of up to 2.2V. It was used for PARIS, and plastic photo-multipliers readout providing time-stamp, TDC, and charge measurements.

The detectors' management by the computer was done through the faster_GUI interface, which allows the user to monitor the module's status, the number of events recorded, and the acquisition time. The user can use this interface to launch the acquisition, record the data in .fast format, switch the channels on and off, and access the control panel of each module. The control panel of each module allows the user to configure the detectors.

The data recorded by FASTER in .fast files can be converted into .root or other files using libraries coded in C/C++. The analysis of the NRI15 data was done using a code developed in this thesis to transform the data into C++ objects (TTree, TH1, TH2 and TGraph) provided by the ROOT libraries.

4.2 The I281 experiment

The second experiment of this PhD thesis, I281, was carried out at the IGISOL facility at the University of Jyväskylä, Finland, in 2022. It was dedicated to studying the β-decay of ^{86}As. The experimental details are provided in the following subsections.

4.2.1 Radioactive ion beams at the IGISOL facility

In section 4.1.1, the ISOL technique was introduced. The method used at ALTO is, as already mentioned, based on bombarding a thick target with light and intense primary beam. In the early 1980s, a gas-cell-based ion-guide method was developed at the University of Jyväskylä [93]. With the Ion Guide Isotope Separator On-Line (IGISOL) technique, any type of target can be used. This technique has the advantage of being faster than the typical ISOL technique, and most importantly, it is chemically insensitive, which was the main reason why the I281 experiment was performed at the IGISOL facility where the ^{86}As beam can be produced with good intensity. In the 1990s, the second phase of IGISOL, called IGISOL-2, was transferred to the Ylistönrinne campus and connected to a new K130 heavy ion cyclotron that can deliver beams with energies of up to 130 Q^2 /A MeV. In 2003, IGISOL-2 was upgraded to IGISOL-3. The new system featured improved radiation shielding. The former system's ion guide was replaced by a SPIG [94] for driving the ions into the mass separator. Then in 2010, the IGISOL facility was moved to a new experimental hall, where, in 2014, it was improved to the latest upgrade IGISOL-4 [95].

The radioactive ion beam at IGISOL can be produced in two ways:

1. Light-particle-induced fission reactions;
2. Fusion reactions induced by medium-heavy beams;

The beams are delivered by the K130 or MCC30 cyclotron onto a thin target in both cases.

The front end of the facility is explained in Fig. 4.8, and the layout of IGISOL is shown in Fig. 4.9. In the ^{86}As experiment, 25 MeV protons with a typical beam intensity of 10 μA were impinging onto 15 mg/cm^2 thick natural uranium target at the fission ion guide at IGISOL. In a gas cell filled with helium, the reaction products were guided to an exit cavity by the gas flow, and the sextupole ion guide SPIG, then the ions were extracted from the gas cell and accelerated to 30 q keV. In most cases, the charge state of the ions q was +1. The ions were then selected based on their mass-to-charge ratio using the 55° dipole magnet with a resolving power of $\frac{M}{\Delta M}$ = 500. Then, the ions could be driven using an electrostatic switchyard either to the spectroscopy line, the radio-frequency cooler-buncher (RFQ) [96], or to the cesium atom trap station [97]. In this work, the ions were decelerated on their way to the cooler-buncher, where they were cooled using helium buffer gas and then bunched at an energy of 800 eV as short bunches, typically 10 - 15 µs

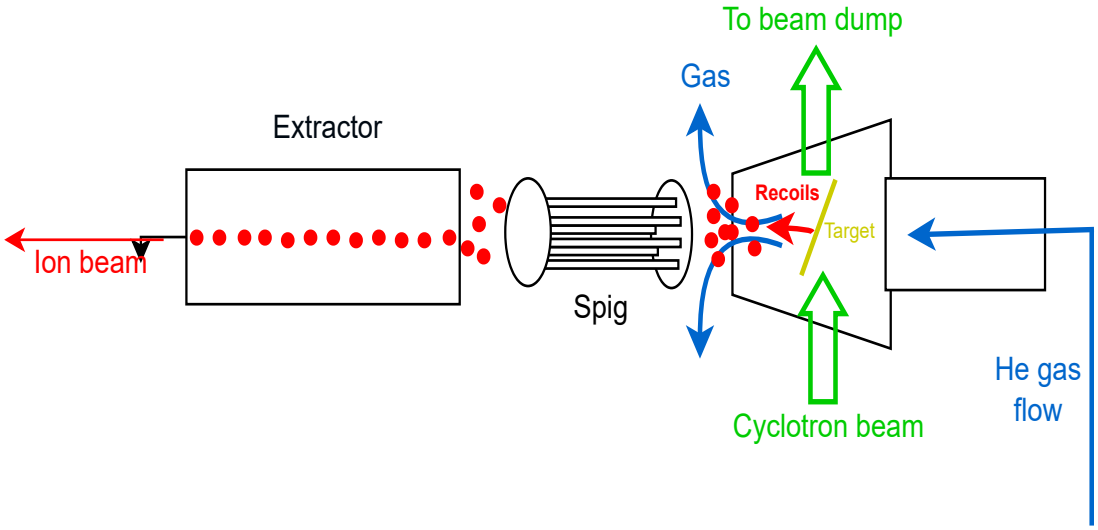

Figure 4.8: Schematic of the IGISOL ion guide.

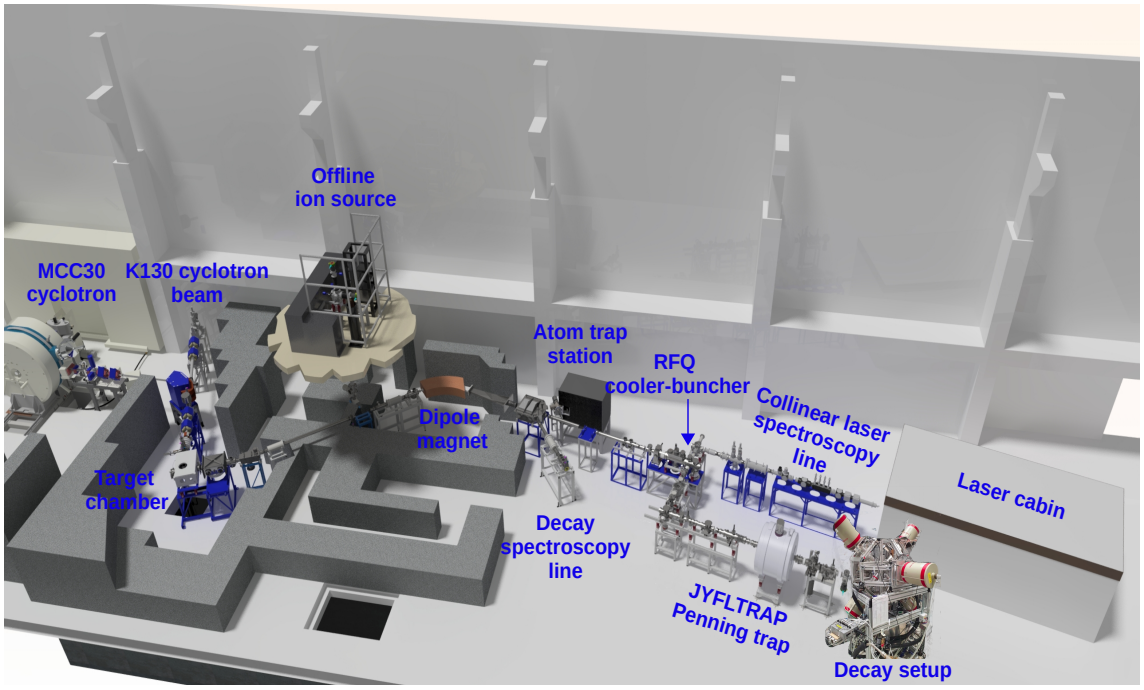

Figure 4.9: Schematic of the IGISOL facility.

in width. Going out of the cooler-buncher, the ions could be transported to the MR-TOF/JYFLTRAP double Penning trap beam lines, after which the decay setup was installed for the ^{86}As decay measurements.

4.2.2 Experimental setup

4.2.2.1 JYFLTRAP double Penning trap for beam purification

A Penning trap, named after the Dutch physicist Frans Michel Penning, can be explained as an instrument that uses a homogeneous magnetic field and a quadrupolar electric field to confine charged particles [98] [99]. It is used to perform very precise mass measurements in principle, but it can also be used as a purification system in decay spectroscopy experiments to deliver an isotopically or even isomerically pure beam. The Penning trap at the IGISOL facility, JYFLTRAP [100], has two cylindrical Penning traps:

1. **The purification trap:** A gas-filled trap explicitly dedicated to beam purification.
2. **The precision trap:** Used for high precision mass measurements.

The two traps consist of a series of gold-plated electrodes of 1046 mm length located inside a 7 T superconducting magnet (figure 4.10).

Figure 4.10: Top: The JYFLTRAP Penning trap superconducting magnet. Bottom: The gold-plated electrodes of the JYFLTRAP [101]

The ion bunches from the RFQ cooler-buncher were then transported to the first trap of JYFLTRAP. The first trap contained helium buffer gas, and it was used in this work to select the $^{86}As^{+}$ ions for the decay spectroscopy using the mass-selective buffer-gas cooling technique [102]. In this technique, all ions in the first trap were first excited to a larger radius using a dipolar magnetron excitation. Then, a mass-selective quadrupolar excitation was applied for 100 ms

at the RF frequency of 1250437 Hz corresponding to the cyclotron frequency of the $^{86}As^{+}$ ions (see the excitation scan in Fig. 4.11). The slow magnetron motion was converted into the much faster cyclotron motion, and the ions collided more with the helium atoms and were centered in the trap center. The centered selected ions could finally be extracted using a diaphragm of 2 mm diameter to the second trap and to the decay spectroscopy setup after it.

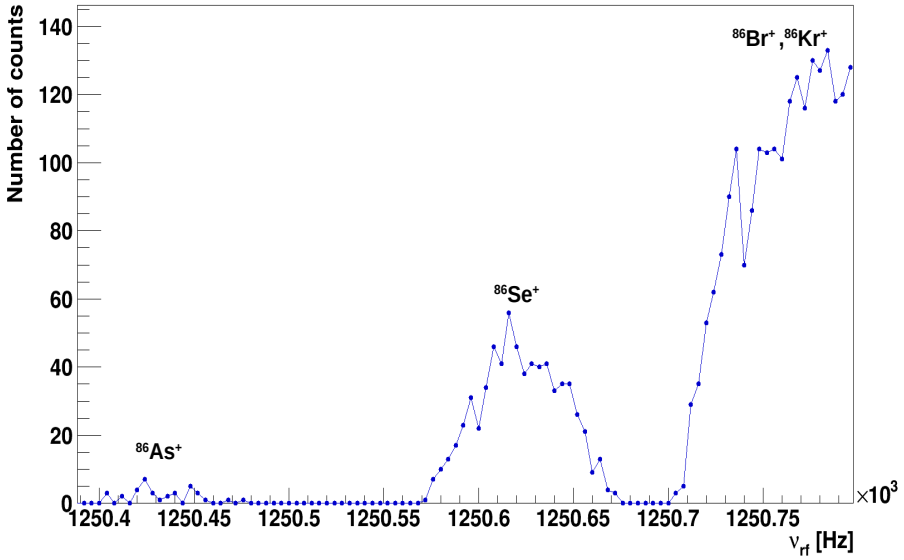

Figure 4.11: A scan of the quadrupole excitation frequency in the first trap of JYFLTRAP showing the different isobars at mass number A=86.

4.2.2.2 Tape and measurement cycle

The $^{86}As^{+}$ ions selected with JYFLTRAP were extracted from the trap and implanted into an Al-coated mylar tape located at the center of the detection setup inside the plastic beta detector's frame (see Fig. 4.12). The IGISOL tape station, shown in Fig. 4.13, is very similar to the one used at ALTO. The trap sent the beam in bunches every 150 ms to the collection point in the center of the decay station. The effect of this discontinuity of the beam can be seen clearly on the implantation and decay curve shown in Fig. 4.14. Then at the end of the tape cycle, the trap sent a signal to the tape controller to move it, so the irradiated part of the tape was removed while a new "clean" portion of the tape went up to the collection point. The principle of the tape controller is the same as explained in section 4.1.2.1, see Fig. 4.4. In fact, the spectroscopy measurement cycle chosen to measure the decay

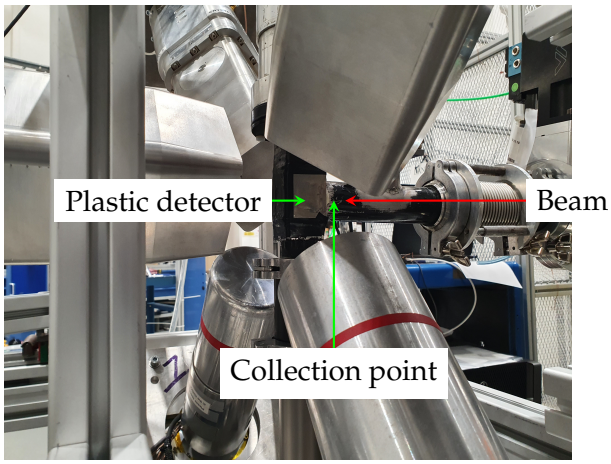

Figure 4.12: The collection point at the center of the decay station.

of ^{86}As was again based on its half-life (945 ms [45]). The details are listed in Table 4.2.

Table 4.2: The choice of the tape cycle for the measurement of the ^{86}As decay and half-life.

	t_{bck} (s)	t_c(s)	t_d(s)
Spectroscopy measurement	0.5	3	3
Half-life measurement	0.5	3	5

Another cycle was defined during the experiment in order to re-measure the half-life of ^{86}As, as there is only one measurement with a reasonable precision that is found in the literature ($T_{\frac{1}{2}}$ = 945 (8) ms [45]). The details of the half-life measurement cycle can be found in Table 4.2. The implantation point of the tape was surrounded by a $3\pi\Delta E\beta$ scintillator detector that was used to tag the beta-decay electrons and was located at the center of the decay station.

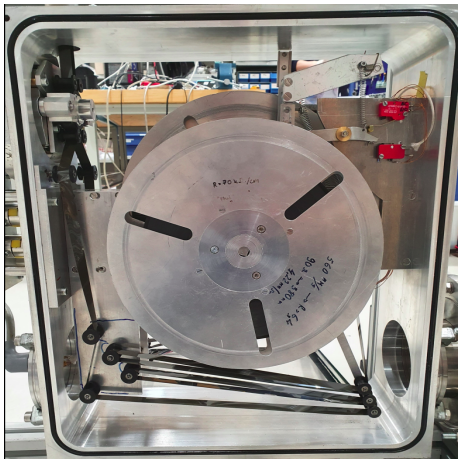

Figure 4.13: The IGISOL tape station as seen from the inside.

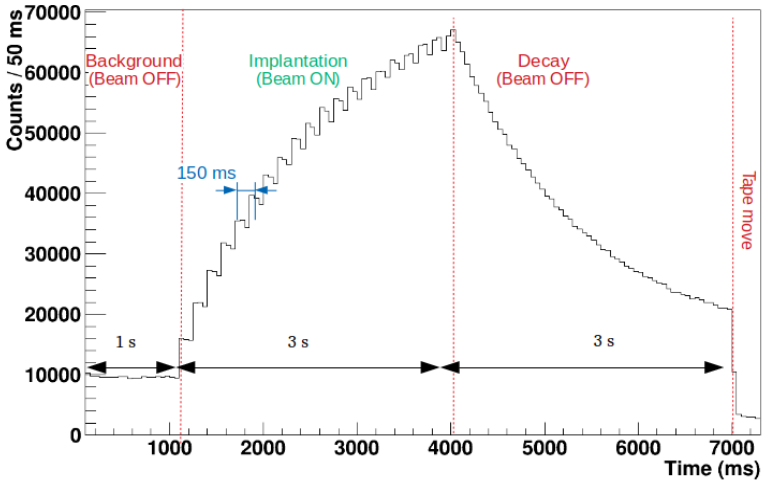

Figure 4.14: The accumulation and decay curve of ^{86}As with the spectroscopy measurement cycle.

4.2.2.3 The γ detection setup

The data analysis of the NRI15 experiment showed that most of the high-energy gamma lines could be seen clearly in the CLOVER detector, which is why this experiment was based only on HPGe detectors since the energy range of interest (up to 7 MeV) can be fully covered by the CLOVER detectors with an energy resolution of $\sim$ 2.3 keV at 1.3 MeV. In addition, CLOVER detectors have excellent peak-to-background ratio and provide very clean gamma spectra resulting from beta decay. Therefore, the decay setup in this experiment was composed of 5 HPGe detectors, as shown in Fig. 4.15. The HPGe detectors were dedicated to gamma spectroscopy, constituting:

– Three CANBERRA segmented CLOVER detectors from IFIN-HH [103] with an average range set to 10 MeV. (Efficiency of the three detectors in add-back mode = 2.04 (1) % at 1.17 MeV, source placed at 7 cm from each one);

– Two Canberra GC7020 coaxial germanium detectors, one with a longer nose (GC7020L) and the other one with a standard configuration (GC7020S). The energy range for GC7020L was set to 3.5 MeV (Efficiency at 1.17 MeV = 0.340 (5) %) while the GC7020S had an average energy range of 2.8 MeV (Efficiency at 1.17 MeV = 0.326 (5) %);

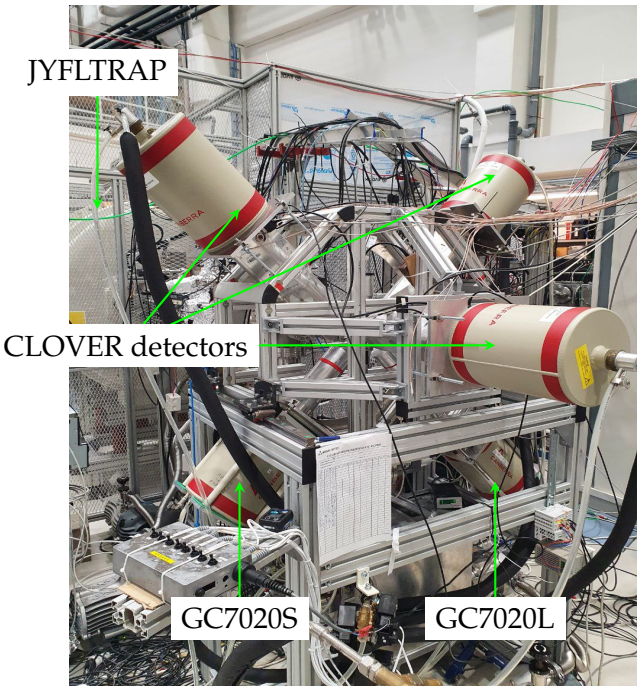

Figure 4.15: A photo of the IGISOL post-trap decay setup.

The signals from all the detectors and the timing signals produced by the JYFLTRAP timing card were sent to the Nutaq digital data acquisition system.

4.2.3 Nutaq data-acquisition system

The Nutaq hardware [104] was used during the I281 experiment at IGISOL for data acquisition, and the Java-based Grain software [105] was used for the online analysis. The Nutaq digital data acquisition system had one 16-channel high-speed multichannel acquisition platform called the VHS-ADC card with a 105 MHz sample rate. With this system, it was possible to record up to 105 MBPS, allowing high-speed data transfer. The trap timing and detector preamplifier signals were all coupled to Nutaq DAQ via an offset and amplifier unit box. The signals accepted by the Nutaq system were from -1V to +1V, so to be able to benefit from the 2V digitization range, the preamplifier signals had to be modified before being sent to the DAQ. The signal's baseline was therefore set to -1V since the height of the signals has to be within $\pm$ 1V range. The data from each detector were timestamped and recorded in triggerless mode. They were then converted into .root files using a C++ code to reconstruct the $\beta - \gamma$ and $\beta - \gamma - \gamma$ events in the offline analysis.

5 DATA ANALYSIS

After converting the faster files from the NRI15's experiment at ALTO, and the Nutaq files from the I281's experiment at IGISOL, into ROOT files, all the recorded data were stored in ROOT trees with branches that could be manipulated easily during the analysis process depending on the need. The considered physical events were those originating only from beta decay. In that case, the beta particle detection signal was considered the reference signal to reconstruct the physical events from the raw data.

5.1 Time alignment and calibration of the detectors

5.1.1 Synchronisation of the signals

The data taken at IGISOL had the time signals well aligned already, so this step was not needed for the data analysis of I281. However, in the case of the NRI15 experiment at ALTO, the reference times for the detectors were not the same (for example, due to different signal rising times or cable lengths.), and they needed to be shifted to one random value, but it had to be the same for all the detectors. The effect of the time shift correction is monitored in Fig. 5.1.

5.1.2 Energy calibration

5.1.2.1 At IGISOL

In order to calibrate the HPGe detectors in energy, sources of ^{152}Eu and ^{133}Ba, placed 1 cm away from the collection point, were used. These sources provided calibration points up to 1.4 MeV, but our energy range of interest went up to 6-7 MeV in the case of the ^{86}As measurements. Therefore, part of the beam time was dedicated to collecting data on the A= 86 mass since many A=86 isobars have well-known spectroscopic information; for example, gamma-ray transitions are

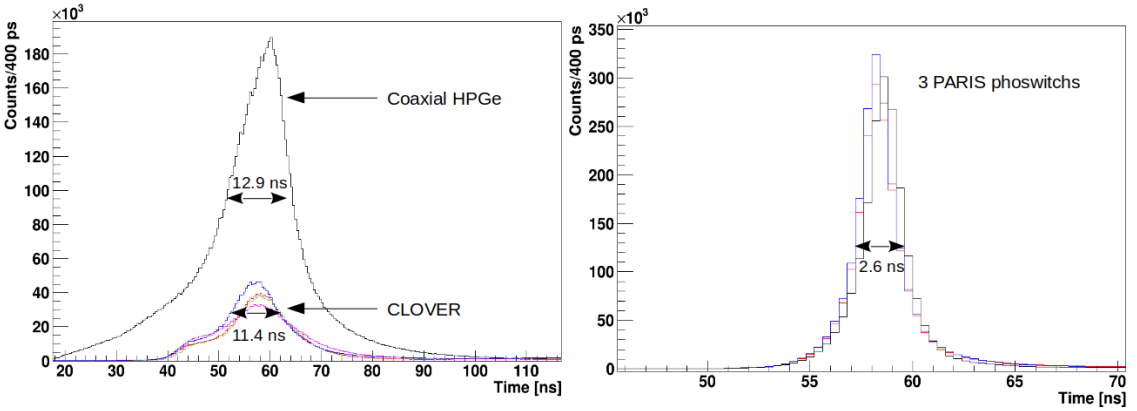

Figure 5.1: The time distribution of the coaxial HPGe detector (FWHM = 12.9 ns), the Clover detector (FWHM = 11.4 ns) (left) and the PARIS array (FWHM = 2.6 ns) (right) with respect to the β time signal.

known up to around 6.7 MeV in ^{86}Kr [106]. The Nutaq electronics present excellent linearity over a large energy range: a calibration with a first-degree polynomial was sufficient. The alignment of the different detectors was checked by plotting the spectra obtained by the different detectors on the same histogram, as shown in Fig. 5.2.

5.1.2.2 At ALTO

The energy calibration of the detectors at ALTO was not as simple. Due to possible DAQ instabilities, a gain drift was noticed in the gamma detectors. In fact, before realizing this problem, the energy calibration was done using ^{152}Eu, ^{60}Co, ^{207}Bi, and ^{137}Cs sources for the low-energy part and for the high-energy region an AmBe source surrounded by nickel plates which gave a γ-ray at 4439.8 keV (AmBe[1]) and another one at 8998.6 keV (AmBe + Ni[2]). After applying the obtained calibration coefficients to the data, all spectra from HPGe detector crystals were summed up to get a combined gamma spectrum from all the Ge detectors, but the energy resolution had completely deteriorated. To identify the source of the problem, the raw data were checked file by file. One could see by superimposing spectra from the same crystal but with data registered at different times that the peaks did not overlap exactly. An example is shown in Fig. 5.3. The only possible solution for this issue was to check all the raw data files, make groups of the files with the same gain, and calibrate each group individually for each crystal. However, in this case, it is not wise to use the calibration sources file recorded at the beginning of the experiment since the gain was drifting with time. In other words, it was crucial to take the calibration points from each group of physics files independently to avoid this problem. Luckily, in the ^{82,83}Ga collected data, there are known gamma-ray transitions up to 6 MeV, enough to perform the energy calibration over an important part of the energy range of interest. This procedure

1 $Am \rightarrow \alpha + {}^{9}Be \rightarrow {}^{13*}C \rightarrow n + {}^{12*}C_{(2^+ \rightarrow 0^+:\,4439.8\ \mathrm{keV})}$

2 $n + {}^{58}Ni \rightarrow {}^{59*}Ni_{((1/2)^+ \rightarrow (3/2)^-:\,8998.6\ \mathrm{keV})}$

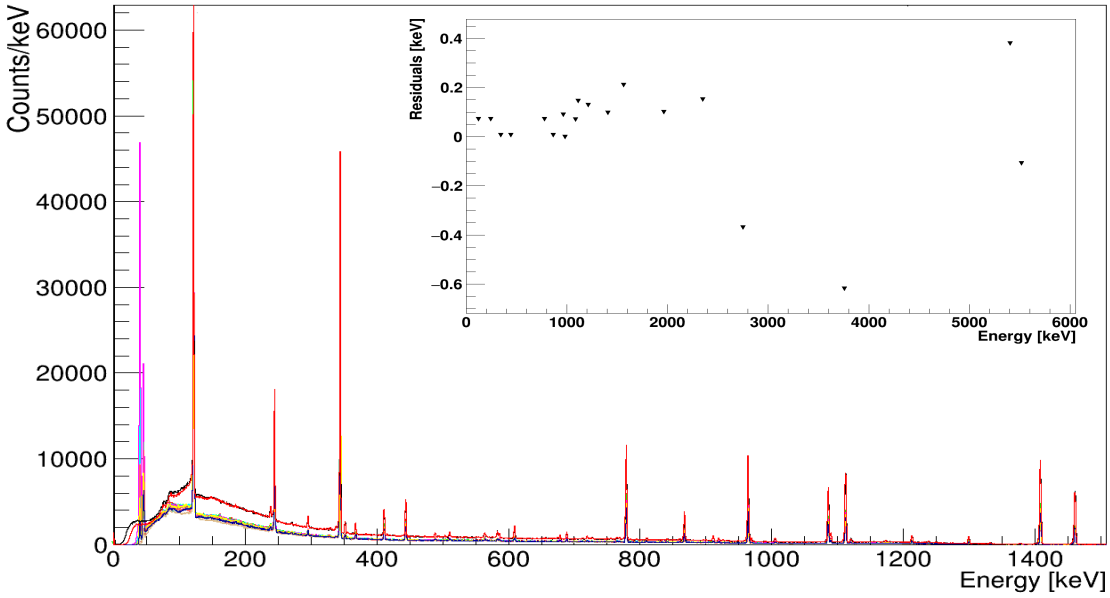

Figure 5.2: The ^{152}Eu spectrum obtained using the 14 germanium crystals of the IGISOL decay setup after energy calibration. Each color represents a crystal. Inset: The residuals as a function of the energy. Points above 1.4 MeV were obtained from the β-decay of ^{86}Br.

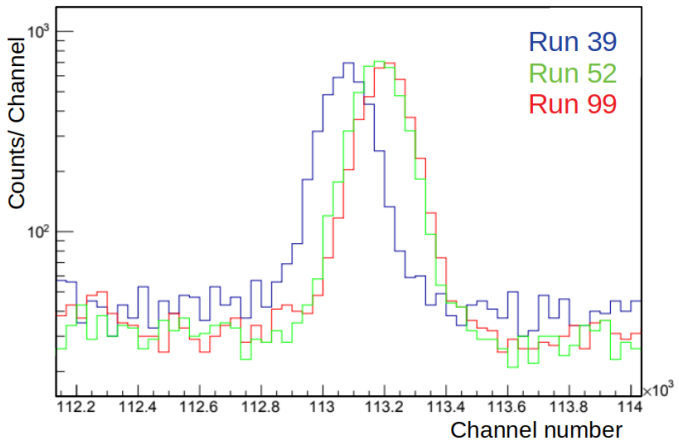

Figure 5.3: Part of a ^{83}Ga raw data spectrum from the coaxial Ge detector, showing the difference in the centroids' positions with respect to the number of file.

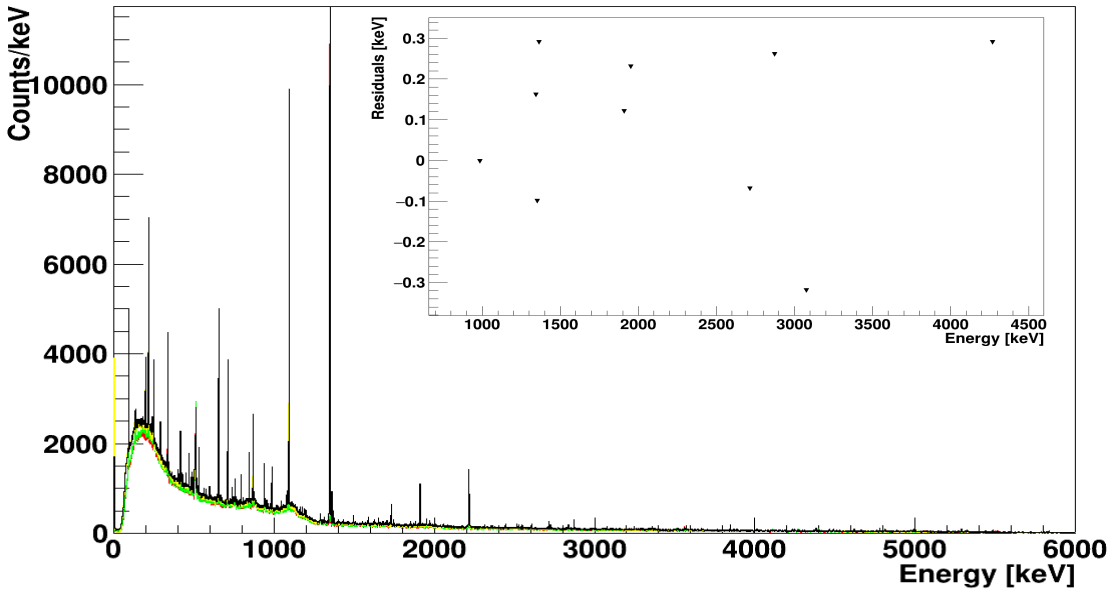

Figure 5.4: ^{82}Ga β-gated γ spectra with all the collected data from the four Clover crystals each one plotted with a different color. Inset: The residuals as function of the energy.

was lengthy but gave a linear fit of the calibration curve when applied to all the Ge detectors. The energy resolution was then checked for all the Ge detectors summed, and the FWHM at 1 MeV was 2.5 keV (while it was 2.43 keV for a single crystal). The linearity check is shown in Fig. 5.4. We note that this procedure was not applied to the data from PARIS, since the gain drift was on the order of a few keV, which is within the scintillator energy resolutions (FWHM/Eγ $\simeq$ 4.5 % at 661 keV for $LaBr_3$ and $\simeq$ 7 % at 661 keV for NaI).

5.1.3 Efficiency calibration

5.1.3.1 At IGISOL

The efficiency calibration of the HPGe detectors at IGISOL up to 1.4 MeV was performed using the standard calibration sources (^{152}Eu and ^{60}Co) placed 1 cm away from the collection point at IGISOL. The efficiency $\varepsilon(E\gamma)$ of a detector at a given energy E_γ is given by equation 5.1.

$$\varepsilon(E_\gamma) = \frac{N(E_\gamma)}{\mathrm{At}I_\gamma} \tag{5.1}$$

where:

- N (E_γ): the area of the photo peak at energy E_γ (background subtracted);
- A: is the activity of the source at the time of the measurement;
- t: the acquisition time;
- I_γ: the absolute branching ratio of the considered transition.

The beta decay measurement of ^{86}As at IGISOL required a large energy detection range since the Q_β value is 11541 (4) keV [107]. Therefore, using the standard calibration sources alone would not have been enough to perform the efficiency calibration over the entire energy range. However, this was anticipated, and a source of ^{56}Co was prepared before the experiment by irradiating with protons an additional iron foil in the IGISOL target chamber. The efficiency was determined in the following way:

1. The efficiency was determined up to 1.4 MeV using standard calibration sources.
2. The strongest line in the decay of ^{56}Co was identified and fitted using a Gaussian function in order to get the peak area (number of counts). In this case, the most intense peak was the one at 846.7 keV (99.9 % of absolute intensity).
3. The gamma lines of interest were selected, and for each one, it was possible to estimate $N_{emitted}$: number of emitted γ-rays relative to the 846.7 keV line using the relative intensities from the literature [107].
4. Then the number of detected gamma rays ($N_{detected}$) at each energy of interest was extracted by fitting the peaks.
5. The ratio $\frac{N_{detected}}{N_{emitted}}$ gave an efficiency value at each energy (ε_{rel}, relative to 846.7 keV) that needed an extra correction factor to fit with the efficiency curve's trend obtained with the standard sources.
6. The correction factor was obtained using a gamma line from the ^{56}Co decay spectrum that has an energy below 1.4 MeV (to be able to estimate the efficiency (ε_{cal}) at this energy from the present efficiency curve). In this measurement, the transition at 846.7 keV was the best candidate since it has the highest intensity. The relative efficiency values obtained in the previous step were then corrected to ε_{cal} (846.7 keV) and added to the efficiency points for fitting, in addition to the points from the standard sources.

After getting efficiency data points up to 4 MeV using the ^{56}Co source and more up to 6 MeV using the collected data of A= 86 mass (using the same procedure), all data points were fitted using the following function:

$$\varepsilon(E\gamma) = exp(p_0 - (p_1 + p_2 exp(-p_3 E))exp(-p_4 E) log(\frac{E}{E_0})) \tag{5.2}$$

The efficiency curve is shown in Fig. 5.5, where all the parameters obtained from a least-squares fit are listed.

Note that for the whole data set of this experiment, the AddBack procedure was applied. This procedure consists of reconstructing the energy of a photon after it has deposited part of its energy by Compton scattering in one of the four crystals of a Clover detector and the rest in its neighboring crystal. For this, we sum the energy deposited in the first crystal with the energy deposited in the second crystal if these energies are deposited in the crystals in a compatible time window corresponding to the response time of the detectors ($\Delta T\ \gamma - \gamma \leq 50$ ns).

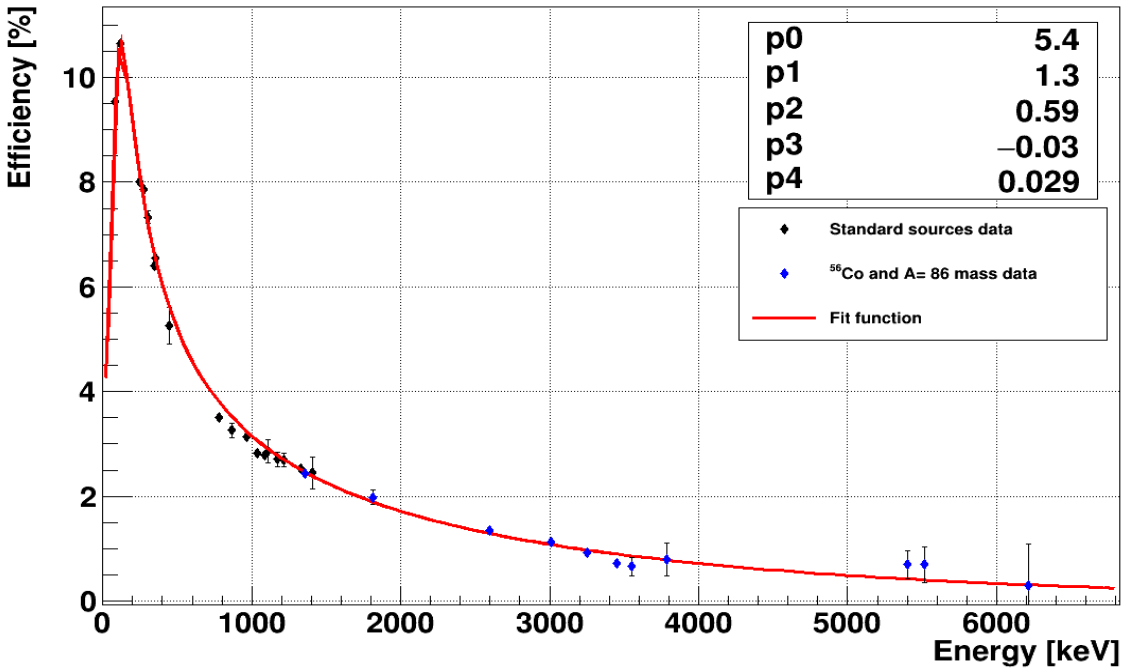

Figure 5.5: The absolute efficiency curve of the whole detection setup at IGISOL. Note that the detectors had different energy ranges: the long and short standard coaxial GC7020 detectors had energy ranges up to 2.8 and 3.6 MeV, respectively, while the ranges for the Clover detectors were up to 9 MeV.

The outcome of this procedure is to reduce the Compton background at low energy and increase the number of counts in the high-energy peaks (Fig. 5.6).

The β-detection efficiency was found to be 30 ± 4% (Fig. 5.7). It was obtained by comparing the peak area between the single gammas and the β-gated gamma spectra.

5.1.3.2 At ALTO

For the NRI15 experiment, the gamma detection efficiency of the detectors was determined using a ^{152}Eu source. This source provides points up to 1.4 MeV, as already mentioned. Unlike in the I281 experiment, no ^{56}Co source or any other physical source was prepared to get higher-energy calibration points. Therefore, numerical simulations were mandatory to cover the Q_β windows in ^{82}Ga and ^{83}Ga decays (12.5 MeV and 8.7 MeV, respectively).

This was done using the SToGS package, developed by the Lyon group [108], based on GEANT4 [109]. The geometry of the Clover detector, as well as PARIS, were defined in the SToGS package. The Coaxial Ge detector showed some efficiency problems, most probably due to the summing effect since it was placed 5 cm away from the collection point; thus, it was excluded, and the Clover detector was enough as a high-resolution detector. The most straightforward method to use them was to reproduce the detection efficiency values acquired with the ^{152}Eu source at the low energy range and then go higher in energies up to 8 MeV (the highest value needed for this analysis) with 100 keV energy steps. The obtained

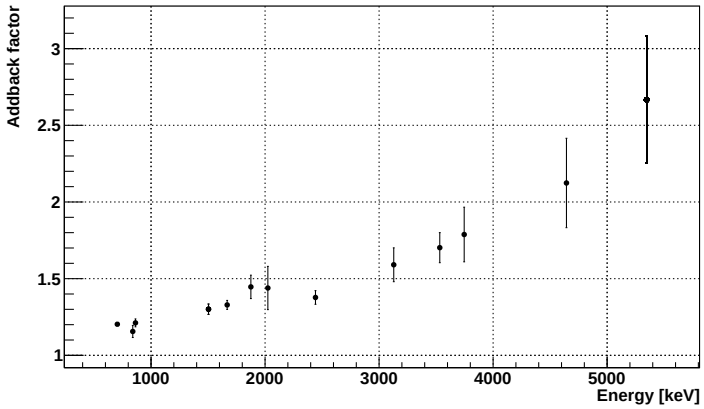

Figure 5.6: Addback efficiency as a function of the energy.

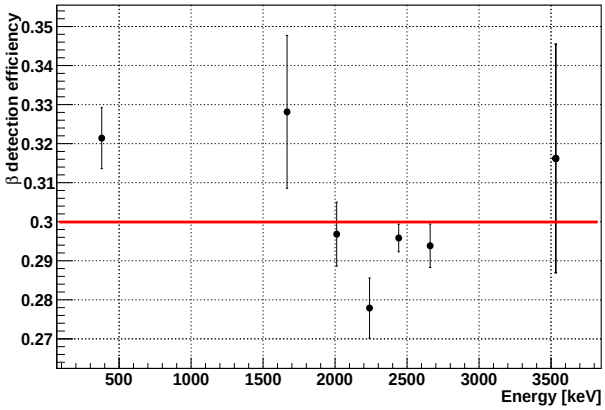

Figure 5.7: The β-detection efficiency of the IGISOL plastic scintillator obtained by comparing γ-ray intensities without and with the β-gate.

points were then fitted using equation 5.2 for the Clover (sum of 4 crystals) and the PARIS detector (sum of 3 clusters, taking into account only the $LaBr_3$ events due to its better energy resolution). The corresponding efficiency curves, along with fitting parameters, are presented in Fig. 5.8. Moreover, comparing the peak areas in the β-gated gamma spectrum to the ungated ones was also used to find the beta-detection efficiency, which was equal to 74 (3) % for this experiment (see Fig. 5.9).

5.2 γ-spectrum construction

In the beta decay of neutron-rich nuclei, the gamma spectrum can be contaminated by ambient activity or possible collection off the tape, for instance. This background was suppressed by using the $\beta - \gamma$ coincidence technique. In other words, from the energy-calibrated γ-spectra, only events in coincidence with an event in the β-detector were selected. This technique was applied to both data sets from NRI15 and I281 experiments, using two different analysis codes but with the same principle. These programs looked for events in the β detector, then took all the γ events before and after within a 50 ns time window. This condition allowed keeping only the γ events from the electromagnetic de-excitation of a nucleus after a β decay and thus strongly suppressed the background in the spectrum. An illustrative example is given in Fig. 5.10 from the ^{86}As decay data set.

5.3 Coincidence matrices

The next step after obtaining the β-gated gamma spectra was to identify the observed lines and associate them with the de-excitation of a particular nucleus. To do so, there are two possibilities:

- The first is to be able to relate the gamma line to a known transition by studying the $\beta - \gamma - \gamma$ coincidences.
- The second is to look at the evolution of the γ activity over time because this temporal distribution depends on the lifetime of the parent nucleus through the Bateman equations.

The procedure to extract the coincidences information can be summarized as follows:

1. The peak of interest was selected to get the $\beta - \gamma$-gated gamma spectrum.
2. The background on the left and right sides of the peak of interest was selected to get an average-background spectrum.
3. This spectrum was then used to get a background-subtracted gamma-gated spectrum.

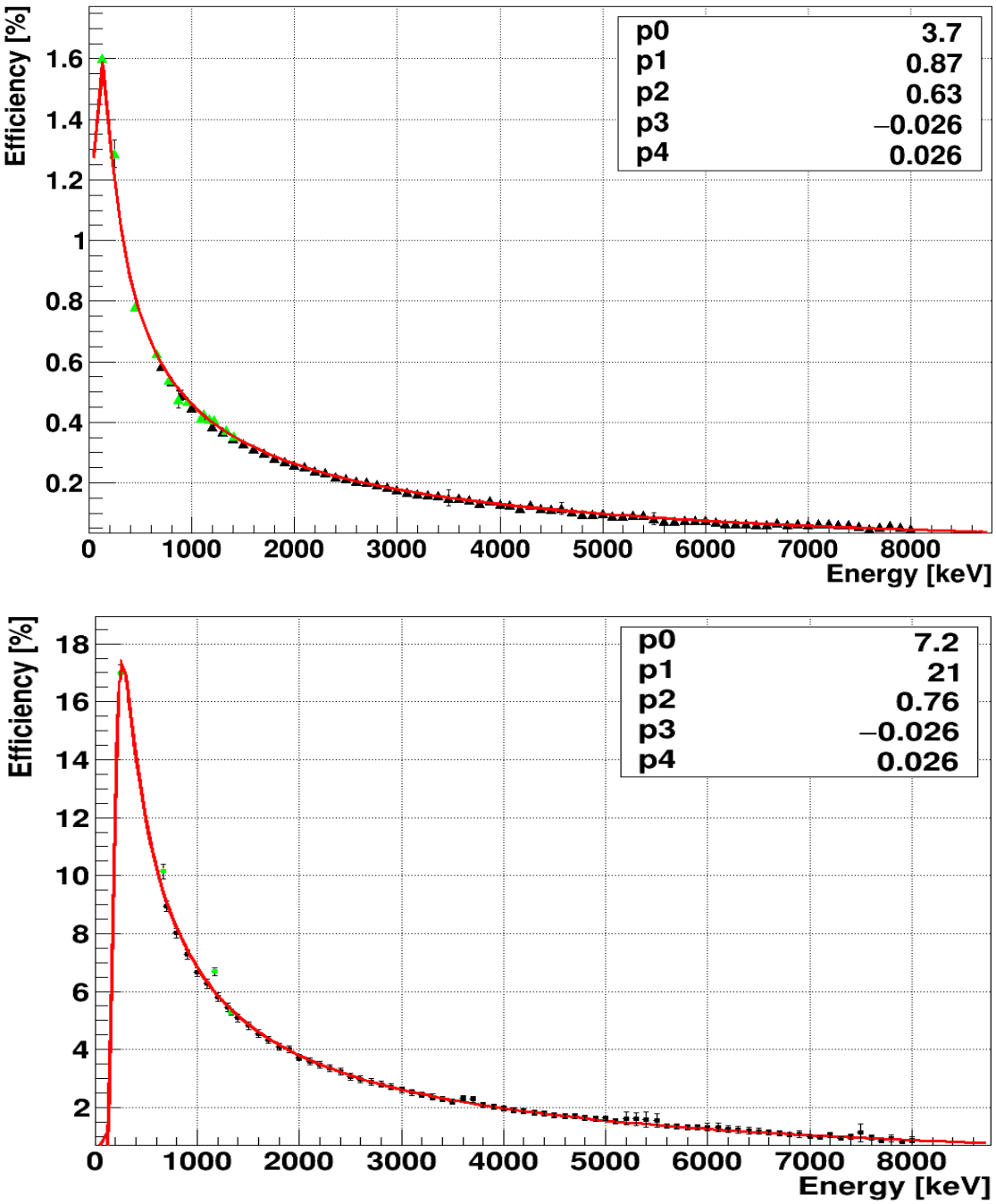

Figure 5.8: The absolute efficiency curves of the Clover detector (top) and the PARIS detector (bottom), the points in green are the experimental data points, the ones in black are those obtained with GEANT4 and the line in red curve is the fit function.

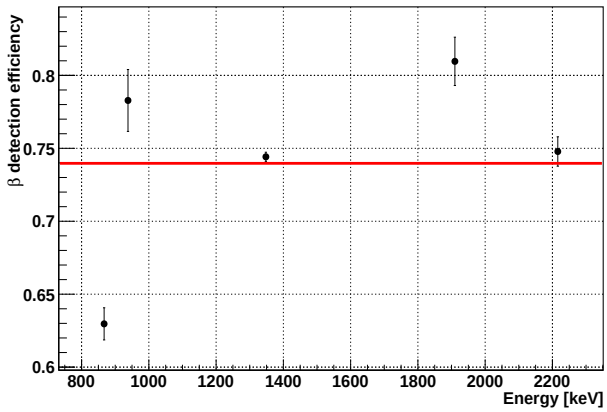

Figure 5.9: The β-detection efficiency of the BEDO plastic scintillator obtained by comparing γ-ray intensities without and with the β-gate.

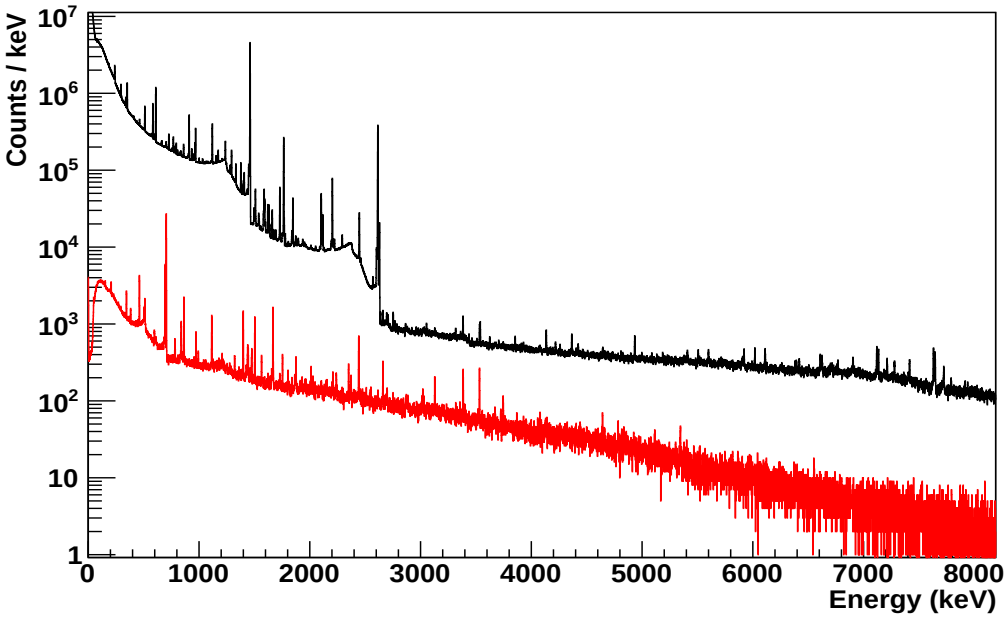

Figure 5.10: γ-spectrum of the β-decay of ^{86}As obtained with the IGISOL decay station (black), compared to the β-gated γ-spectrum (red).

4. The gamma lines seen in the gamma-gated spectrum were marked. Then, the coincidence was double-checked by gating on these lines to see if the original gamma transition was observed in the "inverse gate."

In the following subsections, the different coincidence matrices are presented. In order to avoid overloading this part with 2D histograms, only the ^{82}Ga matrices are presented as an explanatory example.

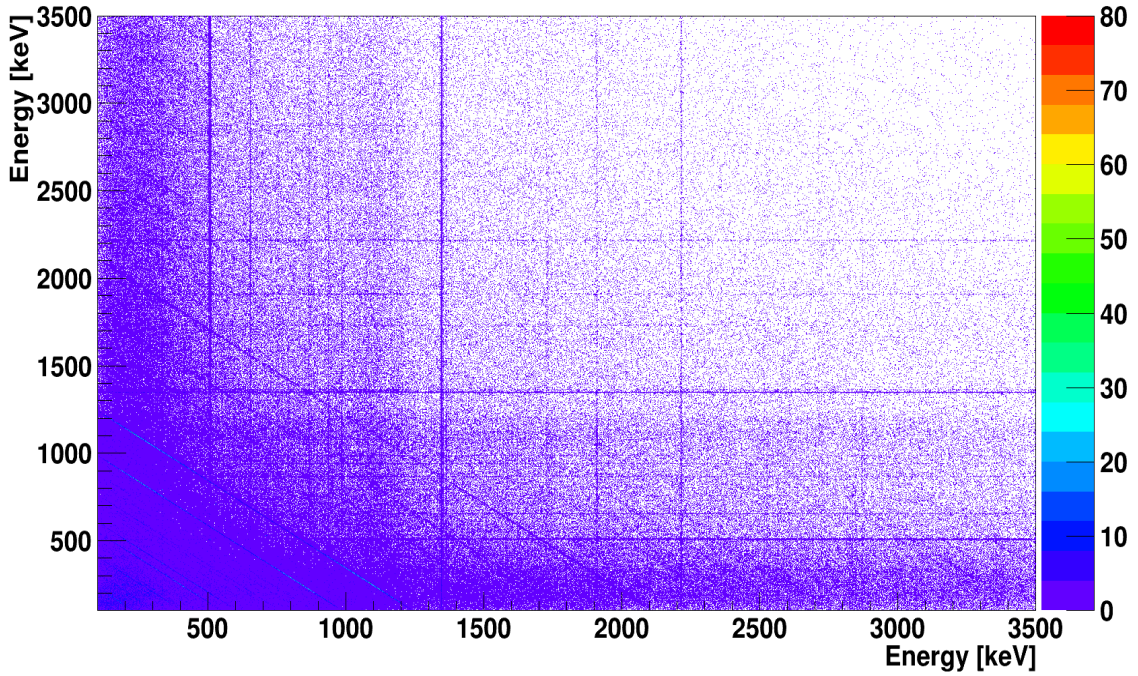

Figure 5.11: Part of the $\beta - \gamma_{HPGe} - \gamma_{HPGe}$ matrix obtained for the β-decay of ^{82}Ga.

$\beta - \gamma - \gamma$ matrix

For the β-decay of ^{82}Ga, the matrix obtained is shown in Fig. 5.11. This matrix has the $\beta - \gamma - \gamma$ coincidence events recorded using the HPGe detectors of the decay setup at ALTO. Each crystal from the Clover detector was treated as a separate detector (add-back was not applied to build the coincidence matrix). The coincidence window between the beta and gamma time window was set to 50 ns. The anti-diagonals observed in these matrices are due to the Compton scattering coincidences.The sum of the two energies deposited is equal to the energy of the incident photon, whatever the energy deposited in the first crystal.

The comparison between the projection spectrum of this matrix and the beta-gated gamma spectrum is shown in Fig. 5.12. This comparison is helpful, for example, when building the level scheme since it helps distinguish the transitions going directly to the ground state from those feeding excited states.

$\beta - \gamma - T$ matrix

This matrix has on the Y-axis the time assigned by the acquisition to the Ge event (i.e., the time difference between a beta-validated gamma event and the beginning of a tape cycle) and on the X-axis the energy deposited in the Ge detector, as shown in Fig. 5.13.

As mentioned before, the time evolution of the β-delayed γ-ray activity depends on the lifetime of the parent nucleus. For example, γ-ray transitions de-exciting the levels in ^{82}Ge populated via the beta decay of ^{82}Ga into ^{82}Ge have a time behavior depending on the lifetime of ^{82}Ga.

This matrix was used to validate the time behavior of a specific gamma ray

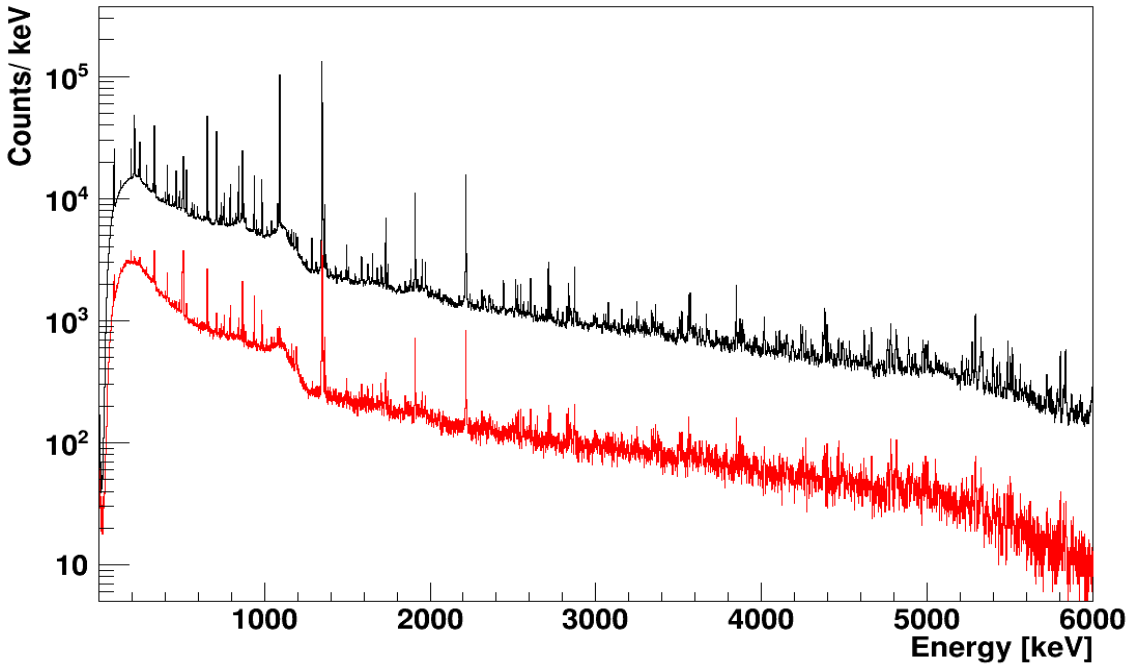

Figure 5.12: β-gated γ-spectrum of ^{82}Ga obtained with the BEDO decay station (black), compared to the projected β-gated $\gamma - \gamma$-spectrum (in red).

by gating on the gamma energy and fitting the corresponding decay curve using the Bateman equations. An example is shown in Fig. 5.14.

In order to construct the decay schemes of ^{82,83}Ga and ^{86}As, the $\beta - \gamma$, $\beta - \gamma - \gamma$ and $\beta - \gamma - T$ matrices constructed as described above were used. In the following chapter, the results of this analysis are presented.

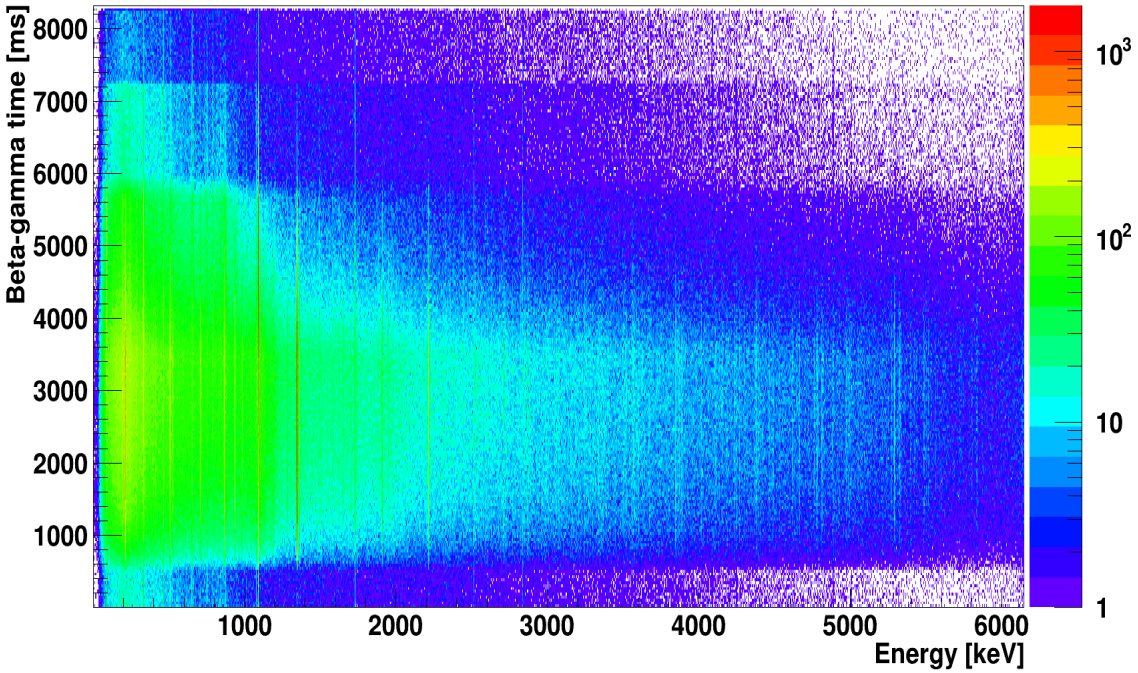

Figure 5.13: $\beta - \gamma - T$ matrix obtained by the β-decay of ^{82}Ga.

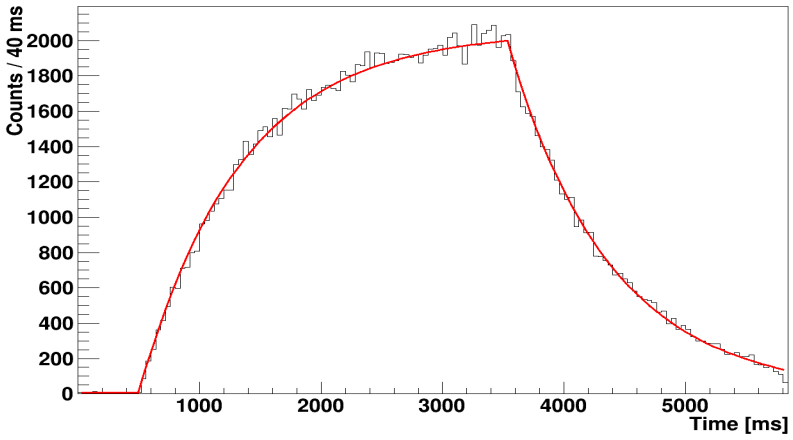

Figure 5.14: $\beta - \gamma$-gated time spectrum fitted with the Bateman equations (gate on the 1348-keV γ-transition in ^{82}Ge).

6 RESULTS

The following chapter includes the spectroscopy results obtained from the two experiments. For the construction of the level scheme, $\beta - \gamma - \gamma$ was used to identify transitions in cascade, and $\beta - \gamma$ spectra were used to count the number of events in each identified peak. The time behavior of each transition was used as a filter for assigning the γ-transition to a specific decay. High energy γ-transitions were validated only if at least the full-peak and the first-escape peak were identified. And additional verification step was applied by comparing the full-energy peak to escape peaks counts ratio (see Fig. 6.1 for explanation).

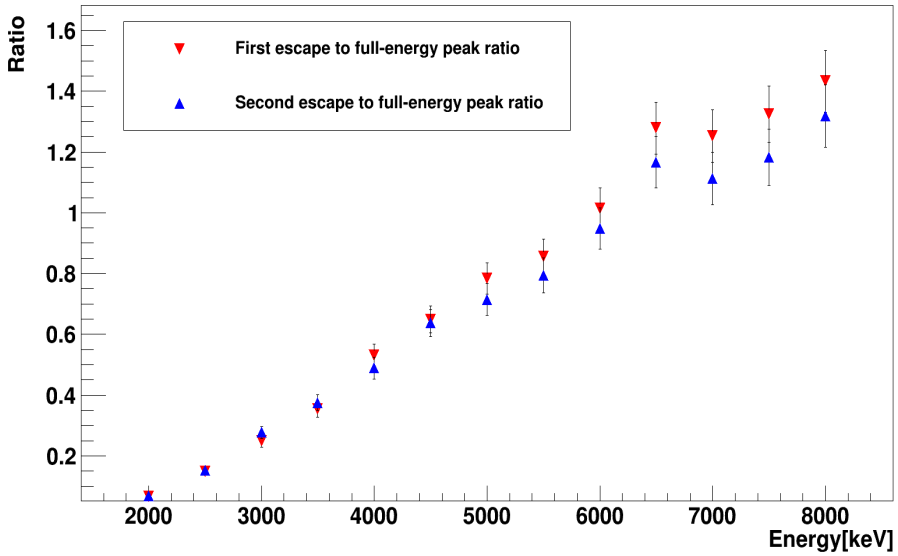

Figure 6.1: Geant4 simulation of the NRI15 Clover detector's response up to 8 MeV to monitor how the number of counts in the first- and second-escape peaks changes compared to the number of counts in the full-energy peak as a function of energy.

After the level scheme construction, the beta-decay feeding probabilities and the associated log *ft* were calculated. The PARIS spectra were analyzed very scarcely, given the amount of new spectroscopy data obtained using only the HPGe detectors in the NRI15 ALTO experiment. A full analysis of PARIS will be

done at a later stage and will not be presented here.

6.1 $\beta - \gamma$ spectra for the decays of ^{82}Ge, ^{83}Ge and ^{86}Se

During a measurement cycle, not only the decay of the implanted ions (^{82,83}Ga and ^{86}As) was observed, but also the decay of the descendants, at least the ones having up to a few seconds lifetime. The total numbers of implanted ions are presented in Table 6.1. The beta-gated gamma spectrum is presented for the beta decay of ^{82}Ga in Figs. 6.2 and 6.3, for the beta decay of ^{83}Ga in Fig. 6.4 and for the beta decay of ^{86}As in Figs. 6.5 and 6.6. The γ activities from the different generations of the descendants can be seen in the γ-spectra. From Figs. 3.6, 3.7 and 3.8, one can see that all the daughter nuclei have significantly longer half-lives. Thus, their gamma-ray transitions can be distinguished easily by fitting their temporal behavior using the matrix of Fig. 5.13 for the ^{82}Ga decay daughters (and similar matrices for ^{83}Ga and ^{86}As). All the unidentified peaks that have no coincidence and unclear time distribution are summarized in Table 6.2.

Table 6.1: Average implantation count rates and the total number of implanted ^{82,83}Ga and ^{86}As.

	Average Implantation rate [ions/s]	Total number of implanted ions
^{82}Ga	6005 (667)	57384118 (6379112)
^{83}Ga	118 (5)	13923928 (279031)
^{86}As	142 (32)	9103595 (2069820)

6.2 $\beta - \gamma - \gamma$ coincidence analysis for the decays of ^{82,83}Ga and ^{86}As

In the following sections, the $\beta - \gamma - \gamma$ coincidence analysis is described. It was applied to reconstruct the γ-ray cascades by assigning the γ- transitions to the decay of the parent nucleus of interest. For each studied γ-ray transition, the procedure started by gating around it in the $\beta - \gamma - \gamma$ matrices (similar to the one in Fig. 5.11), with a subtraction of the background as already explained in section 5.3, to obtain a projection spectrum (energy distribution spectrum) in coincidence with the selected energy. Then, the peaks observed in the γ-gated spectrum were checked one by one. The random coincidences were minimized, thanks to the background subtraction. Then, an "inverse-gate" procedure was applied in order to confirm the real coincidences. For example, if gating on a γ_1 line showed coincidence with γ_2 and γ_3 lines, the γ_1 line should be present in the γ_2 and γ_3 gated spectra to be a convincing coincidence. Furthermore, the relative intensities (calculated using the number of counts of a peak and the γ efficiency at this energy, relative to the intensity of the strongest peak) were used

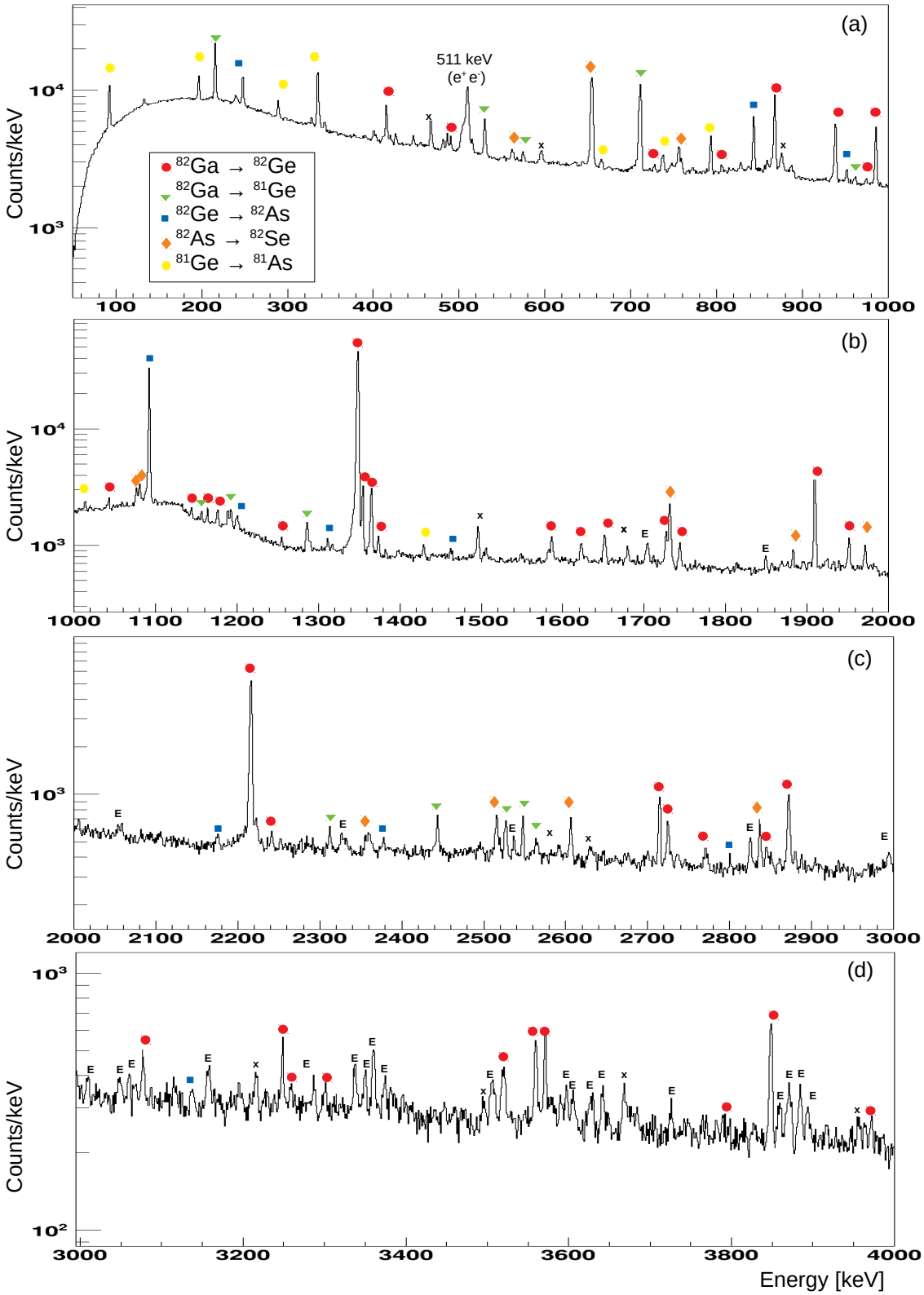

Figure 6.2: The β-gated γ-spectra from the ^{82}Ga decay for the energy ranges of (a) 0-1 MeV, (b) 1-2 MeV, (c) 2-3 MeV and (d) 3-4 MeV. The observed peaks are associated with the different activities using the symbols shown in the top panel. E represents the escape peaks, and X the unidentified lines.

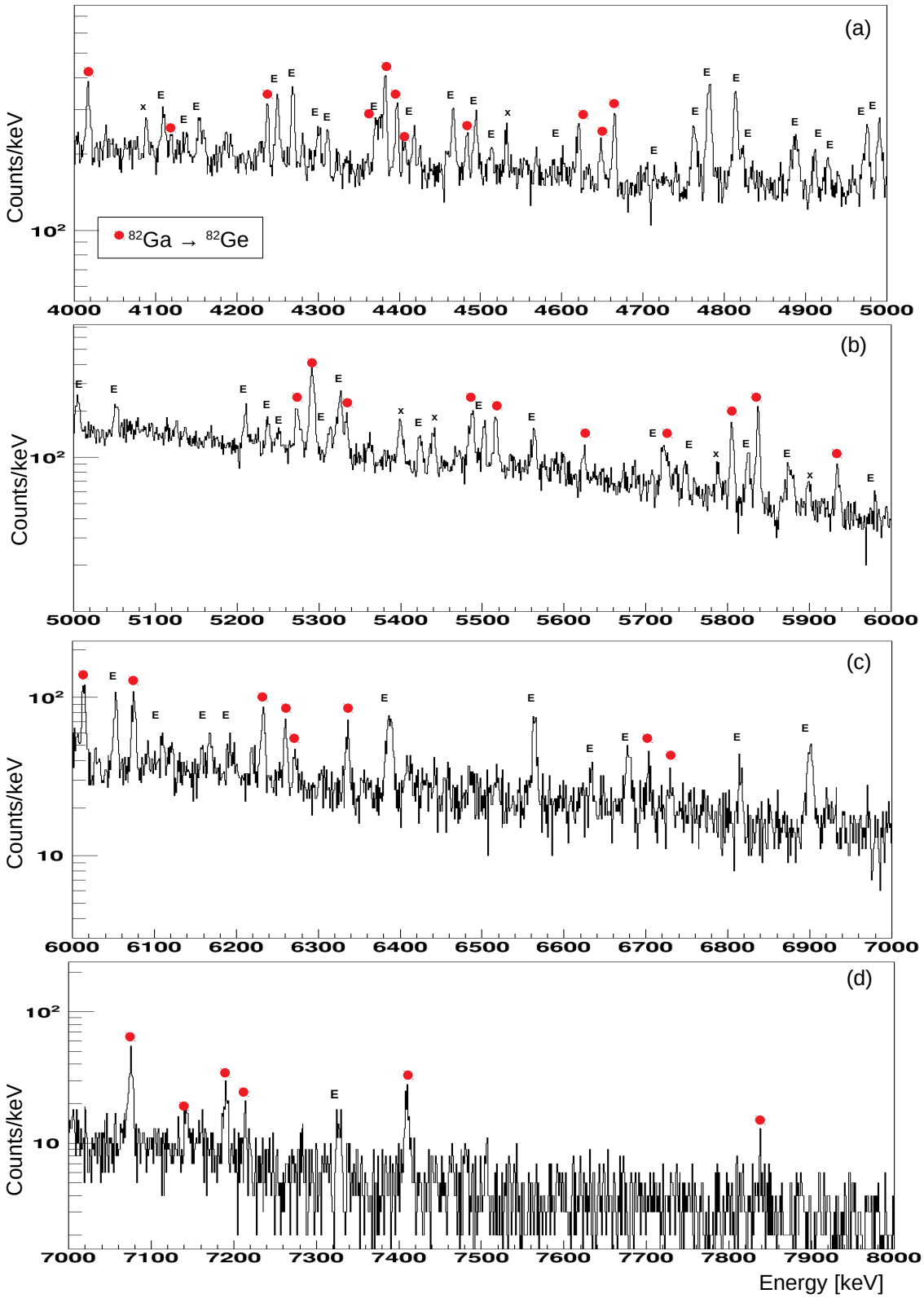

Figure 6.3: The β-gated γ-spectra from the ^{82}Ga decay for the energy ranges of (a) 4-5 MeV, (b) 5-6 MeV, (c) 6-7 MeV and (d) 7-8 MeV. The observed peaks are associated with the different activities using the symbols shown in the top panel. E represents the escape peaks, and X the unidentified lines.

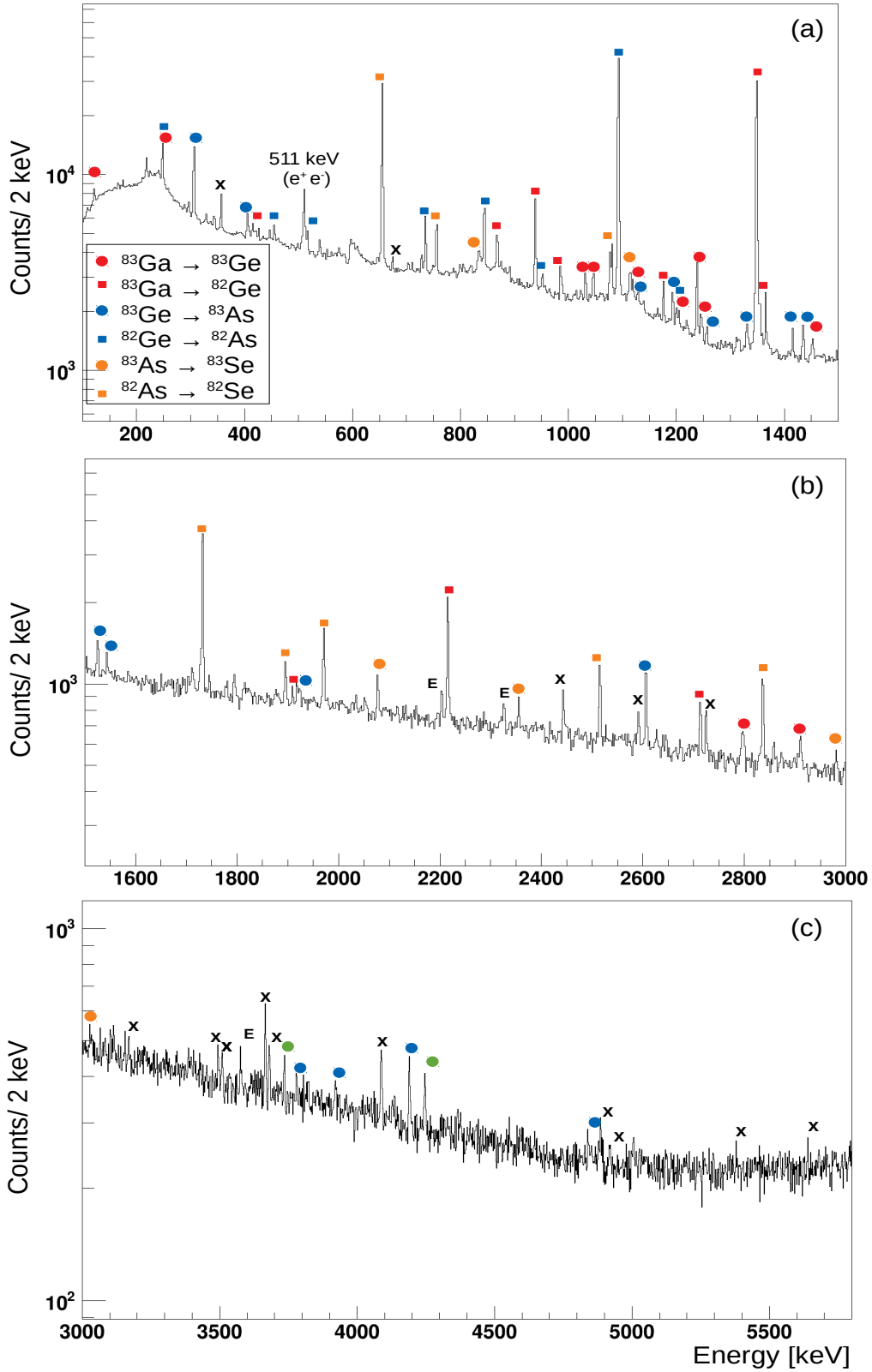

Figure 6.4: The β-gated γ-spectra from the ^{83}Ga decay for the energy ranges of (a) 0-1.5 MeV, (b) 1.5-3 MeV and (c) 3-6 MeV. The observed peaks are associated with the different activities using the symbols shown in the top panel. E represents the escape peaks, and X the unidentified lines.

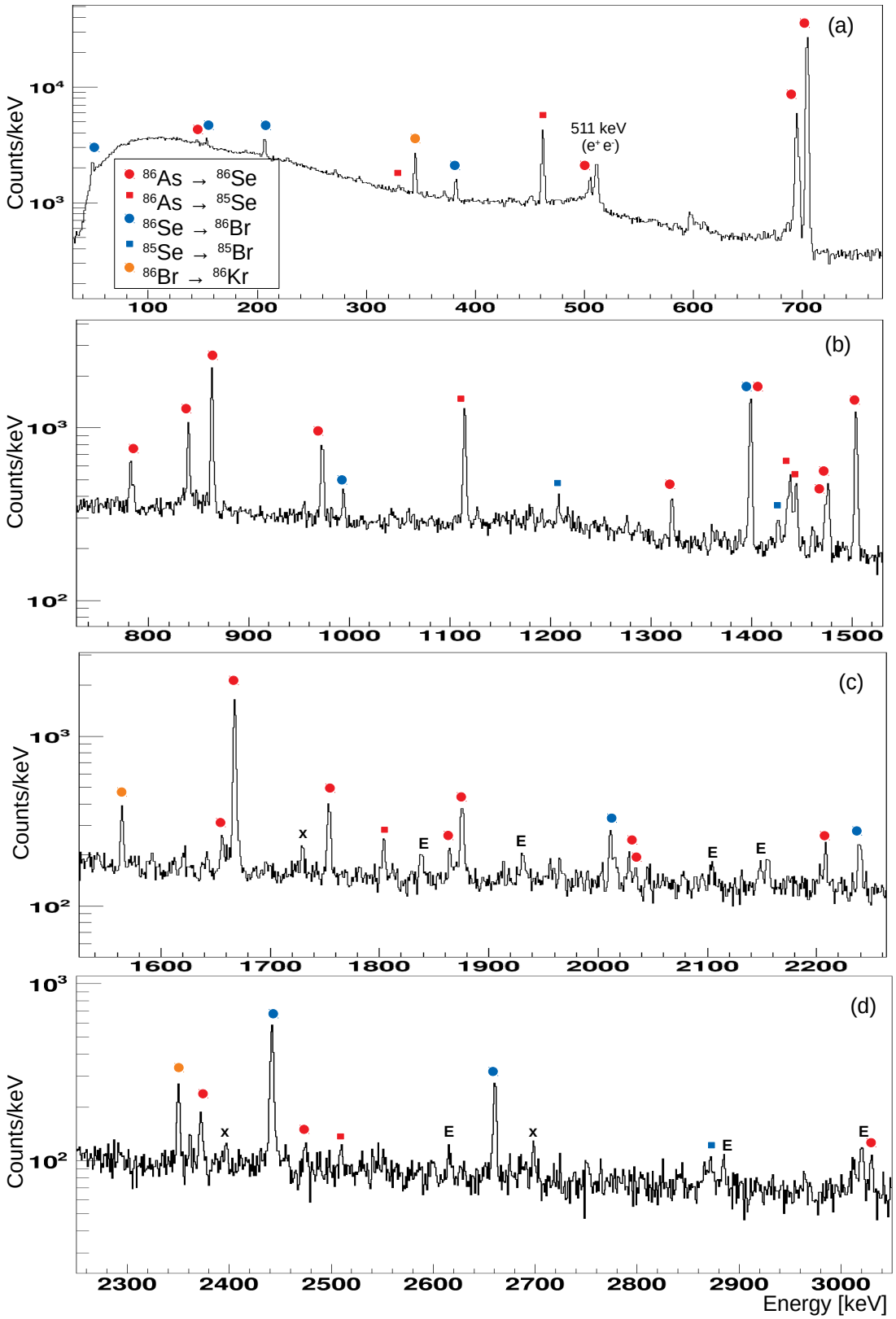

Figure 6.5: The β-gated γ-spectra from the ^{86}As decay for the energy ranges of (a) 0-0.8 MeV, (b) 0.8-1.5 MeV, (c) 1.5-2.3 MeV and (d) 2.3-3 MeV. The observed peaks are associated with the different activities using the symbols shown in the top panel. E represents the escape peaks, and X the unidentified lines.

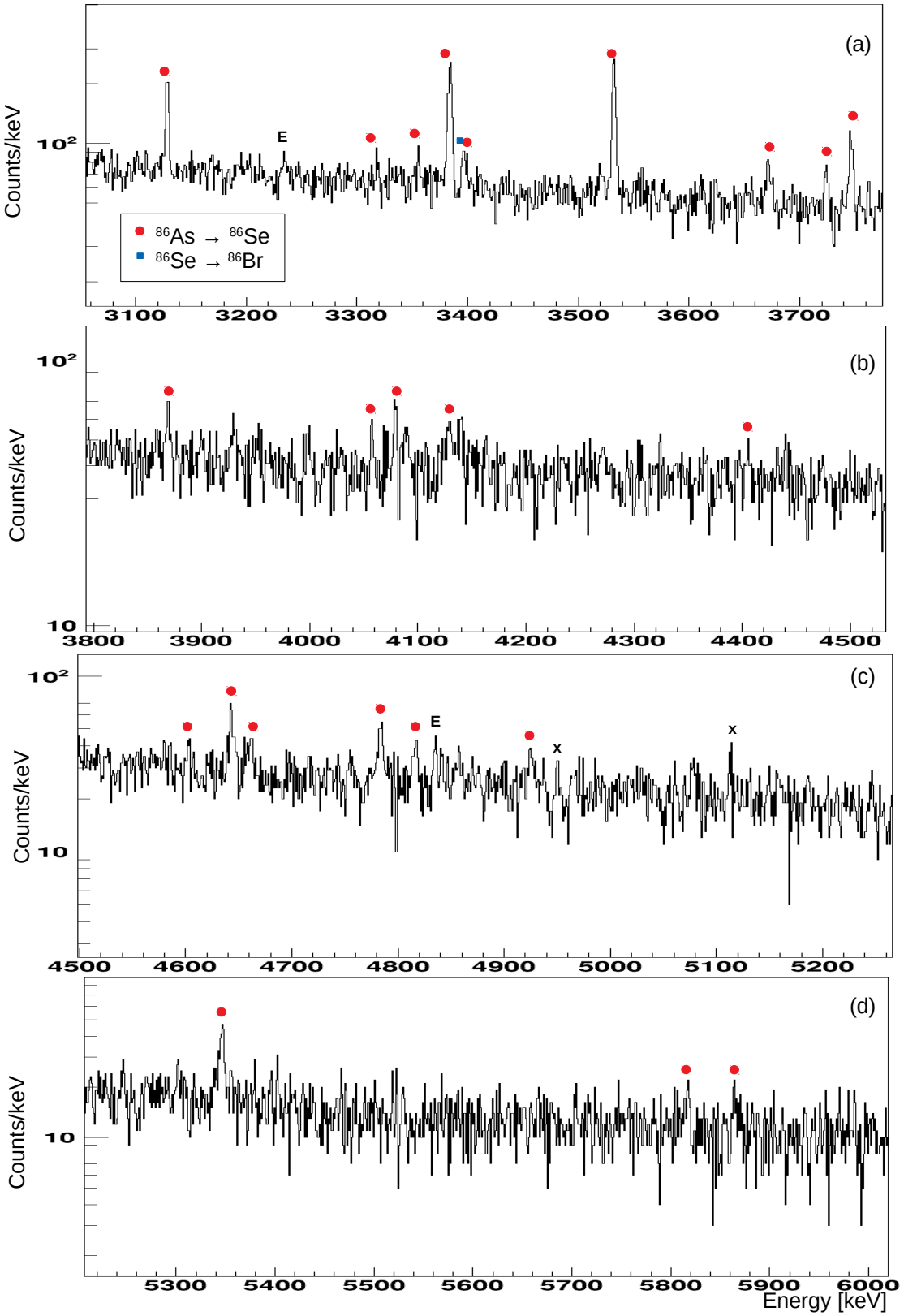

Figure 6.6: The β-gated γ-spectra from the ^{86}As decay for the energy ranges of (a) 3-3.8 MeV, (b) 3.8-4.5 MeV, (c) 4.5-5.2 MeV and (d) 5.2-6 MeV. The observed peaks are associated with the different activities using the symbols shown in the top panel. E represents the escape peaks, and X the unidentified lines.

Table 6.2: List of unidentified peaks in the β-gated γ-spectra of ^{82}Ge, ^{83}Ge and ^{86}Se with their absolute intensities. The energies marked with $*$ were observed in both ^{82}Ga and ^{83}Ga decays, making them potential candidates for the de-excitation spectrum of ^{82}Ge, though they did not pass the filter of either time distribution or the presence of escape peaks in the spectrum.

^{82}Ge		^{83}Ge		^{86}Se	
E_γ (keV)	I_γ(%)	E_γ (keV)	I_γ(%)	E_γ (keV)	I_γ(%)
467.1 (1)	0.12 (1)	356.3 (1)	2.7 (3)	1729.4 (3)	0.39 (7)
596.0 (1)	0.06 (1)	675.2 (4)	1.8 (4)	2397.4 (3)	0.21 (6)
875.6 (1)	0.08 (1)	2442.9 (6)	2.1 (7)	2698.8 (2)	0.36 (7)
1495.7 (1)	0.09 (1)	2591.7 (4)$*$	0.9 (3)	4950.0 (4)	0.25 (8)
2591.6 (5)$*$	0.02 (1)	2724.9 (5)	1.2 (4)	5112.9 (4)	0.33 (10)
2630.1 (8)	0.04 (1)	3508.3 (4)	1.1 (4)		
3215.9 (3)	0.04 (1)	3668.4 (4)$*$	2.8 (7)		
3495.7 (5)	0.03 (1)	3681.5 (5)	1.6 (5)		
3668.4 (3)$*$	0.06 (1)	4089.6 (7)$*$	2.7 (9)		
3956.1 (5)	0.03 (1)	4884.2 (2)	0.8 (8)		
4088.0 (3)$*$	0.03 (1)	4921.8 (4)	1.2 (5)		
4532.0 (2)	0.04 (1)	5379.1 (7)	0.8 (5)		
5399.5 (3)	0.10 (1)	5638.6 (4)	1.0 (4)		
5440.1 (5)	0.06 (1)				
5788.1 (6)	0.03 (1)				
5899.0 (5)	0.02 (1)				

to validate once more the coincidence and to decide the order of the cascade which was required to build the level scheme.

6.2.1 ^{82}Ga

The investigation of the decay of ^{82}Ga led to the discovery of 45 new excited states in ^{82}Ge and three new excited states in ^{81}Ge. The research also assigned a total of 76 gamma transitions to ^{82}Ge, with 54 of them observed for the first time in this study. The γ-ray transitions previously reported in [58, 85] were confirmed and marked with an *a* in Table 6.3.

The 1348.1-keV γ-ray transition

The most intense peak in ^{82}Ge is the one corresponding to the $2_1^+ \rightarrow 0_1^+$ 1348.1-keV transition. The de-excitation of higher energy states mainly feeds this energy level, and 31 γ-ray transitions were observed in coincidence with the 1348.1 keV γ-ray transition (see Fig. 6.7).

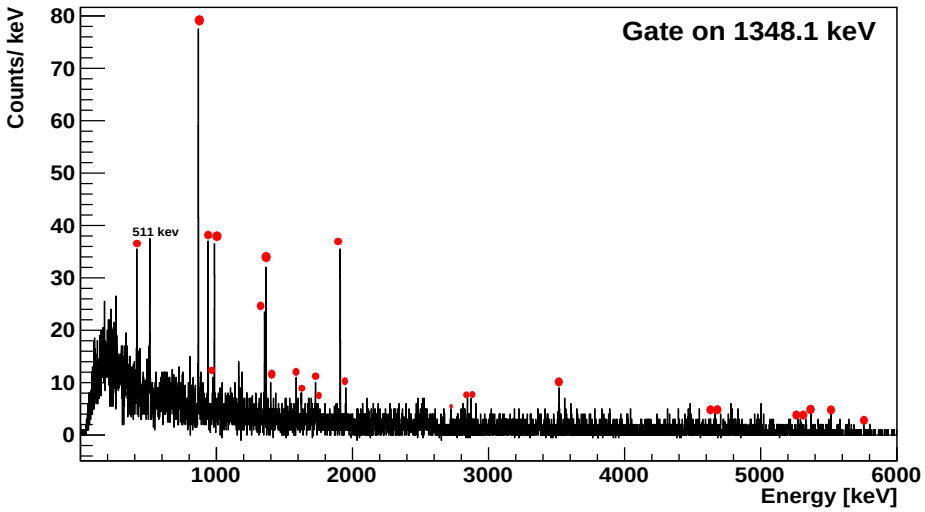

Figure 6.7: γ-ray spectrum gated on the 1348.1 keV gamma-ray transition in ^{82}Ge. The gamma-ray transitions identified to be feeding the 2^+ state are marked with red dots.

The 3848.2-keV γ-ray transition in ^{82}Ge

The 3848.2-keV γ-ray transition, placed tentatively as a direct transition to the ground state in [58], was seen in this work in coincidence with 867.39, 1348.1, and 2216.04 keV γ-rays, as shown in Fig. 6.8.

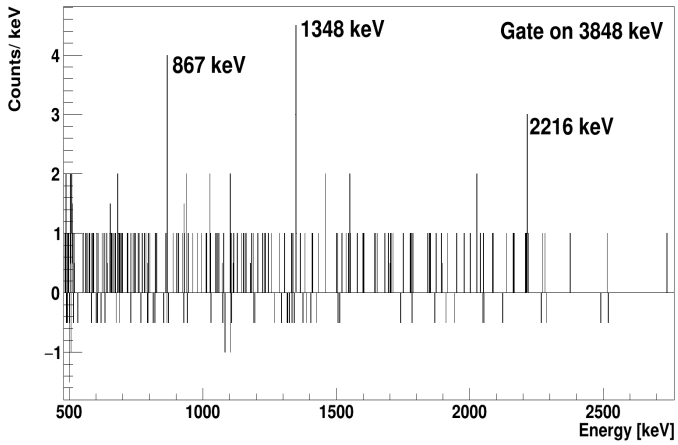

Figure 6.8: The $\beta - \gamma - \gamma$ coincidence spectrum gated on the 3848.2 keV transition in ^{82}Ge.

The 2826-, 3360-, 4269- and 5326-keV γ-ray transitions in ^{82}Ge

In the work of [58], the γ-ray transitions at 2826, 3361, 4270 and 5326 keV were previously attributed to ^{82}Ge. In this work, these transitions have now been identified as escape peaks of 3848.2, 4382.7, 5291.79 and 5837.5 keV transitions, respectively. Escape peaks were identified unambiguously through $\gamma - \gamma$-coincidences (coincidence with 511 keV, see Figs. 6.9, 6.10, 6.11 and 6.12) and by comparing the

full-energy peak to escape peaks counts ratio (see Fig. 6.1).

The 486.44-keV γ-ray transition in ^{82}Ge

Furthermore, the 486.44-keV γ-ray transition seen in the βn-decay of ^{83}Ga in the work of [60] linking the 2702.5 keV level to the second 2^+ excited state in ^{82}Ge (see Fig. 6.13), is confirmed in this work.

The 3014.8-keV excited state in ^{82}Ge

Likewise, the excited state at 3014.8 keV reported in Ref. [60] is confirmed in this work based on the coincidences observed between the 727.97-, 938.75- and 1348.1-keV γ-ray transitions (Fig. 6.14).

The 2524.2-keV excited state in ^{82}Ge

Additionally, the existence of the excited level at 2524.2 keV was reported in ref. [60]. We confirm this by the coincidences observed between the 1176.4- and 1348.1-keV γ-ray transitions (see Fig. 6.15). The 2524.2-keV level was reported for the first time in [63]. However, it was proposed to be de-excited by the 191.4-keV transition to the 0^+ state at 2333.3 keV and 2524.7 keV to the ground state. This is not the case neither in this work nor in the work of [60] where the same state is populated by β-n decay of ^{83}Ga. Therefore, the assigned (2^+) spin-parity needs to be reconsidered. Nevertheless, this case was discussed in Ref. [65] where the ^{82}Ge produced via fission of ^{232}Th was studied. In fact, the 2524 keV state was observed in Ref. [65] with a direct transition to the ground state of ^{82}Ge, and it is not populated by any γ-transition. The intensity of this γ-transition based on the same work is I_γ (2524 keV)= 22 % , which means that the 2524-keV state was produced in a non-yrast low-energy (2^+) state with high intensity, which is not so probable due to the ^{232}Th fission properties. The same work proposed (4^+) as a spin for the 2524.7 keV level. This indeed matches better with the log ft value calculated in this work for the population of this state (log ft = 7.4) that falls in the range of a first-forbidden transition type leading to a (4^+) state taking into account the (2^-) spin of the ^{82}Ga parent nucleus and the β-decay selection rules.

The 2934.8-keV excited state in ^{82}Ge

In addition, the excited state at 2934.8 keV energy was previously reported to de-excite by a cascade of 646, 938.75 and 1348.1 keV gamma transitions. However, in this study, the γ-ray transition at 646 keV was not observed, but the 2934.8-keV state was reconstructed with a different combination of γ-rays at 1586.66 and 1348.1 keV energy (see Fig. 6.16).

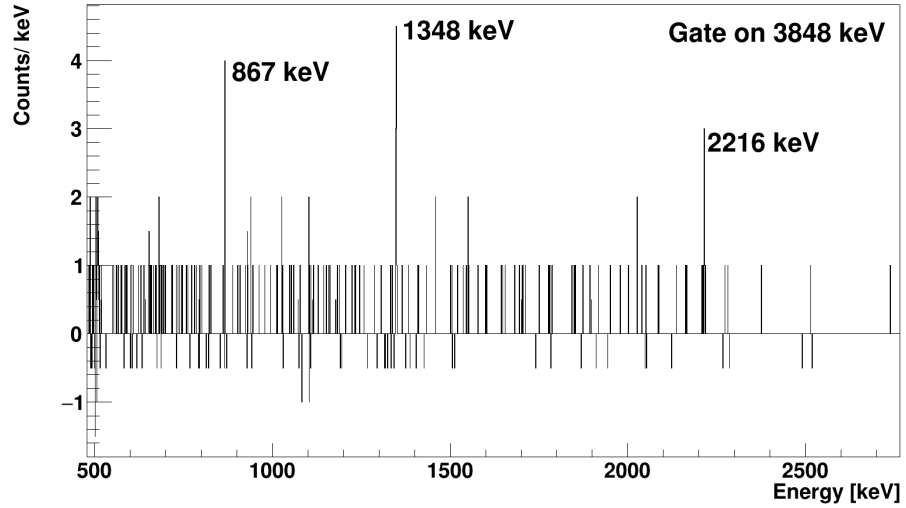

(a)

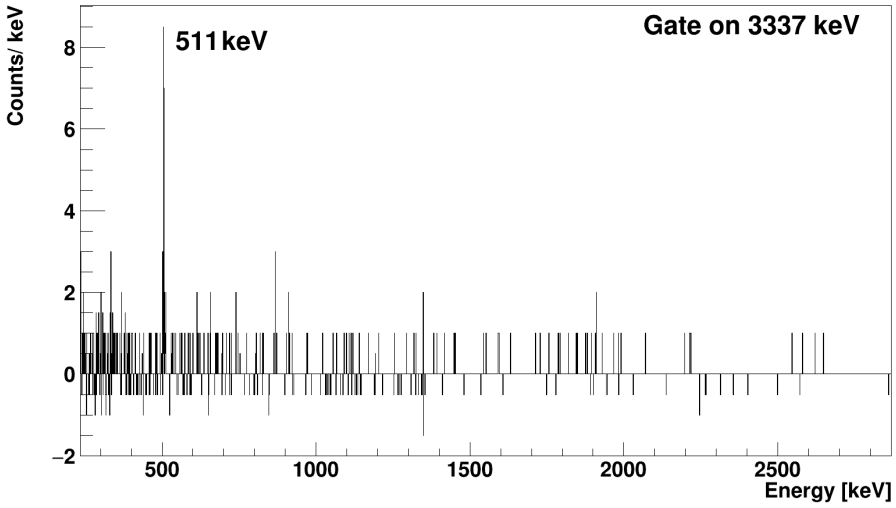

(b)

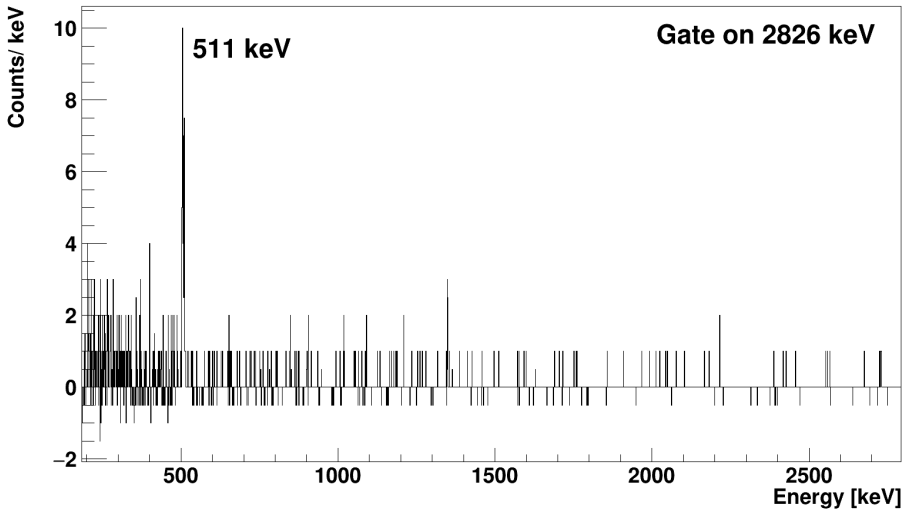

(c)

Figure 6.9: The $\beta - \gamma - \gamma$ coincidence spectrum gated on the 3848.2 keV transition in ^{82}Ge (a), its first-escape peak (b) and its second-escape peak (c). These figures show that the peak at 2826 keV represents the second-escape peak of the 3848.2 keV transition and not a direct transition to the ground state of ^{82}Ge.

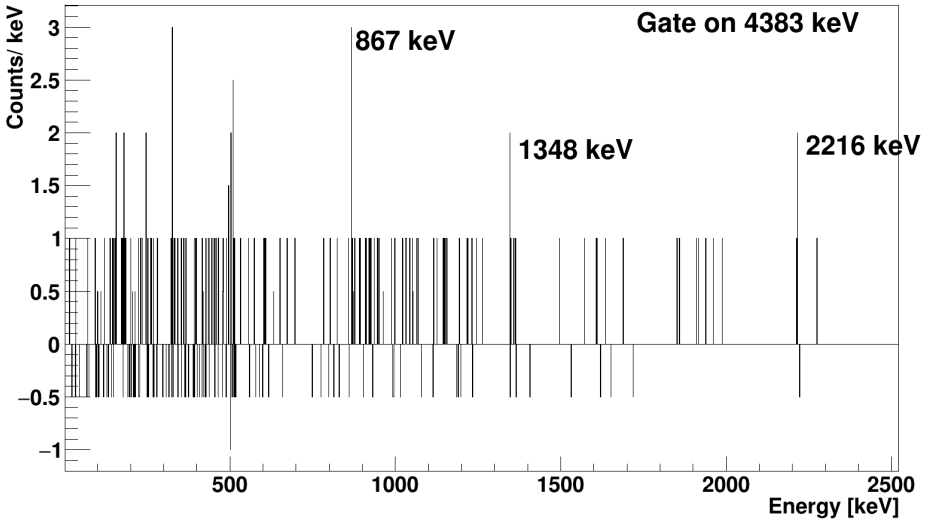

(a)

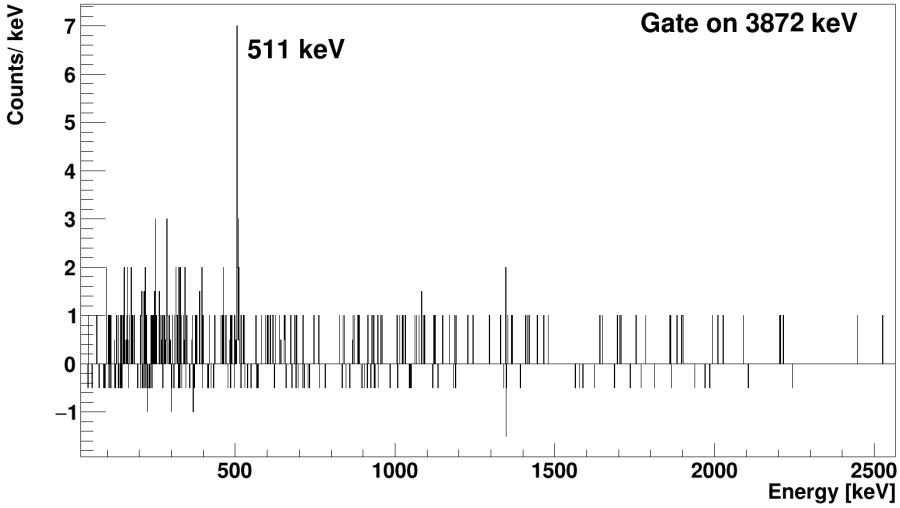

(b)

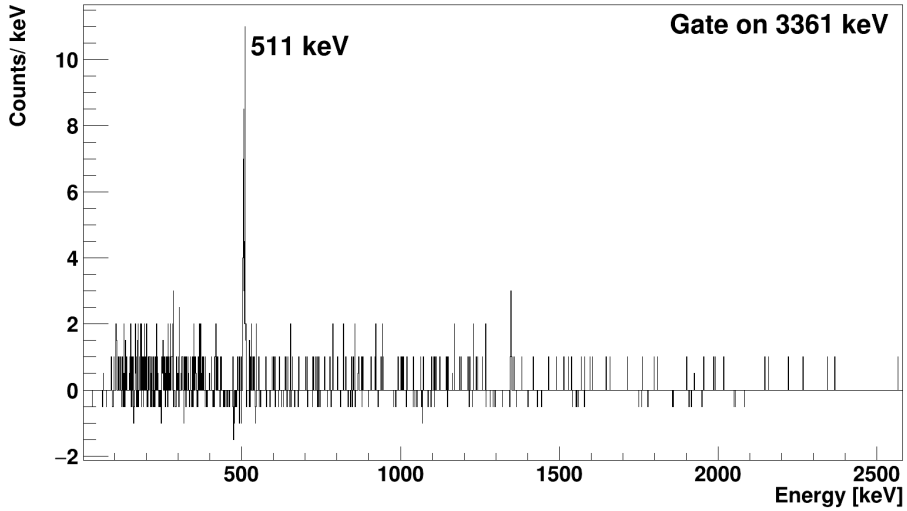

(c)

Figure 6.10: The $\beta - \gamma - \gamma$ coincidence spectrum gated on the 4382.72 keV transition in ^{82}Ge (a), its first-escape peak (b) and its second-escape peak (c). These figures show that the peak at 3361 keV represents the second-escape peak of the 4382.72 keV transition and not a direct transition to the ground state of ^{82}Ge.

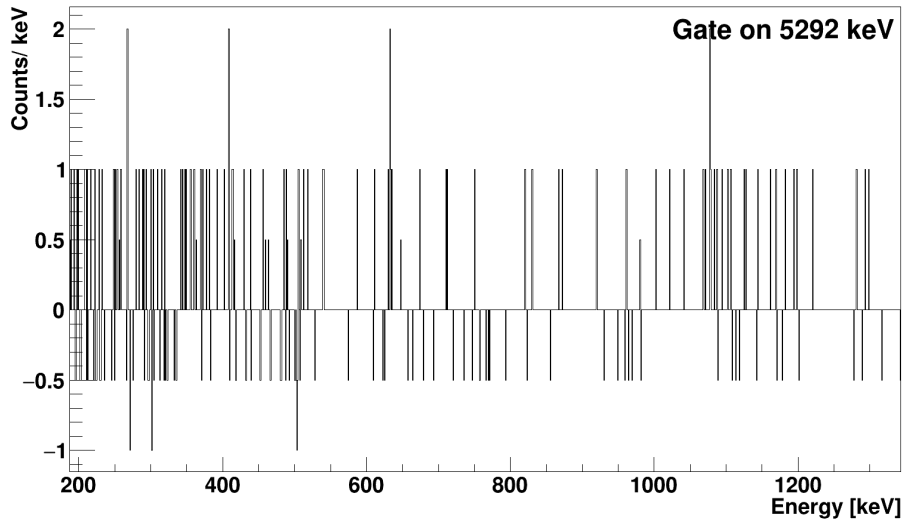

(a)

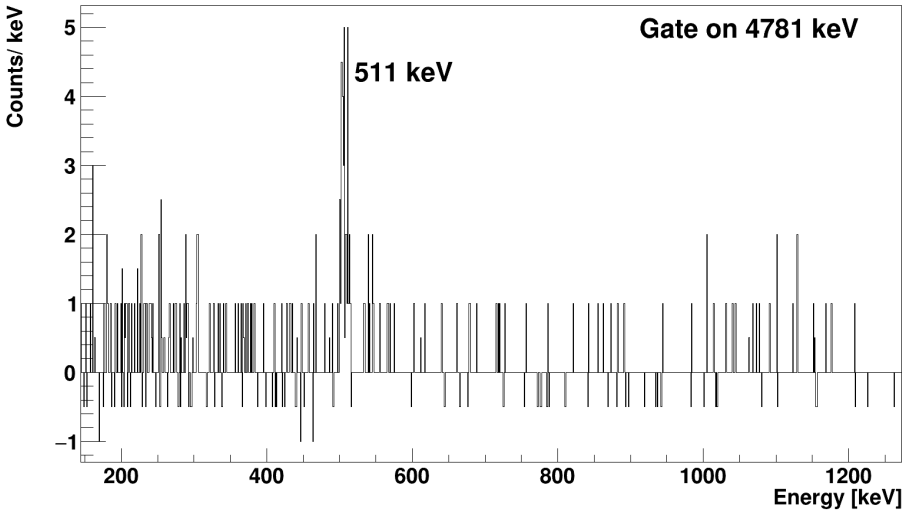

(b)

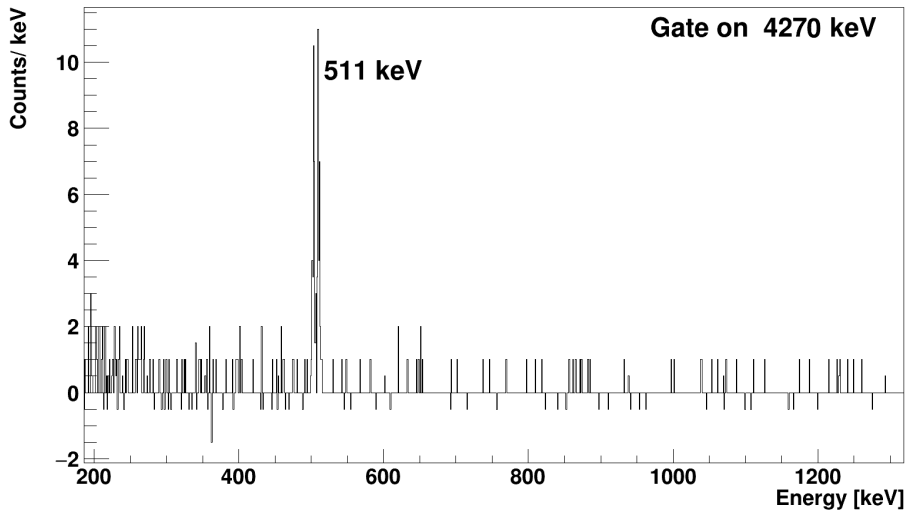

(c)

Figure 6.11: The $\beta - \gamma - \gamma$ coincidence spectrum gated on the 5291.79 keV transition in ^{82}Ge (a), its first-escape peak (b) and its second-escape peak (c). These figures show that the peak at 4270 keV represents the second-escape peak of the 5291.79 keV transition and not a direct transition to the ground state of ^{82}Ge.

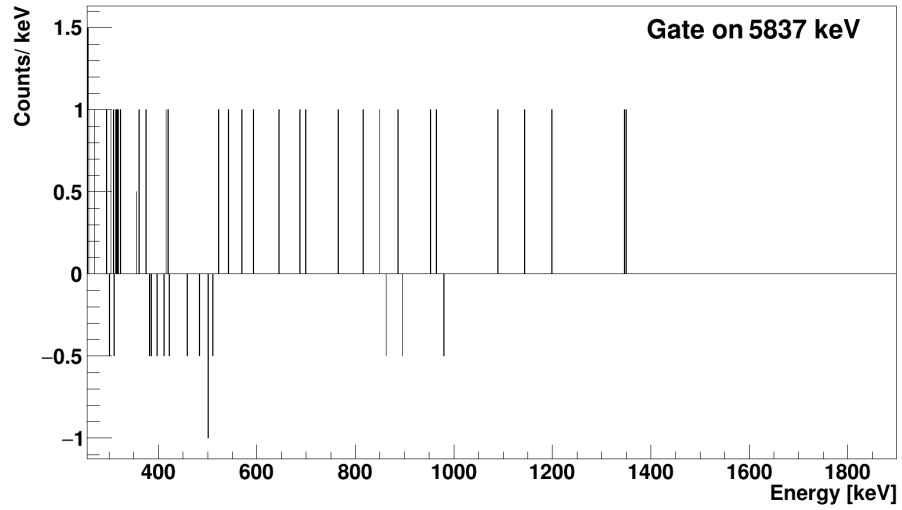

(a)

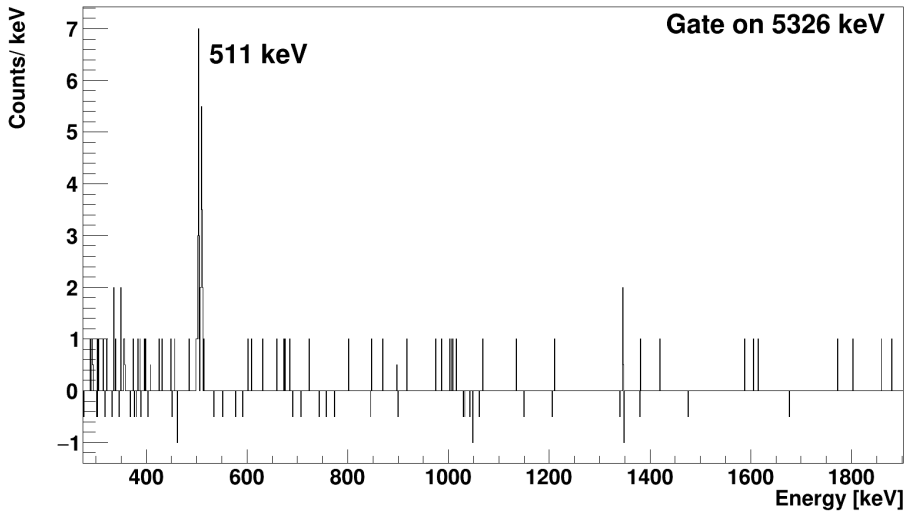

(b)

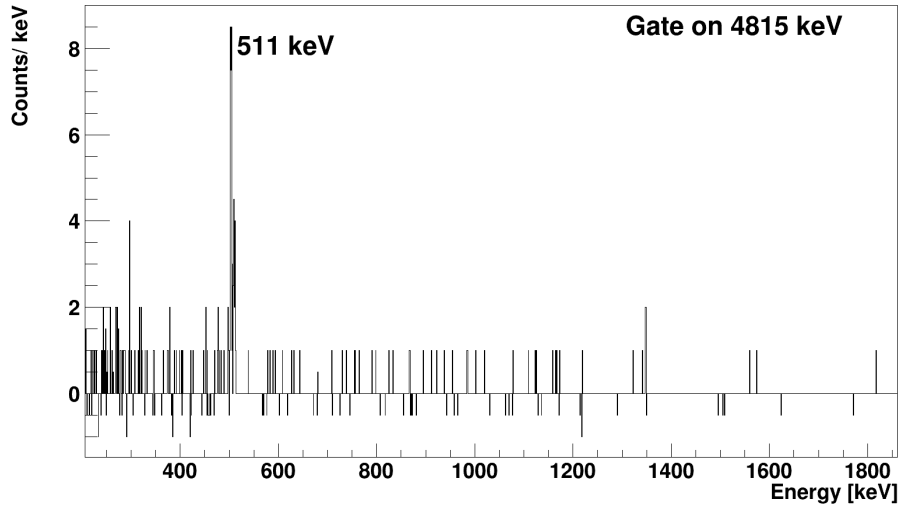

(c)

Figure 6.12: The $\beta - \gamma - \gamma$ coincidence spectrum gated on the 5837.5 keV transition in ^{82}Ge (a), its first-escape peak (b) and its second-escape peak (c). These figures show that the peak at 5326 keV represents the second-escape peak of the 5837.5 keV transition and not a direct transition to the ground state of ^{82}Ge.

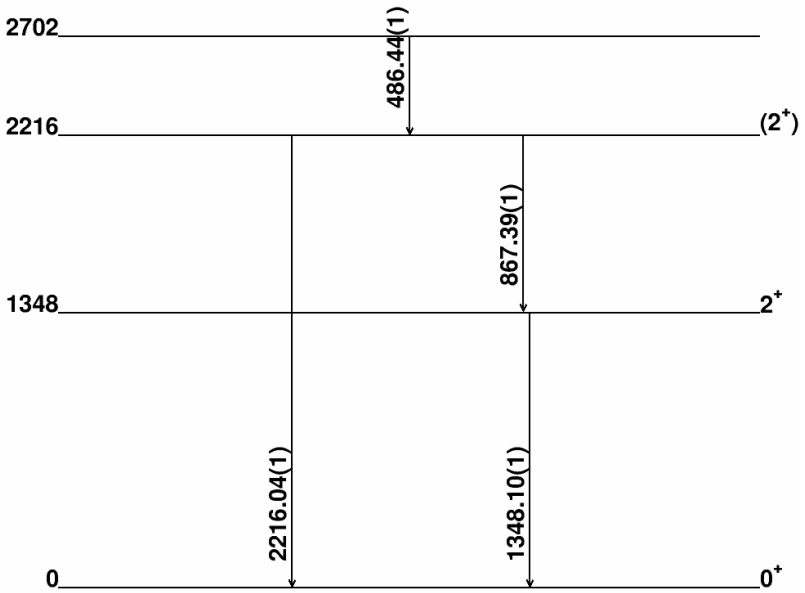

Figure 6.13: Partial decay scheme to determine the energy of the state at 2701.66(3) keV in ^{82}Ge. All energies are given in keV.

States above the neutron separation threshold in ^{82}Ge

In all the studies mentioned earlier, the highest excited state reported is 377 keV below the neutron separation energy (S_n = 7.194 MeV [42]) in ^{82}Ge. However, this work reports, for the first time, excited states around S_n and above, up to 7.89 MeV. This last excited state decays directly to the ground state, and the transition was observed in the PARIS spectrum. The high-energy gamma-ray transitions were assigned unambiguously to ^{82}Ge based on the following. Looking at the decay chain of ^{82}Ga in Fig. 3.6, the $Q_{\beta n}$ window is 5.290 (3) MeV, meaning it is impossible to have gamma transitions with higher energies in ^{81}Ge. The Q_β window of ^{82}Ge is 4.690 (4) MeV, and of ^{81}Ge is 6.242 (3) MeV, which rules out the possibility of assigning gamma-ray transitions with energies higher than that to ^{81,82}As. The half-life of ^{81}As is too large compared to the tape cycle, so it did not contaminate the data. However, ^{82}As, which has a Q_β window of 7.488 (4) MeV, can be present, but the ^{82}Se gamma-ray transitions can be distinguished easily due to the difference between their apparent half-lives and the ^{82}Ga half-life. The apparent half-lives of all the selected ^{82}Ge gamma-ray transitions are compatible with the ^{82}Ga half-life.

The energy levels populated above S_n are at 7191, 7214.1, 7410.1, 7839.20, and 7890.75 keV. These states decay directly to the 0^+ ground state of ^{82}Ge. Nevertheless, some states around S_n de-excite to excited states, mainly to the two first 2^+ excited states.

Yet, there were a couple of exceptional excited states that decayed both to the ground and excited states. For instance, gating on the 4396.75 keV γ-line results in a strong coincidence with the 985 and 1348.1 keV γ-ray transitions (known to be connected), which leads to the proposition of a new excited state at 6729.8 keV. This excited state was also observed by placing a gate on the 4016.37 keV

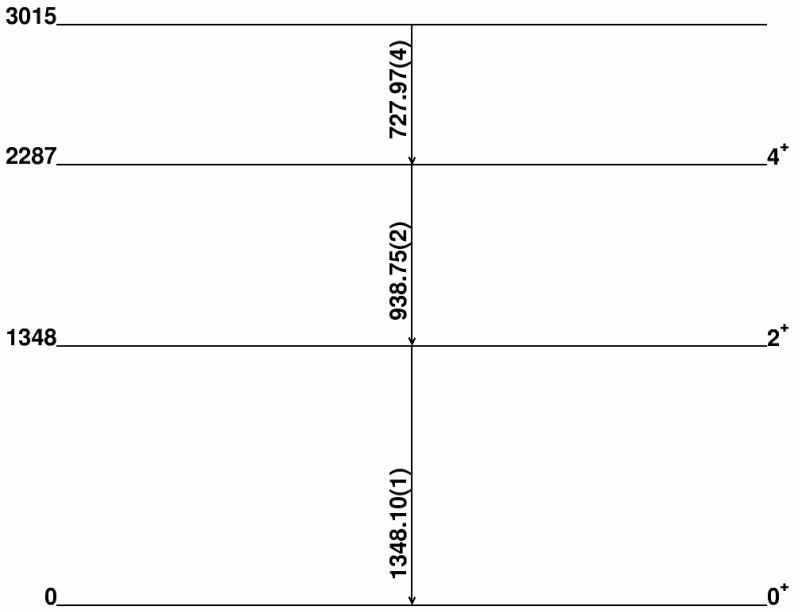

Figure 6.14: Partial decay scheme to determine the energy of the state at 3014.8(1) keV in ^{82}Ge. All energies are given in keV.

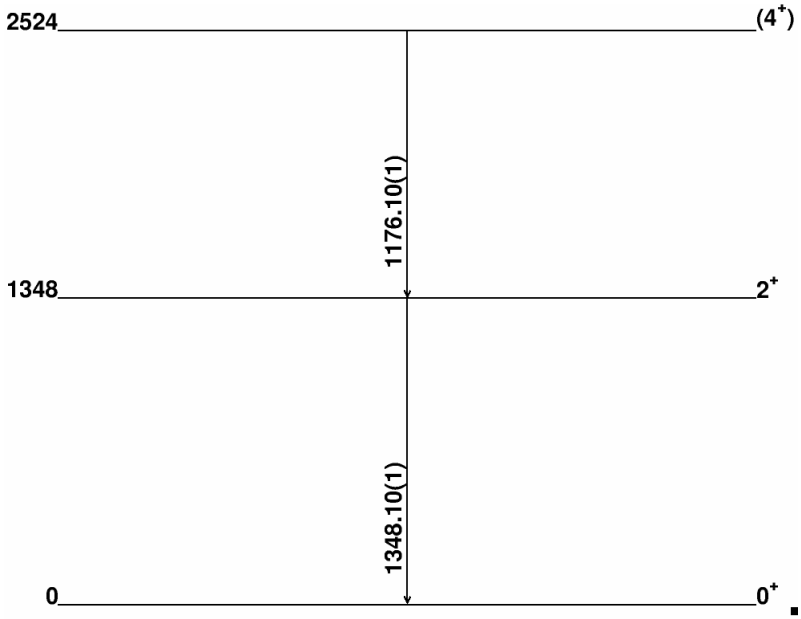

Figure 6.15: Partial decay scheme to determine the energy of the state at 2524.2(1) keV in ^{82}Ge. All energies are given in keV.

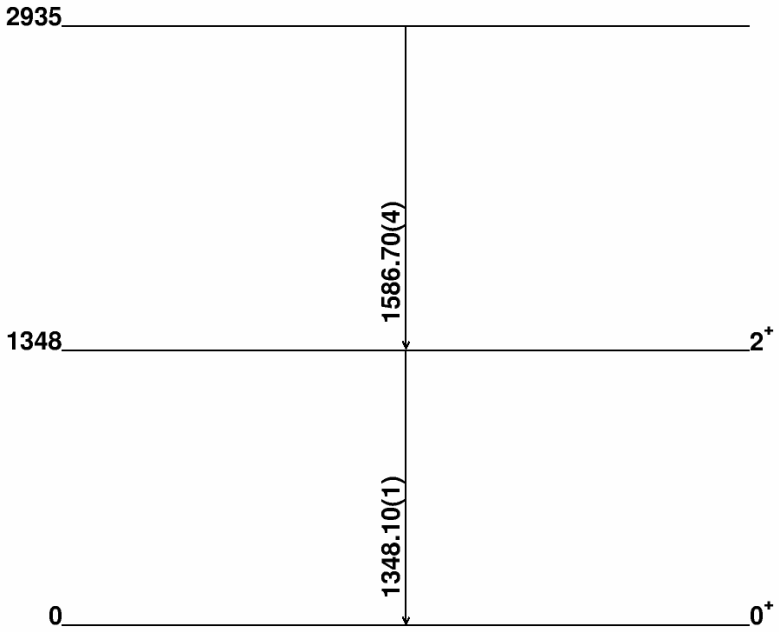

Figure 6.16: Partial decay scheme to determine the energy of the state at 2934.8(1) keV in ^{82}Ge. All energies are given in keV.

transition, which reveals a coincidence with both 1348.1 and 1365.1 keV transitions that are again known to be in cascade (Figs. 6.17 and 6.18).

All $\beta - \gamma - \gamma$ coincidences in ^{82}Ge are summarized in Table 6.3, the relative intensities of the different transitions were calculated with respect to the 1348.1 keV energy transition of ^{82}Ge. The gamma-ray transitions in the beta-n daughter, ^{81}Ge, are marked in Figs. 6.2 and 6.3 with green triangles and are listed in Table 6.4. The gamma-ray transitions at 574.63, 961.7, 1189.15, 2312.47, 3505.5, and 4037.4 keV in ^{81}Ge are seen for the first time in the β-n channel.

Table 6.3: List of γ-ray transitions (E_γ) observed in the β-decay of ^{82}Ga, with their relative intensity to the most intense 1348.1-keV transition (with I_γ =100(12)%) and their $\gamma - \gamma$ coincidences. E_i represents the initial level energy of the E_γ transition, and the uncertainties reported are purely statistical.

E_γ (keV)	I_γ(%)	E_i (keV)	$\gamma - \gamma$
414.80 (1)[a]	2.8 (3)	2701.66 (3)	938.75 , 1163.8, 1348.1
486.44 (2)	1 (1)	2701.66 (3)	2216.04
727.97 (4)	0.3 (1)	3014.8 (1)	938.75, 1348.1
806.32 (3)	0.6 (5)	3092.4 (1)	938.75, 1348.1
867.39 (1)[a]	8.8 (10)	2216.04 (1)	1042.4, 1348.1, 1651.8, 3848.2, 4382.72, 4620.4

Continued on next page

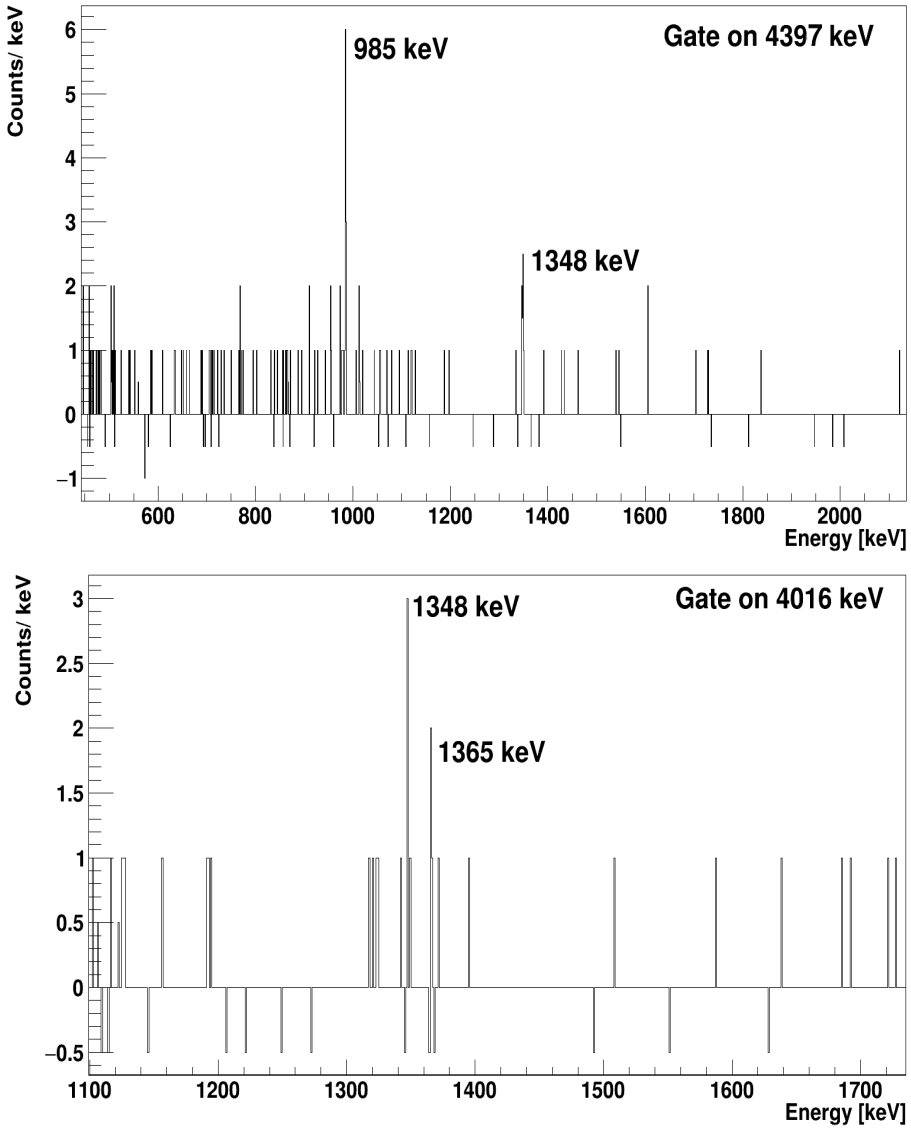

Figure 6.17: Top: The $\beta - \gamma - \gamma$ coincidence spectrum gated on 4396.75 keV γ-line in ^{82}Ge. Bottom: The $\beta - \gamma - \gamma$ coincidence spectrum gated on 4016.37 keV γ-line in ^{82}Ge.

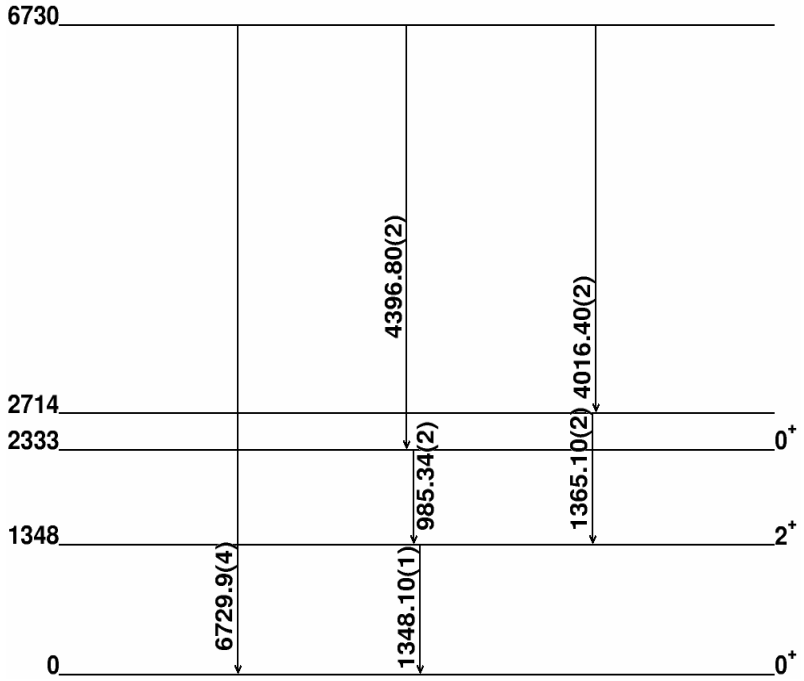

Figure 6.18: Partial decay scheme to determine the energy of the state at 6729.9(4) keV in ^{82}Ge. All energies are given in keV.

Table 6.3: List of γ-ray transitions (E_γ) observed in the β-decay of ^{82}Ga, with their relative intensity to the most intense 1348.1-keV transition (with I_γ =100(12)%) and their $\gamma - \gamma$ coincidences. E_i represents the initial level energy of the E_γ transition, and the uncertainties reported are purely statistical. (Continued)

E_γ (keV)	I_γ(%)	E_i (keV)	$\gamma - \gamma$
938.75 (1)[a]	6 (7)	2286.86 (2)	414.8, 806.3, 1163.8, 1348.1
975.10 (5)	0.3 (1)	2323.2 (1)	1348.1
985.34 (1)[a]	5.1 (6)	2333.44 (2)	1348.1, 4396.8
1042.35 (3)	1 (2)	3258.14 (2)	867.39, 1348.1, 2216.04
1144.35 (3)	0.5 (1)	3360.4 (1)	2216.04
1163.81 (2)	1 (1)	3867.01 (8)	414.8, 938.75, 1348.1, 1354.4
1176.14 (3)	1 (1)	2524.2 (1)	1348.1
1254.43 (4)	0.3 (1)	2602.5 (1)	1348.1

Continued on next page

Table 6.3: List of γ-ray transitions (E_γ) observed in the β-decay of ^{82}Ga, with their relative intensity to the most intense 1348.1-keV transition (with I_γ =100(12)%) and their $\gamma - \gamma$ coincidences. E_i represents the initial level energy of the E_γ transition, and the uncertainties reported are purely statistical. (Continued)

E_γ (keV)	I_γ(%)	E_i (keV)	$\gamma - \gamma$
1348.10 (0)	100 (12)	1348.10 (0)	806.3, 867.39, 975.1, 985.34, 1176.1, 1254.43, 1354.4, 1365.1, 1373.5, 1586.7, 1623.1, 1727.1, 1744.3 , 1910.04, 1951.5, 2241.4, 2725 , 2771.2, 2845.3, 2872.3, 3521.6, 4382.72, 4404.5, 4483.3, 4648.9, 4664.6, 5273.6, 5291.8, 5334.3, 5487.1, 5516.3, 5726.4
1354.39 (1)[a]	4.2 (5)	2701.66 (3)	1163.8, 1348.1
1365.10 (1)[a]	4.9 (6)	2602.5 (1)	1348.1, 3248.4, 4016.4
1373.48 (3)	0.7 (1)	2721.6 (1)	1348.1, 3956.4
1586.66 (3)	1.4 (2)	2934.8 (1)	1348.1
1623.10 (5)	1.3 (2)	2971.20 (7)	1348.1
1651.84 (3)	2 (3)	3867.01 (8)	867.39, 1348.1, 2216.04
1727.10 (3)[a]	2.2 (3)	3076.91 (7)	1348.1
1744.30 (4)	1.4 (2)	3092.4 (1)	1348.1
1910.04 (1)[a]	11.6 (16)	3258.14(2)	1348.1, 3559.7
1951.54 (3)[a]	1.7 (2)	3300.9 (3)	1348.1
2216.04 (1)[a]	20.9 (30)	2216.04 (1)	486.4, 1042.4, 114.4, 1651.8, 3848.2, 4382.7, 4620.4
2241.41 (7)	0.6 (1)	3589.5 (1)	1348.1
2714.37 (3)[a]	3 (5)	2714.37 (3)	–
2725.04 (4)	1.8 (3)	4073.1 (1)	1348.1
2771.21 (8)	1 (2)	4119.2 (5)	1348.1
2845.30 (4)	0.7 (2)	4193.4 (1)	1348.1
2872.32 (3)[a]	4 (6)	4220.4 (6)	1348.1
3076.91 (6)[a]	1.4 (4)	3076.91 (6)	–
3248.40 (5)	1.4 (3)	5961.6 (1)	1348.1, 1365.1
3257.9 (1)	0.2 (1)	3257.9 (1)	–
3300.94 (8)	0.7 (2)	3300.94 (8)	–
3521.58 (6)	0.5 (6)	4869.7 (1)	1348.1

Continued on next page

Table 6.3: List of γ-ray transitions (E_γ) observed in the β-decay of ^{82}Ga, with their relative intensity to the most intense 1348.1-keV transition (with I_γ =100(12)%) and their $\gamma - \gamma$ coincidences. E_i represents the initial level energy of the E_γ transition, and the uncertainties reported are purely statistical. (Continued)

E_γ (keV)	I_γ(%)	E_i (keV)	$\gamma - \gamma$
3559.73 (5)[a]	2.4 (4)	6817.8 (1)	1348.1, 1910.04
3571.04 (4)[a]	2.3 (4)	3571.04 (4)	–
3848.15 (4)	4.5 (8)	6063.6 (1)	867.39, 1348.1, 2216.04
3956.4 (1)	0.4 (1)	6678.0 (5)	1348.1, 1373.5
4016.4 (1)	0.3 (1)	6729.9 (4)	1348.1, 1365.1
4119.2 (1)	0.4 (1)	4119.2 (1)	–
4237.79 (8)	1.4 (3)	4237.79 (8)	–
4371.09 (6)	1.4 (3)	4371.09 (6)	–
4382.72 (5)	3.4 (6)	6598.7 (3)	867.39, 1348.1, 2216.04
4396.75 (7)	1.9 (4)	6729.9 (4)	985.34, 1348.1
4404.5 (1)	0.4 (1)	5752.6 (1)	1348.1
4483.26 (9)	1.1 (2)	5831.3 (1)	1348.1
4620.40 (8)	2.1 (4)	6835.9 (2)	867.39, 1348.1, 2216.04
4648.9 (1)	0.1 (1)	5997.0 (1)	1348.1
4664.62 (7)[a]	1 (2)	6013.3 (2)	1348.1
5273.6 (1)	0.1 (1)	6621.7 (1)	1348.1
5291.79 (6)	0.1 (1)	6639.9 (1)	1348.1
5334.3 (1)	1.2 (3)	6682.4 (1)	1348.1
5487.1 (1)	1.6 (3)	6835.9 (2)	1348.1
5516.30 (9)	0.9 (2)	6864.4 (1)	1348.1
5624.7 (1)	0.5 (1)	5624.7 (1)	–
5726.4 (1)	1.1 (5)	7075.3 (1)	1348.1
5805.20 (8)	1.2 (2)	5805.20 (8)	–
5837.50 (8)	1.7 (4)	5837.50 (8)	–
5934.8 (1)	0.5 (1)	5934.8 (1)	–
6013.27 (1)	0.8 (2)	6013.27 (1)	–
6074.8 (1)	0.8 (2)	6074.8 (1)	–
6232.4 (1)	0.7 (2)	6232.4 (1)	–
6259.7 (1)	0.5 (1)	6259.7 (1)	–

Continued on next page

Table 6.3: List of γ-ray transitions (E_γ) observed in the β-decay of ^{82}Ga, with their relative intensity to the most intense 1348.1-keV transition (with I_γ =100(12)%) and their $\gamma - \gamma$ coincidences. E_i represents the initial level energy of the E_γ transition, and the uncertainties reported are purely statistical. (Continued)

E_γ (keV)	I_γ(%)	E_i (keV)	$\gamma - \gamma$
6271.5 (2)	0.3 (1)	6271.5 (2)	–
6336.1 (1)	0.5 (1)	6336.1 (1)	–
6703.30 (9)	0.3 (1)	6703.30 (9)	–
6729.8 (1)	0.2 (1)	6729.8 (1)	–
7075.3 (1)	0.5 (1)	7075.3 (1)	–
7142.5 (3)	0.2 (1)	7142.5 (3)	–
7191.0 (2)	0.2 (1)	7191.0 (2)	–
7214.1 (2)	0.2 (4)	7214.1 (2)	–
7410.10 (2)	0.3 (1)	7410.10 (2)	–
7839.2 (1)	0.09 (4)	7839.2 (1)	–
7890.75 (45)	0.04 (1)	7890.75 (45)	–

[a] known γ-ray transitions

6.2.2 ^{83}Ga

Three new excited states were tentatively identified in the β-decay of ^{83}Ga. This finding was based on the observation of three γ-ray transitions, which were detected for the first time during this research. The energy levels at 248.76 keV, 1045 keV, and 1237 keV in ^{83}Ge, reported in all previous works mentioned in section 3.4.2 ([59],[69], [58],[71] and [72]) are confirmed in this work.

The 248.76-keV γ-ray transition in ^{83}Ge

At 248.76 keV, there is a known doublet resulting from the beta decays of ^{83}Ga to ^{83}Ge (Eγ=247.7 (3) keV [45]) and ^{82}Ge to ^{82}As (Eγ=249.1 (5) keV [45]) at the end of the beta-n decay chain. To get the 248.76 keV gamma intensity corresponding to ^{83}Ge, the contribution of ^{82}As should be subtracted. The strongest gamma-ray transition in ^{82}As populated via the beta decay of ^{82}Ge is at 1091 keV. The 248.76 keV line's intensity, relative to this line, is 4 %, as reported in [56]. Based on the prior statement, the intensity of 248.76 keV coming from ^{82}As was calculated, and the remaining intensity was assigned to the ^{83}Ga beta decay.

Due to the low statistics, the 798 keV gamma-ray transition previously reported in coincidence with the 248.76-keV gamma-ray transition (in Refs. [58] and [69]) could not be seen either in the beta-gated gamma spectrum of ^{83}Ge or in the

Table 6.4: List of γ-ray transitions (E_γ) observed in ^{81}Ge, the βn daughter of ^{82}Ga, with their relative intensity to the most intense 1348.1-keV transition (with I_γ =100(12)%) and their $\gamma - \gamma$ coincidences. E_i represents the initial level energy of the E_γ transition, and the uncertainties reported are purely statistical.

E_γ (keV)	I_γ(%)	E_i (keV)	$\gamma - \gamma$
215.54 (1)	6.8 (7)	894.54 (2)	936.0, 828.5
481.6 (1)	0.4 (1)	1723.0 (2)	529.54
529.54 (2)	2.9 (3)	1240.70 (3)	481.6, 711.15
561.9 (2)	0.9 (1)	1240.70 (3)	–
574.6 (1)	0.6 (1)	1815.3 (4)	529.54, 711.15
711.15 (1)	13.5 (15)	711.15 (1)	529.54, 574.6, 2725.1
828.5 (2)	0.5 (1)	1723.0 (2)	215.54
936 (1)	0.2 (0)	1830.5 (1)	215.54 ,1189.2*
961.7 (2)	0.6 (1)	2692.3 (3)	1019.5*
1019.5 (4)	0.3 (1)	1731.4 (3)	961.7* 711.15
1189.2 (1)	1.1 (2)	3019.7 (3)	936.0*
1286.5 (1)	1.6 (2)	1286.5 (1)	–
1548.6 (3)	0.4 (1)	1548.6 (3)	–
1731.4 (3)	5.5 (8)	1731.4 (3)	–
2547.8 (1)	1.8 (3)	2547.8 (1)	–
2725.1 (1)	1.9 (3)	3436.3 (1)	711.15
3505.5 (4)	1.4 (3)	3505.5 (4)	–

* Coincidence not confirmed due to weak statistics, but it was observed in previous studies.

248.76 keV gated spectrum. Only one transition, 1204.48 keV, was observed in coincidence with the 248.76-keV transition. This was also observed in Refs. [69], [58],[71] and [72], confirming the energy level at 1453.24 (1) keV.

The 1452.9-keV γ-ray transition in ^{83}Ge

Our work also confirms the direct transition at 1452.9 (6) keV linking this state to the ground state, as observed in [71]. The gate on the 1452.9 keV gamma-ray transition shows a gamma-ray peak at 2570 keV. This coincidence was also established by observing the 2570-keV gated spectrum, which showed a gamma-ray peak at 1452.9 keV (see Figs. 6.19 and 6.20) revealing a new neutron unbound state at 4022.6 keV (S_n (^{83}Ge) = 3632.7 (3.3) keV [42]) observed for the first time in this work.

The 1119- and 1240-keV new excited states in ^{83}Ge

Two additional new energy levels located at 1119 and 1240 keV were added to the decay scheme of ^{83}Ga in this work (see Fig. 6.22). In the 1119.15-keV gamma-gated spectrum, as shown in Fig. 6.21, a gamma-ray peak at 121.29 keV is observed. The inverse gamma gate at 121.29 keV shows a line at 1119.15 keV, which confirms the coincidence between these two gamma transitions.

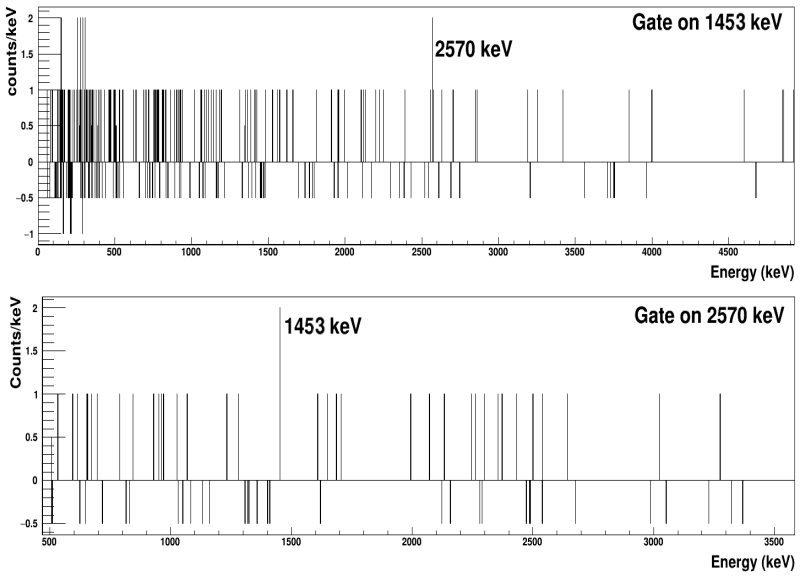

Figure 6.19: Top: The $\beta - \gamma - \gamma$ coincidence spectrum gated on 1452.9 (6) keV γ-line in ^{83}Ge. Bottom: The $\beta - \gamma - \gamma$ coincidence spectrum gated on 2570 (1) keV γ-line in ^{83}Ge.

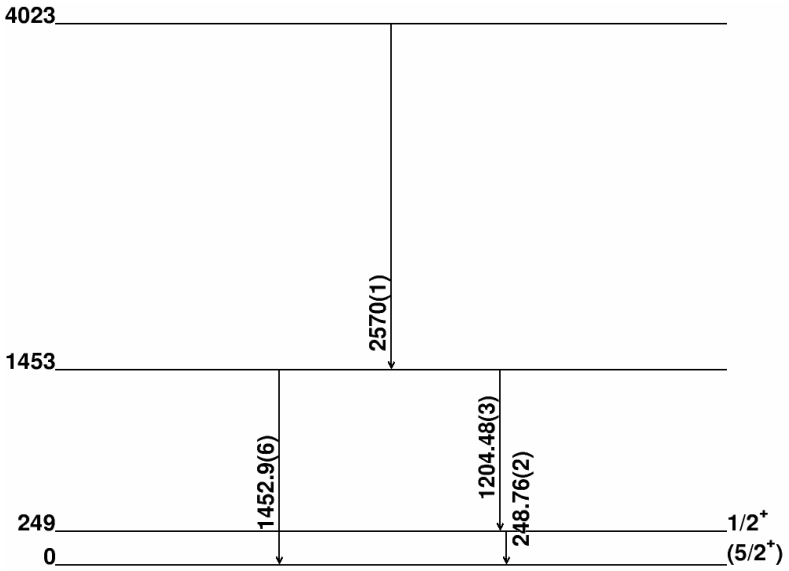

Figure 6.20: Partial decay scheme to determine the energy of the state at 4022.6(2) keV in ^{83}Ge. All energies are given in keV.

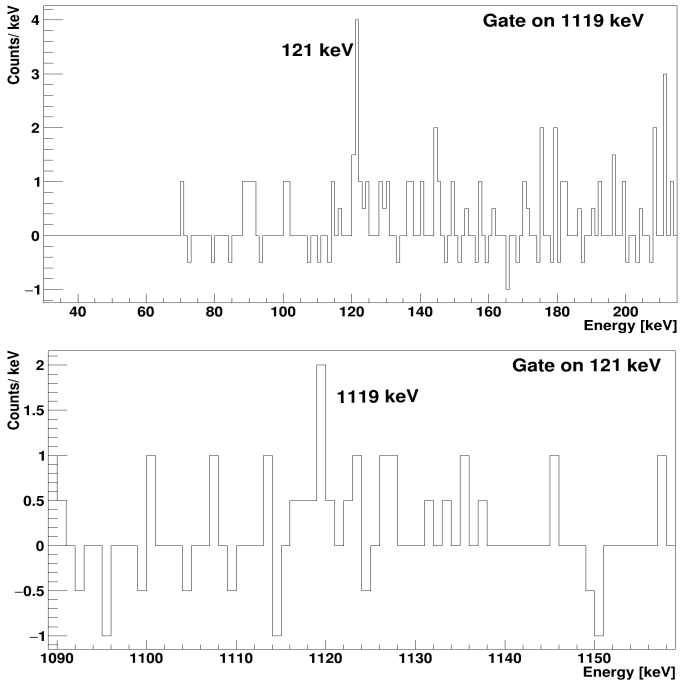

Figure 6.21: Top: The $\beta - \gamma - \gamma$ coincidence spectrum gated on 1119.15 (6) keV γ-line in ^{83}Ge . Bottom: The $\beta - \gamma - \gamma$ coincidence spectrum gated on 121.29 (12) keV γ-line in ^{83}Ge.

The 1246.3- and 2909.91-keV γ-ray transitions in ^{83}Ge

In addition, a 1246.3-keV gamma transition directly populating the ground state of ^{83}Ge was seen clearly in the beta-gated gamma spectrum of Fig. 6.4 confirming what was reported by [72], [71] and [58]. Moreover, the gamma-ray transition at 2909.91 keV, reported for the first time in the work of M. Alshudifat [58], was also observed and added to the ^{83}Ga decay scheme of this work.

All the identified gamma-ray transitions in ^{83}Ge and their relative intensities are reported in Table 6.5. The gamma-ray transitions resulting from the ^{83}Ga beta-n decay are listed in Table 6.6, and they were all observed previously [72].

6.2.3 ^{86}As

Through the analysis of ^{86}As β-decay, this research identified 30 new excited states and 32 new gamma-ray transitions in ^{86}Se. In total, the study observed 48 gamma-ray transitions in ^{86}Se, while also reporting for the first time the identification of six gamma-ray transitions in ^{85}Se resulting from the beta-delayed neutron decay of ^{86}As. All the known gamma transitions reported in literature [77, 76], were confirmed in this work (except for the four uncertain gamma-ray peaks reported at 674 [77], 613, 1943, and 3025 keV [76]).

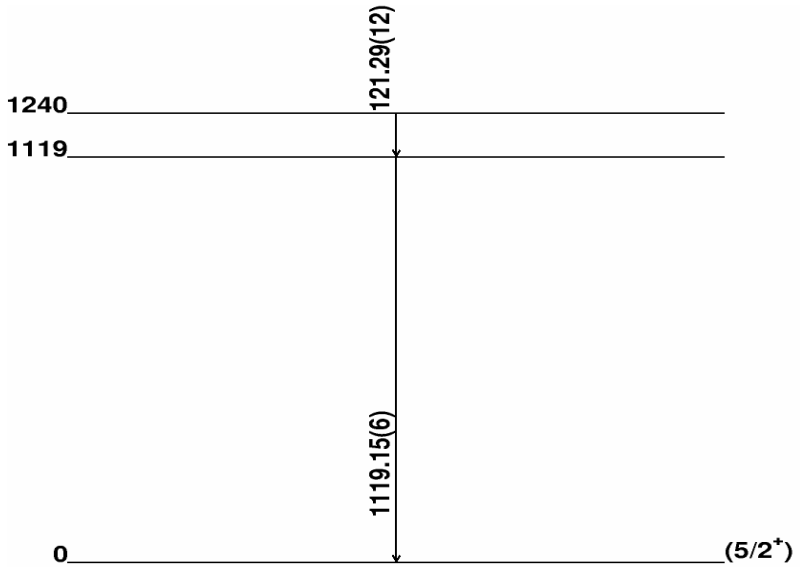

Figure 6.22: Partial decay scheme to determine the energy of the state at 121.29 (12) keV in ^{83}Ge. All energies are given in keV.

Table 6.5: List of γ-ray transitions (E_γ) observed in the β-decay of ^{83}Ga, with their relative intensity to the most intense 1348.1-keV transition (with I_γ =100(13)%) in the beta-n daughter ^{83}Ge and their $\gamma - \gamma$ coincidences. E_i represents the initial level energy of the E_γ transition, and the uncertainties reported are purely statistical.

E_γ (keV)	I_γ(%)	E_i (keV)	$\gamma - \gamma$
121.29 (12)	1.8 (2)	1240.44 (1)	1119.15
248.76 (2)	7.4 (7)	248.76 (2)	1204.48
703.52(6)	0.6 (2)	1941.52 (1)	1238.41
1046.11 (3)	2.4 (4)	1046.11 (3)	–
1119.15 (6)	2.1 (4)	1119.15 (6)	121.29
1204.48 (3)	2.3 (4)	1453.24 (1)	248.76
1238.41 (3)	6.5 (8)	1238.41 (3)	703.52
1246.33 (7)	2 (4)	1246.33 (7)	–
1452.9 (6)	1.7 (4)	1452.9 (6)	2570
2570.00 (14)	0.8 (5)	4022.6 (2)	1452.9
2909.91 (11)	1.8 (7)	2909.91 (11)	–

Table 6.6: List of γ-ray transitions (E_γ) observed in ^{82}Ge, the βn daughter of ^{83}Ga, with their relative intensity to the most intense 1348.1-keV transition (with I_γ =100(13)%) and their $\gamma - \gamma$ coincidences. E_i represents the initial level energy of the E_γ transition, and the uncertainties reported are purely statistical.

E_γ (keV)	I_γ(%)	E_i (keV)	$\gamma - \gamma$
414.52 (5)	1 (2)	2701.7 (1)	939.13, 1348.10
727.22 (9)	0.7 (3)	3014.5 (9)	939.13, 1348.10
867.74 (3)	4.5 (0)	2216.10 (5)	1348.10
939.13 (2)	10.9 (13)	2286.86 (2)	414.52 , 727.22 , 1348.10
985.58 (5)	3.4 (6)	2333.44 (2)	1348.10
1176.40 (4)	3.2 (5)	2524.50 (4)	1348.10
1348.10 (1)	100 (13)	1348.10 (1)	867.74, 939.13, 985.58 ,1176.40 ,1365.31
1365.31 (4)	2.8 (0)	2713.7 (1)	1348.10
2216.10 (5)	9 (1)	2216.10 (5)	–
2713.72 (12)	2.9 (7)	2713.7 (1)	–

The 704-keV γ-ray transition in ^{86}Se

The strongest transition populated in the beta decay of ^{86}As is the 704-keV gamma-ray transition from the first 2^+ state to the ground state of ^{86}Se. The $\beta - \gamma - \gamma$ coincidence spectrum gated on the 704-keV gamma-ray transition is presented in Fig. 6.23. It shows 16 gamma-ray peaks in coincidence with the 704-keV transition, of which 10 were observed for the first time in this work. All the coincidences are listed in Table 6.7.

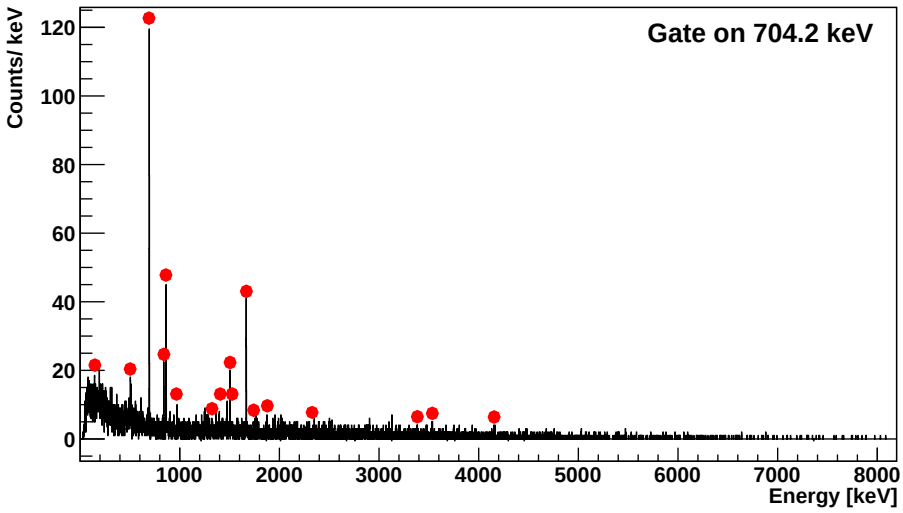

Figure 6.23: γ-ray spectrum gated on the 704.2 keV gamma-ray transition in ^{86}Se. The gamma-ray transitions identified to be feeding the 2^+ state at 704.2 keV are marked with red dots.

The 144.85-keV γ-ray transition in ^{86}Se

The lowest energy gamma-ray transition attributed to ^{86}Se was observed at 144.85 keV. This line is seen in coincidence with the two gamma rays at 694.8 and 704.2 keV (see Fig. 6.24). The cascade of these three gamma transitions puts the energy level at 1543.9 keV (see Fig. 6.25), which was already reported in Ref. [76] based on the coincidence of the two known gamma rays at 839.7 and 704.2 keV. The absolute and relative intensities of the 144.85-keV γ-ray transition were corrected for the internal conversion coefficient ($\alpha = 0.209$ [110]).

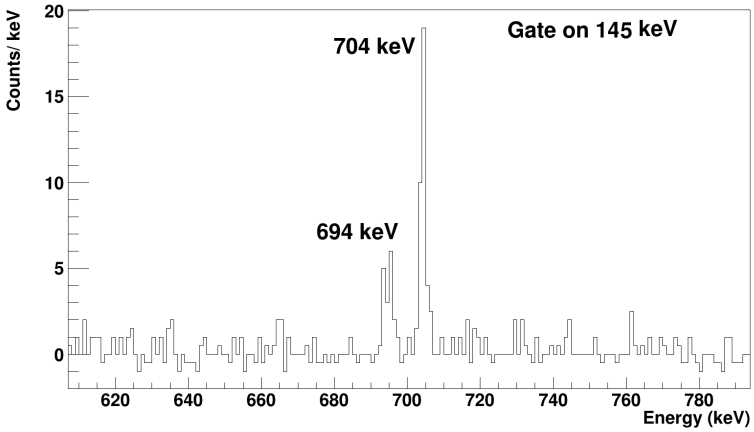

Figure 6.24: The $\beta - \gamma - \gamma$ coincidence spectrum gated on 144.85 (3) keV γ-line in ^{86}Se.

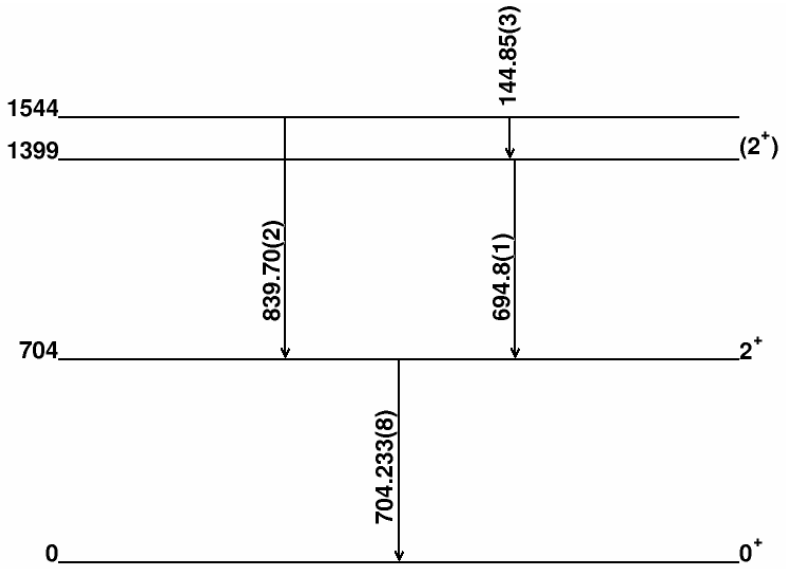

Figure 6.25: Partial decay scheme to determine the energy of the state at 1543.9(1) keV in ^{86}Se. All energies are given in keV.

The 1473.5-1476.7 keV doublet in ^{86}Se

The work of Materna *et al.* [77] reported a gamma transition at 1476 keV feeding the 704 keV level in ^{86}Se. However, a closer look at the 1476 keV peak shows that the structure of the peak is not perfectly Gaussian, which is a sign of an existence of a doublet (see Fig. 6.26). A gate placed on the left or right side of the peak reveals a difference between the lines in coincidence. When the gate is placed on the higher energy part at 1476.7 keV, the 704.2 keV appears, confirming its place in the level scheme of [77], presented in Fig. 6.27. Nevertheless, placing the gate on the left side of the peak at 1473.5 keV shows a strong coincidence with the 863.5 keV and 704.2 keV gamma-ray transitions, as illustrated in Fig. 6.26. The corresponding inverse gates confirm the coincidences, adding a new level at 3041.2 keV to the level scheme of ^{86}Se (see the partial level scheme in Fig. 6.28).

The 2028.2-keV γ-ray transition in ^{86}Se

The gamma-ray transition at 2028.2 keV, already observed in Ref. [77], is seen in the beta-gated spectrum in Fig. 6.5. However, placing a gate at 2028.2 keV does not show a coincidence with the 1503.97 keV gamma-ray transition contrary to what was reported in Ref. [77]. This transition was proposed to originate from a level at 4236.8 keV in Ref. [77]. Our analysis did not find a coincidence between the 2028.2 keV and 1503.97 keV transitions. As a result, the 2028.2 keV gamma-ray transition must be feeding the first 2^+ level since this is the only coincidence seen in the gamma-gated spectrum of Fig. 6.29.

The 1865-keV γ-ray transition in ^{86}Se

The 1865-keV gamma transition reported to be the 4236.8 $\rightarrow$ 2372.3 keV transition in ^{86}Se in [77] is also placed differently in this work. The 1865-keV gated gamma-ray spectrum shows only a gamma-ray peak at 704.2 keV. Hence, in the ^{86}Se level scheme of this work, the 1865-keV gamma transition is placed to feed the 704.2 keV level.

The 2350-keV γ-ray transition in ^{86}Se

In the 704-keV gated spectrum, a coincidence with a 2350-keV gamma-ray transition was noticed. The peak at 2350 keV was observed in the beta-gated gamma spectrum of ^{86}Se but considered at the beginning as a daughter activity since there is a known gamma-ray transition at this energy in the decay of ^{86}Br to ^{86}Kr. The ^{86}Kr gamma-ray transition is reported at 2349.37 (12) keV, with a relative intensity of 15.7 % [45]. The most intense gamma transition observed in the beta-gamma decay of ^{86}Br is at 1564.60 (7) keV [45], and it can also be observed in the beta-gated gamma spectrum of ^{86}Se. However, the number of counts of the most intense ^{86}Kr gamma-ray transition, 1564.6 keV (532 (39) counts), is lower than the number of counts of the 2350-keV peak (558 (38) counts), and these numbers are not corrected for the detection efficiency. This confirms the contribution of

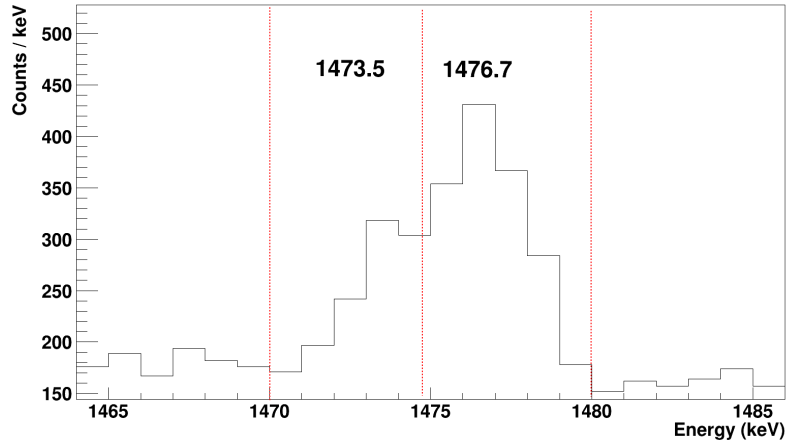

(a)

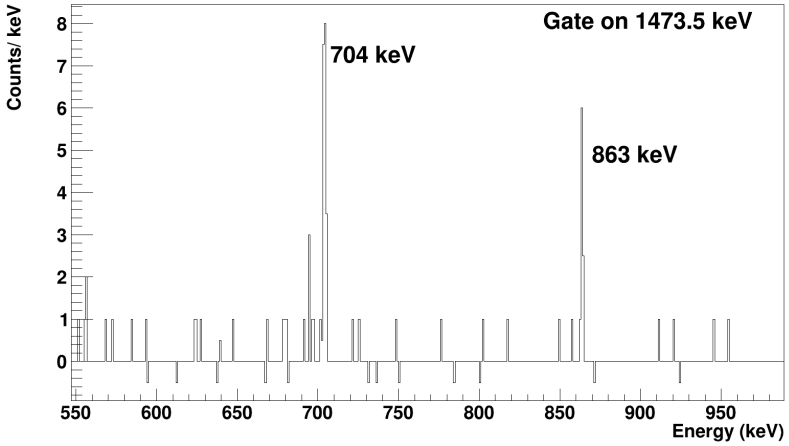

(b)

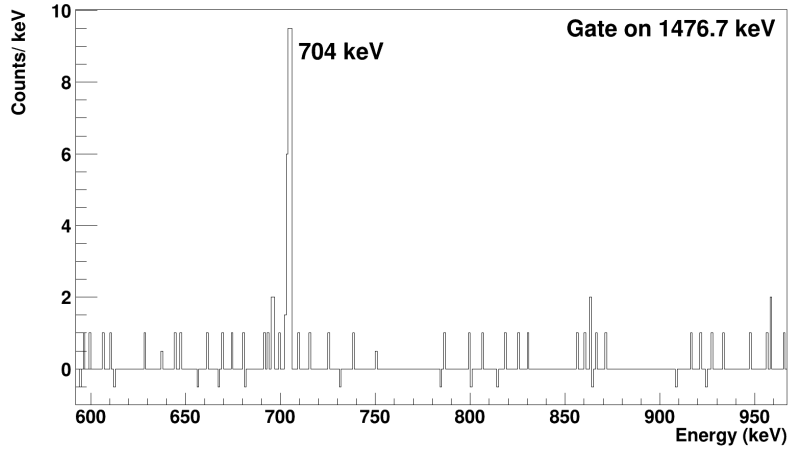

(c)

Figure 6.26: Part of the beta gated ^{86}Se spectrum showing the doublet structure around the 1476 keV peak (a). The $\beta - \gamma - \gamma$ coincidence spectrum gated on 1473.5 keV (b) and 1476.7 keV (c) lines in ^{86}Se.

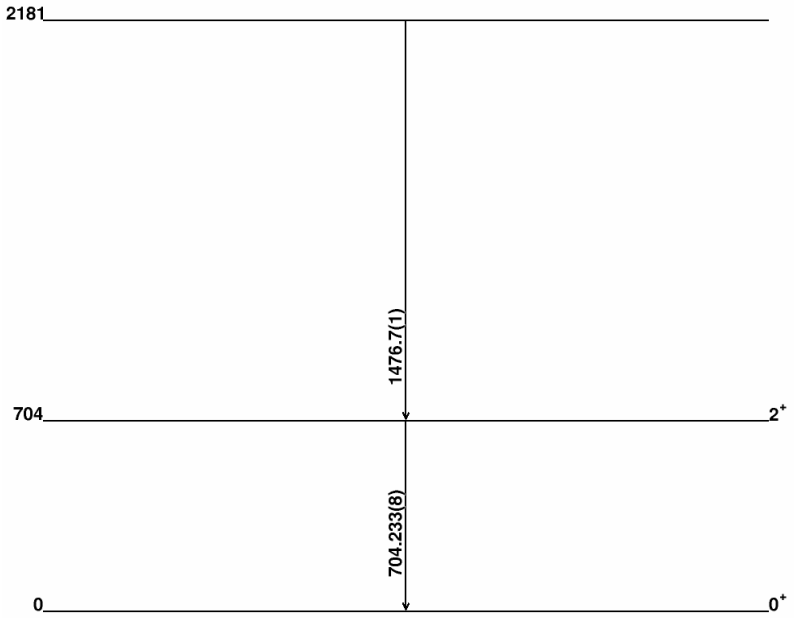

Figure 6.27: Partial decay scheme to determine the energy of the state at 2180.9(1) keV in ^{86}Se. All energies are given in keV.

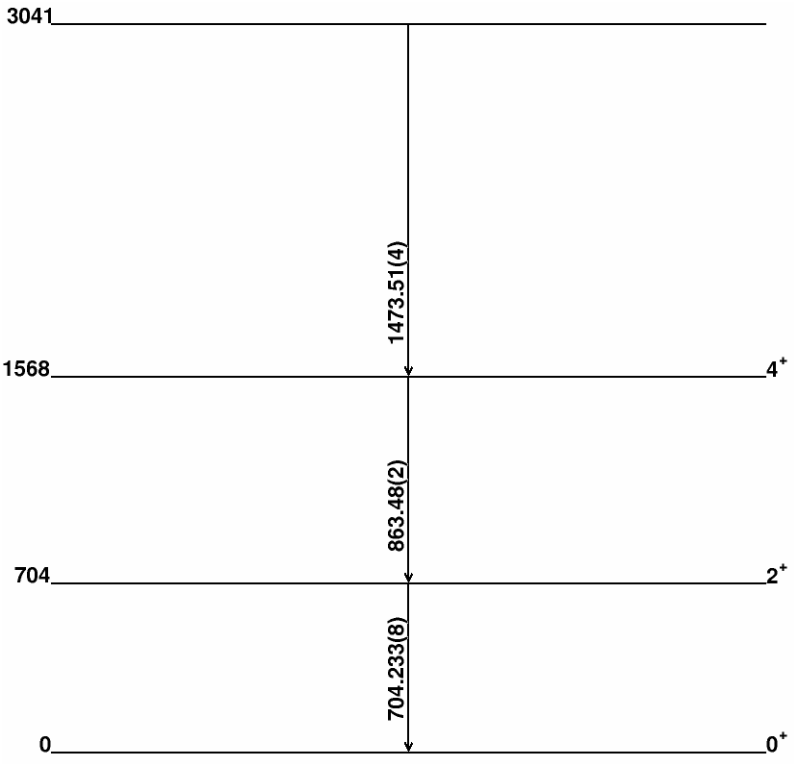

Figure 6.28: Partial decay scheme to determine the energy of the state at 3041.2(1) keV in ^{86}Se. All energies are given in keV.

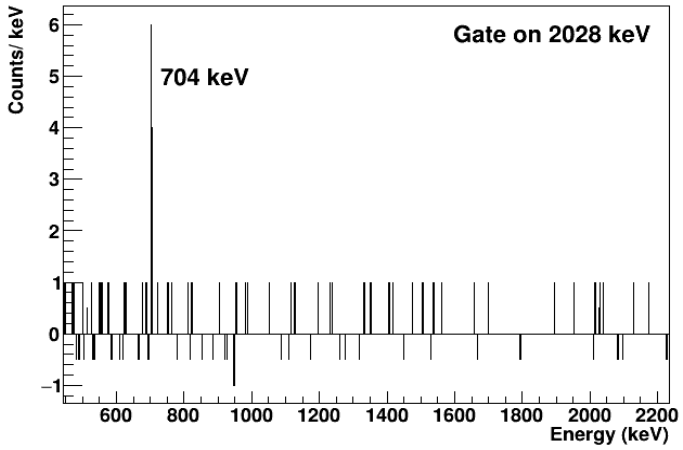

Figure 6.29: Energy distribution of gamma rays in coincidence with the 2028.2 keV line.

^{86}As decay in the gamma-ray transition at 2350 keV. The contribution of ^{86}Kr was calculated using the efficiency-corrected number of counts observed in the 1564.6 keV transition together with the known intensity ratio of the 2349.37-keV and 1564.6-keV transitions. The ^{86}Kr contribution was subtracted to get the correct intensity corresponding to ^{86}Se, which resulted in relative gamma intensity I_γ=1.3(2) % in ^{86}Se.

The 1399-keV γ-ray transition in ^{86}Se

There is another known doublet at 1399 keV resulting from the beta decays of ^{86}As to ^{86}Se (E_γ=1399.1 (2) keV [45]) and the beta daughter ^{86}Se to ^{86}Br ($E\gamma$=1399.0 (3) keV [45]). The contribution of the ^{86}Se beta decay was also calculated, and the relative gamma intensity of the 1399 keV gamma-ray transition in ^{86}Se resulting from the decay of ^{86}As was concluded to be 9.0 (6) %.

Spin-parities of the ^{86}As ground state and the 4236.5-keV and 4783.9-keV excited states of ^{86}Se

The ground-state spin-parity of ^{86}As was suggested in [76] to be (1^-, 2^-). The states populated in ^{85}Se by the beta-n decay of ^{86}As have spin-parities ranging from $1/2^+$ to $9/2^+$ (see Fig. 6.35). The fact that we observe states with spin-parities higher than $7/2^+$ ($9/2^+$) makes it reasonable to exclude the 1^- from the possibilities of the ^{86}As ground state spin-parity. Therefore, in our spin-parity assignments, we will consider that the ground state of ^{86}As has (2^-) as spin-parity.

The states at 4236.5 (1) keV, 4783.9 (4) keV, and 5345.9 (2) keV are populated with higher intensities than those around them. They also have log ft values $<$6.5, which fall within the log ft distribution of allowed transitions [12] (see Fig. 2.2). Therefore, we suggest that the 4236.5 (1) keV, 4783.9 (4) keV, and 5345.9 (2) keV states are populated via allowed beta transitions. The spin-parities previously assigned to the states at 4236.5 (1) keV, and 4783.9 (4) keV are (2,3,4$^+$). Starting from (2^-) ground state spin parity of ^{86}As, the allowed transitions can populate 1^-,2^- or 3^- spin parity levels in ^{86}Se. The 4236.5 (1) keV state is connected only

to the first 2^+ state, which means it cannot be a 1^- because it is not connected to the 0^+ ground state. Therefore, $(2^-, 3^-)$ for the spin and parity of the 4236.5 (1) keV state is proposed. On the other hand, the 4783.9 (4) keV state is connected to both 0^+ ground state and 2^+ excited states of ^{86}Se, which favors 1^- over 2^- or 3^-. As a result, the 4783.9 (4) keV state is suggested to have spin-parity (1^-). The state with energy 5345.9 (2) keV was observed to have a direct connection to the 0^+ ground state in ^{86}Se. This observation indicates a preference for 1^- over 2^- or 3^- spin-parity. Thus, (1^-) spin-parity is suggested for the 5345.9 (2) keV state in ^{86}Se.

The neutron separation energy in ^{86}Se is at 6160.8 (3.6) keV [42]. In this work, 11 new gamma transitions were observed de-exciting states between 4-6 MeV, but no levels above the neutron separation energy could be established.

New γ-ray transitions in βn-daughter ^{85}Se

The gamma-ray transitions in ^{85}Se, following the beta-delayed neutron emission from ^{86}As, are all seen for the first time in this work. The only tentative transition was seen at 1114.87 keV in [76] where it was not possible to disentangle the contributions from β-n decay of ^{86}As and β-decay of ^{85}As (coming from the beta-n decay of ^{86}Ge). In this work, we had a pure sample of ^{86}As and are sure that no contribution came from ^{86}Ge or ^{85}As.

All the gamma rays assigned to the ^{86}Se and ^{85}Se, together with their corresponding relative intensities and coincidences, are summarized in Tables 6.7 and 6.8, respectively. The relative intensities were calculated compared to the 704.2-keV transition in ^{86}Se.

Table 6.7: List of γ-ray transitions (E_γ) observed in the β-decay of ^{86}As, with their relative intensity to the most intense 704-keV transition (I_γ= 100(8)%) and their $\gamma - \gamma$ coincidences. E_i represents the initial level energy of the E_γ transition, and the uncertainties reported are purely statistical.

E_γ (keV)	I_γ(%)	E_i (keV)	$\gamma - \gamma$
144.85 (3)	0.3 (1)	1543.9 (1)	694.8, 704.233
505.06 (3)[a]	2.0 (3)	2072.8 (1)	704.233, 863.48
694.8 (1)[a]	23.6 (2)	1399.0 (1)	144.85, 704.233, 782.42, 972.96, 1321.5, 3030
704.233(4)[a]	100 (8)	704.233 (8)	144.85, 505.06, 694.8, 839.7, 863.48, 972.96, 1321.5,1473.51, 1476.7, 1503.97, 1667.62 ,1753.68, 1865, 2350,44, 3384.2, 3532.2, 4129.7
782.42 (5)[a]	1.6 (2)	2180.9 (1)	694.8, 704.233
839.7 (2)[a]	3.2 (3)	1543.9 (1)	704.233
863.48 (2)[a]	8.4 (6)	1567.7 (1)	505.06, 704.233, 1473.51, 1655.7, 2044.9
972.96 (3)[a]	2.4 (2)	2371.9 (1)	694.8, 704.233, 1399
1321.5 (1)	1.5 (1)	2720.5 (1)	694.8, 704.233, 1399
1399 (1)[a]	9.0 (6)	1399.0 (1)	972.96, 1321.5
1473.51(4)	1.4 (2)	3041.2 (1)	863.48, 704.233
1476.7 (1)[a]	2.5 (3)	2180.9 (1)	704.233
1503.97(2)[a]	9.3 (6)	2208.2 (1)	704.233
1655.7 (1)	0.8 (1)	3223.4 (1)	704.233, 863.48
1667.62(2)[a]	14.0 (9)	2371.9 (1)	704.233, 3350.5
1753.68(4)	2.4 (2)	2457.9 (1)	704.233
1865 (1)[a]	0.9 (2)	2569.2 (1)	704.233
1875.5 (1)	3.0 (2)	2579.8 (1)	704.233
2028.2 (1)[a]	0.7 (1)	2732.4 (1)	704.233
2044.9 (1)	0.4 (1)	4117.7 (1)	505.06, 704.233, 863.48
2208.2 (1)[a]	1.4 (2)	2208.2 (1)	–
2350.4 (1)	1.3 (2)	3054.6 (1)	704.233

Continued on next page

Table 6.7: List of γ-ray transitions (E_γ) observed in the β-decay of ^{86}As, with their relative intensity to the most intense 704-keV transition (I_γ= 100(8)%) and their $\gamma - \gamma$ coincidences. E_i represents the initial level energy of the E_γ transition, and the uncertainties reported are purely statistical. (Continued)

E_γ (keV)	I_γ(%)	E_i (keV)	$\gamma - \gamma$
2372.5 (1)	1.2 (2)	2371.9 (1)	704.233*
2475.2 (1)	0.8 (2)	3179.4 (1)	704.233*
3030 (1)	0.9 (2)	4428.6 (1)	694.8, 704.233
3128.6 (1)	3.2 (3)	3832.8 (1)	704.233
3317.9 (1)	0.4 (1)	4022.1 (1)	704.233*
3350.5 (1)	0.4 (1)	5722.3 (1)	704.233, 1667.62
3384.2 (1)[a]	5.2 (4)	4783.9 (4)	694.8, 704.233
3399 (1)	0.4 (1)	3399 (1)	–
3532.2 (1)[a]	5.5 (4)	4236.5 (1)	704.233
3671.9 (1)	0.8 (2)	5070.9 (1)	694.8, 704.233
3724.3 (1)	0.8 (2)	4428.6 (1)	704.233
3746.2 (1)	1.6 (2)	3746.2 (1)	–
3869.2 (1)	0.6 (1)	4573.5 (1)	704.233
4057 (1)	0.6 (2)	4057 (1)	–
4079.3 (2)	0.5 (1)	4783.9 (4)	704.233
4129.7 (4)	0.6 (2)	4833.9 (4)	704.233
4140 (2)	0.3 (1)	4140 (2)	–
4405.5 (2)	0.5 (3)	5109.8 (2)	704.233
4602.6 (2)	0.5 (2)	4602.6 (2)	–
4606.5 (2)	0.2 (2)	4606.5 (2)	–
4643.2 (1)	1.5 (3)	4643.2 (1)	–
4661.3 (2)	0.7 (3)	4661.3 (2)	–
4783.9 (4)	1.2 (2)	4783.9 (4)	–
4816.9 (2)	0.9 (2)	4816.9 (2)	–
4926 (3)	1.0 (3)	4926 (3)	–
5345.9 (2)	1.7 (3)	5345.9 (2)	–
5817.1 (2)	0.4 (1)	5817.1 (2)	–
5863.9 (3)	0.4 (2)	5863.9 (3)	–

[a] known γ-ray transitions

* The inverse coincident condition is not confirmed

Table 6.8: List of γ-ray transitions (E_γ) observed in ^{85}Se, the βn daughter of ^{86}As, with their relative intensity to the 704-keV transition (I_γ= 100(8)%) in ^{86}Se and their $\gamma - \gamma$ coincidences. E_i represents the initial level energy of the E_γ transition, and the uncertainties reported are purely statistical.

E_γ (keV)	I_γ(%)	E_i (keV)	$\gamma - \gamma$
461.81 (1)	8.2 (7)	461.81 (1)	–
1114.87 (2)	6.6 (5)	1114.87 (2)	2510.2*
1439.12 (4)	3.2 (3)	1439.12 (4)	–
1444.02 (4)	2.1 (2)	1444.02 (4)	–
1803.55 (7)	0.9 (1)	1803.55 (7)	–
2510.2 (1)	0.4 (1)	3954.2 (1)	1114.87*

* Coincidence not confirmed due to weak statistics, but it was observed in previous studies.

6.3 Proposed level-schemes for the decays of ^{82,83}Ga and ^{86}As

6.3.1 Absolute gamma intensities

The absolute intensity of a transition was determined according to the following equation:

$$I_\gamma^{abs} = \frac{N(E_\gamma)}{\varepsilon(E_\gamma)\varepsilon_\beta N_{parent}} \tag{6.1}$$

The $N(E_\gamma)$ corresponds to the number of events in the peak of the spectrum of interest obtained from a Gaussian fit at the transition energy E_γ. This value was therefore corrected by the $\varepsilon(E\gamma)$ and ε_β , corresponding to the γ and beta detector efficiencies, respectively. N_{parent} is the number of parent nuclei decaying during the measurement time.

6.3.2 Beta-decay branching ratios

The beta-decay branching ratios were calculated using the following equation:

$$I_\beta = \frac{N_{\gamma OUT} - N_{\gamma IN}}{\varepsilon_\beta N_{parent}} \tag{6.2}$$

where N_γ is the number of events in the peak of a γ-transition also obtained through a Gaussian fit corrected for the γ efficiency $\varepsilon(E_\gamma)$. The "IN" and "OUT" mean the number of events populating and depopulating the state of interest, respectively. Note that the beta branching ratio value corresponds to an upper value because it is possible that one or more unobserved transitions populate the state, which would lead to an overestimation of the branching ratio.

6.3.3 The log *ft* values

The log *ft* values were calculated using the National Nuclear Data Center log *ft* program [111]. The uncertainties on I_{γ}^{abs} abs and I_{β} were obtained by error propagation.

The decay schemes of ^{82}Ga, ^{83}Ga, and ^{86}As presented in this section, summarize all the assumptions made earlier. The transitions marked in red are seen for the first time in this work.

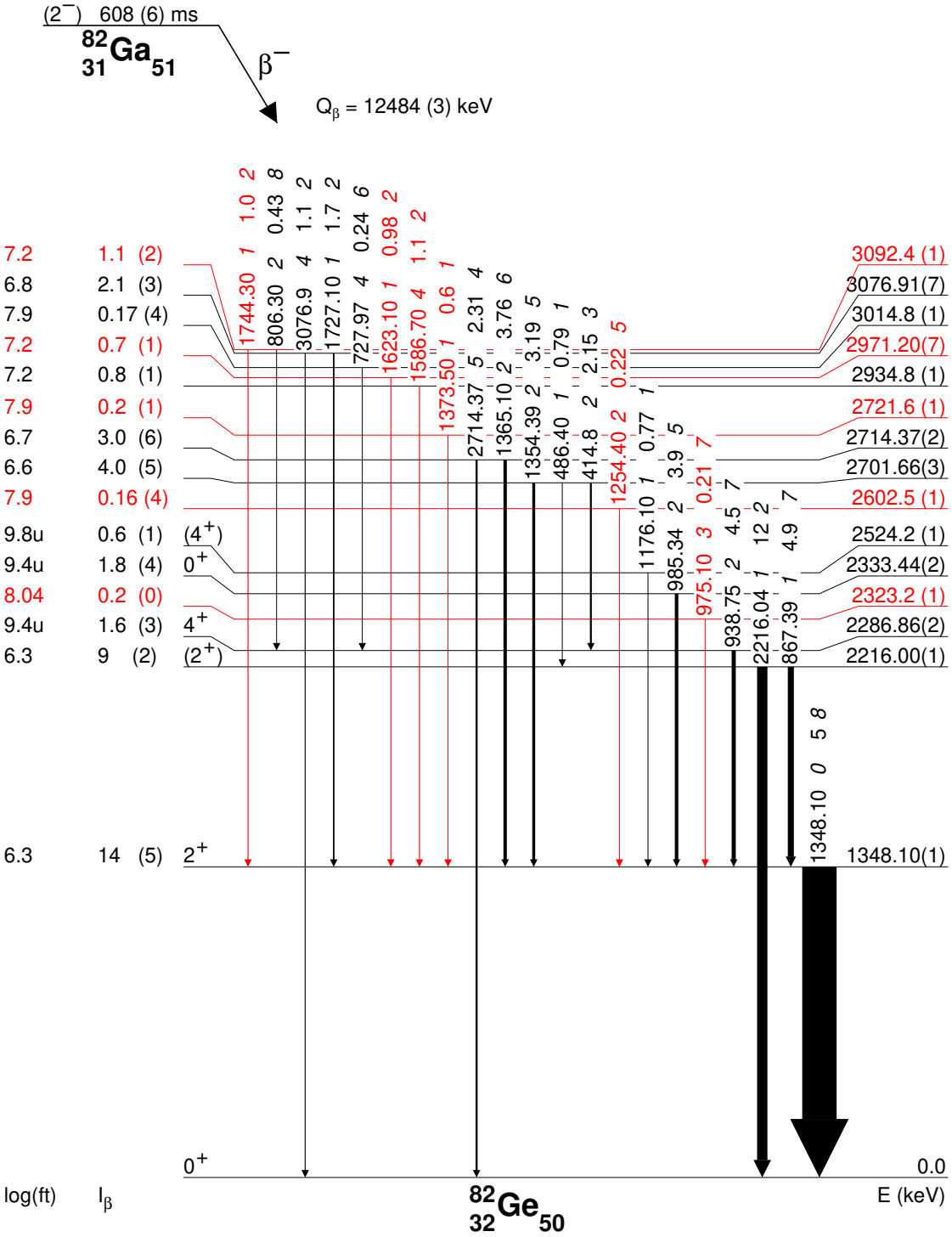

Figure 6.30: **(a)** Level scheme of ^{82}Ge fed by the beta-decay of ^{82}Ga up to 3092.4 keV (to be continued on the next page). The width of the arrows is proportional to the absolute intensity of the transitions, noted next to the transition energy given above the arrows. The determined branching ratios I_β and log *ft* values are listed to the left of each state. Levels and transitions known from the previous studies are plotted in black, newly identified in red. The log *ft* values marked with "u" were calculated with a uniqueness condition. Note: level scheme not to scale for visualization purposes.

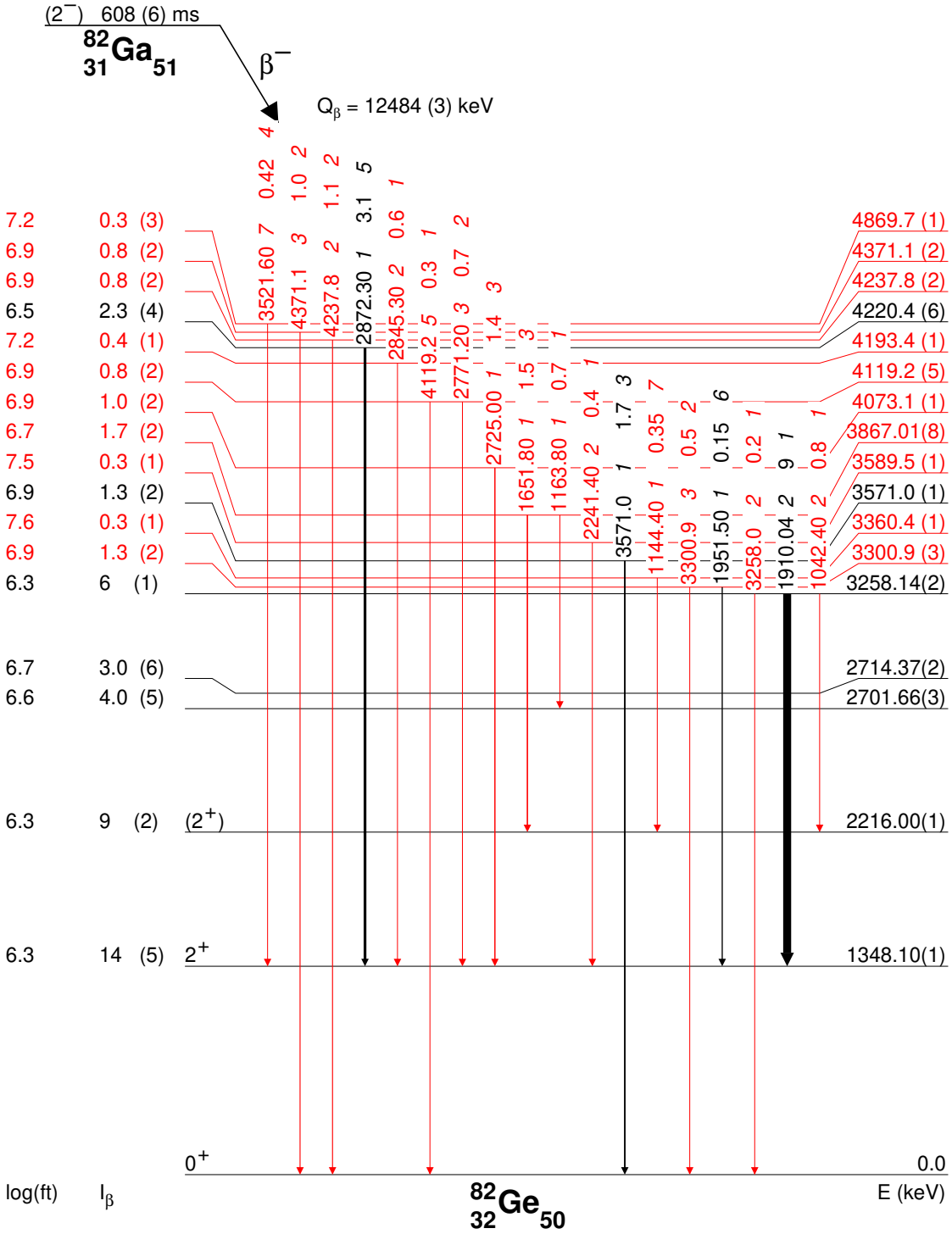

Figure 6.30: **(b)** Level scheme of ^{82}Ge fed by the beta-decay of ^{82}Ga, de-excitations from levels at 3-5 MeV (to be continued on the next page). The width of the arrows is proportional to the absolute intensity of the transitions, noted next to the transition energy given above the arrows. The determined branching ratios I_β and log *ft* values are listed to the left of each state. Levels and transitions known from the previous studies are plotted in black, newly identified in red, and the tentatively placed in red dashed lines. Note: level scheme not to scale for visualization purposes.

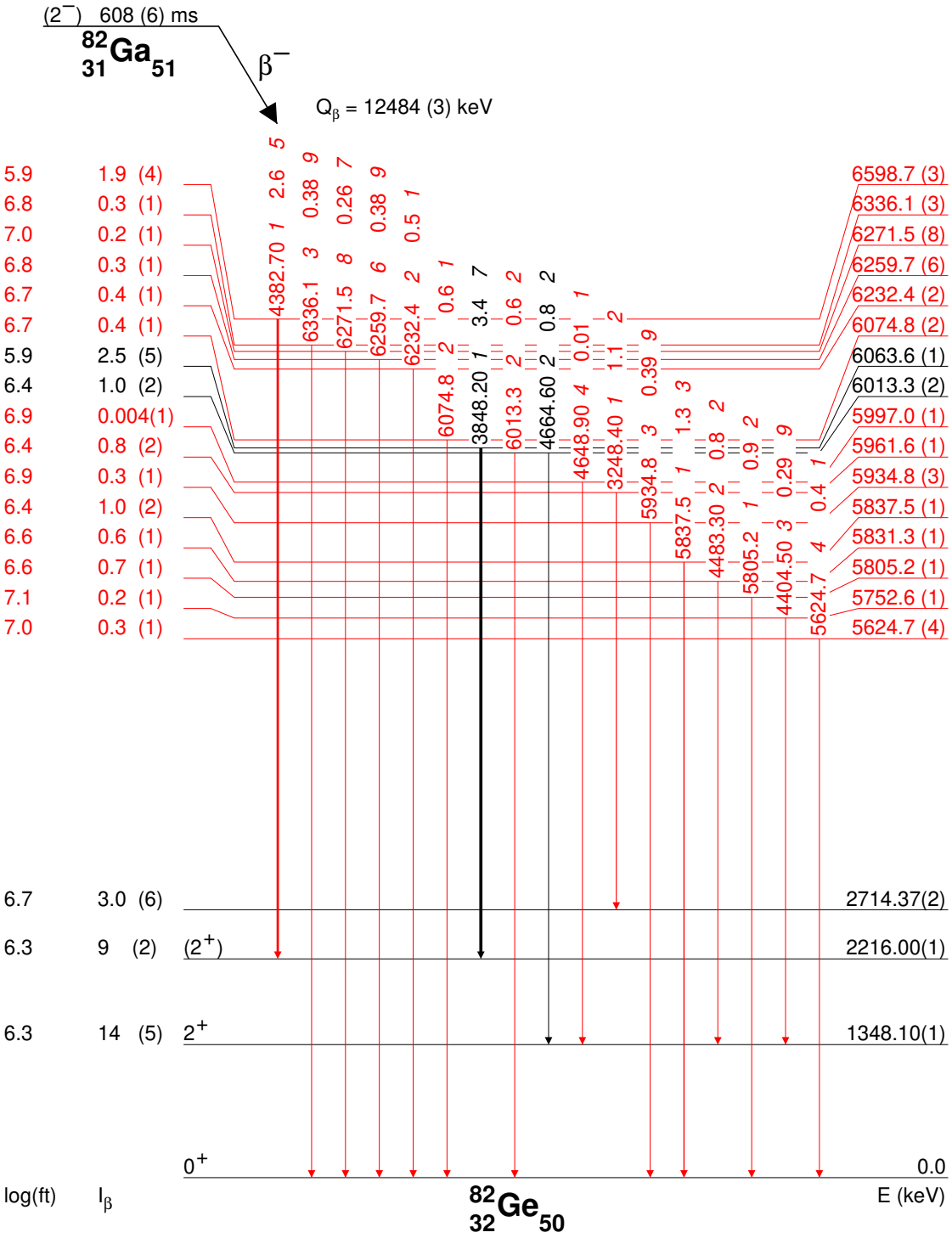

Figure 6.30: **(c)** Level scheme of ^{82}Ge fed by the beta-decay of ^{82}Ga de-excitations from levels at 5-6.6 MeV (to be continued on the next page). The width of the arrows is proportional to the absolute intensity of the transitions, noted next to the transition energy given above the arrows. The determined branching ratios I_β and log *ft* values are listed to the left of each state. Levels and transitions known from the previous studies are plotted in black, newly identified in red. Note: level scheme not to scale for visualization purposes.

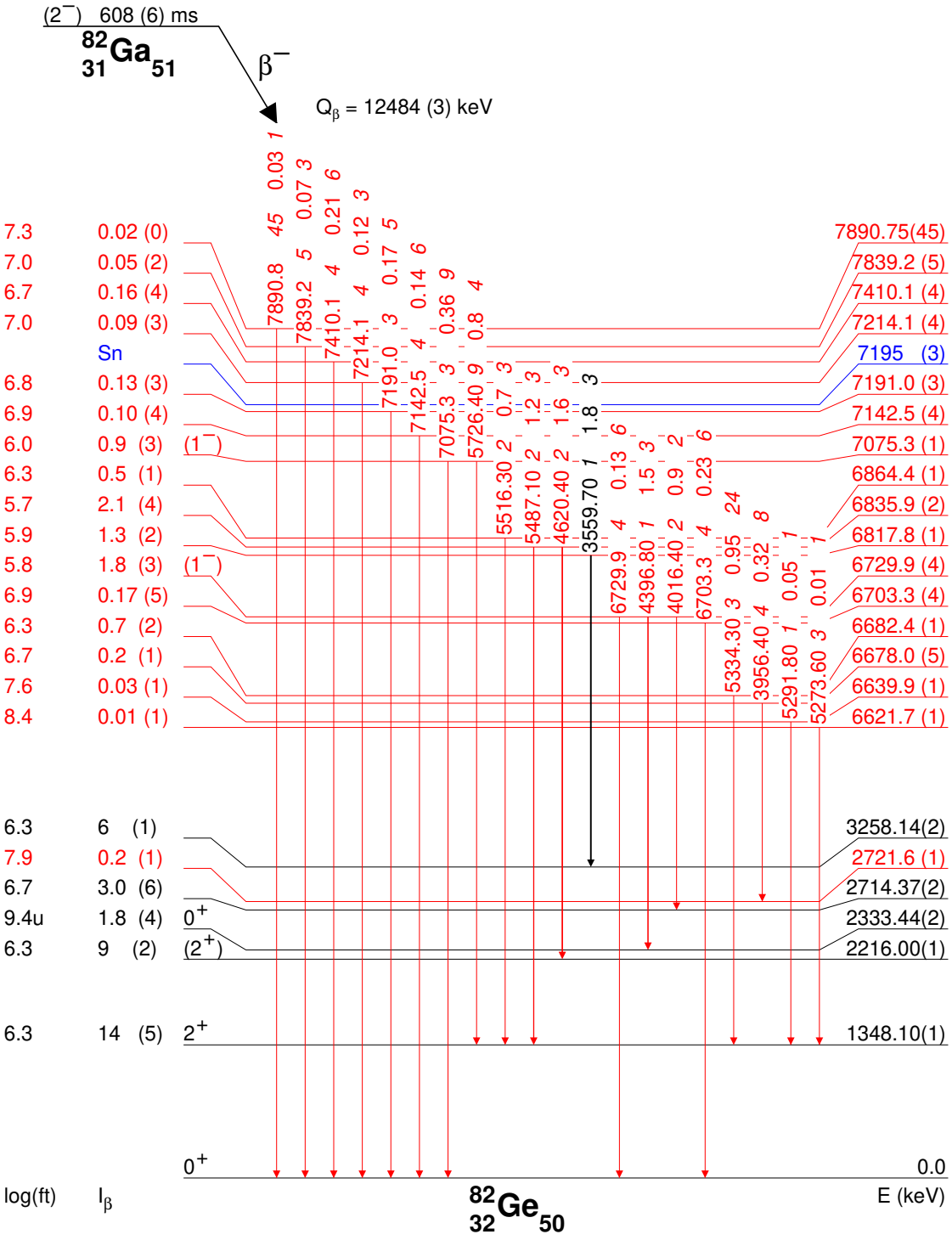

Figure 6.30: **(d)** Level scheme of ^{82}Ge fed by the beta-decay of ^{82}Ga, de-excitations from levels at 6.6-8 MeV. The width of the arrows is proportional to the absolute intensity of the transitions, noted next to the transition energy given above the arrows. The determined branching ratios I_β and log ft values are listed to the left of each state. Levels and transitions known from the previous studies are plotted in black and newly identified in red. The neutron separation energy is indicated in blue. The log ft value marked with "u" was calculated with a uniqueness condition. Note: level scheme not to scale for visualization purposes.

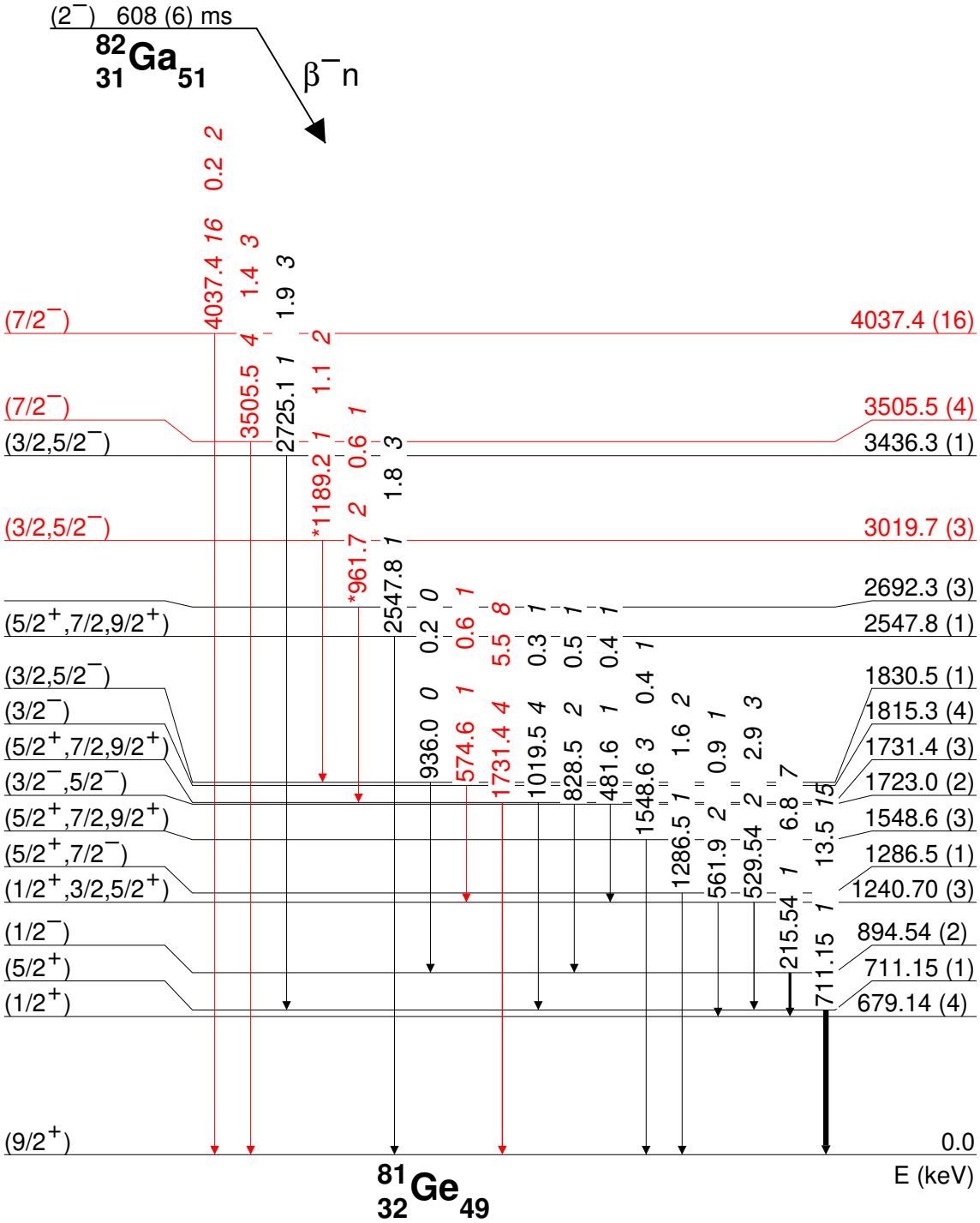

Figure 6.31: Level scheme of ^{81}Ge fed by the beta-delayed neutron emission of ^{82}Ga. The width of the arrows is proportional to the relative intensity of the transitions, noted next to the transition energy given above the arrows. Levels and transitions known from the previous studies are plotted in black, newly identified in solid red lines. The "*" is to mark the γ-ray transitions with uncertain placement. Note: level scheme not to scale for visualization purposes.

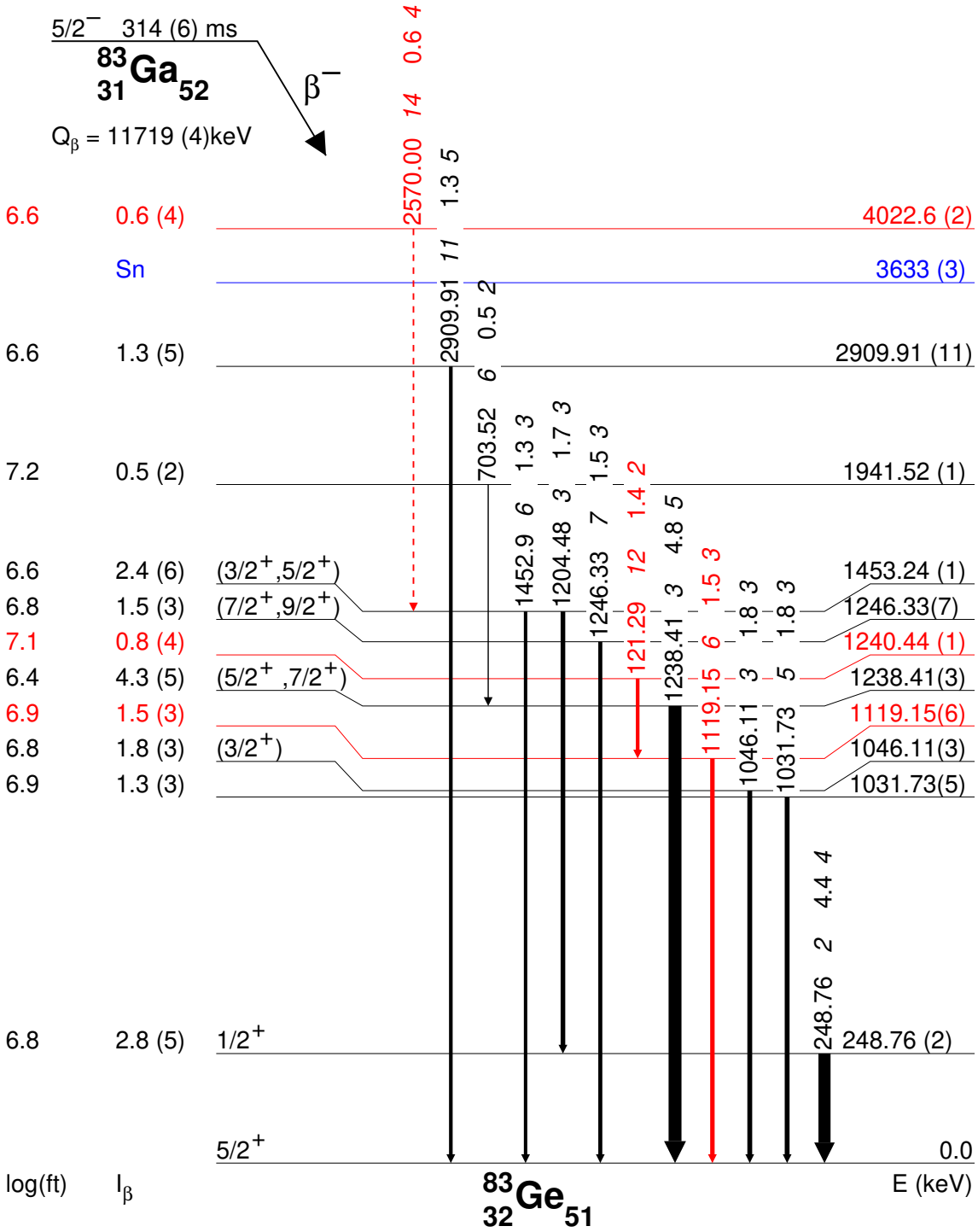

Figure 6.32: Level scheme of ^{83}Ge fed by the beta-decay of ^{83}Ga. The width of the arrows is proportional to the absolute intensity of the transitions, noted next to the transition energy given above the arrows. The determined branching ratios I_β and log *ft* values are listed to the left of each state. Levels and transitions known from the previous studies are plotted in black, newly identified in red, and the tentatively placed in red dashed lines. The neutron separation energy is indicated in blue. Note: level scheme not to scale for visualization purposes.

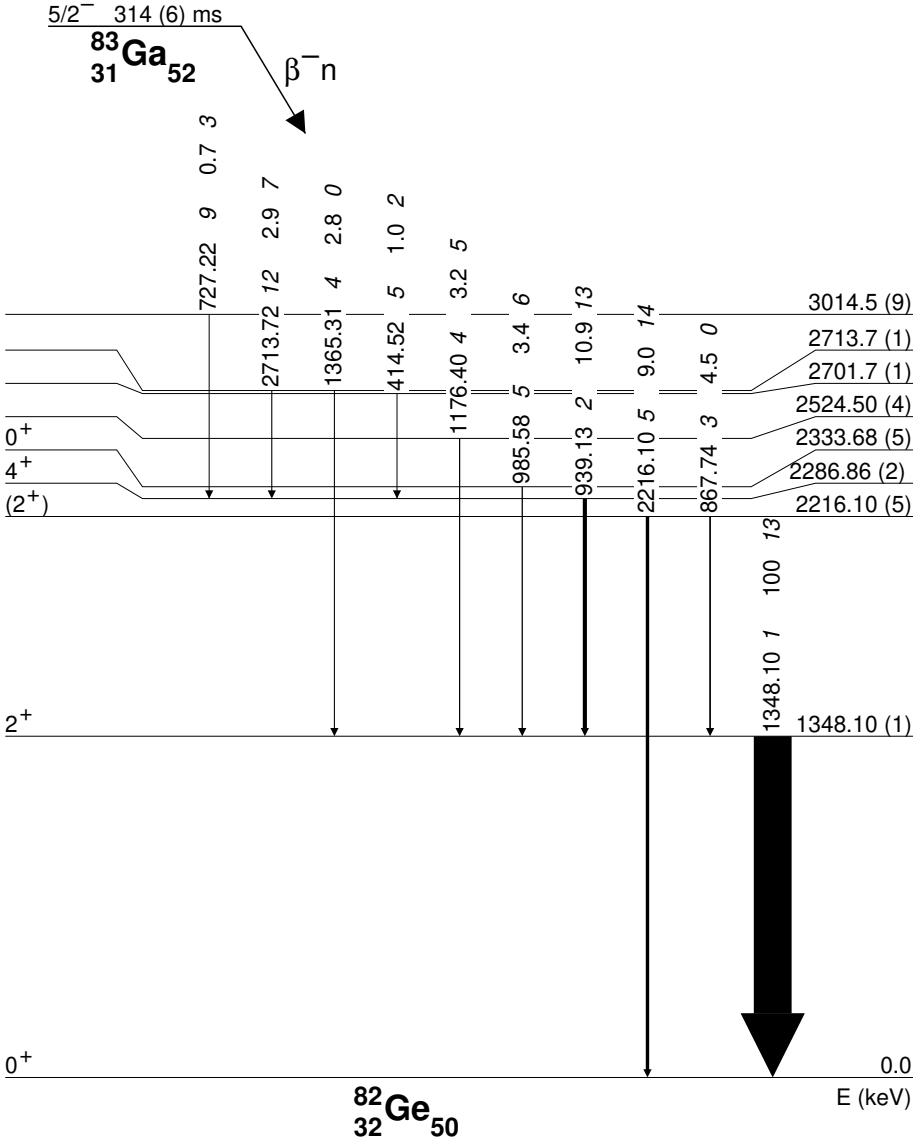

Figure 6.33: Level scheme of ^{82}Ge fed by the beta-delayed neutron emission of ^{83}Ga. The width of the arrows is proportional to the relative intensity of the transitions, noted next to the transition energy given above the arrows. Note: level scheme not to scale for visualization purposes.

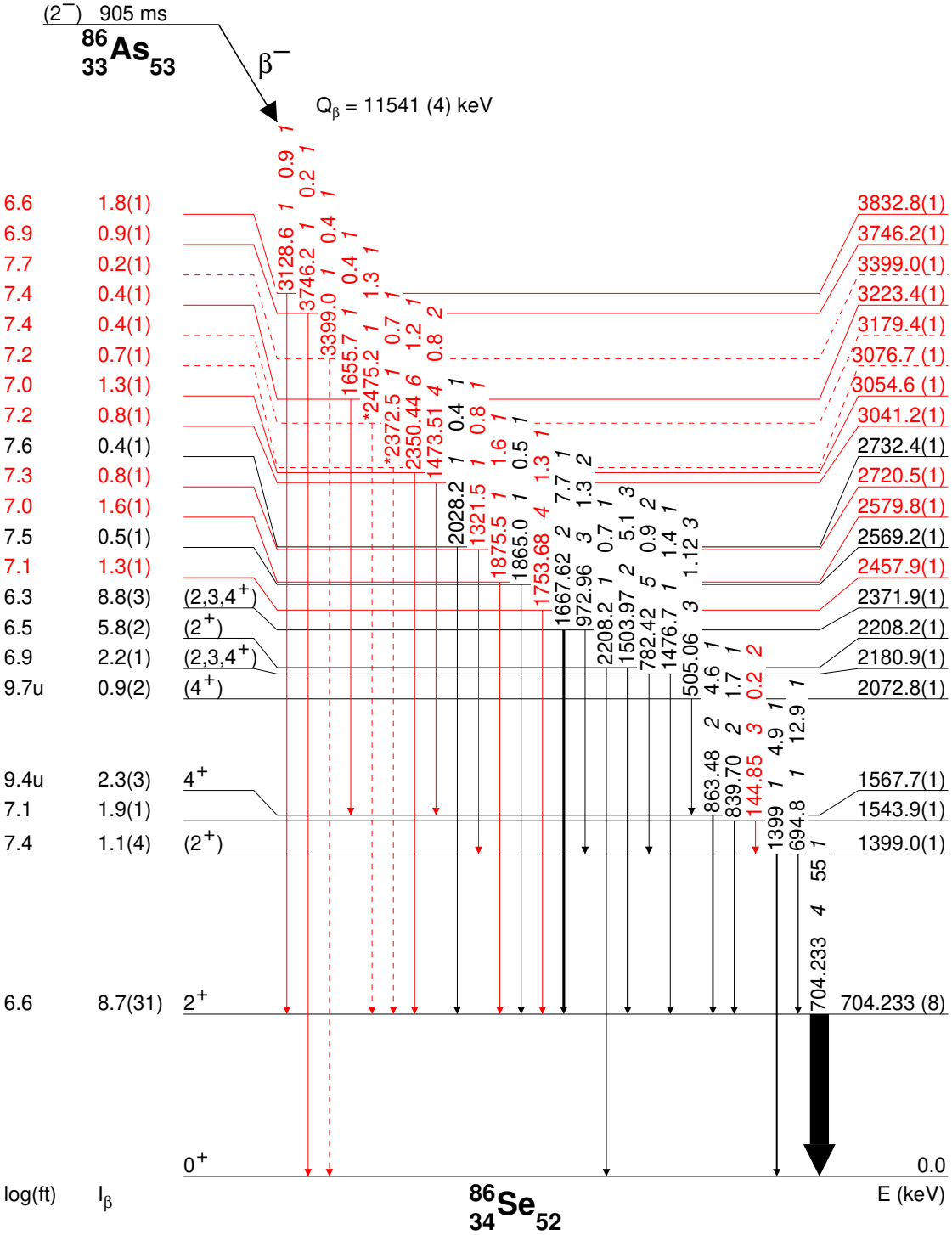

Figure 6.34: **(a)** Level scheme of ^{86}Se fed by the beta-decay of ^{86}As up to 3832.8 keV (to be continued on the next page). The width of the arrows is proportional to the absolute intensity of the transitions, noted next to the transition energy given above the arrows. The determined branching ratios I_β and log ft values are listed to the left of each state. Levels and transitions known from the previous studies are plotted in black, newly identified in red, and uncertain in red dashed lines. The log ft values marked with "u" were calculated with a uniqueness condition. The "*" is to mark the γ-ray transitions with tentative placement. Note: level scheme not to scale for visualization purposes.

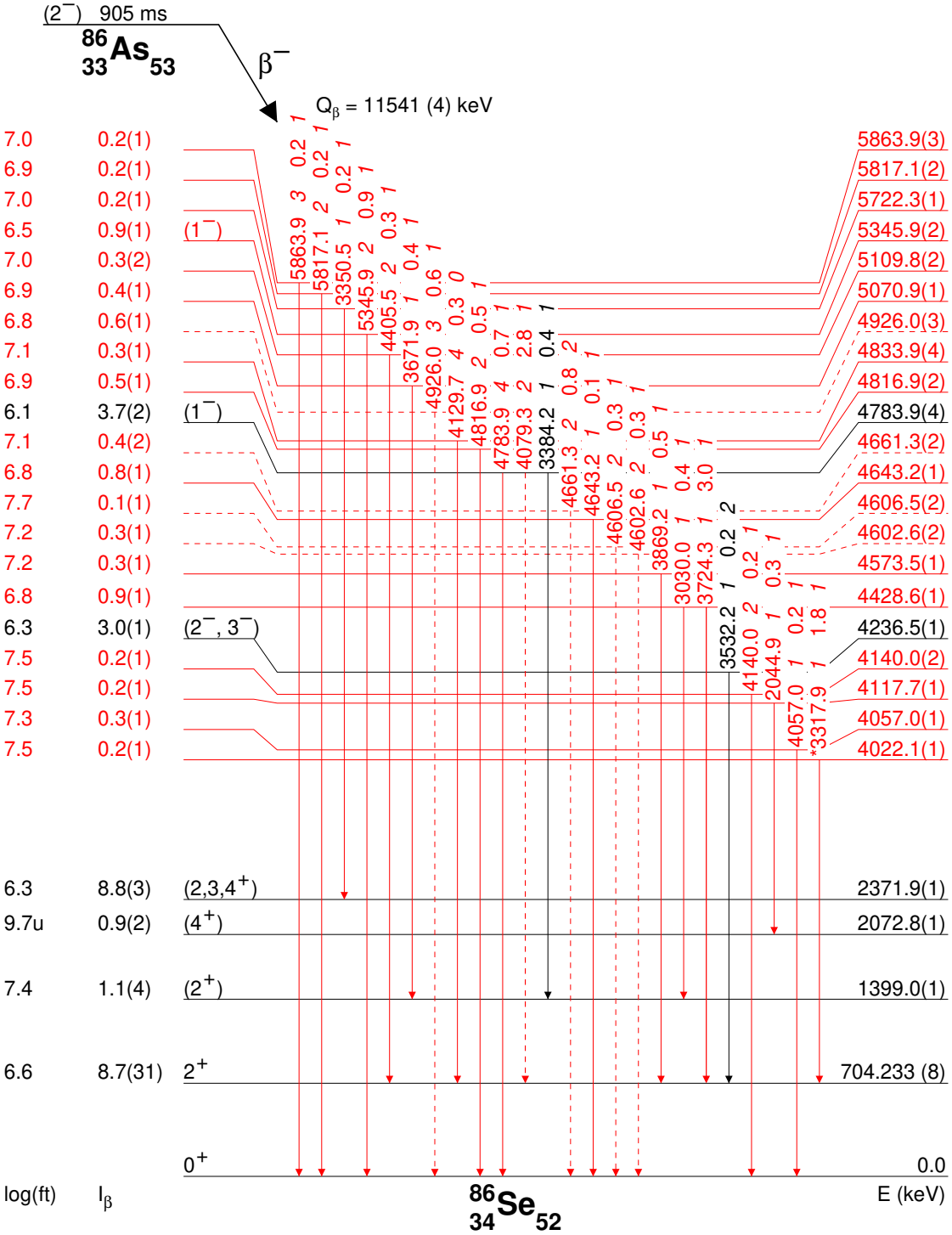

Figure 6.34: **(b)** Level scheme of ^{86}Se fed by the beta-decay of ^{86}As, de-excitations from levels at 4-6 MeV. The width of the arrows is proportional to the absolute intensity of the transitions, noted next to the transition energy given above the arrows. The determined branching ratios I_β and log ft values are listed to the left of each state. Levels and transitions known from the previous studies are plotted in black, newly identified in red, and tentative in red dashed lines. The log ft value marked with "u" was calculated with a uniqueness condition. The "*" is to mark the γ-ray transitions with uncertain placement. Note: level scheme not to scale for visualization purposes.

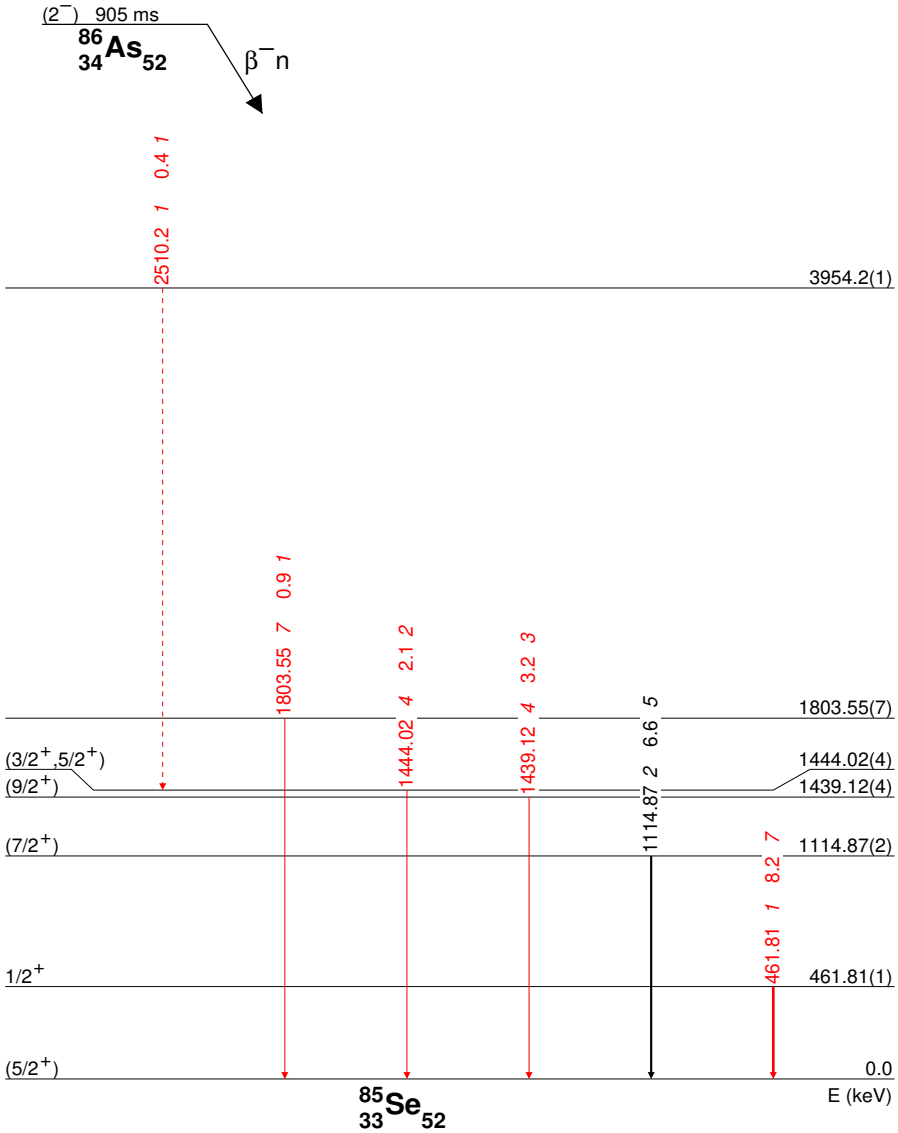

Figure 6.35: Level scheme of ^{85}Se fed by the beta-delayed neutron emission of ^{86}As. The width of the arrows is proportional to the relative intensity of the transitions, noted next to the transition energy given above the arrows. Levels and transitions known from the previous studies are plotted in black, newly identified in red, and tentative in red dashed lines. Note: level scheme not to scale for visualization purposes.

6.4 P_n measurement for ^{83}Ga and ^{86}As nuclei

When the Q_β value exceeds the neutron separation energy (S_n), or in other words, in the case of a positive $Q_{\beta n}$ value, the process of β-delayed neutron emission is energetically allowed, which means that the β-decay can be followed by neutron emission. This happens especially in very neutron-rich nuclei. The fraction of the total decay that proceeds via a neutron emission from the daughter nucleus is called the β-delayed neutron branching ratio P_n.

The following procedure was used to determine the P_n values for ^{83}Ga and ^{86}As[1] (in the description of the steps,^{83}Ga is used as an example, the treatment for ^{86}As was similar):

- Step 1: Calculate the number of ^{82}Ge nuclei that β-decayed to ^{82}As ($N_{decay}(^{82}\text{Ge})$) using an ^{82}As $\gamma-$ray with known absolute intensity.
- Step 2: Calculate the number of ^{82}Ge that did not have enough time to decay within the cycle ($N_{left}(^{82}\text{Ge})$) due to its relatively long half-life (compared to the measurement cycle time). Summing this number to the one we get from step 1 gives the total number of ^{82}Ge produced from the decay of ^{83}Ga ($N_{tot}(^{82}\text{Ge})$).
- Step 3: Calculate the number of ^{83}Ga produced in total ($N_{tot}(^{83}\text{Ga})$) using the Bateman equations (via the result from step 1). The P_n is calculated as the ratio between the total number of ^{82}Ge produced in the decay of ^{83}Ga and the number of implanted ^{83}Ga nuclei (Eq. (6.3)).

$$P_n = \frac{N_{tot}(^{82}Ge)}{N_{tot}(^{83}Ga)} \tag{6.3}$$

In order to calculate $N_{decay}(^{82}\text{Ge})$, the 1092-keV gamma-ray transition following the beta decay of ^{82}Ge to ^{82}As was used. There is no beta-delayed neutron branch in the beta decay of ^{82}Ge. The absolute intensity of the 1092 keV γ-ray peak is $I_{\gamma abs}$ = 77.4 % [112], therefore, the total number of ^{82}Ge that have decayed during the measurement cycle was :

$$N_{decay}(^{82}Ge) = \frac{N_\gamma}{I_{\gamma abs}} = \frac{5421638}{0.774} = 7004701(783612), \tag{6.4}$$

where N_γ is the number of counts of the 1092 keV line corrected for γ and β-efficiencies.

One can use the Bateman equations to estimate the number of decayed ^{82}Ge daughter nuclei as a function of the ^{83}Ga production rate, which can be used later on to deduce the number of ^{83}Ga implanted in total. The number of ^{82}Ge that decayed, is equal to ^{82}Ge $\beta-$decay activity on the tape A_d multiplied by the time interval

[1] For the case of ^{82}Ga, the existence of an isomeric state in the beta-n daughter, ^{81}Ge, makes it more difficult to estimate its beta-delayed neutron branching ratio. Therefore, it was not calculated in this work.

$$N_{decay}(^{82}Ge)(t) = A_d(t) \times \Delta t, \tag{6.5}$$

The activity on the tape can be expressed using the Bateman equations in terms of accumulation and decay cycle as follows

$$A_p(t) = \begin{cases} \phi(1 - e^{-\lambda_p t}) & t_0 < t \leq t_1 \\ \phi(1 - e^{-\lambda_p t_1})e^{-\lambda_p t} & t_1 < t < t_2 \end{cases} \tag{6.6}$$

$$A_d(t) = \begin{cases} \phi\left(\frac{\lambda_d}{\lambda_p - \lambda_d}(e^{-\lambda_p t} - e^{-\lambda_d t}) + (1 - e^{-\lambda_d t})\right) & t_0 < t \leq t_1 \\ A_p(t_1)\frac{\lambda_d}{\lambda_p - \lambda_d}(e^{-\lambda_p t} - e^{-\lambda_d t}) + A_d(t_1)e^{-\lambda_d t} & t_1 < t < t_2 \end{cases} \tag{6.7}$$

where A_p is the parent nucleus activity (^{83}Ga) and A_d is the activity of the daughters. ϕ represents ^{83}Ga production rate, λ_p is the parent's decay constant which is equal to $ln(2)/T_{\frac{1}{2}}(^{83}\text{Ga})$ (λ_d is the daughter's), t_0 seconds is the starting time of the cycle (+ 0.5 seconds of background collection), t_1 is the moment where the accumulation stops (2 seconds in this case) and t_2 is the cycle ending time (0.5 seconds background collection + 2 seconds accumulation time + 2 seconds decay time in total). The number of decayed ^{82}Ge was then calculated using Eqs. (6.5) and (6.7)

$$\begin{aligned} N_{decay}(^{82}Ge) &= \int_{t0}^{t1} \phi\left(\frac{\lambda_d}{\lambda_p - \lambda_d}(e^{-\lambda_p t} - e^{-\lambda_d t}) + (1 - e^{-\lambda_d t})\right) dt \\ &+ \int_{t1}^{t2} A_p(t_1)\frac{\lambda_d}{\lambda_p - \lambda_d}(e^{-\lambda_p t} - e^{-\lambda_d t}) + A_d(t_1)e^{-\lambda_d t}\, dt = 0.69 \times \phi, \end{aligned} \tag{6.8}$$

with t_0=0.5, t_1=2.5 and t_2=4.5 s.

Moving now to step 2, the decay part of our cycle for the case of ^{83}Ga was 2 seconds, which is not enough time for the ^{82}Ge to decay out completely, due to the fact that it has a longer $\beta-$decay half-life (4.56 (26) s [45]).The number of ^{82}Ge ions that will not have the time to decay out can be extracted from the simple decay equation

$$N_{left}(^{82}Ge) = N(^{82}Ge) \times \left(\frac{1}{2}\right)^{\frac{t}{T_{1/2}}}, \tag{6.9}$$

or

$$N_{left}(^{82}Ge) = \int_{t0}^{t2} \left(\frac{1}{2}\right)^{\frac{t2-t}{T_{1/2}}} \times A_d(t) \times \Delta t, \tag{6.10}$$

where $T_{1/2}$ is the $\beta-$decay half-life of ^{82}Ge. Substituting the activity Eq. (6.7) in Eq. (6.10) we get

$$N_{left}(^{82}Ge) = 1.039 \times \phi. \tag{6.11}$$

From Eq. (6.8) and (6.11) we can deduce that the total number of produced ^{82}Ge is equal to 1.73 ϕ, which means that about 60 % of the created ^{82}Ge did not have the opportunity to decay. This obtained factor can be now used to correct the total counts of the 1092 keV $\gamma-$ray transition in the ^{82}Ge $\beta-$decay channel

$N_{decay}(^{82}\text{Ge})$ (Eq. (6.4)) to extract the correct ^{82}Ge number of counts produced by the ^{83}Ga $\beta n-$decay

$$N_{tot}(^{82}Ge) = 1.60 \times N_{decay}(^{82}Ge) = 11207522(1259724). \tag{6.12}$$

The third step consists of calculating the number of ^{83}Ga produced in total, which can be extracted from the Bateman equations straight away since ^{83}Ga has a short half-life (308 ms) which makes the cycle decay time more than enough for it to decay out completely. Therefore, the total number of produced ^{83}Ga is then

$$N_{tot}(^{83}Ga)(t) = A_p(t) \times \Delta t, \tag{6.13}$$

Replacing A_p by the corresponding values from Eq. (6.6) and integrating over the cycle's time we get

$$N_{tot}(^{83}Ga) = \phi \left(\int_{t0}^{t1} (1 - e^{-\lambda_p t})\, dt + \int_{t1}^{t2} (e^{-\lambda_p t_1} - 1) e^{-\lambda_p t}\, dt \right) = 2.295 \times \phi, \tag{6.14}$$

with t_0=0.5, t_1=2.5 and t_2=4.5 seconds. Now to calculate the exact number of counts of ^{83}Ga we need to find ϕ, which can be deduced from Eq. (6.4) and (6.8).

$$\begin{aligned} \int_{t0}^{t2} N_{decay}(^{82}Ge) \times \lambda_d\, dt &= \int_{t0}^{t2} A_d(t)\, dt \\ 7004701 \times \frac{ln(2)}{4.56}(t_2 - t_0) &= 0.69 \times \phi, \end{aligned} \tag{6.15}$$

From Eq. (6.15) we deduce that ϕ = 6180619 (775856). Using this value in Eq. (6.14) we can deduce that the number of counts of ^{83}Ga produced in total is $N_{tot}(^{83}\text{Ga})$=14184519 (1782539). Finally, we can calculate the neutron emission probability, P_n value, using the ratio shown in Eq. (6.3),

$$Pn = \frac{N_{tot}(^{82}Ge)}{N_{tot}(^{83}Ga)} = \frac{11207522\,(1259724)}{14184519\,(1782539)} = 0.79\,(0.13) = 79\,(13)\%. \tag{6.16}$$

This value falls between the published ^{83}Ga P_n values measured using the neutron time-of-flight technique in Refs. [113], [55] and [71] (see Table 6.9).

The ^{86}As beta-delayed neutron branching ratio was calculated using the same procedure, and the obtained P_n value was 35 (9) %. The P_n value of ^{86}As has been measured at IGISOL using the BELEN detector setup to be P_n=35.5 (6) % [73]. Thus, there is an excellent agreement between this work and [73].

Table 6.9: Comparison between the beta-delayed neutron branching ratios P_n calculated in this work and those from the literature.

Nucleus	^{83}Ga	^{86}As
P_n (%) from this work	79 (13)	35 (9)
P_n (%) from literature	85(4) [71] , 62.8 (25) [113], 56 (7)[55]	35.5 (6) [73]

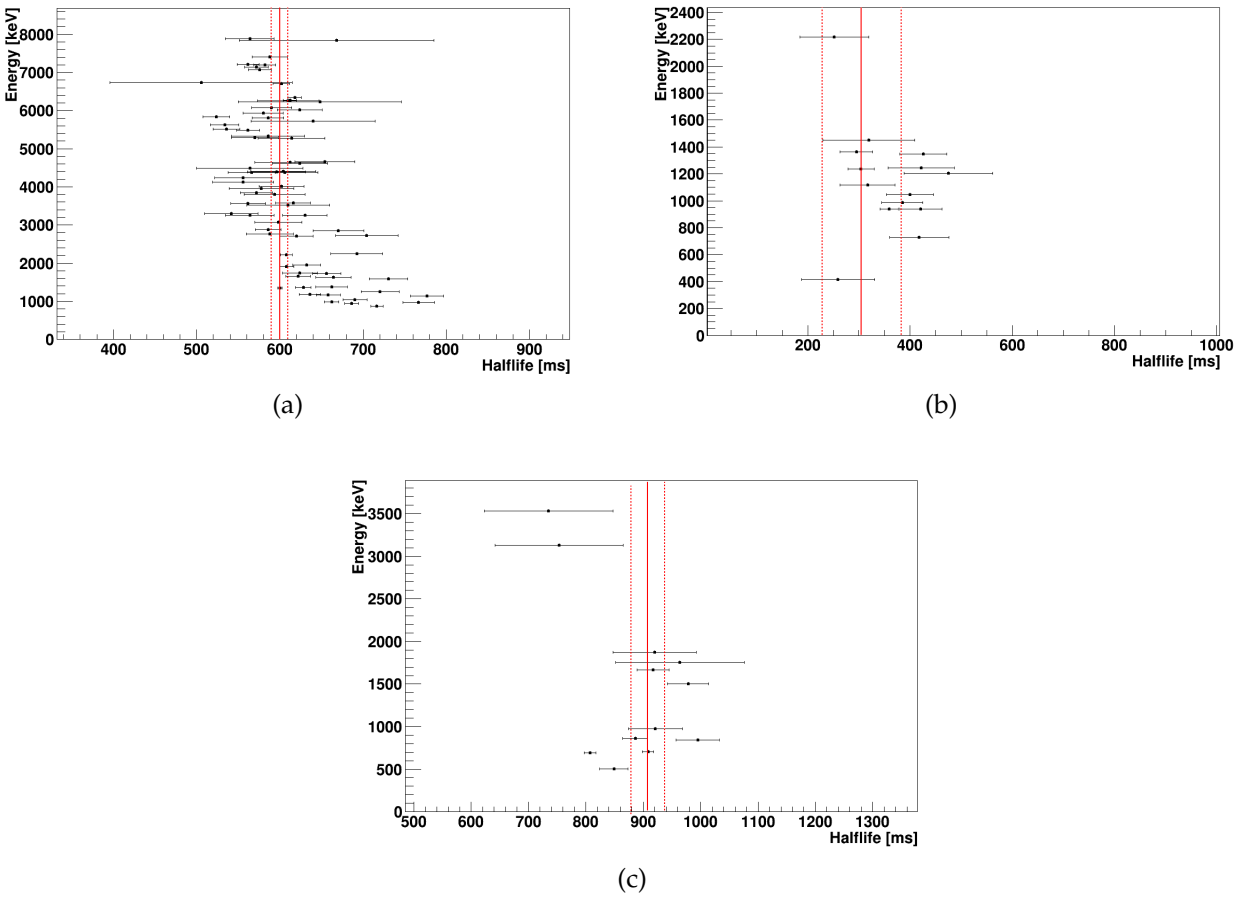

Figure 6.36: Measured half-lives of all γ-ray transitions associated with the beta decays of ^{82}Ga (a), ^{83}Ga (b) and ^{86}As (c). The red lines represent the half-lives of the strongest γ-ray transition in each nucleus $\pm$ 3 σ (dashed lines).

6.5 Half-life measurements of ^{83,82}Ga and ^{86}As

The decay of the parent nucleus feeds the excited states in its daughter that promptly decay by γ-ray emission. Thus, the excited states of the daughter nucleus have an apparent lifetime equal to the β lifetime of the parent nucleus. Using the $\beta - \gamma - T$ matrices, similar to the one in Fig. 5.13, the decay curves of different nuclei can be obtained by setting gates centered on the most intense gamma-ray transitions for each nucleus. The Bateman equations already mentioned (Eqs. 6.6 and 6.7) were used to fit the time behavior of each gamma transition to get the lifetime. Most half-lives of the beta-delayed gamma transitions observed in ^{83,82}Ge and ^{86}Se were measured and used to validate the attribution of these transitions to the corresponding decay of the parent nucleus. A selected set of γ-ray transitions and their fitted half-lives is shown in Fig. 6.36.

As illustrated in Fig. 6.36, there is a clear trend in the $T_{1/2}$ values. Specifically, we observed several sigma deviations from the $T_{1/2}$ determined from the low-energy γ-ray transitions. This is interpreted as being due to the Compton background coming from beta-decay descendants that was not subtracted. As a result, we decided to use the more advanced Markov chain Monte Carlo method

[114] for the most intense peaks of each nucleus. Using this method, we determined the half-lives by fitting the number of events associated with the selected gamma-ray transitions over time (see Fig. 6.37). A detailed description of the fitting approach can be found in Ref. [114]. The model used is the exponential decay model, $A(t) = Ae^{\frac{-ln(2)}{T_{1/2}}t}$, and the likelihood function was constructed by assuming that the counts in each bin follow a Poisson distribution.

For clarity, we have tabulated the selected γ-ray transitions, their respective fitting ranges, and the half-lives obtained from both evaluated data and our work in Table 6.10.

Table 6.10: The half-lives of ^{82}Ga , ^{83}Ga and ^{86}As obtained in this work compared to the evaluated half-life values taken from [45].

Nucleus	^{82}Ga	^{83}Ga	^{86}As
beta-delayed γ-ray transition (keV)	1348.10	248.76	704.23
Fitting range (s)	3.5 to 6	2.5 to 4.5	4 to 9
$T_{1/2}$ (ms) from this work	608 (7)	314 (7)	905^{+29}_{-26}
$T_{1/2}$ (ms) from evaluated data	599 (2)	308 (10)	945 (8)

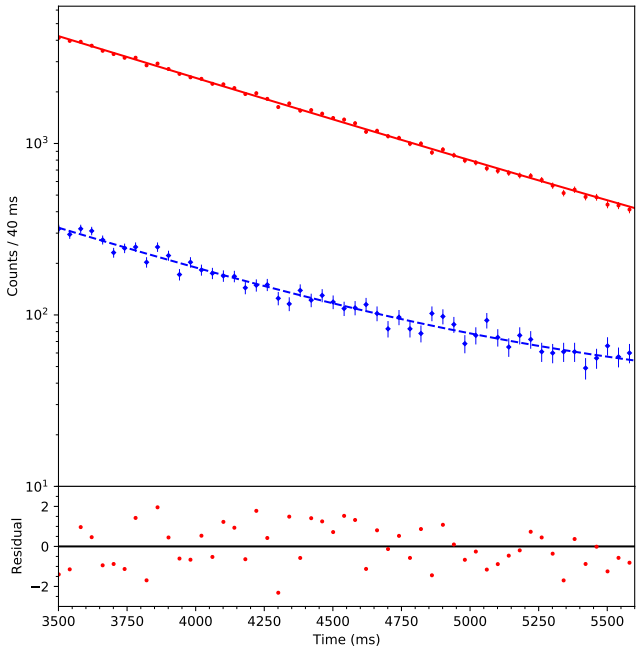

(a) ^{82}Ga

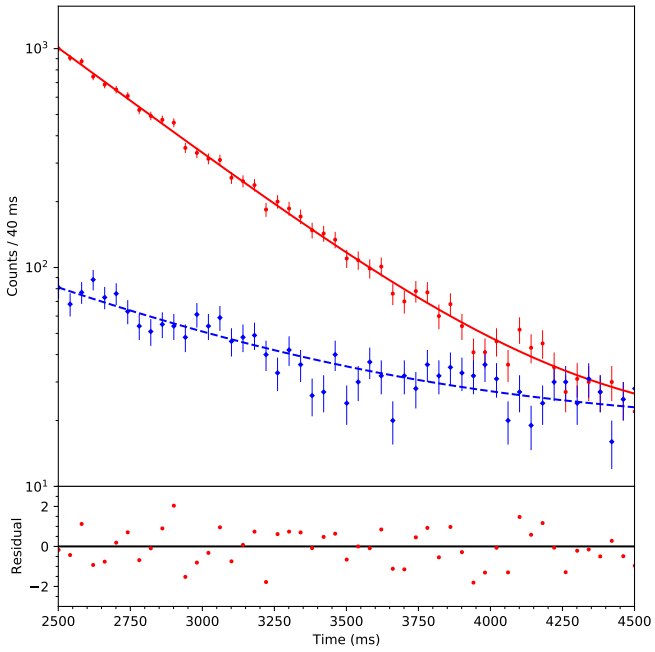

(b) ^{83}Ga

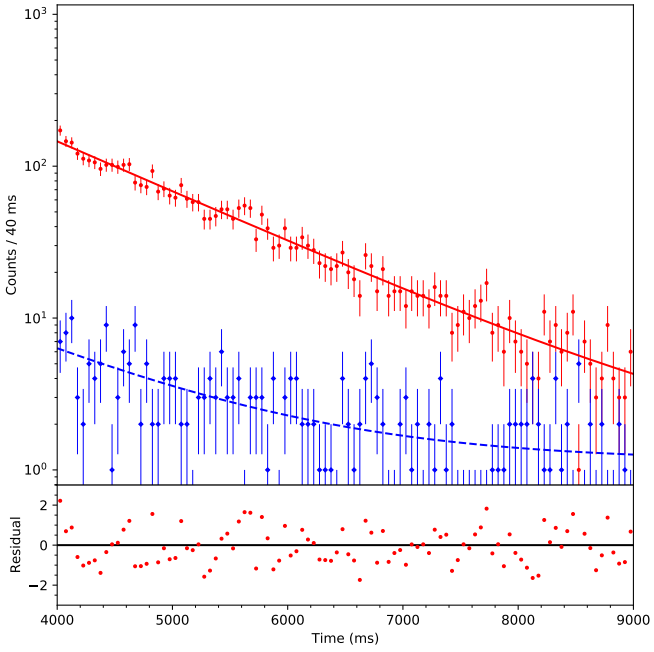

(c) ^{86}As

Figure 6.37: The red curves represent the time behavior of the 1348.1 keV (a), 248.76 keV (b) and 704.23 keV (c) γ-ray transitions as a function of time after the β-signal. The blue curves represent the background events that were subtracted to get the final half-lives presented in Table 6.10.

7 GLOBAL DISCUSSION

In this chapter, we will review the significant results of the work presented in this thesis and, where possible, present a comparison with calculations performed in shell-Model or QRPA formalisms.

7.1 Cumulative β-decay intensity of ^{82}Ga

Several new states were identified in ^{82}Ge, with many of them located at energies higher than 4 MeV and up to 7.9 MeV. The γ-decay spectrum was constructed almost exclusively using high-resolution HPGe detectors. Even if the efficiency is dropping dramatically above a few MeV in such detectors, they are still competitive in measuring high-energy γ-rays in β-decay experiments due to a very good peak-to-background ratio. Although the pandemonium effect [115] cannot be totally excluded, here the focus is on the β-decay strength at and around neutron threshold in very neutron-rich nuclei and how it can be enhanced by particular nuclear structure (see Ref. [71] and references therein).
In Fig. 7.1, the previously measured cumulative ΣI_β distribution for the β-decay of ^{82}Ga is compared to the present work. The total β-strength is comparable with what was previously measured, but its distribution is shifted towards higher energies. The most striking difference can be seen above 6 MeV, where a significant increase in the cumulative distribution relative to the evaluated data is observed.

logft values were calculated for all the measured β-transitions (see Fig. 6.30). States at low energy in ^{82}Ge are mainly populated through forbidden transitions, as they have logft values higher than 6.5. At higher energies, several states have lower logft values. From logft values, one can calculate the Gamow-Teller strength B(GT). Its cumulative distribution in ^{82}Ge, presented in Fig. 7.2, was calculated. The same steep increase as in cumulative ΣI_β can be observed after 6 MeV, with the same structure: one step around 6 MeV and a second step around 7 MeV.

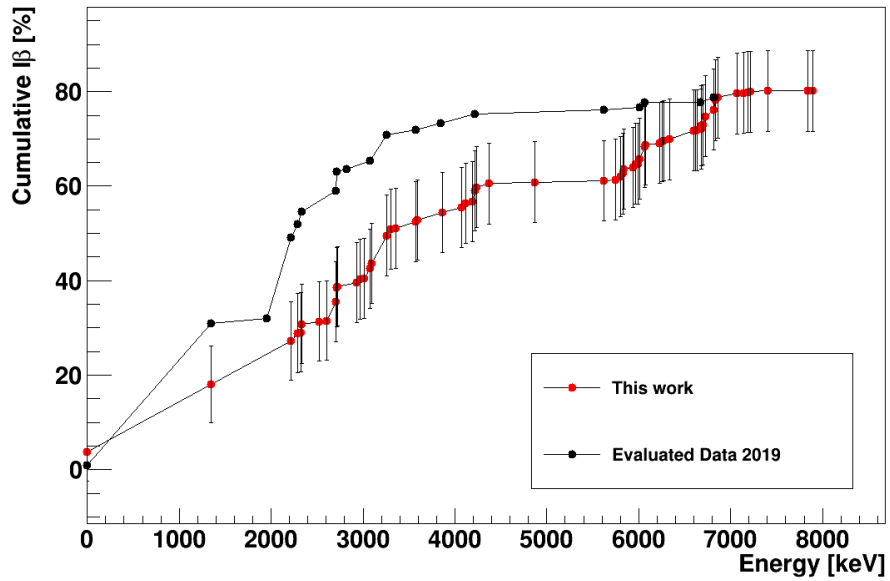

Figure 7.1: Cumulative I_β distribution from Ref. [107] and from present work as a function of the excitation energy in ^{82}Ge .

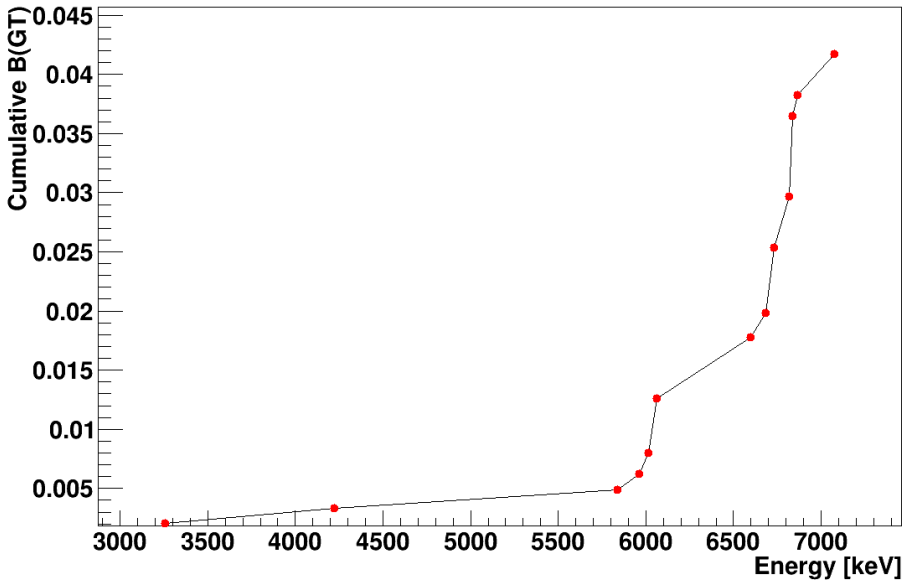

Figure 7.2: Cumulative B(GT) distribution from present work as a function of the excitation energy in ^{82}Ge. Only allowed transitions that have log ft < 6.5 are considered (see Ref. [12])

The ground-state spin and parity of ^{82}Ga was tentatively assigned as $I^\pi=2^-$ [45]. In this case, allowed β-transitions should populate states in ^{82}Ge with spins 1, 2, or 3 and negative parities. Thus, the states above 6 MeV with log ft<6.5 have negative parities and a spin lower or equal to 3. Among these states, two groups [6.2−6.4] MeV and [7.1−7.9] MeV decay directly to the 0^+ ground state. With the experimental setup used in this work, the γ-ray multipolarity could not be determined, at least for transitions to the ground state of the daughter

nucleus. However, it is reasonable to assume that the states falling in these two groups are 1^- states. The single-particle transition probabilities for electromagnetic transitions, B(σL), see Eq. 2.13, drop by about three orders of magnitude for electric transitions from L to L+1 for the same energy, and the electric transitions are typically around 30 times stronger than magnetic transitions of the same multipolarity. In order to compete with neutron emission or transitions to other lower-lying states, the transitions leading to the ground state have to be fast. Therefore, E1 is the most likely multipolarity for these transitions.

The populated states above S_n were not included in the B(GT) distribution as the log(ft) is not compatible with our rule of defining an allowed transition. This is likely due to missed feeding to these states as they can also decay by neutron emission.

In the following, the calculated B(GT) and B(E1) distributions obtained with an HFB+(pn)QRPA formalism [30, 116] are reported. The interaction used was Gogny D1M, and the same interaction was used to calculate the HFB ground state and the QRPA excited states. This QRPA formalism can be applied for spherical and axially deformed nuclei and can calculate not only proton-proton (pp) or neutron-neutron (nn) quasi-particles (qp), but also proton-neutron (pn) qp allowing for the calculation of B(GT) strength.

The resulting cumulative B(GT) strength obtained from the calculations is presented in Fig. 7.3, where the experimental B(GT) was superimposed on the calculated B(GT) by shifting the energy scale such that the steep increase in both strength distributions is aligned. The distributions were calculated for a ^{82}Ga ground-state spin of both 2 and 3. The shapes of the distributions are very similar, but there is a slightly better agreement with the data when considering the spin to be 2. The good agreement between calculations and experiment allows us to suppose that the HFB states and the pnQRPA calculations using D1M Gogny interaction give good results for this region of nuclei. This should also be the case for the QRPA calculations performed within the same framework for the excitation spectrum of ^{82}Ge.

7.2 Dipole strength distribution in ^{82}Ge

The electric dipole distribution in ^{82}Ge was thus calculated and is presented in Fig. 7.4. The spectrum was corrected for the spurious center-of-mass motion even though these spurious states hardly mix with the calculated 1^- states. It can be immediately observed that the calculated spectrum is several MeV higher in energy than the states that were tentatively assigned to be 1^- based on the measurement. It is known that one usually needs to couple the QRPA states with collective states, like phonon-excitations (see, for example, Ref. [52] and references therein).

To test the isoscalar−isovector composition of the calculated electric dipole

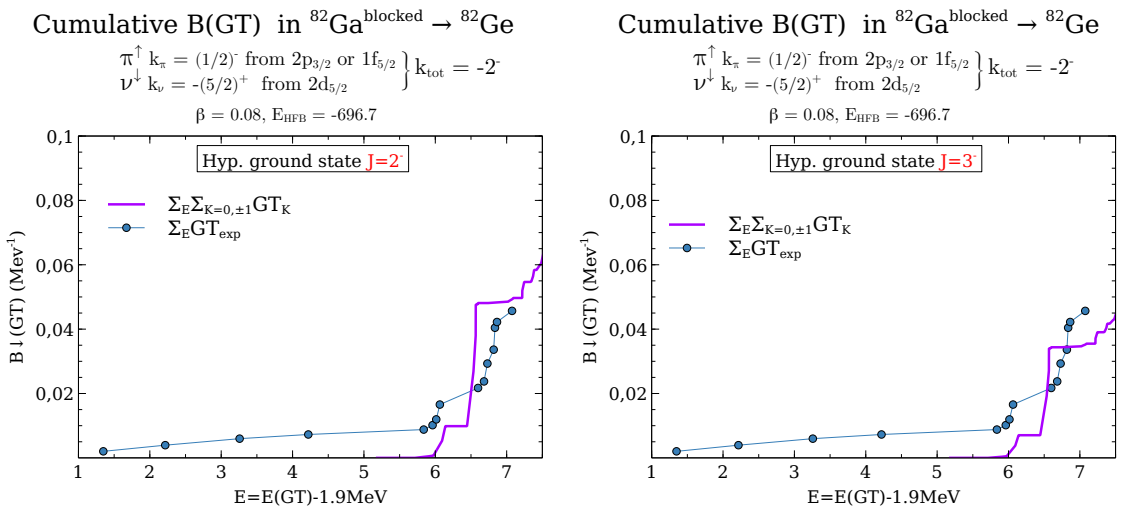

Figure 7.3: Calculated and experimental cumulative B(GT) distributions considering the spin of ^{82}Ga ground state to be 2 (left) and 3 (right). Calculations are from [117].

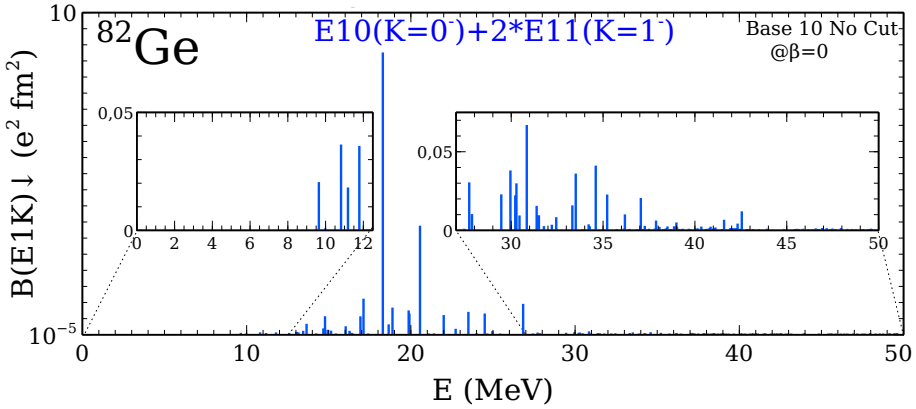

Figure 7.4: Calculated isovector B(E1) strength distribution [118], using the formalism described in Ref. [31].

states, the isoscalar dipole operator ($r^3Y_{10}(r)$), was used. The result is presented in Fig. 7.5. By comparing the two figures, one can see that the low-lying dipole strength has an important isoscalar character, and this can be seen by comparing the ratios between the strength around 17 MeV (where the GDR is situated and that has an isovector character) and below 11 MeV (where these low lying states are calculated) both for B(E1) and B(IS1) distributions.

In order to assign a PDR-like behavior to a nuclear state, one needs to fulfill the following conditions: i. the neutron transition densities should show an enhancement at the surface of the nucleus, or the proton and neutron densities are out of phase, and ii. the state should not carry more than a few percent of the total electric dipole strength. All the states below 11 MeV carry a very small percentage of the total dipole strength. Concerning the transition densities behavior, only two

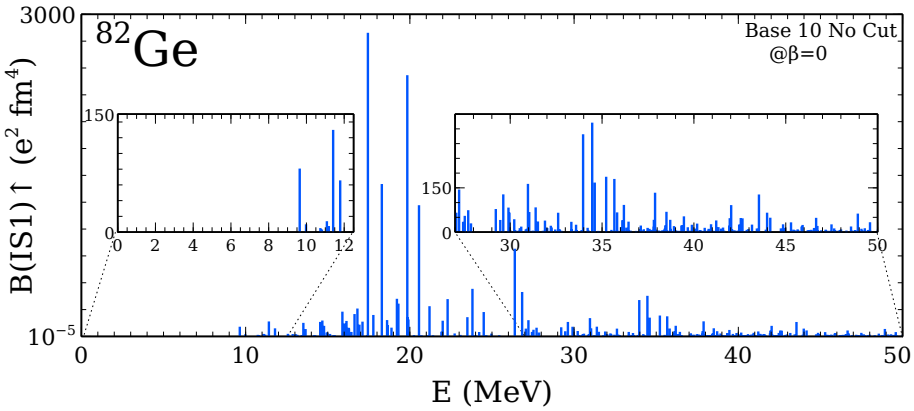

Figure 7.5: Calculated isoscalar B(IS1) strength distribution [118], using the formalism described in Ref. [31].

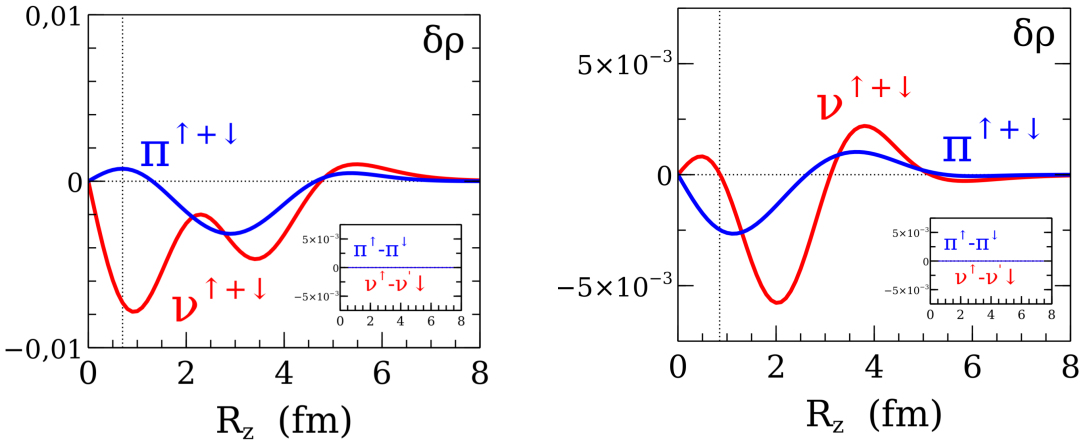

Figure 7.6: Transition densities calculated for the 9.6 MeV (left) and 10.8 MeV (right) states. From [118].

of them, at 9.6 MeV and 10.8 MeV, approach the PDR description (Fig. 7.6), but their evolution inside the nucleus is complex.

As said earlier, the QRPA states overestimate the energies and the strength of the calculated states. In order to see the effect of the coupling with phonon states, the E1 spectrum of ^{82}Ge was calculated using relativistic QRPA (RQRPA) and relativistic quasiparticle time-blocking approximation (RQTBA), with the NL3 interaction (see Ref. [119] and references therein for the details of the calculations). These calculations do not include the deformation of nuclei, but this should not be a problem as ^{82}Ge is calculated to have a very small β-deformation. The results are presented in Fig. 7.7. The transition densities for the lowest calculated state using RQTBA (multiplied by r^2) show a very nice PDR-like behavior (see Fig. 7.8).

To conclude, the observed experimental states between 6 and 8 MeV are compatible with a spin/parity of 1^-. Axially deformed QRPA calculations for B(GT) show nice agreement with the experimental B(GT) spectrum obtained from the ex-

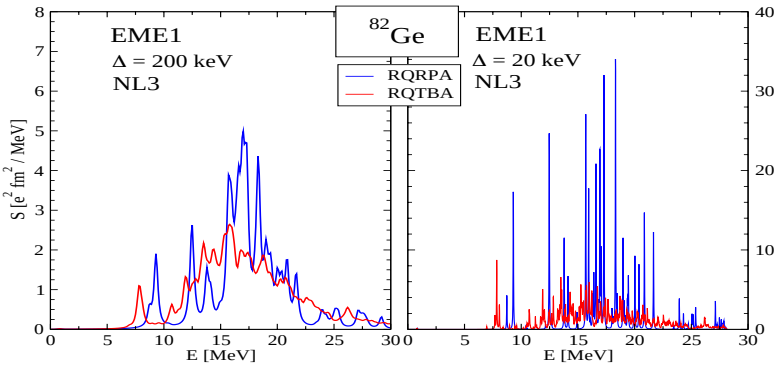

Figure 7.7: B(E1) distribution. The RQRPA results are those obtained within the relativistic quasiparticle random-phase approximation, confined by two-quasiparticle (2q) configurations. RQTBA, the relativistic quasiparticle time-blocking approximation, includes the major fragmentation mechanism via the 2q+phonon configurations (see Ref. [119]). Each calculation (left and right figures) was done for two values of the smearing parameter Δ: Δ = 20 keV (fine resolution) and 200 keV (low resolution). Figure courtesy of Elena Litvinova.

periment, but the B(E1) strength distribution is several MeV higher than what was observed experimentally. In addition, the lowest states calculated within QRPA formalism described in [30] have transition density distributions only slightly compatible with PDR. Calculations, which take into account coupling of the quasiparticle RPA states with phonon excitations (RQTBA), provide a more fragmented B(E1) distribution and are shifted to lower energies and closer to what we observe to be 1^- states, with the lowest state having a nice PDR-like transition density distributions.

7.3 Shell-model predictions of the states in ^{86}Se

To obtain more insight into the observed levels in ^{86}Se, shell-model calculations were performed in a large valence space comprising the ($1f_{5/2}$, $2p_{3/2}$, $2p_{1/2}$, $1g_{9/2}$) orbitals for protons and the ($2d_{5/2}$, $3s_{1/2}$, $1g_{7/2}$, $2d_{3/2}$,$1h_{11/2}$) orbitals for neutrons, outside the ^{78}Ni core. The effective interaction utilized in this study was based on the interaction described in Refs. [120, 121] although the proton-proton part of the interaction was updated to reproduce the available data in N = 50 isotones [122]. These same calculations were used to compare with the experimental spectrum from [77]. In Ref. [77], few selected states were used for the comparison. Figure 7.9 shows the total calculated spectrum up to 7.2 MeV with the inclusion of newly calculated 1^- states. Given the valence space used for the calculations, negative-

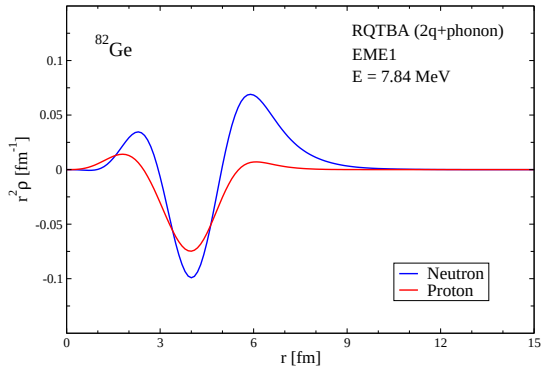

Figure 7.8: Transition densities for the low-lying state at 7.8 MeV calculated within the RQTBA framework. Figure courtesy of Elena Litvinova.

parity states necessarily include one proton excitation into the $\pi g_{9/2}$ orbital.

Based on the β-delayed gamma-ray transitions, the β decay of ^{86}As feeds states at 4236.5 keV and 4783.9 keV more strongly than the other states above 4 MeV. The 4236.5 keV is given a tentative spin assignment of $(2^-, 3^-)$ in this work, in agreement with the shell-model prediction of a 3^- state at 4333.6 keV. This state has a very fragmented composition according to the shell-model calculations. It dominantly consists of seniority-4 configurations which make up 38.1% of all configurations.

The 4783.9 keV state has been tentatively assigned as a (1^-) state in this work. This is also supported by the shell-model calculations, predicting 1^- states at 4521.4 keV and 4631.7 keV. The state at 5345.9 (2) keV was also tentatively assigned as (1^-) in this work based on its low log ft value and decay to the 0^+ ground state. The shell-model prediction for the 1^- state at 5329.25 keV fits very well with this state. The 1^- states typically have a leading configuration of $(\pi\ 1f_{5/2})^4(\pi\ 2p_{3/2})^1(\pi\ 1g_{9/2})^1(\nu\ 2d_{5/2})^2$, with a one broken proton pair and one broken neutron pair.

For the other states, the experimental spin-parities could not be constrained and therefore, the comparisons to the shell-model calculations were not feasible.

7.4 Cumulative β-decay intensity of ^{86}As

In Fig. 7.10, the previously measured cumulative ΣI_β distribution for the β-decay of ^{86}As is compared to the present work. As for the case of ^{82}Ga β-decay, the total strength does not change, but the distribution shifts towards higher energies.

The cumulative B(GT) strength for the beta decay of ^{86}As (see Fig. 7.11) was determined using the same shell-model framework as for the level scheme of ^{86}Se. The calculation was done for the beta decay of a 2^- state because the experimental

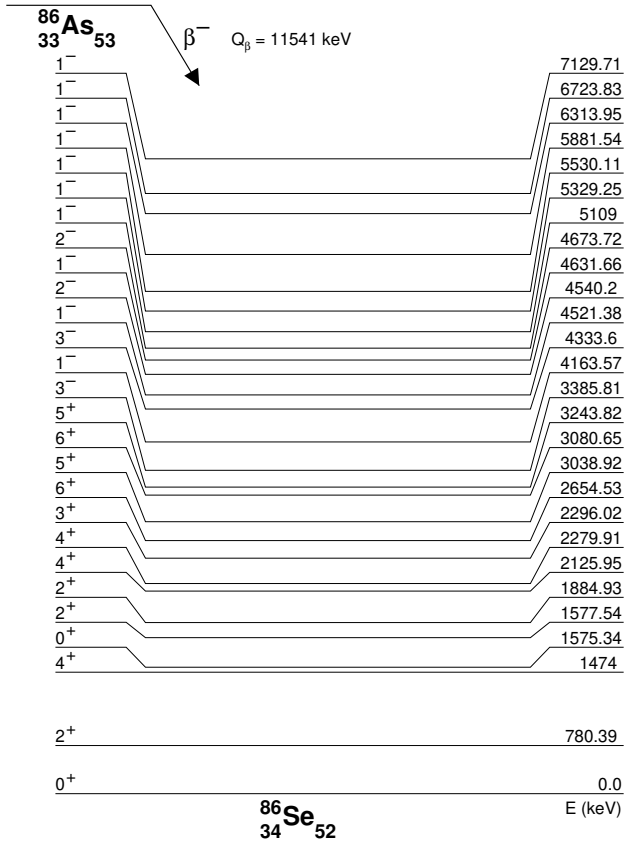

Figure 7.9: Level scheme of ^{86}Se based on the shell-model calculations.

β-n spectrum fixed this spin-parity.

Using the same rule to select allowed transitions from the experimental spectrum as for ^{82}Ga decay, three states were identified above 4 MeV: 4236.5 keV, 4783.9 keV and 5345.9 keV. The associated cumulative values are also reported in Fig. 7.11. A quantitative and even qualitative comparison is hard to do. One should keep in mind that in order to connect the shell-model orbitals by a GT operator, these orbitals should belong to the same major shell and have the same orbital angular momentum, l. Because the fpg shell is closed in neutrons, the GT operator can only connect $\nu d_{5/2}$ with the proton $\pi d_{5/2}$ orbital.

7.5 Implications for the astrophysical r process

The region near ^{78}Ni is of great interest for the r process as the first abundance peak is situated at $A \approx 80$. The recent detection of the GW170817 [123, 124] neutron-star merger (NSM) has confirmed that the r process occurs in such compact binary mergers, with the observed kilonova [125] changing its color from blue to red, indicating the creation of heavier elements across a broad mass region up to at least lanthanides. Additionally, the observation of strontium absorption lines [126] in the kilonova spectrum demonstrates the production of elements in the $A \approx 80 - 90$

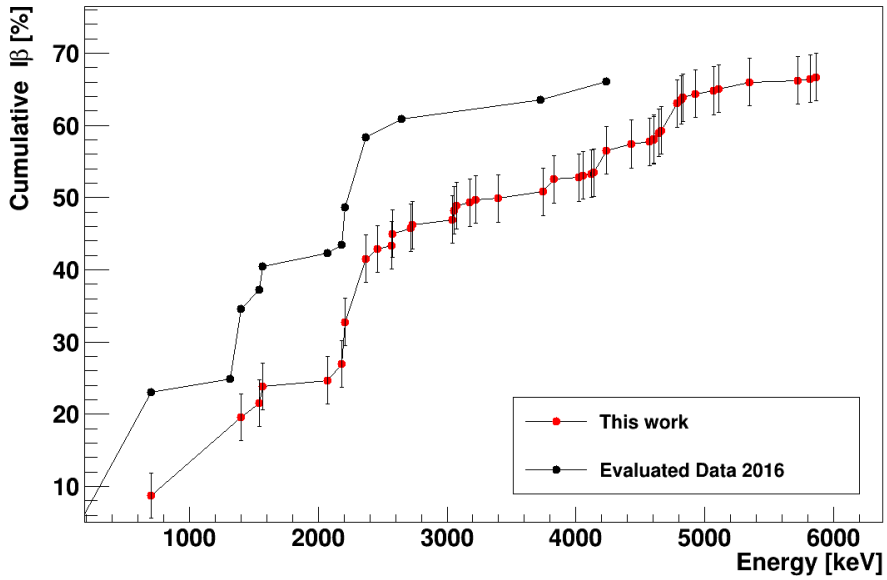

Figure 7.10: Cumulated I_β distribution from Ref. [45] in blue and from present work as a function of the excitation energy in ^{86}Se.

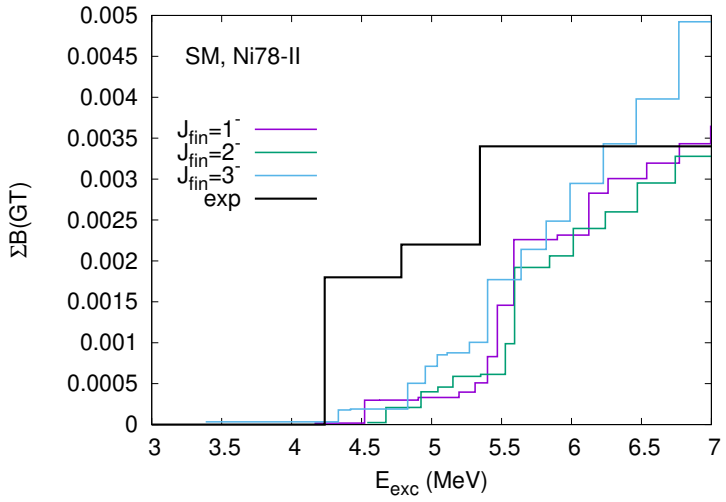

Figure 7.11: Cumulative B(GT) values calculated and experimental for the decay of ^{86}As versus excitation energy of the final states in ^{86}Se. Figure courtesy of Kamila Sieja.

range, making this a significant region to study the impact of nuclear properties on the final abundances. *r*-process reaction network calculations for a narrow range of entropy and electron fraction Y_e conditions have shown remarkable agreement with the solar *r*-process abundances in the first *r*-process abundance peak region at $A \approx 80$ [127], allowing for a sensitive study of the impact of nuclear properties on the final abundances.

7.5.1 Studied beta decays and the *r* process

As discussed in Section 3.1, beta-decay half-lives and beta-delayed neutron branching ratios P_n are important inputs for the *r*-process calculations. In this work, the determined beta-decay half-lives of ^{82,83}Ga and ^{86}As are in agreement with the previous literature values. Since the studied nuclei are still rather close to stability and the competition between the beta decays and neutron captures does not play a central role, the newly measured half-lives do not significantly change the final abundances of the process. However, the beta-delayed neutron branching ratios can drastically alter the local *r*-process abundance peak structure by shifting abundances from a mass number A to a mass number $A-1$ (or $A-2$ in the case of beta-delayed two-neutron emission) when *r*-process material is decaying back to stability [128].

In this thesis, the β-delayed neutron branching ratio P_n was determined for ^{83}Ga and ^{86}As. For ^{86}As, the result is in good agreement with the more precise P_n measurement performed with the BELEN detector at IGISOL [73] and therefore the impact on the *r* process was not studied. For ^{83}Ga, the P_n values reported in the literature vary a lot, from 56(7)% [55] and 62.5(25)% [113] to 85(4)% [60]. The new P_n value determined in this thesis, P_n =79(13)%, confirms that the beta-delayed neutron branching is large for this beta decay. The impact of this new P_n value on the *r*-process abundances in the first *r*-process peak region was studied using the nuclear reaction network code *GSINet*. A parameterized thermodynamic evolution assuming a free homologous expansion according to [129] was used for astrophysical conditions with an electron fraction $0.30 \leq Y_e \leq 0.39$ and entropy $S = 10k_b$/baryon. These moderately neutron-rich conditions lead to a negligible amount of neutron captures at late times when the material is decaying to stability and beta-decays dominate the material flow.

Figure 7.12 shows the solar *r*-process abundances from Ref. [130], together with the results from the *r*-process calculations. The abundances Y are determined as $Y = X/A$, where X is the mass fraction, and are normalized to 10^6 silicon atoms. The calculations were performed using the P_n value from this work, $P_n = 79(13)\%$, and the values reported by Winger et al. [113] ($P_n = 62.5(25)\%$) and Madurga et al. [55] ($P_n = 56(7)\%$) . Otherwise, the nuclear data used for the *r*-process calculations were kept the same in all calculations. From the lower panel of Fig. 7.12, one can clearly see that the larger beta-delayed neutron branching shifts material from $A = 83$ to $A = 82$ and leads to changes of up to $\approx 25\%$ in the abundances at A=83 depending on which P_n value is adopted. The P_n value determined in this thesis is in agreement with the value reported in Ref. [60] ($P_n = 85(4)\%$) and confirms that the beta-delayed neutron branching is close to 80 % for ^{83}Ga. It also reproduced the observed *r*-process pattern better in the region $A = 82-84$, with a steeper dip in the abundances from $A = 84$ to $A = 83$.

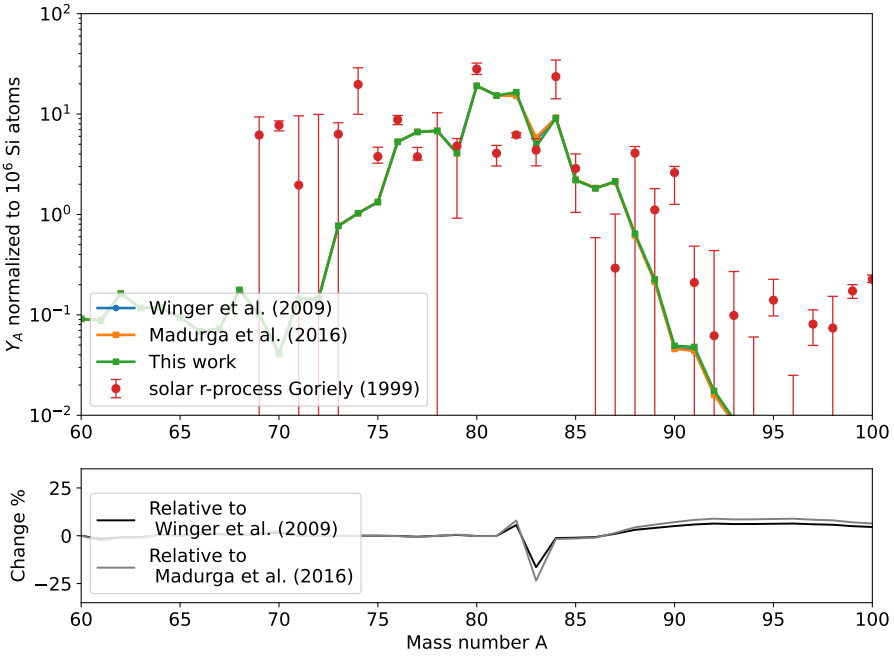

Figure 7.12: Top: The solar *r*-process abundances in the first *r* process abundance peak region (red data points) normalized to 10^6 silicon atoms, adopted from Ref. [130], in comparison with the calculated *r*-process abundances adopting the P_n value of ^{83}Ga from this work (green line), from Winger et al. [113] (blue line) and Madurga et al. [55] (orange line). The abundances have been averaged for $0.37 \leq Y_e \leq 0.39$. Bottom: Change, in %, between the *r*-process abundances calculated using the P_n value from this work and the literature values from Winger et al. [113] (black line) and Madurga et al. [55] (grey line). Figure courtesy of Stylianos Nikas.

7.5.2 Enhanced $E1$ strength above the neutron emission threshold and the *r* process

This thesis aimed at observing gamma-ray transitions from highly excited states in ^{82,83}Ge and ^{86}Se fed via beta decays of ^{82,83}Ga and ^{86}As, respectively, in order to explore the PDRs and enhanced $E1$ strength above at around the neutron separation energy. In ^{82}Ge, gamma-ray transitions from states above the neutron separation energy ($S_n = 7195(3)$ keV [42]), located at 7214.1 keV, 7410.1 keV, 7839.2 keV and 7890.75 keV, to the 0^+ ground state were observed. Taking into account that the ground state of ^{82}Ga has $J^\pi = (2^-)$, these would be ideal candidates for $E1$ transitions from above the neutron emission threshold.

The enhanced $E1$ strength has an impact on the *r*-process calculations, see e.g. Refs. [131, 132, 133, 134, 135]. In the *r* process, the neutron captures typically occur resonantly to unbound states, although direct captures can also play a role in the *r* process [136]. The populated unbound states can decay via an emission of a neutron or via gamma-ray transitions. Thus, an increased gamma-ray transition probability of a neutron-unbound state will increase the population of the ground

state of that nucleus and hence its abundance in the *r* process.

The astrophysical impact of the newly observed gamma-ray transitions from states above the neutron separation energy in ^{82}Ge is not straightforward to study. However, the impact of the chosen gamma-ray strength function on the neutron-capture reaction rate for $^{81}\mathrm{Ge}(n,\gamma)^{82}\mathrm{Ge}$ was explored. The neutron-capture rate was calculated using the statistical Hauser-Feshbach approach with the TALYS code [137]. Five different $E1$ gamma-ray strength function models were employed, two of which are semi-microscopic (Hartree-Fock BCS + QRPA [138], Hartree-Fock-Bogolyubov + QRPA [139]), while the rest are phenomenological (Kopecky-Uhl generalized Lorentzian [140], Brink-Axel Lorentzian [141], Modified Lorentzian [142]). The neutron-capture rates were calculated with otherwise similar nuclear input, utilizing the experimental mass values from AME2020 [42] and FRDM2012 [143] for the experimentally unknown nuclei. In addition, the Konig-Delaroche optical potential [144] and the Back-shifted Fermi Gas level density [145] were incorporated to account for the effects of nuclear structure and interactions between particles. The neutron-capture reaction rate for $^{81}\mathrm{Ge}(n,\gamma)^{82}\mathrm{Ge}$ obtained with these different gamma-ray strength functions is shown in Fig. 7.13. The reaction rate clearly depends sensitively on the chosen model. This highlights the impact of the $E1$ gamma strength function on the calculated reaction rates as also shown in Refs. [135, 146, 147].

In ^{83}Ge, only one tentative gamma-ray transition from a state above the neutron separation energy ($S_n = 3633(3)$ keV [42]) was observed. This tentative transition from a state at 4022.6 keV to a $(3/2^+, 5/2^+)$ state at 1543 keV leaves the type of the transition open but nevertheless indicates that gamma decay can compete with neutron emission despite of the very large beta-delayed neutron branch of ^{83}Ga. The impact of different gamma-strength functions on the $^{82}\mathrm{Ge}(n,\gamma)^{83}\mathrm{Ge}$ reaction rate is shown in Fig. 7.14.

In this thesis, no gamma-ray transitions from states above the neutron separation energy at 6161(4) keV [42] were observed in ^{86}Se following the beta decay of ^{86}As. The highest level fed was at 5863.9 keV, around 300 keV below the neutron separation energy. It might be that the gamma-decay branches are very weak and are missed (pandemonium effect [115]). The impact of different gamma-strength functions on the $^{85}\mathrm{Se}(n,\gamma)^{86}\mathrm{Se}$ reaction rate is shown in Fig. 7.15.

As shown in Figs. 7.13, 7.14 and 7.15, the phenomenological gamma-strength models yield roughly an order of magnitude higher reaction rates for the studied neutron-capture reactions than the semi-microscopic models. Nevertheless, all models systematically show that the neutron-capture rates on ^{81}Ge and ^{85}Se leading to ^{82}Ge with $N = 50$ and ^{86}Se with $N = 52$, respectively, have much higher reaction rates than the captures on ^{82}Ge leading to ^{83}Ge, which has an odd number of neutrons. This is expected based on the reaction Q values. The trends in the reaction rates in all models are also very similar. Whereas neutron captures on ^{81}Ge have a rather flat temperature dependence, the reaction rates on ^{82}Ge and ^{85}Se peak at around 7 GK. More experimental data would be needed to validate the best models to be used for the astrophysical calculations. In the future, beta-decay studies employing total absorption gamma-ray spectroscopy or

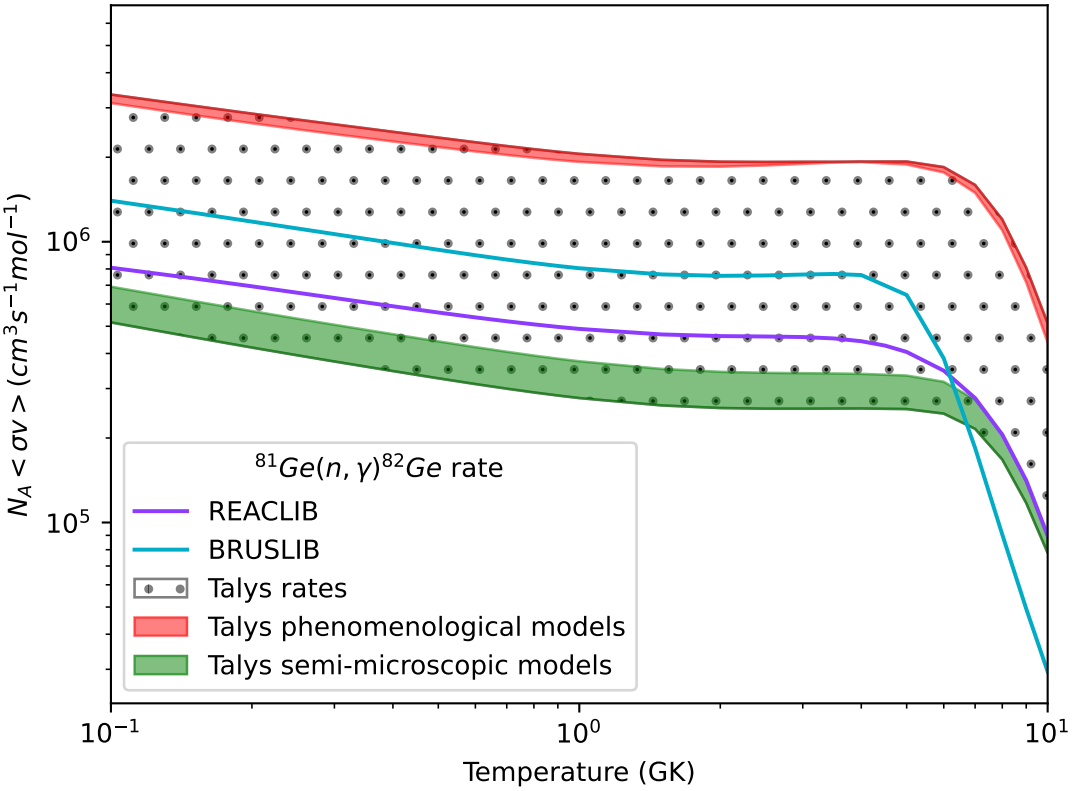

Figure 7.13: The impact of different models of $E1$ γ-strength function on the calculated ^{81}Ge$(n,\gamma)^{82}$Ge reaction rate. See text for details of the calculations. The results are compared to those obtained using two commonly used astrophysics reference libraries, REACLIB [148] and BRUSLIB [149]. Figure courtesy of Stylianos Nikas.

beta-Oslo method [135] might provide more complete information on the gamma strength around the neutron threshold.

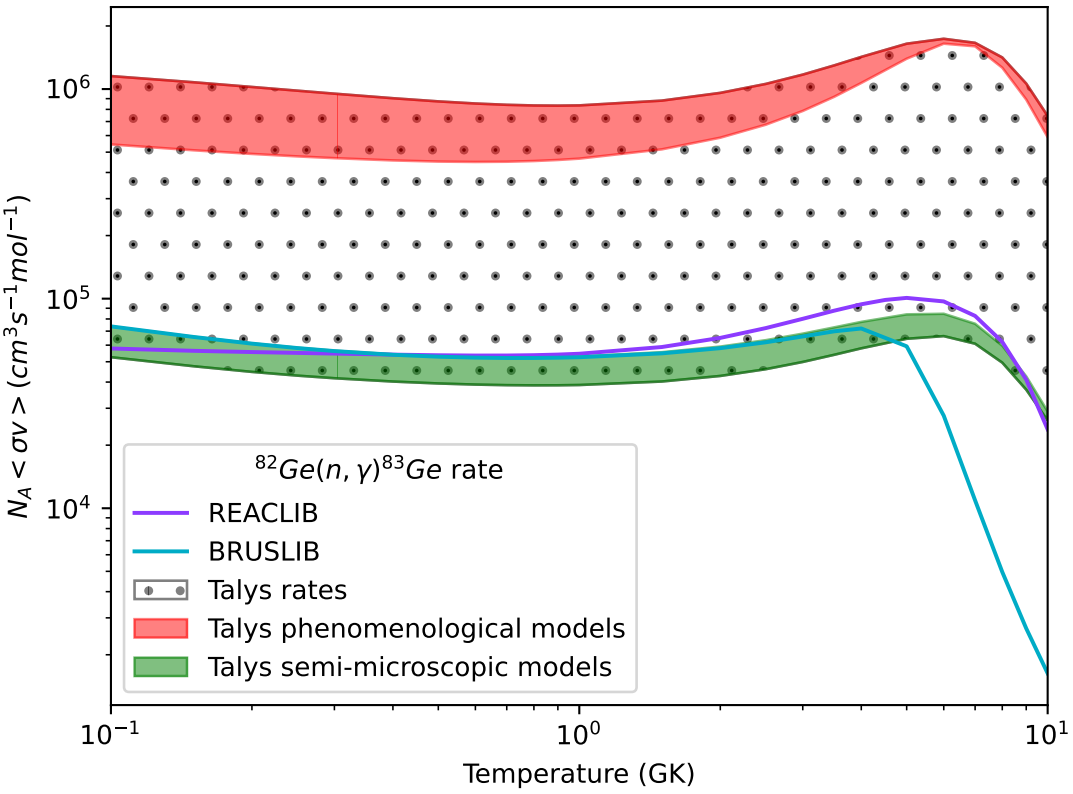

Figure 7.14: The impact of different models of $E1$ γ-strength function on the calculated ^{82}Ge$(n,\gamma)^{83}$Ge reaction rate. See text for details of the calculations. The results are compared to those obtained using two commonly used astrophysics reference libraries, REACLIB [148] and BRUSLIB [149]. Figure courtesy of Stylianos Nikas.

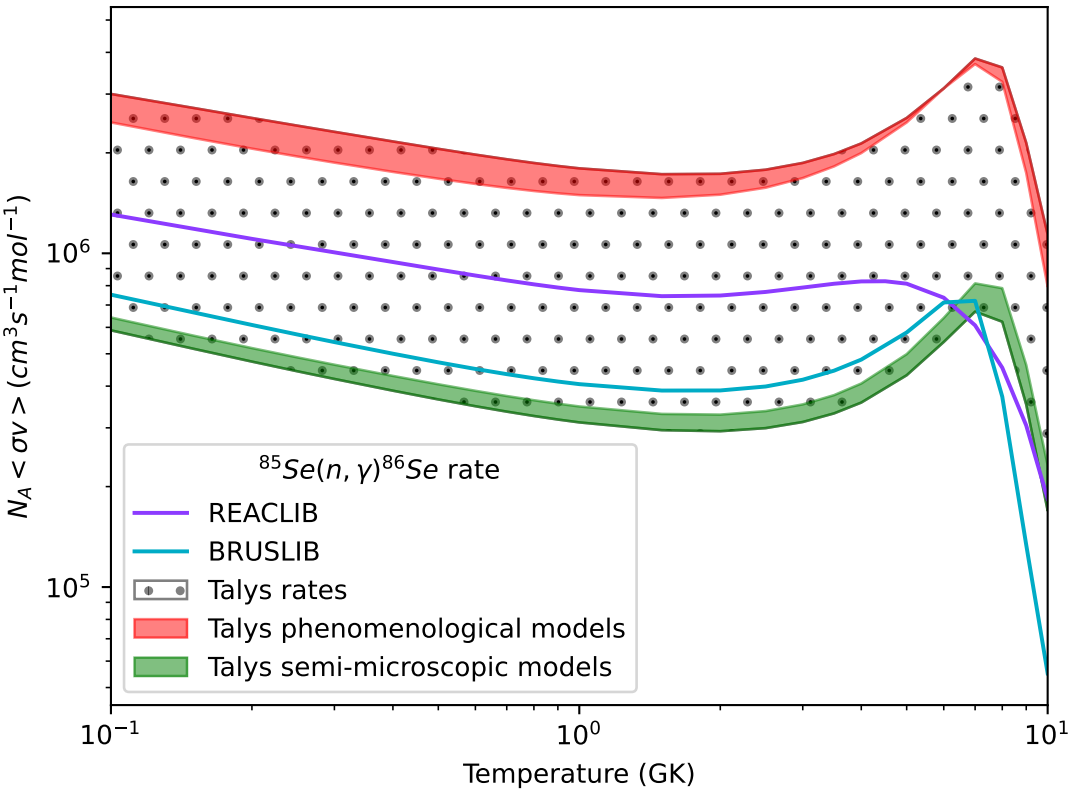

Figure 7.15: The impact of different models of $E1$ γ-strength function on the calculated $^{85}\mathrm{Se}(n,\gamma)^{86}\mathrm{Se}$ reaction rate. See the text for details of the calculations. The results are compared to those obtained using two commonly used astrophysics reference libraries, REACLIB [148] and BRUSLIB [149]. Figure courtesy of Stylianos Nikas.

8 SUMMARY AND OUTLOOK

This Ph.D. thesis was centered on the study of β-decay in neutron-rich nuclei around the N=50 shell closure, with a particular focus on the high-energy states around the neutron emission threshold. This research aimed to determine the structure of these states, identify whether they are Pygmy Dipole Resonance (PDR) states, and investigate if and how β-decay is connected to PDR states. To achieve this, two complementary experiments were conducted. The first experiment utilized PARIS scintillators and HPGe detectors to study β-delayed gamma spectroscopy of ^{82,83}Ge at the ALTO facility. The second experiment used the JYFLTRAP Penning trap to provide pure samples of ^{86}As for the study of β-delayed gamma spectroscopy of ^{86}Se, which was performed with high-resolution germanium detectors at the IGISOL facility of the JYFL Accelerator Laboratory at the University of Jyväskylä.

The data analysis yielded updated level schemes of ^{82,83}Ge and ^{86}Se and enabled the observation of over 80 new γ-ray transitions, including those with energies above the neutron separation energy for the first time in ^{82}Ge. Furthermore, new γ-ray transitions in both ^{81}Ge and ^{85}Se, which are β-n daughters of ^{82}Ga and ^{86}As, respectively, were also observed in this study.

Half-lives of ^{82}Ga, ^{83}Ga, and ^{86}As were measured, and the reported values of 608 (7) ms, 314 (7) ms, and 905^{+29}_{-26} ms, respectively, are in agreement with previous measurements. Furthermore, the neutron emission probabilities of ^{83}Ga and ^{86}As were calculated. The impact of the updated β-delayed emission rates on the production of the A $\approx$ 80 region of the first r-process peak was also investigated, revealing a 10% increase in the abundance at A=82 and around 25% reduction in the abundance at A=83.

Additionally, QRPA and pnQRPA calculations were performed to analyze the electric dipole and Gamow-Teller strength distributions for ^{82}Ge. By comparing the experimental and calculated B(E1) and B(GT) distributions, the structure and dipole character of the high-energy states that were populated by the β-decay of ^{82}Ga were discussed. As a result, it was possible to conclude that the β-decay of ^{82}Ga populates states compatible with a 1^- spin-parity between 6 and 8 MeV in ^{82}Ge, however, their PDR character could not be firmly confirmed. Furthermore,

shell-model calculations were performed for ^{86}Se, and the calculated spectrum was compared to selected states showing agreement with the newly assigned spin and parities in ^{86}Se.

The data acquired with the PARIS scintillators for ^{82,83}Ge were not explored in this thesis. This was partially due to the wealth of spectroscopic data from the high-resolution detection part of the setup in the ALTO experiment. The analysis of PARIS spectra remains to be done. In order to do this, one needs to simulate the response function of the PARIS setup carefully and employ unfolding techniques to extract the decay information from the spectrum [150].

It is obvious from the work presented in this study that the measurement of low-energy dipole strength in (very) neutron-rich nuclei is not an easy task. The experimental methods allowing for this type of investigation are basically limited only to β-decay studies. The low production rates of these nuclei makes it difficult, if not impossible, to measure the multipolarity of the observed γ-rays depopulating states at high energy. A systematic study along the N=50 isotonic chain starting close to stability and going towards the nuclei measured in this thesis and using different experimental techniques where possible could help in bringing more light on how the dipole strength evolves with « exoticity » of the nuclei.

Previously, the β-decay of ^{86}As was examined at IGISOL and the β-delayed neutron emission was measured with the MOdular Neutron time-of-flight SpectromeTER (MONSTER). The experiment detected robust β-delayed neutron branches from states around 1 MeV above the neutron emission threshold. However, as no gamma-ray transitions above S_n were observed in ^{86}Se in this work, the competition between the β-delayed neutron and gamma emission in the neutron-unbound states in ^{86}Se remained unanswered. The observed neutron structure could not be connected to gamma-ray de-excitations. One possible explanation is the insufficient statistics of ^{86}As during the beam time, which could be attributed to problems with the gas purification system at IGISOL. The measurement can be replicated at IGISOL using the same decay setup with improved statistics due to various factors. First, in order to prevent the molecular formation of $^{86}As^{+}$ ions, it is important that the helium gas used by the cooler-buncher is purified, removing reactive gases such as H_2O and O_2. To achieve this, the cold-trap gas purification system can be employed. The Multi-Reflection Time-of-Flight Mass Separator (MR-TOF), recently installed into the IGISOL beam line, can provide quicker mass separation, which can be another option to enhance the statistics at the decay setup. It should be noted that the primary beam intensity at the Accelerator Laboratory is now two times more intense than during our experiment, which partially compensates for the low efficiency of the germanium detectors. Despite the lower statistics, the purity of the ^{86}As beam allowed for unambiguous identification of many gamma transitions in ^{85}Se following the β-delayed neutron emission. In future, combining these data with the β-delayed neutron data would yield a better understanding of the excitation energies of the states in ^{86}Se populated via β decay of ^{86}As.

New, more exotic neutron-rich nuclei will become accessible for experiments via improved detection methods at new or upgraded radioactive beam facilities.

With their higher Q_β values and lower neutron separation energies, new possibilities for β-decay studies exploring the nuclear structure at and around the neutron threshold will become available in the future. This thesis has provided an important step in this respect with the studies in the N=50 region.

9 RÉSUMÉ EN FRANÇAIS

La physique au seuil d'émission d'un neutron (S_n) apporte une importante quantité d'informations utiles pour l'astrophysique nucléaire, la physique des réacteurs, la formation des clusters dans le noyau ou plus généralement la structure nucléaire, etc. Dans les noyaux stables et proches de la stabilité, S_n se situe autour de 8 MeV et en dehors de la fenêtre en énergie où la décroissance β est énergétiquement permise ($Q_\beta \geq 0$). En s'éloignant de la vallée de la stabilité, la fenêtre Q_β augmente en même temps que S_n diminue en énergie jusqu'à ce que, en atteignant la "drip-line", le neutron supplémentaire ne puisse plus être lié dans le noyau par l'interaction forte. Avant même d'arriver à la "drip-line", ces variations en énergie ouvrent des canaux de décroissance de plus en plus exotiques, comme β-n ou β-2n. Cette région des noyaux exotiques riches en neutrons est le terrain de jeu du processus astrophysique de capture rapide des neutrons (processus **r**) qui est responsable de la production d'éléments lourds dans l'Univers.
Le processus **r** nécessite une bonne compréhension des propriétés des états fondamentaux des noyaux riches en neutrons, telles que leurs masses, leurs durées de vie et leurs probabilités d'émission de neutrons retardés, qui sont autant d'éléments cruciaux pour les calculs du chemin que ce processus astrophysique rapide suit [151]. De plus, les taux de capture des neutrons et une bonne compréhension de la distribution de la force γ dans ces noyaux sont impératifs pour la modélisation de ce processus. La force dipolaire domine la distribution de la force γ dans les noyaux. Il a été observé (voir, par exemple, [19]) que dans les noyaux riches en neutrons elle possède une composante à basse énergie (par rapport à la Résonance Dipolaire Géante) que nous appelons Résonance Dipolaire Pygmée (PDR). Les modèles astrophysiques montrent que la présence de la PDR autour du seuil S_n pourrait influencer l'abondance des noyaux plus lourds (A$\sim$130) car elle interfère avec l'équilibre des processus (γ,n) et (n,γ) en augmentant les taux (n,γ) [152]. Du point de vue de la structure nucléaire, la PDR peut être conceptualisée comme l'oscillation d'un peau de neutrons contre un noyau avec un nombre équilibré de protons et neutrons. Des questions sur sa nature isoscalaire ou isovectorielle [134], sur sa composition en quelques (quasi-)particules ou (très) collective (voir, par exemple, [153, 154]), sur la manière dont elle peut être peuplée par des processus

tel que la décroissance β [25], restent ouvertes et doivent être répondues pour mettre plus de lumière sur cette organisation particulière de la matière nucléaire dans le noyau.

Le travail présenté dans cette thèse en cotutelle entre l'Université Paris-Saclay et l'Université de Jyväskylä est axé sur l'étude de la décroissance β des noyaux riches en neutrons autour de la fermeture de couches N=50, en s'intéressant plus particulièrement à la population des états de haute énergie, situés autour du seuil d'émission d'un neutron. Quelle est la structure de ces états, s'agit-il d'états dipolaires pygmées (PDR) et, si c'est le cas, comment la décroissance β est-elle liée aux états PDR sont quelques-unes des questions qui ont motivé cette étude. Les recherches ont été menées au moyen de deux expériences complémentaires. La première a été réalisée auprès d'ALTO (Accélérateur Linéaire et Tandem d'Orsay) et a été dédiée à l'étude par spectroscopie γ-retardée de ^{82,83}Ge en utilisant le détecteur PARIS [155] et des détecteurs HPGe. Les faisceaux de ^{82,83}Ga ont été obtenus à partir de la photo-fission induite sur une cible de UCx par le rayonnement de freinage d'un faisceau d'électrons accélérés à 50 MeV par un accélérateur linéaire. En employant une technique de type ISOL, associée à une ionisation par LASER et à une séparation en masse par le spectromètre magnétique PARRNe (M/ΔM = 1500), des faisceaux de ^{82}Ga et ^{83}Ga ont été sélectionnés et implantés sur une bande en mylar aluminisée qui permet d'évacuer la radioactivité selon un cycle spécifique d'accumulation et de décroissance pour chaque noyau étudié. La décroissance des noyaux radioactifs a été observée dans un scintillateur plastique (BC408) qui détecte l'électron β émis avec une efficacité de l'ordre de 75%. Le détecteur PARIS (environ 1.5% d'efficacité à 5 MeV) et des détecteurs HPGe (avec une efficaicté d'environs 2.5% à 1.173 MeV) placés autour du point d'implantation (voir Fig. 9.1) ont été utilisés pour détecter le rayonnement γ émis en coïncidence avec les électrons β. La seconde expérience, visant à étudier la spectroscopie γ retardée par β de ^{86}Se, a été réalisée auprès de l'installation IGISOL (Ion Guide Isotope Separator On-Line) [95] du JYFL Accelerator Laboratory de l'Université de Jyväskylä. Les noyaux radioactifs riches en neutrons ont été produits par la fission d'Uranium naturel induite par un faisceau de protons de 25 MeV avec une intensité de 10 µA. Le guide d'ions IGISOL permet l'extraction des fragments de fission dans un flux de gaz (He). En sortie les fragments acquièrent 30 qkeV d'énergie, sont sélectionnés par un dipôle magnétique (M/ΔM = 500) et ensuite décélérés à 800 eV. En aval d'IGISOL, le piège de Penning JYFLTRAP [156] a été utilisé pour obtenir un faisceau pur de ^{86}As avant l'implantation sur une bande magnétique entourée par un détecteur plastique (efficacité $\sim$30%) et 5 détecteurs HPGe (dont 3 clovers) avec une efficacité totale d'environs 2.7% à 1.173 keV (voir Fig. 9.2). Dans les deux expériences, les systèmes d'acquisition utilisés (FASTER [157] et Nutaq [104]) ont été basés sur des numériseurs et les données ont été enregistrées en mode trigger-less.
Comme déjà mentionné, cet étude s'intéresse à des états autour du seuil d'émission d'un neutron, S_n, peuplés par décroissance β et qui se connectent directement avec l'état fondamental du noyau fils (ou des états 2^+ de basse énergie) par des transitions γ. Ceci implique donc la caractérisation du dispositif expérimentale de

détection γ sur une large plage en énergie. La calibration en énergie des détecteurs HPGe utilisés dans les deux expériences a été faite en utilisant des sources standard, des transitions connues est observées dans la chaîne de décroissance β des masses 82 et 83 (à ALTO) ou 86 (à IGISOL). Pour couvrir le spectre jusqu'à $\sim$ 8 MeV, nous avons aussi utilisé à ALTO une source d'AmBe placée dans un récipient en polyéthylène et entouré des feuilles de ^{nat}Ni, dispositif permettant de produire par capture des neutrons thermiques des γ de 9 MeV. Les détecteurs PARIS ont été calibrés de la même manière. Pour la calibration en efficacité γ du système utilisé à IGISOL, nous avons utilisé des sources standards, une source de ^{56}Co et des transitions connues dans la chaîne de décroissance de la masse A=86 qui ont permis d'avoir un mesure de l'efficacité photoélectrique pour des énergies jusqu'à $\sim$6.3 MeV. A ALTO, nous avons utilisé seulement des sources standard pour avoir une mesure de l'efficacité jusqu'à $\sim$1.4 MeV et pour avoir une estimation de l'efficacité jusqu'à 8 MeV, nous avons fait des simulations GEANT4 en utilisant le package SToGS [108]. En même temps, les simulations ont été utilisées pour avoir une estimation des rapports entre les événements γ observés dans les détecteurs avec un dépôt complet d'énergie, un dépôt avec un échappement de 511 keV ou un dépôt avec un échappement de 2x511 keV et ceci en fonction de l'énergie du γ incident. Ces estimations ont été utilisées comme condition pour assigner des pics observés dans les spectres γ à des transitions entre deux états. D'autres critères pour assigner des pics γ dans le spectre mesuré à des transitions dans le noyau étudié ont été : i. la durée de vie mesurée en sélectionnant le pic γ d'un évènement $\beta - \gamma$ doit être celle du noyau parent; ii. dans certains cas, les coïncidences avec des transitions γ déjà connues sont utilisées comme critère; iii. l'observation de 511 keV en coïncidence avec un pic γ est utilisé comme critère pour considèrer que le pic corresponds à une mesure avec simple ou double échappement de 511 keV.
Une analyse détaillée des deux expériences est présentée dans ce manuscrit. Les schémas de niveaux des noyaux fils de la décroissance β, ^{82}Ge (N=50), ^{83}Ge (N=51), et ^{86}Se (N=52), ont été construits et plus de 80 nouvelles transitions γ ont été observées.
La décroissance de ^{82}Ga a mener à l'identification de 45 nouveaux états excités dans le noyau fils, ^{82}Ge, et trois supplémentaires dans le noyau β-n, ^{81}Ge. La durée de demi-vie mesurée, $T_\beta(^{82}Ga)$ = 608(7) ms, est en accord la valeur NNDC évaluée, 600(2) ms. Au totale, 76(6) % de la décroissance β a été mesurée en coïncidence avec des γ's. En considérant la valeur évaluée $P_n(^{82}Ga)$ = 22.7(20) %, on peut déduire que la transition β vers l'état fondamentale de ^{82}Ge est compatible avec zéro. Concernant le spectre d'excitation de ^{82}Ge, nous avons observé pour la première fois la population des états au dessus du seuil d'émission de neutron ($S_n(^{82}Ge)$ = 7.195(3) MeV) par décroissance β-γ. Ces états se désexcitent vers l'état fondamentale de ^{82}Ge. Considérant la compétition avec l'émission de neutron, il est raisonnable de considérer que le rayonnement γ ainsi émis soit électrique dipolaire et que ces états excités aient un moment angulaire totale $I^\pi = 1^-$. D'autres états liés d'énergie supérieure à 6 MeV ont aussi des caractéristiques compatibles avec un moment angulaire totale $I^\pi = 1^-$. Ces résultats ont été comparés avec des calculs QRPA [30, 116] et RQTBA [158]. En utilisant les méthodes des références

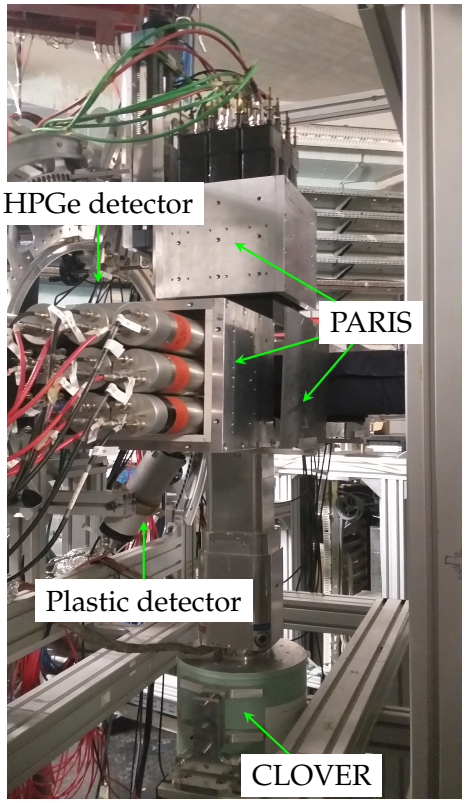

Figure 9.1: Photographie du dispositif expérimental installé à ALTO.

[30, 116], les distributions théoriques de la force dipolaire (B(E1)) et de la distribution de Gamow-Teller (B(GT)) dans ^{82}Ge ont été confrontées aux observations. Les calculs reproduisent bien la distribution B(GT) expérimentale, mais ne prédisent pas des états $I^{\pi} = 1^{-}$ en dessous de 9.5 MeV. Le modèle RQTBA, en couplant des états QRPA de 2-qp avec 1 phonon, permet de calculer des états dipolaires autour de 8 MeV dont un état à 7.84 MeV qui présente toutes les caractéristiques d'un état Pygmée dipolaire. Il n'est pourtant pas évident de conclure sur la population des états PDR par décroissance β, car le calcul de la force Gamow-Teller n'a pas été effectué dans la même base. Ces calculs seront faites dans un futur proche.
Trois nouveaux états ont été ajoutés au spectre d'excitation de ^{83}Ge. La durée de demi-vie mesurée, $T_{\beta}(^{83}Ga)$ = 314(7) ms, est en accord la valeur NNDC évaluée, 308(10) ms. Les valeurs P_n de ^{83}Ga rapportées dans différents travaux antérieurs s'étalent entre 50 % et 90 % [55, 113, 60]. Nous avons mesuré une probabilité d'émission d'un neutron $P_n(^{83}Ga)$ = 79(13) %, compatible avec [60]. L'impact de cette nouvelle mesure sur la production des éléments stables dans la région de masse A $\sim$ 80 par le processus **r** a été calculé, révélant une augmentation de 10 % de l'abondance à A = 82 et une réduction d'environ 25 % de l'abondance à A = 83.
La décroissance de ^{86}As a mener à l'identification de 30 nouveaux états excités dans le noyau fils, ^{86}Se, et six états supplémentaires dans le noyau β-n, ^{85}Se. La durée de demi-vie mesurée, $T_{\beta}(^{86}As) = 905^{29}_{26}$ ms, est en accord la valeur NNDC évaluée, 945(8) ms. La valeur mesurée de $P_n(^{86}As)$ = 35(9) % confirme une mesure antérieure [73]. A partir de la décroissance β-n, nous avons pu contraindre la valeur du moment angulaire totale de l'état fondamentale de ^{86}As à $\vec{I} = \vec{2}$. Des

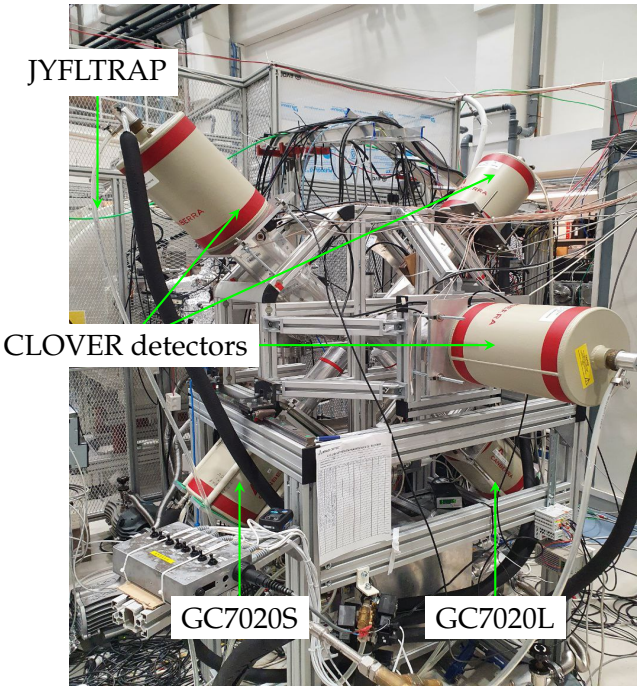

Figure 9.2: Photographie du dispositif expérimental installé à IGISOL.

états excités jusqu'à 300 keV en dessous de $S_n(^{86}Se)$ = 6.161(4) MeV ont été peuplés dans la décroissance β. Nous n'avons pas observé en spectroscopie $\beta - \gamma$ des transitions vers des états d'énergie supérieure à S_n. Pour les états de basse énergie, nous avons trouvé un relativement bon accord avec les calculs de modèle en couches publiés dans la référence [77] pour les valeurs de spin nouvellement attribués. Le calcul de la force B(E1) dans ^{86}Se par RQTBA n'est pour le moment pas possible étant donné que ces calculs se font dans une base sphérique et ce noyau est prédit déformé [159].
Pour tous les noyaux étudiés, nous avons calculé l'impact des différents calculs de la distribution de la force E1 sur le taux du processus de capture d'un neutron, (n,γ). Les modèles phénoménologiques prédisent des taux de réaction jusqu'à un ordre de magnitude supérieurs aux taux obtenus avec des modèles sémi-microscopiques. En même temps, tous les modèles montrent un taux de capture radiative des neutrons beaucoup plus important pour ^{85}As(n,γ)^{86}As et ^{81}Ge(n,γ)^{82}Ge que pour ^{82}Ge(n,γ)^{83}Ge, le dernier impliquant la capture d'un neutron sur un noyau pair-pair. Ceci est cohérent avec les valeurs de chaleurs de réaction.
Les travaux présentés dans cette étude montrent clairement que la mesure de la force dipolaire à basse énergie dans les noyaux (très) riches en neutrons n'est pas une tâche facile. Les méthodes expérimentales permettant ce type d'investigation sont fondamentalement limitées aux études par décroissance β. Les faibles taux de production de ces noyaux font qu'il est difficile, voire impossible, de mesurer la multipolarité des rayons γ de haute énergie observés en coïncidence avec le β-électron. Ce travail de thèse à aussi montrer la pertinence des mesures de spectroscopie γ de haute résolution jusqu'à $\sim$ 8 MeV en utilisant des détecteurs à base de Ge. Une étude systématique le long de la chaîne isotonique N = 50

commençant près de la stabilité et allant vers les noyaux mesurés dans le cadre de cette thèse et en utilisant différentes techniques expérimentales lorsque cela est possible, pourrait aider à suivre l'évolution de la force dipolaire en fonction de l'"exotisme" des noyaux. De nouveaux noyaux riches en neutrons, plus exotiques, deviendront bientôt accessibles aux expériences grâce à des méthodes de détection et production améliorées dans des installations de faisceaux radioactifs nouvelles ou modernisées. Cette thèse a permis de franchir une étape importante à cet égard grâce aux études de la structure nucléaire au seuil des neutrons.

REFERENCES

[1] K.-L. Kratz, J.-P. Bitouzet, F.-K. Thielemann, P. Moeller and B. Pfeiffer. *Astrophysical Journal*, **403**, 216 (1993). doi:10.1086/172196.

[2] H. Becquerel. *Journal de Physique Théorique et Appliquée*, **9**, 190 (1900).

[3] C. D. Anderson. *Science*, **76**, 238 (1932).

[4] F. Joliot. *Journal de Chimie Physique*, **31**, 611 (1934).

[5] G. C. Wick. *Atti R. Accad. Naz. Lincei. Ren*, **19**, 319 (1934).

[6] H. Yukawa and S. Sakata. *Proceedings of the Physico-Mathematical Society of Japan. 3rd Series*, **17**, 467 (1935).

[7] L. W. Alvarez. *Physical Review*, **52**, 134 (1937).

[8] W. Pauli. *Letter to physicists at Tubingen*, page 71 (1930).

[9] E. Fermi. *Il Nuovo Cimento (1924-1942)*, **11**, 1 (1934).

[10] K. S. Krane. *Introductory nuclear physics*. John Wiley & Sons (1991).

[11] D. B. Chitwood, T. I. Banks, M. J. Barnes, S. Battu, R. M. Carey, S. Cheekatmalla, S. M. Clayton, J. Crnkovic, K. M. Crowe, P. T. Debevec, S. Dhamija, W. Earle, A. Gafarov, K. Giovanetti, T. P. Gorringe, F. E. Gray, M. Hance, D. W. Hertzog, M. F. Hare, P. Kammel, B. Kiburg, J. Kunkle, B. Lauss, I. Logashenko, K. R. Lynch, R. McNabb, J. P. Miller, F. Mulhauser, C. J. G. Onderwater, C. S. Özben, Q. Peng, C. C. Polly, S. Rath, B. L. Roberts, V. Tishchenko, G. D. Wait, J. Wasserman, D. M. Webber, P. Winter and P. A. Żołnierczuk. *Phys. Rev. Lett.*, **99**, 032001 (2007). URL https://link.aps.org/doi/10.1103/PhysRevLett.99.032001.

[12] B. Singh, J. Rodriguez, S. Wong and J. Tuli. *Nuclear Data Sheets*, **84**, 487 (1998). ISSN 0090-3752. URL https://www.sciencedirect.com/science/article/pii/S0090375298900151.

[13] G. Gamow. *Proceedings of the Royal Society of London. Series A, Containing Papers of a Mathematical and Physical Character*, **146**, 217 (1934).

[14] G. Gamow and E. Teller. *Physical Review*, **49**, 895 (1936).

[15] P. Ring and P. Schuck. *The nuclear many-body problem*. Springer Science & Business Media (2004).

[16] W. Bothe and W. Gentner. *Zeitschrift für Physik*, **106**, 236 (1937).

[17] A. Migdal. *Zhurnal Eksperimentalnoi i teoreticheskoi Fiziki*, **15**, 81 (1945).

[18] W. Kuhn. *Zeitschrift für Physik*, **33**, 408 (1925).

[19] D. Savran, T. Aumann and A. Zilges. *Prog. Part. Nucl. Phys.*, **70**, 210 (2013).

[20] U. Kneissl, H. Pitz and A. Zilges. *Prog. Part. Nucl. Phys.*, **37**, 349 (1996).

[21] P. Adrich, A. Klimkiewicz, M. Fallot, K. Boretzky, T. Aumann, D. Cortina-Gil, U. D. Pramanik, T. W. Elze, H. Emling, H. Geissel, M. Hellström, K. L. Jones, J. V. Kratz, R. Kulessa, Y. Leifels, C. Nociforo, R. Palit, H. Simon, G. Surówka, K. Sümmerer and W. Waluś. *Phys. Rev. Lett.*, **95**, 132501 (2005). URL https://link.aps.org/doi/10.1103/PhysRevLett.95.132501.

[22] A. Krumbholz, P. von Neumann-Cosel, T. Hashimoto, A. Tamii, T. Adachi, C. Bertulani, H. Fujita, Y. Fujita, E. Ganioglu, K. Hatanaka *et al.* *Physics Letters B*, **744**, 7 (2015).

[23] J. Endres, D. Savran, A. van den Berg, P. Dendooven, M. Fritzsche, M. N. Harakeh, J. Hasper, H. Wörtche and A. Zilges. *Phys. Rev. C*, **80**, 034302 (2009).

[24] L. Pellegri, A. Bracco, F. Crespi, S. Leoni, F. Camera, E. Lanza, M. Kmiecik, A. Maj, R. Avigo, G. Benzoni, N. Blasi, C. Boiano, S. Bottoni, S. Brambilla, S. Ceruti, A. Giaz, B. Million, A. Morales, R. Nicolini, V. Vandone, O. Wieland, D. Bazzacco, P. Bednarczyk, M. Bellato, B. Birkenbach, D. Bortolato, B. Cederwall, L. Charles, M. Ciemala, G. De Angelis, P. Désesquelles, J. Eberth, E. Farnea, A. Gadea, R. Gernhäuser, A. Görgen, A. Gottardo, J. Grebosz, H. Hess, R. Isocrate, J. Jolie, D. Judson, A. Jungclaus, N. Karkour, M. Krzysiek, E. Litvinova, S. Lunardi, K. Mazurek, D. Mengoni, C. Michelagnoli, R. Menegazzo, P. Molini, D. Napoli, A. Pullia, B. Quintana, F. Recchia, P. Reiter, M. Salsac, B. Siebeck, S. Siem, J. Simpson, P.-A. Söderström, O. Stezowski, C. Theisen, C. Ur, J. Valiente Dobon and M. Zieblinski. *Physics Letters B*, **738**, 519 (2014). ISSN 0370-2693. URL https://www.sciencedirect.com/science/article/pii/S0370269314005966.

[25] M. Scheck *et al.* *Phys. Rev. Lett.*, **116**, 132501 (2016). URL https://link.aps.org/doi/10.1103/PhysRevLett.116.132501.

[26] P. J. Brussaard and P. W. M. Glaudemans. *Shell-model applications in nuclear spectroscopy*. North-Holland publishing company (1977).

[27] W. M. Elsasser. *J. Phys. Radium*, **5**, 389 (1934).

[28] M. G. Mayer. *Physical Review*, **75**, 1969 (1949).

[29] O. Haxel, J. H. D. Jensen and H. E. Suess. *Phys. Rev.*, **75**, 1766 (1949). URL https://link.aps.org/doi/10.1103/PhysRev.75.1766.2.

[30] S. Peru and M. Martini. *The European Physical Journal A*, **50**, 1 (2014).

[31] I. Deloncle, S. Péru and M. Martini. *The European Physical Journal A*, **53**, 1 (2017).

[32] J. J. Cowan, C. Sneden, J. E. Lawler, A. Aprahamian, M. Wiescher, K. Langanke, G. Martínez-Pinedo and F.-K. Thielemann. *Reviews of Modern Physics*, **93**, 015002 (2021).

[33] F.-K. Thielemann, A. Arcones, R. Käppeli, M. Liebendörfer, T. Rauscher, C. Winteler, C. Fröhlich, I. Dillmann, T. Fischer, G. Martinez-Pinedo *et al. Prog. Part. Nucl. Phys.*, **66**, 346 (2011).

[34] S. Goriely, A. Bauswein and H.-T. Janka. *The Astrophysical Journal Letters*, **738**, L32 (2011).

[35] B. P. Abbott, R. Abbott, T. Abbott, M. Abernathy, F. Acernese, K. Ackley, C. Adams, T. Adams, P. Addesso, R. Adhikari *et al. Phys. Rev. Lett.*, **116**, 061102 (2016).

[36] L. S. Collaboration and V. Collaboration. *The Astrophysical Journal Letters*, **848**, 27pp (2017).

[37] B. Pfeiffer, K.-L. Kratz and P. Möller. *Progress in Nuclear Energy*, **41**, 39 (2002).

[38] S. Goriely. *Physics Letters B*, **436**, 10 (1998).

[39] E. M. Burbidge, G. R. Burbidge, W. A. Fowler and F. Hoyle. *Reviews of Modern Physics*, **29**, 547 (1957).

[40] K. Langanke and G. Martínez-Pinedo. *Reviews of Modern Physics*, **75**, 819 (2003).

[41] Y.-Z. Qian and G. Wasserburg. *Physics Reports*, **442**, 237 (2007).

[42] M. Wang, W. Huang, F. G. Kondev, G. Audi and S. Naimi. *Chinese Physics C*, **45**, 030003 (2021).

[43] J. Hakala, S. Rahaman, V.-V. Elomaa, T. Eronen, U. Hager, A. Jokinen, A. Kankainen, I. D. Moore, H. Penttilä, S. Rinta-Antila, J. Rissanen, A. Saastamoinen, T. Sonoda, C. Weber and J. Äystö. *Phys. Rev. Lett.*, **101**, 052502 (2008). URL https://link.aps.org/doi/10.1103/PhysRevLett.101.052502.

[44] Z. Y. Xu, S. Nishimura, G. Lorusso, F. Browne, P. Doornenbal, G. Gey, H.-S. Jung, Z. Li, M. Niikura, P.-A. Söderström, T. Sumikama, J. Taprogge, Z. Vajta, H. Watanabe, J. Wu, A. Yagi, K. Yoshinaga, H. Baba, S. Franchoo, T. Isobe, P. R. John, I. Kojouharov, S. Kubono, N. Kurz, I. Matea, K. Matsui, D. Mengoni, P. Morfouace, D. R. Napoli, F. Naqvi, H. Nishibata, A. Odahara, E. Şahin, H. Sakurai, H. Schaffner, I. G. Stefan, D. Suzuki, R. Taniuchi and V. Werner. *Phys. Rev. Lett.*, **113**, 032505 (2014). URL https://link.aps.org/doi/10.1103/PhysRevLett.113.032505.

[45] https://www.nndc.bnl.gov/ensdf/.

[46] R. Broda, B. Fornal, W. Królas, T. Pawłat, D. Bazzacco, S. Lunardi, C. Rossi-Alvarez, R. Menegazzo, G. de Angelis, P. Bednarczyk, J. Rico, D. De Acuña, P. J. Daly, R. H. Mayer, M. Sferrazza, H. Grawe, K. H. Maier and R. Schubart. *Phys. Rev. Lett.*, **74**, 868 (1995). URL https://link.aps.org/doi/10.1103/PhysRevLett.74.868.

[47] R. Grzywacz, R. Béraud, C. Borcea, A. Emsallem, M. Glogowski, H. Grawe, D. Guillemaud-Mueller, M. Hjorth-Jensen, M. Houry, M. Lewitowicz, A. C. Mueller, A. Nowak, A. Płochocki, M. Pfützner, K. Rykaczewski, M. G. Saint-Laurent, J. E. Sauvestre, M. Schaefer, O. Sorlin, J. Szerypo, W. Trinder, S. Viteritti and J. Winfield. *Phys. Rev. Lett.*, **81**, 766 (1998). URL https://link.aps.org/doi/10.1103/PhysRevLett.81.766.

[48] M. Sawicka, R. Grzywacz, I. Matea, H. Grawe, M. Pfützner, J. M. Daugas, M. Lewitowicz, D. L. Balabanski, F. Becker, G. Bélier, C. Bingham, C. Borcea, E. Bouchez, A. Buta, M. La Commara, E. Dragulescu, G. de France, G. Georgiev, J. Giovinazzo, M. Górska, F. Hammache, M. Hass, M. Hellström, F. Ibrahim, Z. Janas, H. Mach, P. Mayet, V. Méot, F. Negoita, G. Neyens, F. de Oliveira Santos, R. D. Page, O. Perru, Z. Podolyák, O. Roig, K. P. Rykaczewski, M. G. Saint-Laurent, J. E. Sauvestre, O. Sorlin, M. Stanoiu, I. Stefan, C. Stodel, C. Theisen, D. Verney and J. Żylicz. *Phys. Rev. C*, **68**, 044304 (2003). URL https://link.aps.org/doi/10.1103/PhysRevC.68.044304.

[49] C. Mazzocchi, R. Grzywacz, J. Batchelder, C. Bingham, D. Fong, J. Hamilton, J. Hwang, M. Karny, W. Krolas, S. Liddick, A. Lisetskiy, A. Morton, P. Mantica, W. Mueller, K. Rykaczewski, M. Steiner, A. Stolz and J. Winger. *Physics Letters B*, **622**, 45 (2005). ISSN 0370-2693. URL https://www.sciencedirect.com/science/article/pii/S0370269305009561.

[50] J. Daugas, R. Grzywacz, M. Lewitowicz, L. Achouri, J. Angélique, D. Baiborodin, K. Bennaceur, R. Bentida, R. Béraud, C. Borcea, C. Bingham, W. Catford, A. Emsallem, G. de France, H. Grawe, K. Jones, R. Lemmon, M. Lopez Jimenez, F. Nowacki, F. de Oliveira Santos, M. Pfützner, P. Regan, K. Rykaczewski, J. Sauvestre, M. Sawicka, G. Sletten and M. Stanoiu. *Physics Letters B*, **476**, 213 (2000). ISSN 0370-2693. URL https://www.sciencedirect.com/science/article/pii/S0370269300001775.

[51] R. Taniuchi, C. Santamaria, P. Doornenbal, A. Obertelli, K. Yoneda, G. Authelet, H. Baba, D. Calvet, F. Château, A. Corsi *et al. Nature*, **569**, 53 (2019).

[52] R. Schwengner, R. Massarczyk, G. Rusev, N. Tsoneva, D. Bemmerer, R. Beyer, R. Hannaske, A. R. Junghans, J. H. Kelley, E. Kwan, H. Lenske, M. Marta, R. Raut, K. D. Schilling, A. Tonchev, W. Tornow and A. Wagner. *Phys. Rev. C*, **87**, 024306 (2013). URL https://link.aps.org/doi/10.1103/PhysRevC.87.024306.

[53] T. N. S. Ebata and T. Inakura. *Phys. Rev. C*, **90**, 024303 (2014). URL https://link.aps.org/doi/10.1103/PhysRevC.90.024303.

[54] A. Gottardo *et al. Physics Letters B*, **772**, 359 (2017). ISSN 0370-2693. URL https://www.sciencedirect.com/science/article/pii/S0370269317305269.

[55] M. Madurga, S. V. Paulauskas, R. Grzywacz, D. Miller, D. W. Bardayan, J. C. Batchelder, N. T. Brewer, J. A. Cizewski, A. Fijałkowska, C. J. Gross, M. E. Howard, S. V. Ilyushkin, B. Manning, M. Matoš, A. J. Mendez, K. Miernik, S. W. Padgett, W. A. Peters, B. C. Rasco, A. Ratkiewicz, K. P. Rykaczewski, D. W. Stracener, E. H. Wang, M. Wolińska-Cichocka and E. F. Zganjar. *Phys. Rev. Lett.*, **117**, 092502 (2016). URL https://link.aps.org/doi/10.1103/PhysRevLett.117.092502.

[56] J. Tuli. *Nuclear Data Sheets*, **98**, 209 (2003). ISSN 0090-3752. URL https://www.sciencedirect.com/science/article/pii/S0090375203900020.

[57] P. Hoff and B. Fogelberg. *Nuclear Physics A*, **368**, 210 (1981).

[58] M. Alshudifat, R. Grzywacz, M. Madurga, C. Gross, K. Rykaczewski, J. Batchelder, C. Bingham, I. Borzov, N. Brewer, L. Cartegni *et al. Phys. Rev. C*, **93**, 044325 (2016).

[59] J. A. Winger, K. P. Rykaczewski, C. J. Gross, R. Grzywacz, J. C. Batchelder, C. Goodin, J. H. Hamilton, S. V. Ilyushkin, A. Korgul, W. Królas, S. N. Liddick, C. Mazzocchi, S. Padgett, A. Piechaczek, M. M. Rajabali, D. Shapira, E. F. Zganjar and J. Dobaczewski. *Phys. Rev. C*, **81**, 044303 (2010). URL https://link.aps.org/doi/10.1103/PhysRevC.81.044303.

[60] D. Verney, D. Testov, F. Ibrahim, Y. Penionzhkevich, B. Roussière, V. Smirnov, F. Didierjean, K. Flanagan, S. Franchoo, E. Kuznetsova *et al. Phys. Rev. C*, **95**, 054320 (2017).

[61] D. Testov. *Effect of shell closure N = 50 and N = 82 on the structure of very neutron-rich nuclei produced at ALTO : measurements of neutron emission probabilities and half lives of nuclei at astrophysical r-processes path*. Theses, Université Paris Sud - Paris XI (2014). URL https://tel.archives-ouvertes.fr/tel-01059803.

[62] T. Rząca-Urban, W. Urban, J. Durell, A. Smith and I. Ahmad. *Phys. Rev. C*, **76**, 027302 (2007).

[63] J. Hwang, J. Hamilton, A. Ramayya, N. Brewer, Y. Luo, J. Rasmussen and S. Zhu. *Phys. Rev. C*, **84**, 024305 (2011).

[64] E. Sahin, G. De Angelis, G. Duchene, T. Faul, A. Gadea, A. Lisetskiy, D. Ackermann, A. Algora, S. Aydin, F. Azaiez *et al. Nuclear Physics A*, **893**, 1 (2012).

[65] D. Thisse. *Étude des états particule-trou dans les noyaux de la région du Ni avec le spectromètre γ-Ball*. Ph.D. thesis, Université Paris-Saclay (2021).

[66] O. Perru, D. Verney, F. Ibrahim, O. Bajeat, C. Bourgeois, F. Clapier, E. Cottereau, C. Donzaud, S. Du, M. Ducourtieux *et al. Eur. Phys. J. A*, **28**, 307 (2006).

[67] J. S. Thomas, D. W. Bardayan, J. C. Blackmon, J. A. Cizewski, U. Greife, C. J. Gross, M. S. Johnson, K. L. Jones, R. L. Kozub, J. F. Liang, R. J. Livesay, Z. Ma, B. H. Moazen, C. D. Nesaraja, D. Shapira and M. S. Smith. *Phys. Rev. C*, **71**, 021302 (2005). URL https://link.aps.org/doi/10.1103/PhysRevC.71.021302.

[68] J. S. Thomas, G. Arbanas, D. W. Bardayan, J. C. Blackmon, J. A. Cizewski, D. J. Dean, R. P. Fitzgerald, U. Greife, C. J. Gross, M. S. Johnson, K. L. Jones, R. L. Kozub, J. F. Liang, R. J. Livesay, Z. Ma, B. H. Moazen, C. D. Nesaraja, D. Shapira, M. S. Smith and D. W. Visser. *Phys. Rev. C*, **76**, 044302 (2007). URL https://link.aps.org/doi/10.1103/PhysRevC.76.044302.

[69] K. Kolos, D. Verney, F. Ibrahim, F. Le Blanc, S. Franchoo, K. Sieja, F. Nowacki, C. Bonnin, M. Cheikh Mhamed, P. V. Cuong, F. Didierjean, G. Duchêne, S. Essabaa, G. Germogli, L. H. Khiem, C. Lau, I. Matea, M. Niikura, B. Roussière, I. Stefan, D. Testov and J.-C. Thomas. *Phys. Rev. C*, **88**, 047301 (2013). doi:10.1103/PhysRevC.88.047301. URL https://link.aps.org/doi/10.1103/PhysRevC.88.047301.

[70] M. Lebois, D. Verney, F. Ibrahim, S. Essabaa, F. Azaiez, M. C. Mhamed, E. Cottereau, P. V. Cuong, M. Ferraton, K. Flanagan, S. Franchoo, D. Guillemaud-Mueller, F. Hammache, C. Lau, F. Le Blanc, J. F. Le Du, J. Libert, B. Mouginot, C. Petrache, B. Roussière, L. Sagui, N. de Séréville, I. Stefan and B. Tastet. *Phys. Rev. C*, **80**, 044308 (2009). URL https://link.aps.org/doi/10.1103/PhysRevC.80.044308.

[71] D. Verney, D. Testov, F. Ibrahim, Y. Penionzhkevich, B. Roussière, V. Smirnov, F. Didierjean, K. Flanagan, S. Franchoo, E. Kuznetsova, R. Li, B. Marsh, I. Matea, H. Pai, E. Sokol, I. Stefan and D. Suzuki. *Phys. Rev. C*, **95**, 054320 (2017). URL https://link.aps.org/doi/10.1103/PhysRevC.95.054320.

[72] C. Delafosse. *Etude des dérives monopolaires neutron au-delà du 78Ni par spectroscopie gamma avec BEDO à ALTO et AGATA au GANIL*. Ph.D. thesis (2018). URL http://www.theses.fr/2018SACLS199. Thèse de doctorat dirigée par Verney, David Structure et réactions nucléaires Université Paris-Saclay (ComUE) 2018.

[73] J. Agramunt, A. García, A. Algora, J. Äystö, R. Caballero-Folch, F. Calviño, D. Cano-Ott, G. Cortés, C. Domingo-Pardo, T. Eronen, W. Gelletly, M. Gómez-Hornillos, J. Hakala, A. Jokinen, D. Jordan, A. Kankainen, V. Kolkinen, T. Martínez, P. Mason, I. Moore, H. Penttilä, Z. Podolyák, M. Reponen, A. Riego, J. Rissanen, B. Rubio, A. Saastamoinen, J. Tain and E. Valencia. *Nucl. Data Sheets*, **120**, 74 (2014). ISSN 0090-3752. URL https://www.sciencedirect.com/science/article/pii/S0090375214004621.

[74] J. Kratz, H. Franz, N. Kaffrel and G. Herrmann. *Nuclear Physics A*, **250**, 13 (1975). ISSN 0375-9474. URL https://www.sciencedirect.com/science/article/pii/0375947475901979.

[75] M. Hurdus and L. Tomlinson. *Journal of Inorganic and Nuclear Chemistry*, **37**, 1 (1975). ISSN 0022-1902. URL https://www.sciencedirect.com/science/article/pii/002219027580114X.

[76] C. Mazzocchi *et al. Phys. Rev. C*, **92**, 054317 (2015). URL https://link.aps.org/doi/10.1103/PhysRevC.92.054317.

[77] T. Materna, W. Urban, K. Sieja, U. Köster, H. Faust, M. Czerwiński, T. Rząca-Urban, C. Bernards, C. Fransen, J. Jolie, J.-M. Regis, T. Thomas and N. Warr. *Phys. Rev. C*, **92**, 034305 (2015). URL https://link.aps.org/doi/10.1103/PhysRevC.92.034305.

[78] A. Korgul, K. P. Rykaczewski, R. Grzywacz, C. R. Bingham, N. T. Brewer, A. A. Ciemny, C. J. Gross, C. Jost, M. Karny, M. Madurga, C. Mazzocchi, A. J. Mendez, K. Miernik, D. Miller, S. Padgett, S. V. Paulauskas, D. W. Stracener and M. Wolińska-Cichocka. *Phys. Rev. C*, **92**, 054318 (2015). URL https://link.aps.org/doi/10.1103/PhysRevC.92.054318.

[79] E. F. Jones, P. M. Gore, J. H. Hamilton, A. V. Ramayya, J. K. Hwang, A. P. deLima, S. J. Zhu, C. J. Beyer, Y. X. Luo, W. C. Ma, J. O. Rasmussen, I. Y. Lee, S. C. Wu, T. N. Ginter, M. Stoyer, J. D. Cole, A. V. Daniel, G. M. Ter-Akopian and R. Donangelo. *Phys. Rev. C*, **73**, 017301 (2006). URL https://link.aps.org/doi/10.1103/PhysRevC.73.017301.

[80] K. Li, J. H. Hamilton, A. V. Ramayya, S. H. Liu, X. Q. Zhang, N. T. Brewer, J. K. Hwang, C. Goodin, S. J. Zhu, Y. X. Luo, J. O. Ramussen, I. Y. Lee, S. C. Wu, R. Donangelo, A. V. Daniel, G. M. Ter-Akopian, Y. T. Oganessian, A. Unzhakova, J. D. Cole, W. C. Ma and M. A. Stoyer. *International Journal of Modern Physics E*, **20**, 1825 (2011). URL https://doi.org/10.1142/S0218301311019635.

[81] J. Litzinger, A. Blazhev, A. Dewald, F. Didierjean, G. Duchêne, C. Fransen, R. Lozeva, K. Sieja, D. Verney, G. de Angelis, D. Bazzacco, B. Birkenbach, S. Bottoni, A. Bracco, T. Braunroth, B. Cederwall, L. Corradi, F. C. L. Crespi, P. Désesquelles, J. Eberth, E. Ellinger, E. Farnea, E. Fioretto, R. Gernhäuser, A. Goasduff, A. Görgen, A. Gottardo, J. Grebosz, M. Hackstein, H. Hess, F. Ibrahim, J. Jolie, A. Jungclaus, K. Kolos, W. Korten, S. Leoni, S. Lunardi, A. Maj, R. Menegazzo, D. Mengoni, C. Michelagnoli, T. Mijatovic, B. Million, O. Möller, V. Modamio, G. Montagnoli, D. Montanari, A. I. Morales, D. R. Napoli, M. Niikura, G. Pollarolo, A. Pullia, B. Quintana, F. Recchia, P. Reiter, D. Rosso, E. Sahin, M. D. Salsac, F. Scarlassara, P.-A. Söderström, A. M. Stefanini, O. Stezowski, S. Szilner, C. Theisen, J. J. Valiente Dobón, V. Vandone and A. Vogt. *Phys. Rev. C*, **92**, 064322 (2015). URL https://link.aps.org/doi/10.1103/PhysRevC.92.064322.

[82] F. Ibrahim, D. Verney, M. Lebois, B. Roussière, S. Essabaa, S. Franchoo, S. Gales, D. Guillemaud-Mueller, C. Lau, F. Le Blanc *et al. Nuclear Physics A*, **787**, 110 (2007).

[83] A. Etilé, D. Verney, N. Arsenyev, J. Bettane, I. Borzov, M. C. Mhamed, P. Cuong, C. Delafosse, F. Didierjean, C. Gaulard *et al.* *Phys. Rev. C*, **91**, 064317 (2015).

[84] T. Martínez, D. Cano-Ott, J. Castilla, A. Garcia, J. Marin, G. Martinez, E. Mendoza, C. Santos, F. Tera, D. Villamarin, J. Agramunt, A. Algora, C. Domingo, M. Jordan, B. Rubio, J. Taín, C. Bhattacharya, K. Banerjee, S. Bhattacharya, P. Roy, J. Meena, S. Kundu, G. Mukherjee, T. Ghosh, T. Rana, R. Pandey, A. Saxena, B. Behera, H. Penttilä, A. Jokinen, S. Rinta-Antila, C. Guerrero and M. Ovejero. *Nuclear Data Sheets*, **120**, 78 (2014). ISSN 0090-3752. URL https://www.sciencedirect.com/science/article/pii/S0090375214004633.

[85] D. Testov, D. Verney, B. Roussière, J. Bettane, F. Didierjean, K. Flanagan, S. Franchoo, F. Ibrahim, E. Kuznetsova, R. Li *et al.* *Nuclear Instruments and Methods in Physics Research Section A: Accelerators, Spectrometers, Detectors and Associated Equipment*, **815**, 96 (2016).

[86] A. Étilé. *Etude de la structure nucléaire de noyaux exotiques à ALTO : développements et résultats de deux nouvelles installations*. Ph.D. thesis (2014). URL http://www.theses.fr/2014PA112396. Thèse de doctorat dirigée par Audi, Georges Physique Paris 11 2014.

[87] V. Kolhinen, M. Bussmann, D. Habs, J. Neumayr, U. Schramm, C. Schürmann, M. Sewtz, J. Szerypo and P. Thirolf. *Nuclear Instruments and Methods in Physics Research Section B: Beam Interactions with Materials and Atoms*, **266**, 4547 (2008). ISSN 0168-583X. URL https://www.sciencedirect.com/science/article/pii/S0168583X08007738. Proceedings of the XVth International Conference on Electromagnetic Isotope Separators and Techniques Related to their Applications.

[88] G. Tocabens. *Conception et exploitation d'un dispositif pour la spectroscopie d'électrons de conversion β-retardés, application à l'étude de la région des noyaux riches en neutrons de masse A˜100*. Ph.D. thesis, Université Paris-Saclay (2022).

[89] D. Verney (2016). URL https://hal.in2p3.fr/medihal-01524177.

[90] S. Tusseau-Nenez, B. Roussière, N. Barré-Boscher, A. Gottberg, S. Corradetti, A. Andrighetto, M. C. Mhamed, S. Essabaa, H. Franberg-Delahaye, J. Grinyer *et al.* *Nuclear Instruments and Methods in Physics Research Section B: Beam Interactions with Materials and Atoms*, **370**, 19 (2016).

[91] http://paris.ifj.edu.pl/index.php?lng=en.

[92] C. Fontbonne. *"Acquisition multiparamétrique de signaux de décroissance radioactive pour la correction des défauts instrumentaux : application à la mesure de la durée de vie du 19Ne"*. Ph.D. thesis, Normandy Université (2017).

[93] J. Ärje, J. Äystö, H. Hyvönen, P. Taskinen, V. Koponen, J. Honkanen, K. Valli, A. Hautojärvi and K. Vierinen. *Nuclear Instruments and Methods in Physics*

Research Section A: Accelerators, Spectrometers, Detectors and Associated Equipment, **247**, 431 (1986). ISSN 0168-9002. URL https://www.sciencedirect.com/science/article/pii/0168900286904043.

[94] P. Karvonen, I. Moore, T. Sonoda, T. Kessler, H. Penttilä, K. Peräjärvi, P. Ronkanen and J. Äystö. *Nuclear Instruments and Methods in Physics Research Section B: Beam Interactions with Materials and Atoms*, **266**, 4794 (2008). ISSN 0168-583X. URL https://www.sciencedirect.com/science/article/pii/S0168583X08009191.

[95] I. Moore, T. Eronen, D. Gorelov, J. Hakala, A. Jokinen, A. Kankainen, V. Kolhinen, J. Koponen, H. Penttilä, I. Pohjalainen, M. Reponen, J. Rissanen, A. Saastamoinen, S. Rinta-Antila, V. Sonnenschein and J. Äystö. *Nuclear Instruments and Methods in Physics Research Section B: Beam Interactions with Materials and Atoms*, **317**, 208 (2013). ISSN 0168-583X. URL https://www.sciencedirect.com/science/article/pii/S0168583X13007143. XVIth International Conference on ElectroMagnetic Isotope Separators and Techniques Related to their Applications, December 2–7, 2012 at Matsue, Japan.

[96] A. Nieminen, J. Huikari, A. Jokinen, J. Äystö, P. Campbell and E. Cochrane. *Nuclear Instruments and Methods in Physics Research Section A: Accelerators, Spectrometers, Detectors and Associated Equipment*, **469**, 244 (2001). ISSN 0168-9002. URL https://www.sciencedirect.com/science/article/pii/S0168900200007506.

[97] A. Giatzoglou, T. Poomaradee, I. Pohjalainen, S. Rinta-Antila, I. D. Moore, P. M. Walker, L. Marmugi and F. Renzoni. *Nuclear Instruments and Methods in Physics Research Section A: Accelerators, Spectrometers, Detectors and Associated Equipment*, **908**, 367 (2018). ISSN 0168-9002. URL https://www.sciencedirect.com/science/article/pii/S0168900218310532.

[98] L. S. Brown and G. Gabrielse. *Rev. Mod. Phys.*, **58**, 233 (1986). URL https://link.aps.org/doi/10.1103/RevModPhys.58.233.

[99] K. Blaum. *Physics Reports*, **425**, 1 (2006). ISSN 0370-1573. doi:https://doi.org/10.1016/j.physrep.2005.10.011. URL https://www.sciencedirect.com/science/article/pii/S0370157305004643.

[100] Eronen, T., Kolhinen, V. S., Elomaa, V. -V., Gorelov, D., Hager, U., Hakala, J., Jokinen, A., Kankainen, A., Karvonen, P., Kopecky, S., Moore, I. D., Penttilä, H., Rahaman, S., Rinta-Antila, S., Rissanen, J., Saastamoinen, A., Szerypo, J., Weber, C. and Äystö, J. *Eur. Phys. J. A*, **48**, 46 (2012). doi:10.1140/epja/i2012-12046-1. URL https://doi.org/10.1140/epja/i2012-12046-1.

[101] L. Canete. *High precision mass measurements for nuclear astrophysics*. Ph.D. thesis, University of Jyväskylä (2019).

[102] G. Savard, G. Bollen, H.-J. Kluge, R. Moore, T. Otto, L. Schweikhard, H. Stolzenberg, U. Wiess *et al. Physics Letters A*, **158**, 247 (1991).

[103] https://www.nipne.ro/.

[104] https://nutaq.com/.

[105] P. Rahkila. *Nuclear Instruments and Methods in Physics Research Section A: Accelerators, Spectrometers, Detectors and Associated Equipment*, **595**, 637 (2008). ISSN 0168-9002. URL https://www.sciencedirect.com/science/article/pii/S0168900208011698.

[106] A. Negret and B. Singh. *Nuclear Data Sheets*, **124**, 1 (2015). ISSN 0090-3752. URL https://www.sciencedirect.com/science/article/pii/S0090375214007455.

[107] https://www.nndc.bnl.gov/.

[108] https://atrium.in2p3.fr/nuxeo/nxpath/default/Atrium/sections/Public/IPNL/MatNuc/SToGS_UsersGuide@view_documents?tabIds=%3A&conversationId=0NXMAIN1.

[109] https://geant4.web.cern.ch/.

[110] T. Kibedi, T. Burrows, M. B. Trzhaskovskaya, P. M. Davidson and C. W. Nestor Jr. *Nuclear Instruments and Methods in Physics Research Section A: Accelerators, Spectrometers, Detectors and Associated Equipment*, **589**, 202 (2008).

[111] https://www.nndc.bnl.gov/logft/.

[112] K. Miernik, K. P. Rykaczewski, C. J. Gross, R. Grzywacz, M. Madurga, D. Miller, J. C. Batchelder, N. T. Brewer, C. U. Jost, K. Kolos, A. Korgul, C. Mazzocchi, A. J. Mendez, Y. Liu, S. V. Paulauskas, D. W. Stracener, J. A. Winger, M. Wolińska-Cichocka and E. F. Zganjar. *Phys. Rev. C*, **90**, 034311 (2014). URL https://link.aps.org/doi/10.1103/PhysRevC.90.034311.

[113] J. A. Winger, S. V. Ilyushkin, K. P. Rykaczewski, C. J. Gross, J. C. Batchelder, C. Goodin, R. Grzywacz, J. H. Hamilton, A. Korgul, W. Królas, S. N. Liddick, C. Mazzocchi, S. Padgett, A. Piechaczek, M. M. Rajabali, D. Shapira, E. F. Zganjar and I. N. Borzov. *Phys. Rev. Lett.*, **102**, 142502 (2009). URL https://link.aps.org/doi/10.1103/PhysRevLett.102.142502.

[114] M. Stryjczyk. *Shape coexistence in the nickel (Z= 28) and mercury (Z= 80) regions probed through decay studies*. Ph.D. thesis, Stryjczyk, Marek (2021).

[115] J. Hardy, L. Carraz, B. Jonson and P. Hansen. *Physics Letters B*, **71**, 307 (1977). ISSN 0370-2693. URL https://www.sciencedirect.com/science/article/pii/0370269377902234.

[116] M. Martini, S. Péru and S. Goriely. *Phys. Rev. C*, **89**, 044306 (2014).

[117] M. Martini and S. Peru, private communication.

[118] S. Peru and I. Deloncle, private communication.

[119] D. Negi, M. Wiedeking, E. Lanza, E. Litvinova, A. Vitturi, R. Bark, L. Bernstein, D. Bleuel, S. Bvumbi, T. Bucher *et al. Phys. Rev. C*, **94**, 024332 (2016).

[120] K. Sieja, F. Nowacki, K. Langanke and G. Martínez-Pinedo. *Phys. Rev. C*, **79**, 064310 (2009). URL https://link.aps.org/doi/10.1103/PhysRevC.79.064310.

[121] K. Sieja, T. R. Rodríguez, K. Kolos and D. Verney. *Phys. Rev. C*, **88**, 034327 (2013). URL https://link.aps.org/doi/10.1103/PhysRevC.88.034327.

[122] M. Czerwiński, T. Rząca-Urban, W. Urban, P. Bączyk, K. Sieja, B. M. Nyakó, J. Timár, I. Kuti, T. G. Tornyi, L. Atanasova, A. Blanc, M. Jentschel, P. Mutti, U. Köster, T. Soldner, G. de France, G. S. Simpson and C. A. Ur. *Phys. Rev. C*, **92**, 014328 (2015). URL https://link.aps.org/doi/10.1103/PhysRevC.92.014328.

[123] B. P. Abbott, R. Abbott, T. Abbott, F. Acernese, K. Ackley, C. Adams, T. Adams, P. Addesso, R. Adhikari, V. Adya *et al. Phys. Rev. Lett.*, **119**, 161101 (2017).

[124] B. P. Abbott, R. Abbott, T. D. Abbott, F. Acernese, K. Ackley, C. Adams, T. Adams, P. Addesso, R. X.Adhikari *et al. The Astrophysical Journal Letters*, **848**, L13 (2017). URL http://stacks.iop.org/2041-8205/848/i=2/a=L13.

[125] A. Sneppen, D. Watson, A. Bauswein, O. Just, R. Kotak, E. Nakar, D. Poznanski and S. Sim. *Nature*, **614**, 436 (2023). doi:10.1038/s41586-022-05616-x. URL https://doi.org/10.1038/s41586-022-05616-x.

[126] D. Watson, C. J. Hansen, J. Selsing, A. Koch, D. B. Malesani, A. C. Andersen, J. P. Fynbo, A. Arcones, A. Bauswein, S. Covino *et al. Nature*, **574**, 497 (2019).

[127] M. P. Reiter, S. Ayet San Andrés, S. Nikas, J. Lippuner, C. Andreoiu, C. Babcock, B. R. Barquest, J. Bollig, T. Brunner, T. Dickel, J. Dilling, I. Dillmann, E. Dunling, G. Gwinner, L. Graham, C. Hornung, R. Klawitter, B. Kootte, A. A. Kwiatkowski, Y. Lan, D. Lascar, K. G. Leach, E. Leistenschneider, G. Martínez-Pinedo, J. E. McKay, S. F. Paul, W. R. Plaß, L. Roberts, H. Schatz, C. Scheidenberger, A. Sieverding, R. Steinbrügge, R. Thompson, M. E. Wieser, C. Will and D. Welch. *Phys. Rev. C*, **101**, 025803 (2020). URL https://link.aps.org/doi/10.1103/PhysRevC.101.025803.

[128] S. Nikas, G. M. Pinedo *et al.* In *Journal of Physics: Conference Series*, volume 1668, page 012029. IOP Publishing (2020).

[129] J. Lippuner, R. Fernández, L. F. Roberts, F. Foucart, D. Kasen, B. D. Metzger and C. D. Ott. *Monthly Notices of the Royal Astronomical Society*, **472**, 904 (2017). URL http://dx.doi.org/10.1093/mnras/stx1987.

[130] S. Goriely. *Astron. Astrophys.*, **342**, 881 (1999).

[131] S. Goriely, E. Khan and M. Samyn. *Nuclear Physics A*, **739**, 331 (2004). ISSN 0375-9474. URL https://www.sciencedirect.com/science/article/pii/S0375947404006578.

[132] E. Litvinova, P. Ring, V. Tselyaev and K. Langanke. *Phys. Rev. C*, **79**, 054312 (2009). URL https://link.aps.org/doi/10.1103/PhysRevC.79.054312.

[133] I. Daoutidis and S. Goriely. *Phys. Rev. C*, **86**, 034328 (2012). URL https://link.aps.org/doi/10.1103/PhysRevC.86.034328.

[134] A. Bracco, E. Lanza and A. Tamii. *Prog. Part. Nucl. Phys.*, **106**, 360 (2019). ISSN 0146-6410. URL https://www.sciencedirect.com/science/article/pii/S0146641019300031.

[135] S. N. Liddick, A. Spyrou, B. P. Crider, F. Naqvi, A.-C. Larsen, M. Guttormsen, M. Mumpower, R. Surman, G. Perdikakis, D. L. Bleuel *et al. Phys. Rev. Lett.*, **116**, 242502 (2016).

[136] S. Goriely. *Physics Letters B*, **436**, 10 (1998). ISSN 0370-2693. URL https://www.sciencedirect.com/science/article/pii/S0370269398009071.

[137] S. Goriely, S. Hilaire and A. J. Koning. *Astronomy & Astrophysics*, **487**, 767 (2008). doi:10.1051/0004-6361:20078825. URL https://doi.org/10.1051%2F0004-6361%3A20078825.

[138] S. Goriely and E. Khan. *Nuclear Physics A*, **706**, 217–232 (2002). ISSN 0375-9474. doi:10.1016/S0375-9474(02)00860-6. URL http://www.sciencedirect.com/science/article/pii/S0375947402008606.

[139] S. Goriely, E. Khan and M. Samyn. *Nuclear Physics A*, **739**, 331–352 (2004). ISSN 0375-9474. URL http://www.sciencedirect.com/science/article/pii/S0375947404006578.

[140] J. Kopecky and M. Uhl. *Phys. Rev. C*, **41**, 1941–1955 (1990). URL http://link.aps.org/doi/10.1103/PhysRevC.41.1941.

[141] P. Axel. *Phys. Rev.*, **126**, 671–683 (1962). URL http://link.aps.org/doi/10.1103/PhysRev.126.671.

[142] S. Goriely. *Physics Letters B*, **436**, 10–18 (1998). ISSN 0370-2693. URL http://www.sciencedirect.com/science/article/pii/S0370269398009071.

[143] P. Möller, A. Sierk, T. Ichikawa and H. Sagawa. *Atomic Data and Nuclear Data Tables*, **109-110**, 1 (2016). ISSN 0092-640X. URL https://www.sciencedirect.com/science/article/pii/S0092640X1600005X.

[144] V. Konig and J. P. Delaroche. *Nuclear Physics A*, **361**, 189 (1981). doi:10.1016/0375-9474(81)90220-8.

[145] W. Dilg, W. Schantl, H. Vonach and M. Uhl. *Nuclear Physics A*, **217**, 269 (1973). ISSN 0375-9474. doi:10.1016/0375-9474(73)90297-1.

[146] S. Nikas, G. Perdikakis, M. Beard, R. Surman, M. Mumpower and P. Tsintari. *arXiv preprint arXiv:2010.01698* (2020).

[147] P. Denissenkov, G. Perdikakis, F. Herwig, H. Schatz, C. Ritter, M. Pignatari, S. Jones, S. Nikas and A. Spyrou. *Journal of Physics G: Nuclear and Particle Physics*, **45**, 055203 (2018).

[148] R. H. Cyburt, A. M. Amthor, R. Ferguson, Z. Meisel, K. Smith, S. Warren, A. Heger, R. D. Hoffman, T. Rauscher, A. Sakharuk, H. Schatz, F. K. Thielemann and M. Wiescher. *The Astrophysical Journal Supplement Series*, **189**, 240 (2010). URL https://dx.doi.org/10.1088/0067-0049/189/1/240.

[149] Y. Xu, S. Goriely, A. Jorissen, G. L. Chen and M. Arnould. *Astron. Astrophys.*, **549**, A106 (2013). doi:10.1051/0004-6361/201220537.

[150] M. Guttormsen, T. Tveter, L. Bergholt, F. Ingebretsen and J. Rekstad. *Nuclear Instruments and Methods in Physics Research Section A: Accelerators, Spectrometers, Detectors and Associated Equipment*, **374**, 371 (1996). ISSN 0168-9002. URL https://www.sciencedirect.com/science/article/pii/0168900296001970.

[151] M. Mumpower, R. Surman, G. McLaughlin and A. Aprahamian. *Prog. Part. Nucl. Phys.*, **86**, 86 (2016). ISSN 0146-6410. URL https://www.sciencedirect.com/science/article/pii/S0146641015000897.

[152] S. Goriely. *Physics Letters B*, **436**, 10 (1998). ISSN 0370-2693. doi:https://doi.org/10.1016/S0370-2693(98)00907-1. URL http://www.sciencedirect.com/science/article/pii/S0370269398009071.

[153] X. Roca-Maza, G. Pozzi, M. Brenna, K. Mizuyama and G. Colò. *Phys. Rev. C*, **85**, 024601 (2012).

[154] M. Spieker, A. Heusler, B. A. Brown, T. Faestermann, R. Hertenberger, G. Potel, M. Scheck, N. Tsoneva, M. Weinert, H.-F. Wirth and A. Zilges. *Phys. Rev. Lett.*, **125**, 102503 (2020). doi:10.1103/PhysRevLett.125.102503.

[155] A. Maj, F. Camera and I. F. J. im. Henryka Niewodniczanskiego. *PARIS White Book*. Henryk Niewodniczanski Institute of Nuclear Physics. Polish Academy of Sciences (2021). ISBN 9788363542221. URL https://books.google.fr/books?id=NTeHzgEACAAJ.

[156] T. Eronen, V. Kolhinen, V.-V. Elomaa, D. Gorelov, U. Hager, J. Hakala, A. Jokinen, A. Kankainen, P. Karvonen, S. Kopecky *et al. Three decades of research using IGISOL technique at the University of Jyväskylä: A Portrait of the Ion Guide Isotope Separator On-Line Facility in Jyväskylä*, pages 61–81 (2014).

[157] http://faster.in2p3.fr.

[158] E. Litvinova, P. Ring and V. Tselyaev. *Phys. Rev. C*, **78**, 014312 (2008). doi:10.1103/PhysRevC.78.014312. URL https://link.aps.org/doi/10.1103/PhysRevC.78.014312.

[159] *HFB results based on the Gogny Force, Calculated Database*. https://www-phynu.cea.fr/science_en_ligne/carte_potentiels_microscopiques/carte_potentiel_nucleaire_eng.htm#tech.